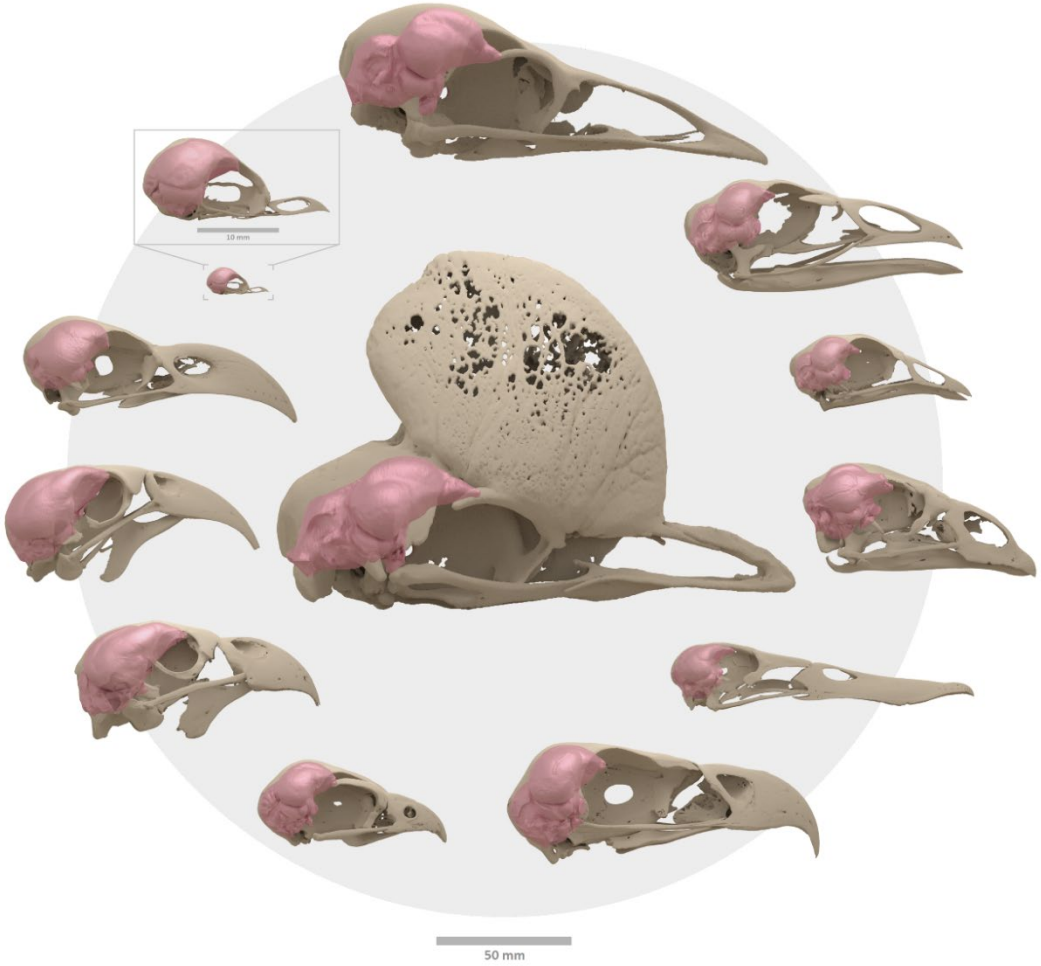

Cephalic and encephalic arterial anatomy and perfusion in birds and mammals assessed via microsphere circulation, contrast injection, and osteoforamina measurement

Thomas Jack Nelson

A thesis submitted toward the degree of

Doctor of Philosophy

August 2022

The University of Adelaide
School of Biological Sciences
Department of Ecology and Evolutionary Biology

SCHOOL OF
BIOLOGICAL SCIENCES

THE UNIVERSITY of ADELAIDE

Title Image: Different avian species present with vastly different brain architecture, presenting problems for the direct comparison of intelligence via measurements of absolute brain metabolism. Clockwise from top are an emu, turkey, malleefowl, cape barren goose, Australian shoveler, wedge-tailed eagle, peregrine falcon, kakapo, kea, white necked raven, and spotted pardalote. Centre is a southern cassowary. Specimens from Chapter 3 of this thesis. Rendered images were produced by exporting segmented structures from Avizo into Blender 2.90.1 (Open Source, www.blender.org).

Dedicated to my family and friends.

“I not only use all the brains that I have, but all that I can borrow.”

– Woodrow Wilson

DECLARATION

I certify that this work contains no material which has been accepted for the award of any other degree or diploma in my name, in any university or other tertiary institution and, to the best of my knowledge and belief, contains no material previously published or written by another person, except where due reference has been made in the text. In addition, I certify that no part of this work will, in the future, be used in a submission in my name, for any other degree or diploma in any university or other tertiary institution without the prior approval of the University of Adelaide and where applicable, any partner institution responsible for the joint award of this degree.

I give permission for the digital version of my thesis to be made available on the web, via the University's digital research repository, the Library Search and also through web search engines, unless permission has been granted by the University to restrict access for a period of time.

I acknowledge the support I have received for my research through the provision of an Australian Government Research Training Program Scholarship.

Thomas Jack Nelson

August 2022

ACKNOWLEDGMENTS

I first wish to express my appreciation of my supervisor Professor Roger Seymour for his considerable intellectual support, patience, and compassion throughout the duration of my candidature. Thank you to Doctor Emma Sherratt for your understanding, guidance, and generous help during the crunch which went above and beyond. Thank you to Associate Professor David Paton for his backing and encouragement. Doctor Marc Jones, thank you for your constructive discussions, valuable advice, and willingness to dedicate your time to my constant questions. Thanks to Doctor Edward Snelling for being a tremendous source of support and brainpower. Thank you to Associate Professor Phillip Cassey for your enthusiasm and dedication. I look forward to working with all of you on future projects.

An enormous thank you to Doctor Qiaohui 'Vivi' Hu. I will not forget working side by side with you on so many peculiar problems, on late nights and early mornings, through harrowing and hilarious experiences. I would not have been able to complete this thesis without your camaraderie. I also appreciate the long discussions and many jokes I shared with Doctor Karl Jones across my candidature. Further gratitude goes to Vanya Bosiocic. Thank you all for making incredible office and lab mates. How about a food challenge?

All my love goes to my parents Jackie and Kevin who have supported me all of my life and nurtured my inquisitive nature that led me to pursue science. Love you mum and dad! Just as much adoration for my siblings Sam and Max and their partners Sammy and Grace who have been there for me through thick and thin. And love to Olive, Ivy, Holly, and Matilda, the very best good girls there are! Here's to all of you!

I am deeply grateful to those who provided their time, assistance, and kind words across the duration of my degree. I thank Ruth Williams and Doctor Agatha Labrinidis from Adelaide Microscopy, Centre for Advanced Microscopy and Microanalysis, The University of Adelaide. X-ray Micro CT scans used in each of the chapters of this thesis were performed on the Skyscan1076 and Skyscan1276 Micro CT machines at Adelaide Microscopy. Particularly, thanks to Ruth for your expert advice, humour, and drive. Thank you to Ben Whigmore and Doctor Bill Loftus of Sound Radiology for always being keen to provide help with access to your facilities. Scans from multiple chapters of this thesis were performed at Sound Radiology, Parkside, South Australia, on a Philips Ingenuity Core 128 scanner. Further thanks are in order to Doctor Steve Delean; Christopher Leigh; Amy Watson; Darcy MacCartie; John Snelling; Professor Craig White; Doctor David Taggart, and Professor Shane Maloney for their contributions.

I appreciate the work of employees and volunteers from the South Australian Museum, without whom my thesis would not be what it is. Thank you to Maya Penck and Doctor Philippa Horton for their assistance in accessing avian specimens for my work. Thank

you to David Stemmer and Doctor Cath Kemper for their cheerful assistance in accessing the museums world class maceration facilities at Bolivar, South Australia. Thank you to Doctor Mark Hutchinson and Doctor Alessandro Palci for their assistance in accessing the museum facilities and computers.

Thank you to Dona Kireta and Andre Scaffidi for being an unceasing wellspring of kindness and friendship all throughout my time at university and beyond. All my love to Georgia, Tom, Ellie, and Ziggy. Katherine Hill - my clever statistician and source of unending support. Thank you in so many ways for helping push me when I could not push myself, finding mistakes when I was lost, and being there to pick up the pieces. Thank you for your sacrifices in helping to keep Brian going when he could not or would not. Thank you for everything Bug!

Thank you to everyone who made up the incredible and supportive cohort who helped me across my prolonged university studies – particularly Molly; Jimmy; Erica; Gus; Zeus; Hannah; Bowie; Rhys; Chris; James; Tim; Henry; Alex; James; Sarah; Ray; Alan; Peri; Brock; Alana; James; Kiri; Nicole; Colette; Adam; Charlotte; Andrew; Tyler; Eilish; Keira; Eliza; Lachlan; Tim; Ruby; Kendra; Theresa; Yan Hao; Elisabetta; Martino; Miriam; Chris; Chris; and Sally. Cara McMeel: thank you for being such a wonderful person and positive influence on my psyche. Tasya, your understated, outsized, joyful support holds a great significance. Thank you all for providing an environment that made it all worth it!

To Ana Bellico: for your patience and compassion across so many late nights, early mornings, missed dinners, and skipped breakfasts, thank you from the bottom of my heart. Jordan, Chris, Liz, Louise, Koko, and the gang – you know what you did. Samantha Farrow and Mary Kinton – unforgettable. An immense amount of gratitude to Rowan, Emma, Sarah, Chris, Stephen, Curtis, Ray, Meryl, Eira, Mariana, Jo, Grace, Julia, Laura, Hannah, Svjetlana, Edo, and Lara for putting up with me.

Thank you to Doctor Martha Landman and Doctor Charles Christie for helping keep me sane throughout the process.

I am grateful for feedback received on early versions of my chapters at the Australian and New Zealand Society for Comparative Physiology and Biochemistry (ANZSCPB) Conferences at Fowlers Gap Arid Zone Research Station (University of New South Wales) in 2015; Western Sydney University, Hawkesbury in 2016; James Cook University's Daintree Rainforest Observatory in 2018; and at the University of Western Australia in 2019.

I thank the examiners of this thesis for their helpful and detailed input which greatly improved the quality of the work.

I acknowledge the support I have received for my research through the provision of an Australian Government Research Training Program Scholarship. Thank you to the School of Biological Sciences and my supervisor Professor Roger Seymour for providing

financial support at the end of my candidature – I would not have been able to complete this journey without this assistance and I will forever be grateful for this generosity. This research was supported by the Australian Research Council (DP120102081 and DP170104952). Doctor Marc Jones was supported by an Australian Research Grant (DE130101567). Doctor Edward Snelling holds a South African Claude Leon Foundation Postdoctoral Fellowship. Doctor Emma Sherratt holds an Australian Research Council Future Fellowship.

I would also like to acknowledge the sacrifice made by the animals that were the research subjects in this thesis, sincerely and in good conscience. Approval of the use of euthanised animals and animal tissues for the investigations herein was provided by University of Adelaide Animal Ethics Committee (S-2011-223 and S-2017-058).

Finally, I would like to thank anyone else who has helped me over these past years – I haven't forgotten you!

This thesis was written on Kaurna land. Always was, always will be.

ABSTRACT

Traditionally, great emphasis has been placed on the perceived importance of measurements of brain size in examinations of animal cognition and intelligence, where larger is expected to be better. However, rather than rely on absolute brain size, relative brain size, encephalisation quotients, or other such indexes, the goal of this thesis is to infer animal cognition through the measurement of brain metabolism. Cerebral metabolism relies upon a constant supply of glucose and oxygen delivered via blood flow, and hence measurement of cerebral perfusion rate works as a proxy for cerebral metabolism. The experimental work contained in this thesis explored cephalic circulation in birds and mammals and applied current best-practices in blood flow measurement to these clades. In the developing western grey kangaroos a biphasic growth pattern for brain growth was found, with a break 620 g that coincides with the period immediately prior to first pouch exit. Brain perfusion increases constantly across the life history sequence, scaling according to $V_{br}^{1.14\pm0.07}$. The proportion of blood flow through the major cerebral feeder arteries was found to be constant across development, with internal carotids supplying about 70-80% of brain perfusion with the remaining 20-30% coming from the vertebral arteries. In the metabolic scaling of brain metabolism in avian taxa, aves are shown to possess scaling exponents for blood flow rate on brain volume ($V_{br}^{0.77\pm0.12}$) similar to haplorrhine primates ($V_{br}^{0.95\pm0.08}$). Some but not all avian clades exhibit scaling rates in line with those of primates, lending credence to the assertion that cognition in primates and some birds evolved convergently. A three-dimensional map and description chicken cephalic arteries is produced, with the major connections to the braincase identified and a novel vascular structure discovered. Finally brain perfusion rates in chickens obtained from microsphere perfusion matched those obtained from foramen measurements in immature hens and roosters, but not in laying hens. A higher volumetric perfusion rate in the forebrain of laying hens is suggested to be related to a significant change in cognitive behaviour in adult hens to facilitate raising of chicks. Much of the thesis is centred around the how blood flow relates to brain metabolism in order to make inferences about cognition and intelligence. However, the examination of cognition is complex, and often subjective. The limited scope of the current literature only affords a snapshot of the relationship between foramina, blood flow, cerebral metabolism, and intelligence. As it stands, currently linking cerebral metabolism directly to intelligence across disparate taxa is a difficult task due to differences in brain architecture and regional metabolism, and how different brain regions impact cognition and intelligence. These cognitive trade-offs must be pervasive throughout evolutionary history and the tree of life. In order to properly understand the interactions of cerebral metabolism and intelligence future investigations into the interactions of cerebral metabolism and intelligence should focus upon expanding the number of taxa assessed with this approach. This thesis also raises many questions and suggests areas of research that are primed for future study.

TABLE OF CONTENTS

Declaration ..... **i**

Acknowledgments ..... **iii**

Abstract ..... **vii**

Table Of Contents ..... **viii**

List Of Abbreviations ..... **x**

List Of Figures ..... **xv**

List Of Tables ..... **xviii**

List Of Equations ..... **xxii**

Chapter 1 — Introduction **1**

The Brain And Its Metabolism 1

An Introduction To Allometric Analysis 2

Haemodynamics – The Mathematics Of Circulation 3

Measurement Of Brain Metabolism 8

Thesis Aims And Structure 14

Chapter 2 — Brain Perfusion In The Western Grey Kangaroo **19**

Abstract 19

Introduction 20

Methods 23

Results 27

Discussion 53

Conclusion 59

Chapter 3 — Bird Brained? Cerebral Blood Flow In The Aves **61**

Abstract 61

Introduction 62

Methods 66

Results 69

Discussion 85

Conclusion 91

Chapter 4 — Cephalic Arterial Anatomy Of The Domestic Fowl (*Gallus Gallus Domesticus)* 99

Abstract 99

Introduction 100

Methods 101

Results 103

Discussion 114

Conclusion 119

Chapter 5 — Cerebral Blood Flow Rate In The Domestic Fowl (*Gallus Gallus Domesticus)* 121

Abstract 121

Introduction 122

Methods 125

Results 132

Discussion 140

Conclusion 147

Chapter 6 — Discussion And Concluding Remarks 149

Cephalic And Encephalic Arterial Anatomy And Perfusion In Birds And Mammals Assessed Via Microsphere Circulation, Contrast Injection, And Osteoforamina Measurement 149

Does Metabolism Describe Cognition And Intelligence? 151

Future Perspectives 156

Concluding Remarks 161

References 163

Appendix A: 3D Figure Instructions 184

Appendix B: Supplementary Material (Data And Statistics) 186

Appendix C: Scan Parameters, Reconstruction Settings, Measurement Resolution (Metadata) 212

LIST OF ABBREVIATIONS

The following abbreviations are used in this thesis.

AICc	Akaike information criterion
ANCOVA	Analysis of covariance
ATP	Adenosine triphosphate
AVC	Anterior ventral cerebellar artery
B	Basilar artery
BMR	Basal metabolic rate
Bonfer.	Bonferroni correction
BP	Basisphenoid plexus
BS	Brainstem
C1, C2, etc	First cervical vertebrae, second cervical vertebrae, etc
CA	Carotid artery – internal carotid artery (mammals) or cerebral carotid artery (birds)
ca.	Circa
CauC	Caudal cerebral artery
CauE	Caudal cephalic artery
Cb	Cerebellum
CC	Common carotid artery
CE	Common encephalic artery
CeC	Cerebral carotid artery
CeE	Cerebroethmoid artery
CF	Carotid foramen
CI	Confidence interval
cm	Centimetre
CN	Common nasal artery
comb	Comb arteries
CT	Computed tomography
DCDVI	Differential contrast dual vascular injection
Di	Diencephalon

dyn	Dyne
E	Ethmoid artery
EC	External carotid artery
EO	External ophthalmic artery
EQ	Encephalisation quotient
F	Facial artery
fMRI	Functional magnetic resonance imaging
g	Gram
Hct	Haematocrit
IC	Internal carotid artery
IC ana.	Intercarotid anastomosis
ICA	Internal carotid artery
ILN	Inferior lateral nasal artery
IM	Intramandibular artery
InO	Infraorbital artery
IU	International units
J–N test	Johnson–Neyman Test
K	Potassium
kg	Kilogram
l	Length
L Tec, R Tec	Left optic tectum, right optic tectum
L Tel, R Tel	Left telencephalon, right telencephalon
LAF	Lateral atlantal foramen
LN	Lateral nasal artery
LP	Lateral palatine artery
M	Maxillary artery
M_b	Body mass
MC	Middle cerebral artery
mg	Milligram
min	Minute

ml	Millilitre
mm	Millimetre
mmHg	Millimetres of mercury
Mn	Medial nasal artery
MP	Medial palatine artery
MS	Microsphere
MTC	Minor temporal cerebral artery
N	Newtons
n	Sample size
n/a	Not applicable, not available
Na	Sodium
nm	Nanometre
OA	Orbital artery
Oc	Occipital artery
OM	Oromandibular artery
OP	Orbital plexus
OR	Ophthalmic rete
OT	Opthalmotemporal artery
OV	Occipitovertebral artery
P	Pressure
Pagels λ	Pagels Lambda
Pal	Palatine artery
PDF	Portable document format
pers. obs.	Personal observations
PGLS	Phylogenetic generalized least squares
POL	Point-of-lay
PVC	Posterior ventral cerebellar artery
$\dot{Q}$	Blood flow rate
$\dot{Q} \cdot V_{br}^{-1}$	Volumetric brain perfusion
$\dot{Q}_{CA}$	Blood flow rate through a carotid artery/arteries – internal carotids in mammals, cerebral carotids in birds

$\dot{Q}_{CeCA}$	Blood flow rate through the cerebral carotid artery/arteries
Qi	Blood flow index
$\dot{Q}_{ICA}$	Blood flow rate through the internal carotid artery/arteries
$\dot{Q}_{ICA+VA}$	Blood flow rate through the internal carotid and vertebral arteries, added together
$\dot{Q}_{VA}$	Blood flow rate through the vertebral artery/arteries
r	Radius
r^2	Coefficient of determination
RA	Rostral auricular artery
RBS	Relative brain size
r_{CF}	Radius of the carotid foramen or carotid canal
RE	Rostral encephalic artery
r_f	Foramen radius
r_i	Internal radius of a vessel, or lumen radius.
r_{LAF}	Radius of the lateral atlantal foramen
r_o	Vessel external radius
RO	Ophthalmic rete
s	Second
Sep	Septum arteries
SLN	Superior lateral nasal artery
SO	Supraorbital artery
SpM	Sphenomaxillary artery
SpP	Sphenopalatine artery
ST	Superficial temporal artery
STP	Stapedial, temporoorbital, and profundus arteries
TM	Temporomandibular
VA	Vertebral artery
V_{br}	Brain volume
VOI	Volume of interest
VOL	Ventral optic lobe artery
VS	Ventral spinal artery

V_{tele}	Telencephalon volume
w	Wall thickness to lumen radius conversion ratio
η	Blood viscosity
η_{plasma}	Plasma viscosity
µg	Microgram
µm	Micrometre
π	Pi
σ	Stress
τ	Shear stress
$\propto$	Proportional
$\not\propto$	Not proportional
°C	Degrees centigrade

LIST OF FIGURES

Chapter 1

Figure 1-1. *A schematic diagram representing some of the variables associated with Equation 2, Equation 3, and Equation 4.* *4*

Figure 1-2. *A Venn diagram showing the interrelationship of some haemodynamic equations.* *7*

Figure 1-3. *Computed tomography basics.* *11*

Figure 1-4. *Different methods of foramen measurement offer distinct advantages and disadvantages.* *12*

Figure 1-5. *Simplified tree of life showing the evolutionary relationships of extant amniotes.* *15*

Chapter 2

Figure 2-1. *Development of the lateral atlantal foramen in kangaroos.* *27*

Figure 2-2. *Simplified path of the vertebral artery in kangaroos.* *29*

Figure 2-3. *Dissection of the cervical region of the head of the western grey kangaroo.* *30*

Figure 2-4. *Comparison between regressions in haplorrhine primates from original Seymour et al. (2015) blood flow study compared with a remeasurement and analysis of the dataset using the most recent approaches.* *32*

Figure 2-5. *Comparison between regressions in diprotodont marsupials from original Seymour et al. (2015) blood flow study compared with a remeasurement and analysis of the dataset using the most recent approaches.* *33*

Figure 2-6. *Brain volume compared with body mass across the development of the western grey kangaroo.* *35*

Figure 2-7. *Graphs (A-D) of internal carotid foramen radius and carotid arterial blood flow rate across the development of the western grey kangaroo.* *36*

Figure 2-8. *Blood flow rate across the development of the western grey kangaroo.* *41*

Figure 2-9. *Digital cranial endocasts and foramina of cerebral feeder arteries in an 80 g western grey kangaroo joey.* *44*

Figure 2-10. *Digital cranial endocasts and foramina of cerebral feeder arteries in a 62 kg adult male western grey kangaroo.* *45*

Chapter 3

Figure 3-1. *The intracranial course of the cerebral carotid artery in a cockatiel (Nymphicus hollandicus).* *64*

Figure 3-2. *Avian evolutionary tree simplified from Prum et al. (2015).* *65*

Figure 3-3. *Phylogeny of the avian species examined in this chapter. 70*
Figure 3-4. *Graphs (A-D) of the relationships between M_b, V_{br}, r_{CF}, and $\dot{Q}_{CA}$ for the avian taxa examined compared with two mammalian clades. 74*
Figure 3-5. *Graphs (A-D) of the relationships between M_b, V_{br}, r_{CF}, and $\dot{Q}_{CA}$ for the avian clades examined compared with two mammalian clades. 77*
Figure 3-6. *Comparing relationships between M_b, V_{br}, r_{CF}, and $\dot{Q}_{CA}$ for Aves with precocial and altricial young. 80*
Figure 3-7. *Digital renderings of the skulls of two palaeognath birds examined in this study, with endocranial casts overlain. 92*
Figure 3-8. *Digital renderings of the skulls of two galliform birds examined in this study, with endocranial casts overlain. 93*
Figure 3-9. *Digital renderings of the skulls of two anseriform birds examined in this study, with endocranial casts overlain. 94*
Figure 3-10. *Digital renderings of the skulls of two birds of prey examined in this study, with endocranial casts overlain. 95*
Figure 3-11. *Digital renderings of the skulls of two psittaciform birds examined in this study, with endocranial casts overlain. 96*
Figure 3-12. *Digital renderings of the skulls of two passeriform birds examined in this study, with endocranial casts overlain. 97*

Chapter 4

Figure 4-3D. *An interactive three-dimensional model of the skull and blood vessels of an ISA Brown chicken (Gallus gallus domesticus). 103*
Figure 4-3D / 1. *Three-dimensional model of the cephalic arteries of the domestic chicken, lateral posterior aspect with arteries of the cervical region highlighted. 104*
Figure 4-3D / 2. *Three-dimensional model of the cephalic arteries of the domestic chicken, lateral aspect cut away at the midline with arteries of the endocranial region highlighted. 106*
Figure 4-3D / 3. *Three-dimensional model of the cephalic arteries of the domestic chicken, lateral aspect with arteries as they appeared before simplification. 108*
Figure 4-3D / 5. *Three-dimensional model of the cephalic arteries of the domestic chicken, lateral aspect with arteries of the oral region highlighted. 112*
Figure 4-3D / 6. *Three-dimensional model of the cephalic arteries of the domestic chicken, lateral aspect with arteries of the nasal region highlighted. 113*
Figure 4-7. *Simplified diagram illustrating the arrangement of the major arteries of the chicken head with respect to the brain. 116*
Table S 2 - 6. *Statistical information for the ANCOVAs relating body mass, brain volume, and total flow through cerebral feeding arteries across two phases of a western grey kangaroo life history sequence. 192*
Table S 2 - 6. *Statistical information for the ANCOVAs of two sets of measurements of diprotodont marsupial and haplorrhine primate body masses, brain volumes, foramina dimensions, and carotid blood flow rates. 193*

Chapter 5

Figure 5-1. *A simplified diagram of the surgical procedure involved in the microsphere perfusion approach. 127*

Figure 5-2. *Brain regions of the chicken. 128*

Figure 5-3. *Diagram of the apparatus used to perfuse contrast media into specimens at a desired pressure. 130*

Figure 5-4. *Masses of seven brain regions in pre-point-of-lay hens, post-point-of-lay hens, and roosters. 132*

Figure 5-5. *Absolute blood flow rate to seven brain regions in pre-point-of-lay hens, post-point-of-lay hens, and roosters determined by microsphere perfusion..... 133*

Figure 5-6. *Volumetric blood flow rate to seven brain regions in pre-point-of-lay hens, post-point-of-lay hens, and roosters determined by microsphere perfusion..... 134*

Figure 5-7. *Two way ANOVA multi-comparison confidence interval plots for brain segment mass, brain segment blood flow rate, and volumetric blood flow rate in different life classes of chickens..... 136*

Figure 5-8. *Comparison between whole brain absolute blood flow values calculated from the foramen dimension measurement technique, pressurised contrast perfusion technique, and fluorescent microsphere infusion technique. 139*

Figure 5-9. *An image of a contrast perfused carotid artery typical of those obtained during this study..... 146*

Chapter 6

Figure 6-1. *Different avian species present with vastly different brain architecture, presenting problems for the direct comparison of intelligence via measurements of absolute brain metabolism..... 153*

Appendix A: 3D Figure Instructions

Figure I - 1. *Instructions for activating Figure 4-3D..... 184*

Figure I - 2. *Diagram displaying the navigation tools for Figure 4-3D. 185*

LIST OF TABLES

Chapter 2

Table 2-1. *Allometric equations in haplorrhine primates from the original Seymour et al. (2015) blood flow study compared with a remeasurement and analysis of the dataset using the most recent approaches.* *46*

Table 2-2. *Allometric equations in diprotodont marsupials from the original Seymour et al. (2015) blood flow study compared with a remeasurement and analysis of the dataset using the most recent approaches.* *47*

Table 2-3. *Allometric equations and ANCOVAs relating body mass, brain volume, total flow through both internal carotid arteries and carotid foramen radius across two phases of a western grey kangaroo life history sequence, and in diprotodonts and haplorrhine primates interspecifically for comparison.* *48*

Table 2-4. *Allometric equations and ANCOVAs relating body mass, brain volume, total flow through both internal carotid arteries and carotid foramen radius across two phases of a western grey kangaroo life history sequence, and in diprotodonts and haplorrhine primates interspecifically for comparison.* *49*

Table 2-5. *Allometric equations and ANCOVAs relating body mass, brain volume, total flow through both vertebral arteries and lateral atlantal foramina radius across two phases of a western grey kangaroo life history sequence.* *50*

Table 2-6. *Allometric equations and ANCOVAs relating body mass, brain volume, and total flow through cerebral feeding arteries across two phases of a western grey kangaroo life history sequence.* *51*

Table 2-7. *Significant differences between cerebral feeding arteries and their foramina in different life history stages according to ANCOVA.* *52*

Chapter 3

Table 3-1. *Model support for phylogenetic least squares models of total cerebral carotid blood flow rate in the Aves.* *81*

Table 3-2. *Support for phylogenetic signal in the examined variables in the Aves.* *81*

Table 3-3. *Allometric equations relating body, relating body mass, brain volume, total flow through left and right cerebral carotid arteries and carotid foramen radius in the Aves following PGLS correction.* *81*

Table 3-4. *Allometric equations and ANCOVAs relating body mass, brain volume, total flow through both cerebral carotid arteries and carotid foramen radius in the Aves and two groups of mammals.* *82*

Table 3-5. *Allometric equations and ANCOVAs relating body mass, brain volume, total flow through both cerebral carotid arteries and carotid foramen radius in the Aves and two groups of mammals. 83*

Table 3-6. *Allometric equations and ANCOVAs relating body, relating body mass, brain volume, total flow through both cerebral carotid arteries and carotid foramen radius in the Aves by degree of developmental maturity at hatching. 84*

Chapter 5

Table 5-1. *Results of two-way ANOVA for different variables from the microsphere infusion technique. 135*

Table 5-2. *Average whole brain perfusion rates of Gallus gallus domesticus calculated from the dimensions of the cerebral carotid lumen according to the lumen contrast dimension measurement technique. 138*

Table 5-3. *Average whole brain perfusion rates of Gallus gallus domesticus calculated from the dimensions of the cerebral carotid canal according to the foramen dimension measurement technique. 138*

Appendix B: Supplementary material (data and statistics)

Table S 2 - 1. *Relationship between total cerebral arterial blood flow rate, brain volume and body mass across an ontological sequence in a large-bodied diprotodont marsupial, the western grey kangaroo, Macropus fuliginosus. 186*

Table S 2 - 2. *Comparison between lateral atlantal and carotid foramina measurements obtained by different measurement approaches. 187*

Table S 2 - 3. *Relationship between total carotid arterial blood flow rate, brain volume and body mass in haplorrhine primates. 188*

Table S 2 - 4. *Relationship between total carotid arterial blood flow rate, brain volume and body mass in Diprotodont marsupials. 189*

Table S 2 - 5. *Statistical information for the ANCOVAs relating body mass, brain volume, and total flow through carotid arteries across two phases of a western grey kangaroo life history sequence (part a) 190*

Table S 2 - 6. *Statistical information for the ANCOVAs relating body mass, brain volume, and total flow through carotid arteries across two phases of a western grey kangaroo life history sequence (part b) 191*

Table S 3 - 1. *Relationship between total cerebral arterial blood flow rate, brain volume and body mass across in Palaeognaths. 194*

Table S 3 - 2. *Relationship between total cerebral arterial blood flow rate, brain volume and body mass across in Galliformes. 194*

Table S 3 - 3. *Relationship between total cerebral arterial blood flow rate, brain volume and body mass across in Anseriformes 195*

Table S 3 - 4. *Relationship between total cerebral arterial blood flow rate, brain volume and body mass across in Accipitriformes. 195*
Table S 3 - 5. *Relationship between total cerebral arterial blood flow rate, brain volume and body mass across in Falconiformes. 195*
Table S 3 - 6. *Relationship between total cerebral arterial blood flow rate, brain volume and body mass across in Psittaciformes. 196*
Table S 3 - 7. *Relationship between total cerebral arterial blood flow rate, brain volume and body mass across in Passeriformes. 196*
Table S 3 - 8. *Statistical information for the ANCOVAs relating body mass, brain volume, foramina dimensions, and total carotid flow in the Aves, with comparisons to diprotodont and haplorrhine mammals (part a). 197*
Table S 3 - 9. *Statistical information for the ANCOVAs relating body mass, brain volume, foramina dimensions, and total carotid flow in the Aves, with comparisons to diprotodont and haplorrhine mammals (part b). 198*
Table S 3 - 10. *Statistical information for the ANCOVAs relating body mass, brain volume, foramina dimensions, and total carotid flow in the Aves, with comparisons to diprotodont and haplorrhine mammals (part c). 199*
Table S 3 - 11. *Statistical information for the ANCOVAs relating body mass, brain volume, foramina dimensions, and total carotid flow in the Aves, with comparisons to diprotodont and haplorrhine mammals (part d). 200*
Table S 3 - 12. *Statistical information for the ANCOVAs relating body mass, brain volume, foramina dimensions, and total carotid flow in the Aves, with comparisons to diprotodont and haplorrhine mammals (part e). 201*
Table S 3 - 13. *Statistical information for the ANCOVAs relating body mass, brain volume, foramina dimensions, and total carotid flow in the Aves, with comparisons to diprotodont and haplorrhine mammals (part f). 202*
Table S 3 - 14. *Statistical information for the ANCOVAs relating body mass, brain volume, foramina dimensions, and total carotid flow in the Aves with respect to hatchling maturity. 203*

Table S 4/5 - 1. *Perfusion rates of seven brain regions of Gallus gallus domesticus calculated according to the microsphere perfusion quantification technique (part a). 204*
Table S 4/5 - 2. *Perfusion rates of seven brain regions of Gallus gallus domesticus calculated according to the microsphere perfusion quantification technique (part b). 205*
Table S 4/5 - 3. *Whole brain perfusion rates of Gallus gallus domesticus calculated from the dimensions of the cerebral carotid canal according to the foramen dimension measurement technique. 206*
Table S 4/5 - 4. *Whole brain perfusion rates of Gallus gallus domesticus calculated from the dimensions of the arterial lumen according to the pressurised contrast perfusion technique. 207*
Table S 4/5 - 5. *Perfusion rates of the spleen and left and right kidneys of recorded from five Gallus gallus domesticus laying hens calculated according to*

the microsphere perfusion quantification technique as reported in Hu et al. (2021). *208*
Table S 4/5 - 6. *Full two-way ANOVA multiple comparisons descriptive statistics table for brain segment masses from the microsphere infusion technique.* *209*
Table S 4/5 - 7. *Full two-way ANOVA multiple comparisons descriptive statistics table for blood flow rate from the microsphere infusion technique.* *210*
Table S 4/5 - 8. *Full two-way ANOVA multiple comparisons descriptive statistics table for volumetric blood flow from the microsphere infusion technique.* *211*

Appendix C: Scan parameters, reconstruction settings, measurement resolution (metadata)

Table M 2 - 1. *Selected imaging and reconstruction parameters for western grey specimens scanned using the Skyscan-1076 Micro-CT scanner at Adelaide Microscopy.* *212*
Table M 2 - 2. *Selected imaging and reconstruction parameters for western grey specimens scanned using the Philips Ingenuity Core 128 scanner at Sound Radiology.* *213*
Table M 2 - 3. *Voxel dimensions used for various aspects of Chapter 2.* *214*

Table M 3 - 1. *Selected imaging and reconstruction parameters for Avian specimens from Chapter 3. These were scanned using the Skyscan-1076 Micro-CT scanner at Adelaide Microscopy.* *215*
Table M 3 - 2. *Selected imaging and reconstruction parameters for Avian specimens from Chapter 3 which were scanned using the Skyscan-1076 Micro-CT scanner at Adelaide Microscopy, continued.* *216*
Table M 3 - 3. *Selected imaging and reconstruction parameters for Avian specimens from Chapter 3 which were scanned using the Philips Ingenuity Core 128 scanner at Sound Radiology.* *217*
Table M 3 - 4. *Voxel dimensions used for various aspects of Chapter 3.* *218*
Table M 3 - 5. *Voxel dimensions used for various aspects of Chapter 3 continued.* *219*

Table M 4/5 - 1. *Selected imaging and reconstruction parameters for chicken specimens scanned using the Skyscan-1276 Micro-CT scanner at Adelaide Microscopy.* *220*
Table M 4/5 - 2. *Voxel dimensions used for various aspects of Chapter 4 and Chapter 5.* *221*

LIST OF EQUATIONS

Equation 1 – The allometric equation.

$$Y = a \times M^b$$

where *Y* is a specific variable of interest; *M* is usually body mass; *a* is the Y intercept*;* and *b* is the scaling exponent.

Equation 2 – The principle of Laplace for wall circumferential stress in thick-walled vessels.

$$\sigma(r) = \frac{P.{r_i}^2(1 + \frac{{r_o}^2}{r^2})}{({r_o}^2 - {r_i}^2)}$$

where σ (dynes · cm^{-2}) is circumferential stress at a position *(r)* in the vessel wall; *P* is blood pressure (dynes · cm^{-2}); r_i is internal vessel radius (cm); r_o is external vessel radius (cm).

Equation 3 – The shear stress equation.

$$\dot{Q} = \tau\pi r^3 / 4\eta$$

where $\dot{Q}$ is blood flow rate (cm^3 · s^{-1}); τ is wall shear stress (dynes · cm^{-2}); *r* is internal vessel radius (cm); and η is blood viscosity (dynes s · cm^{-2}).

Equation 4 – The Poiseuille-Hagen equation.

$$\dot{Q} = \pi\, r_i^4 \Delta P \;/\; 8\,\eta\, L$$

where $\dot{Q}$ is blood flow rate (cm^3 · s^{-1}); r_i is vessel lumen radius (cm); η is blood viscosity (dynes s · cm^{-2}); and ΔP is pressure drop (dynes · cm^{-2}) across a vessel of length *L* (cm).

Equation 5 – The hydrostatic pressure equation.

$$p = \rho\, g\, h$$

where *p* is pressure (dynes · cm^{-2}); ρ is density of the fluid (kg · m^{-3}); h is height (m); and *g* is acceleration due to gravity (9.81 m · s^{-2}).

Equation 6 – The blood flow index.

$$Q_i = r_o^4 / L$$

where Q_i is the blood flow index in arbitrary units, r_f is foramen radius (cm), and L is femur length (cm).

Equation 7 – The Seymour et al. (2019b) mammalian equation.

$$log\ \dot{Q} = -0.20\ log\ r_i^2 + 1.91\ log\ r_i + 1.82$$

where $\dot{Q}$ is blood flow rate ($cm^3\ s^{-1}$); and r_i is the arterial internal lumen radius (cm).

Equation 8 – The Seymour et al. (2019b) cephalic arteries equation.

$$\dot{Q} = 155\ r_i^{\ 2.49}$$

where $\dot{Q}$ is blood flow rate ($cm^3\ s^{-1}$); and r_i is the arterial internal lumen radius (cm).

Equation 9 – Einstein's blood viscosity formula.

$$\eta_{whole\ blood} = \eta_{plasma}\ (1 + 2.5\ Hct)$$

where $\eta_{whole\ blood}$ is whole blood viscosity (dynes · cm^{-2}); η_{plasma} is plasma viscosity (dynes · cm^{-2}); and *Hct* is haematocrit value (arbitrary units).

Equation 10 – Microsphere deposition and blood flow.

$$Blood\ flow\ in\ tissue\ sample\ (cm^3\ s^{-1}) = \frac{Harvard\ Pump\ Withdrawal\ Rate\ (cm^3\ s^{-1}) \times Number\ of\ MS\ in\ tissue\ sample}{Number\ of\ MS\ in\ reference\ sample}$$

Equation 11 – Microsphere deposition and cardiac output.

$$Cardiac\ Output\ (cm^3\ s^{-1}) = \frac{Harvard\ Pump\ Withdrawal\ Rate\ (cm^3\ s^{-1}) \times Number\ of\ MS\ injected}{Number\ of\ MS\ in\ reference\ sample}$$

CHAPTER 1

INTRODUCTION

THE BRAIN AND ITS METABOLISM

The brain is the centre of existence. The brain, along with the wider accompanying nervous system, encompass everything about an animal's conscious and unconscious function, from movement, to memory, perception, behaviour, experience, thoughts, emotion, cognition, and intelligence. However, due to the sheer complexity of the structure our understanding of the brain is in many respects limited. One chief area of investigation in relation to the brain is of the closely related concepts of cognition and intelligence. Intelligence describes the ability to understand perception, to learn, and to reason, while cognition describes the processes driving this thought or understanding, including experience, perception, and senses. The complex and interconnected nature of cognition and intelligence underlies the difficulty in the measurement or relation of these concepts.

Through scientific history, brain size has been used as an indicator of cognition and intelligence, where animals with smaller brains in proportion to their body size are thought to be less cognitively capable than those with proportionally larger brain sizes (Whiting and Barton 2003; Pollen *et al.* 2007; Burkart *et al.* 2017; Fristoe *et al.* 2017). More recently, however, examinations have been made into the energy use of the brain as a gauge of activity, as an alternative to the comparative brain size hypothesis (Bottoncetti *et al.* 1997; Karbowski 2012; Seymour *et al.* 2015).

The brain is an exceptionally expensive organ as neurons are energy hungry cells. Most brain energy is used on synaptic transmission that makes up roughly 50-90% of the metabolic rate of the brain (Harris *et al.* 2012; Karbowski 2012). The brain's high metabolic rate is likely tied to synaptic density, which is strongly correlated with glucose consumption rate (Karbowski 2012). Sixty percent of the brain's mitochondria are found in the dendrites of neurons, indicating that synapses require high levels of metabolic energy (Attwell and Laughlin 2001). To fund this great level of energy consumption, continuous cerebral perfusion (that is, blood flow) is required because of the brain's aerobic nature and its inability to store glucose or glycogen (Weisbecker and Goswami 2010; Karbowski 2011). However, the regional distribution of this perfusion is important to consider, as the metabolic requirements of the brains sensory systems may effectively offset the metabolism used for higher processing and cognition, obfuscating how much energy is actually 'invested' in intelligence. The cost of building and maintaining a brain increases

with brain size and composition (Attwell and Laughlin 2001; Herculano-Houzel 2011a). However, the metabolic rates of animals and their organs are not always directly proportional to their size. Therefore, in order to examine brain metabolism, I take differences in size and physiology into account using allometric analysis.

AN INTRODUCTION TO ALLOMETRIC ANALYSIS

Everything in physiology can be related to size. The size of an organism affects its entire biology, including its anatomy, physiology, ecology and behaviour in diverse ways (Calder 1984). The study of how body size relates to shape, anatomy, physiology, and behaviour is referred to as allometry. Scaling can indicate evolutionary opportunities or constraints relative to body size or provide benchmarks for future estimates of variables that depend on body size in living and extinct species. Just as Dobzhansky stated that "nothing in biology makes sense except in the light of evolution", nothing in physiology makes sense except in the light of allometry. Allometric analysis is a powerful tool in comparative physiology with a broad applicability for predicting or testing individual species data (Nijhout and McKenna 2019). The allometric power equation describes the interrelation of one variable, *M* (usually body mass) to a specific variable of interest (*Y*) (Huxley and Teissier 1936b; Huxley and Teissier 1936a);

$$Y = a \times M^{b}$$

Equation 1 – The allometric equation.

where *Y* is a specific variable of interest; *M* is usually body mass; *a* is the Y intercept*;* and *b* is the scaling exponent.

Generally, of greatest interest when analysing allometric relationships is the scaling exponent, *b*. The variable of interest can scale independently of body mass ($\propto M0$), increase disproportionately lower than body mass ($\propto M<1$), increase proportionately with body mass ($\propto M1$), or increase disproportionately higher than body mass ($\propto M>1$). Scaling is considered allometrically negative (hypoallometric) when $b<1$, and allometrically positive (hyperallometric) when $b>1$ (Calder 1984). Allometric analyses generally fall under three different levels: ontogenetic, static, or evolutionary (Cock 1966; Gould 1966; Calder 1984; Gayon 2015).

Static allometry describes shape differences in individuals of the same age or developmental stage. Static allometry can elucidate the degree of size or shape variation within a group at specific ontogenetic stages (Leamy and Atchley 1984; Bonduriansky and Day 2003; Browne and Gwynne 2022). Evolutionary allometric studies examine shape changes interspecifically across a range of body sizes. Evolutionary allometry allows examination of how a lineage changes over its evolutionary history at a particular life history stage (Pilbeam and Gould 1974; Seymour *et al.* 2016; Seymour *et al.* 2019a).

Ontogenetic allometric studies focus on shape changes across the development of an organism. Ontogeny refers to the study of the entirety of an organism's lifespan from conception to maturity (Kodric-Brown *et al.* 2006; Snelling *et al.* 2015b; Harrington *et al.* 2019b). Most organisms change considerably over the course of their life. Allometric scaling can be examined within a species across ontogenetic ranges to determine the specifics of how the organism develops morphologically and physiologically. The three classes of allometric analyses are closely interrelated. Changes in morphology or physiology that occur on an evolutionary scale will inevitably be accompanied by changes at ontogenetic and static scales (Gould 1966; Klingenberg and Zimmermann 1992). Allometric analysis can be applied to an endless number of size dependent relationships, and has often been applied to studies of blood circulation.

The size of an animal's body directly influences blood circulation dynamics in a wide variety of ways. The heart, which is responsible for the perfusion of oxygenated blood throughout the body, has been shown among mammals to have many different exponents for the allometric relationship with body mass, ranging from 0.96 to 1.06 (Stahl 1967; Holt *et al.* 1968; Seymour and Blaylock 2000). Variation in the scaling exponent for mammalian heart mass can generally be explained by factors independent of body mass, such as variation in the athleticism of species of specific sizes. It is generally accepted that mammalian heart mass scales in approximately direct proportion to body mass ($\propto M_b^1$). However, vertical height is important in determining terrestrial mammalian heart mass, as gravitational forces act upon systemic arterial pressure in animals with large vertical distances from the heart to the head. Thus, the scaling exponent of heart mass in terrestrial mammals is likely closer to 1.06 (Seymour and Blaylock 2000). Furthermore, mean blood pressure which drives the perfusion of blood against gravity scales positively with body mass ($M_b^{0.05}$), indicating that systolic blood pressure is greater in larger animals (Seymour and Blaylock 2000; White and Seymour 2014). Mammalian blood volume and heart stroke volume scale isometrically with body mass (Stahl 1967). Mammalian arterial blood pressure, flow velocity and red blood cell size are all independent of body mass (M_b^0) (Calder 1984). Haematocrit and haemoglobin concentration have been calculated to either decrease with body mass ($M_b^{-0.024}$ and $M_b^{-0.021}$ respectively) (Kjeld and Ólafsson 2008), or to be independent of body mass (M_b^0) (Calder 1984). Therefore, because of the many ways size and its impacts can be related to circulation, understanding allometry is vital when examining the mechanisms of blood circulation.

HAEMODYNAMICS – THE MATHEMATICS OF CIRCULATION

The mechanical principles that describe the circulation of blood through the body are known as haemodynamics. Haemodynamic forces control the geometry of blood vessels by driving vascular remodelling, which is the process of alteration in vessel diameter or

wall thickness resulting from persistent changes to flow rates and blood pressures that impart forces on the vessels. Vascular remodelling sustains normal levels of stress on vessel walls and ensures laminar blood flow, thereby minimising the energy required for blood circulation (Ward *et al.* 2000; Lehoux and Tedgui 2003; Fischer *et al.* 2006; Lehoux *et al.* 2006). Haemodynamics principles and haemodynamic forces can be described by a number of equations which will be introduced in this section. A visual representation of the variables and forces is presented in Figure 1-1.

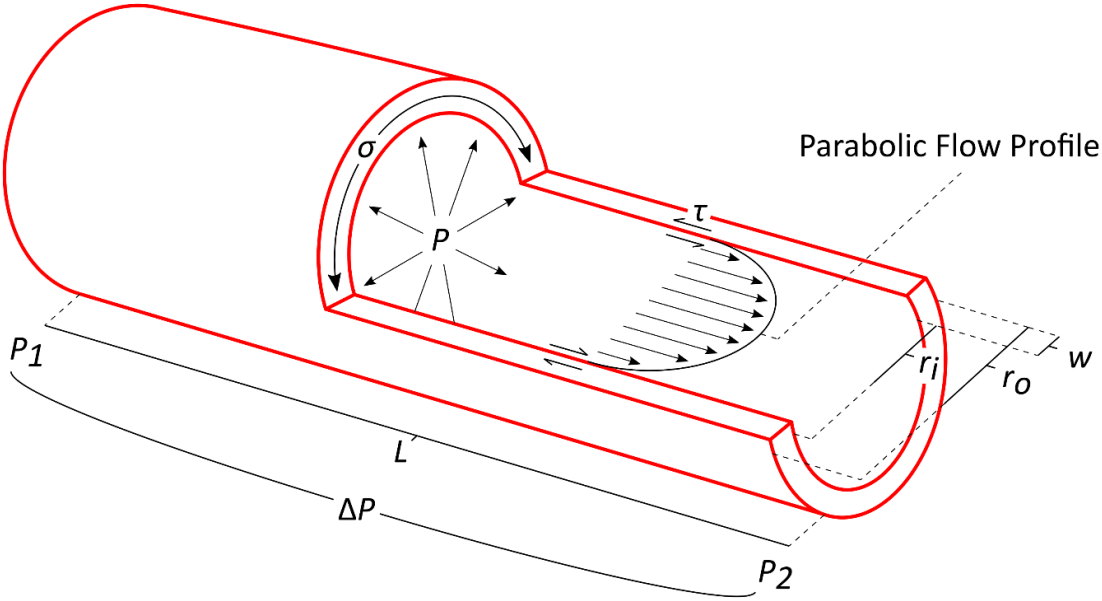

Figure 1-1. A schematic diagram representing some of the variables associated with *Equation 2, Equation 3,* and *Equation 4.* P represents pressure blood exerts on the vessel, generating a circumferential stress, σ, on the vessels wall, as in *Equation 2*. Shear stress, τ, is the frictional force generated by blood as it flows across the innermost layer of a blood vessel as in *Equation 3*. The parabolic flow profile shows how this frictional force slows blood flow at the walls to near zero. r_i is the internal radius and r_o is the external radius of the blood vessel, while w is the thickness of the vessels wall. The Poiseuille-Hagen equation (*Equation 4*) describes blood flow along a vessel of length L, and the change in pressure, ΔP, across this length. Not represented visually are blood flow rate, $\dot{Q}$, and blood viscosity, η.

Vessel walls experience stresses generated by blood flow in the form of shear stress and tensile stress. Tensile stress on the wall of a thick-walled vessel is proportional to the product of blood pressure and vessel radius, and inversely proportional to vessel wall thickness according to the principle of Laplace. In mammals, major vessels including the common, internal, and external carotid arteries are thick-walled, with radius-to-wall-thickness ratios of less than ten (Rees and Jepson 1970; Orsi *et al.* 2006; Skilton *et al.* 2011). In thick-walled vessels where the ratio of radius-to-wall-thickness is less than ten, stress can be calculated using the following equation (Ødegaard *et al.* 2005; Westerhof 2006; Pahwa and Pahwa 2014);

$$\sigma(r) = \frac{P.{r_i}^2(1 + \frac{{r_o}^2}{r^2})}{({r_o}^2 - {r_i}^2)}$$

Equation 2 – The principle of Laplace for wall circumferential stress in thick-walled vessels.

where σ (dynes · cm^{-2}) is circumferential stress at a position *(r)* in the vessel wall; *P* is blood pressure (dynes · cm^{-2}); r_i is internal vessel radius (cm); r_o is external vessel radius (cm).

This equation assumes linear elasticity to calculate an average stress (σ) across the vessel wall but provides no information about the distribution of stress across the wall (Westerhof 2006). The larger the internal vessel radius, the larger the wall tension required to withstand a given internal fluid pressure. Vessels with thicker walls are able to withstand higher levels of tensile stress as the tensile force is dissipated across a larger cross section; this allows thick-walled vessels to withstand higher pressures. A vessel with a smaller volume and thinner walls can withstand the same pressure as one with a larger volume and thicker walls. Thus, the principle of Laplace explains the thickening of arteries to accommodate a given blood pressure.

Shear stress is the frictional force of blood flowing across the endothelium of a vessel in units dyne cm^{-2} (1 dyne = 10^{-5} N). Shear stress generated by blood flow across a vessel can be calculated using the shear stress equation (Lehoux and Tedgui 2003);

$$\dot{Q} = \tau\pi r^3 / 4\eta$$

Equation 3 – The shear stress equation.

where $\dot{Q}$ is blood flow rate (cm^3 · s^{-1}); τ is wall shear stress (dynes · cm^{-2}); *r* is internal vessel radius (cm); and η is blood viscosity (dynes s · cm^{-2}).

This equation indicates that shear stress is proportional to blood flow rate and blood viscosity, and inversely proportional to vessel radius to the third power (Lehoux and Tedgui 2003). Blood viscosity is constant in the large vessels of mammals (0.04 dynes cm^{-1}) regardless of body mass (Langille 1996). Vascular remodelling responds to shear stress by inducing modification of vessel geometry; an increase in blood flow rate increases shear stress across the endothelium of a vessel, resulting in an increase in vessel radius. A decrease in blood flow rate decreases shear stress across the endothelium of a vessel, resulting in a decrease in vessel radius (Kamiya and Togawa 1980; Guyton and Hartley 1985; Langille *et al.* 1989; Langille 1996). Shear stress appears to decrease in the major arteries of larger mammals (Greve *et al.* 2006; Weinberg and Ethier 2007; Seymour *et al.* 2015; Seymour *et al.* 2019b).

The Poiseuille-Hagen equation relates the complex relationship between pressure drop across vessel length, flow rate, fluid viscosity, and vessel radius. Radius has a strong

influence on the equation as indicated by the fourth power. The Poiseuille-Hagen equation essentially relates resistance to flow; pressure, length, radius, and viscosity to Q̇;

$$\dot{Q} = \pi r_i^4 \Delta P \; / \; 8 \eta L$$

Equation 4 – The Poiseuille-Hagen equation.

where $\dot{Q}$ is blood flow rate ($cm^3 \cdot s^{-1}$); r_i is vessel lumen radius (cm); η is blood viscosity (dynes $s \cdot cm^{-2}$); and ΔP is pressure drop (dynes $\cdot cm^{-2}$) across a vessel of length L (cm).

Blood flow rate increases with increasing differential pressure and lumen radius but decreases with increasing length and viscosity. Both the Poiseuille-Hagen equation and the shear stress equation assume that blood is incompressible and Newtonian; that vessels are stiff, straight and have a constant circular cross-section; and that flow is steady (not pulsatile), and laminar (not turbulent), with a parabolic velocity profile giving zero velocity at the wall (Lehoux and Tedgui 2003; Westerhof 2006). In circulatory systems these assumptions are met in some cases, but not in others. For instance, blood is a non-Newtonian fluid, but follows Newtonian principles when subjected to a shear rate is 100 s^{-1} (Kumar *et al.* 2017). Further, blood flow is laminar in capillaries and small vessels, but can be turbulent in large arteries (Westerhof 2006; Seymour *et al.* 2019b). Regardless, the Poiseuille-Hagen equation and the shear stress equation are accepted as tools in the examination of blood flow.

The hydrostatic pressure equation describes the relationship between the height of a column of fluid, fluid density, and the pressure exerted by that column of fluid at its base. In haemodynamics, this equation is used to describe the pressure required to pump blood from the heart to the top of the animal. The pressure generated by a hydrostatic head (a vertical column of liquid) can be calculated using the equation using the hydrostatic pressure equation;

$$p = \rho \, g \, h$$

Equation 5 – The hydrostatic pressure equation.

where p is pressure (dynes $\cdot cm^{-2}$); ρ is density of the fluid ($kg \cdot m^{-3}$); h is height (m); and g is acceleration due to gravity ($9.81 \; m \cdot s^{-2}$).

A greater vertical distance between the heart and the brain requires the heart to sustain greater pressures to ensure adequate brain perfusion. Mean blood pressure, which drives the perfusion of blood against gravity, scales positively with body mass ($M_b^{0.05\pm0.01}$), indicating that systolic blood pressure is greater in larger animals (Seymour and Blaylock 2000; White and Seymour 2014; Sandal *et al.* 2020). This increase in systolic pressure compensates for the vertical distance between the heart and the brain, and thus blood pressure in the brain is assumed to be independent of body size.

These four haemodynamic equations are closely interrelated and can be used to examine and describe the circulatory system in different animal systems (Figure 1-2). For example, haemodynamic forces vary between veins and arteries because of their different functions. In humans, large arteries experience high pressure pulsatile flows, with shear stresses peaking around 10-70 dynes cm^{-2}. Veins, on the other hand, experience lower blood pressures and shear stresses around 1-2 dynes cm^{-2} (García-Cardeña and Gimbrone 2006). Hence, veins possess walls that are thinner and less elastic than those of arteries (du Boulay *et al.* 1998; Wang *et al.* 1998; Gridley 2010). The Poiseuille-Hagen equation (*Equation 4*) has been used to calculate cerebral blood flow based on measurements of vessel dimensions (Ashwell and Shulruf 2015; Ashwell and Shulruf 2016; Yu *et al.* 2020). The hydrostatic pressure equation (*Equation 5*) has been used in the examination of the systemic blood pressure of mammals (White and Seymour 2014). Given the right measurements, it is possible to examine blood flow through any artery by using these heamodynamic principles. By examining the rate of blood flow through the arteries that supply the brain, it is possible to calculate the rate of cerebral metabolism.

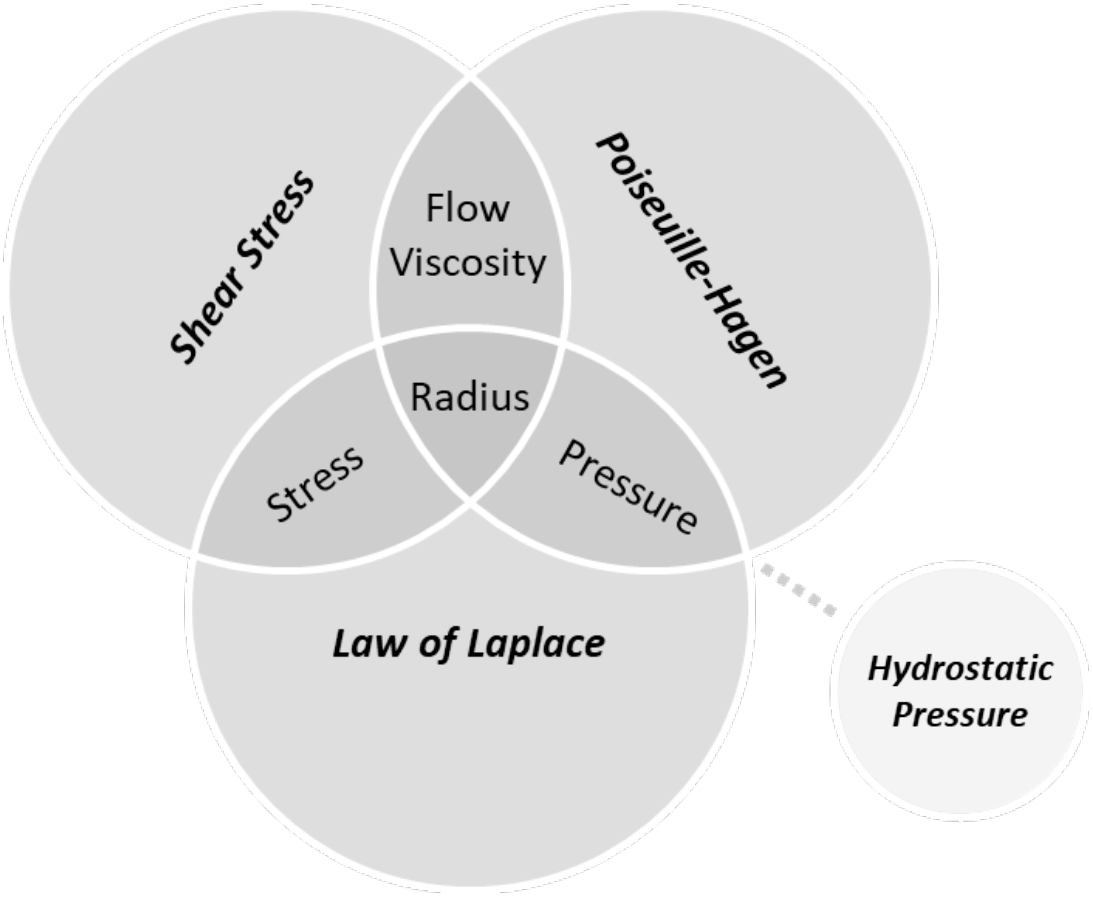

Figure 1-2. A Venn diagram showing the interrelationship of some haemodynamic equations. The shear stress equation, Poiseuille-Hagen equation, and the principle of Laplace contain interrelated variables in their descriptions of haemodynamic properties. While the variables for flow and viscosity are identical in the Poiseuille-Hagen and shear stress equations, the specific way stress and pressure are considered in each equation differs. The hydrostatic pressure equation shares pressure as a variable with the principle of Laplace and the Poiseuille-Hagen equation.

MEASUREMENT OF BRAIN METABOLISM

Measurements of cerebral metabolism have been performed since at least the early 1900s, however, their use as a gauge of brain activity, cognition, or intelligence has been overshadowed by other approaches to the evaluation of intelligence (Mosso 1892; Hill and Nabarro 1895; Scott 1906). In particular, brain size has been a common proxy for inferring animals' intelligence. According to this approach, animals which have smaller brains in proportion to their body size are less cognitively capable than those with proportionally larger brain sizes (Jerison 1977; Whiting and Barton 2003; Smaers *et al.* 2021). However, despite the prominence of this approach, it is fundamentally flawed as it fails to account for differences in how the brain is utilised. Roughly 50-90% of the metabolic rate of the brain is used on synaptic transmission and the brains high metabolic rate is likely tied to synaptic density which is strongly correlated with glucose consumption rate (Harris *et al.* 2012; Karbowski 2012). However, while the synaptic density per unit brain volume remains constant, the energy consumption per synapse is species and volume-dependent (Karbowski 2012). Hence, brain energetics can vary significantly between taxa. Therefore, there is no strict reason that relative brain size should relate to intelligence. Logically, intelligence must be a result of brain activity, and thus measurement of brain activity must be a better assessment of cognition or intelligence than relative brain size. As the old adage goes – it's not the size, it's the way you use it. As many techniques exist which allow measurement of cerebral blood flow rate or brain metabolism, it is perhaps surprising that relative brain size continues to pervade throughout the literature.

A limited number of studies have examined mass-specific brain metabolism and blood flow to the brain of mammals. Literature is lacking primarily because the often-invasive methodology necessary to acquire data results in animal death. Some of the more direct approaches for brain metabolism measurement involve examination of the rate of oxygen or glucose elimination by the brain itself (Vannucci and Vannucci 2000; Herculano-Houzel 2011b; Karbowski 2012). An alternative to metabolism measurement by consumption is the measurement of metabolism by blood supply (Goldman and Sapirstein 1973; Yamakami and McIntosh 1989; Ridgway *et al.* 2006). While less direct, these approaches are equally valid as tissues determine the amount of blood supply they require, based on their metabolic demand.

Several approaches to blood supply calculation exist. Doppler ultrasound can be used to estimate blood flow velocity and vessel lumen dimensions, thereby allowing calculation of blood flow rate through an artery (Hoskins 1999; Oglat *et al.* 2018). Computed tomographic angiography utilises radiopaque contrasts injected into the blood stream in order to medically assess the vascular system, including vessel dimensions and flow rates (Barfett *et al.* 2014; Eslami *et al.* 2022). Functional magnetic resonance imaging (fMRI) can be used to detect regional blood flow based on the magnetic properties in blood

(Logothetis *et al.* 2001). fMRI can be applied to any region of the body (Sandrasegaran 2014) but is of particular use when applied to the central nervous system as blood flow and neuronal activation are coupled (Logothetis *et al.* 2001).

Another common technique for measurement of blood flow which has been applied to the brain is the indicator dilution approach. In its simplest form, the indicator dilution approach works by introducing a known amount of a known substance into the bloodstream at one location and then measuring the concentration of the substance as it passes another location to allow calculation of a flow rate (Westerhof 2006). Indicators may be a dye, chemical, saline, or blood with a different temperature from the rest of the body (Westerhof 2006). If the location where the indicator is introduced to the blood stream is the heart, it is possible to calculate the cardiac output to the second location as the indicator is distributed evenly throughout the bloodstream (Serrat 2009). Using this principle, adaptations of the indicator dilution method have been developed which utilise microspheres to measure cardiac output and blood flow rate (Neutze *et al.* 1968; Anetzberger *et al.* 2004; Anetzberger and Birkenmaier 2016).

One of the benefits of using microspheres for blood flow calculation is in that it allows easy measurement of regional blood flow distribution. This aspect of microsphere infusion is possible as once introduced into the bloodstream, microspheres gradually move through the circulatory system towards smaller and smaller vessels and eventually become lodged in capillaries (Anetzberger *et al.* 2004). When microspheres are introduced to the bloodstream via the left atrium or left ventricle of the heart, the number of microspheres that become trapped in the capillaries of a given tissue represents the cardiac output to that tissue and is proportional to the tissues regional perfusion rate (Gjedde *et al.* 1977; Bottoncetti *et al.* 1997; Anetzberger *et al.* 2004; Anetzberger and Birkenmaier 2016). This proportional relationship can be converted to an absolute rate of flow by using a pump to withdraw blood at a known rate during the microsphere infusion process (Kaihara *et al.* 1968; Makowski *et al.* 1968; Neutze *et al.* 1968). Microspheres can be radioactively or fluorescently tagged for ease of distribution measurement, although fluorescent microspheres have begun to enter more common usage over radioactive microspheres due to the shortcomings of radioactive microspheres including cost, health risk, and difficulty of disposal (Neutze *et al.* 1968; Aref *et al.* 2017). However, unlike the traditional indicator dilution technique, the microsphere infusion technique is necessarily destructive as it requires the death of the animal so end microsphere distributions can be determined.

Many of the aforementioned methods were able to be applied to tissues other than the brain to obtain metabolic measurements in other tissues. These approaches are sound as blood supply matches metabolic demand according to the principal of symmorphosis. However, all metabolic measurement techniques that rely upon measurement of blood flow rely upon the assumption that blood oxygen content and oxygen extraction

coefficients are constant. Regardless, in light of these modes of metabolism measurement, a novel approach for investigating brain metabolism was developed starting a decade ago based around the measurement of osteoforamina – holes in bone that carry arteries that supply blood to tissues (Seymour *et al.* 2012). This approach is termed the foramen technique.

Foramen technique

The foramen technique uses haemodynamic principles to calculate blood flow rates of arteries that pass-through bones. Essentially, where an artery passes through bony tissue there is a hole in the bone – a foramen or several foramina – which can be measured. The dimensions of these bony holes correspond to the dimensions of the arteries which they pass (Jamniczky and Russell 2004; Seymour *et al.* 2019b). Blood flow through an artery is proportional to the size of the hole. This technique is proven, with calibration against actual blood flow measurements showing a tight relationship (Seymour *et al.* 2015; Seymour *et al.* 2019b). These foramina measurements are much simpler to take because they represent a static measurement, in comparison to the measurements taken by other approaches which may change dynamically in response many variables. Initial studies using the foramen technique examined femoral blood supply from measurement of nutrient foramina for the purpose of investigating locomotion and activity metabolism (Seymour *et al.* 2012; Allan *et al.* 2014; Hu *et al.* 2019; Hu 2021; Hu *et al.* 2022). That cortical brain blood flow rate might be measured by the size of the carotid foramen was independently recognised by Seymour *et al.* (2015) and Boyer *et al.* (2016), leading to several studies of the carotid foramina as a measurement of brain metabolism (Seymour *et al.* 2015; Boyer *et al.* 2016; Seymour *et al.* 2016; Boyer and Harrington 2018; Boyer and Harrington 2019; Seymour *et al.* 2019a; Seymour and Snelling 2019; Seymour *et al.* 2020). Additionally, there has to date been one technical paper on the foramen technique (Hu *et al.* 2020).

The technical paper by Hu *et al.* (2020) establishes best practices for foramen blood flow calculations. The body contains many structures that are referred to as foramen (plural, foramina), including the foramen ovale of the heart, the interventricular foramina connecting the ventricles of the brain, and the plentiful foramina delineated by bony tissue. To differentiate between these soft tissue and hard tissue foramina the term 'osteoforamina' can be used specifically for hard tissue (bony) foramina. Osteoforamina can be categorised into two distinct types; type I foramina carry arteries in combination with other structures such as veins or nerves; while type II foramina pass essentially only one artery (Hu *et al.* 2020). Categorisation in this way is not overly strict in practice as many foramina carry structures other than arteries, but when a foramen carries another structure of such a minor size that the impact on the arterial calibre would be negligible it can be said to be type II (Hu *et al.* 2020). Type I foramina include the nutrient foramina of the femora which passes both a nutrient artery and a vein in many animals (Singh *et*

al. 1991; Hu *et al.* 2020). Type II foramina include the internal carotid canal which passes the internal carotid artery as well as sympathetic nerves and a venous plexus which have insignificant impact on the size of the internal carotid (Paullus *et al.* 1977; von Overbeeke *et al.* 1991; Hu *et al.* 2020; Imai *et al.* 2022).

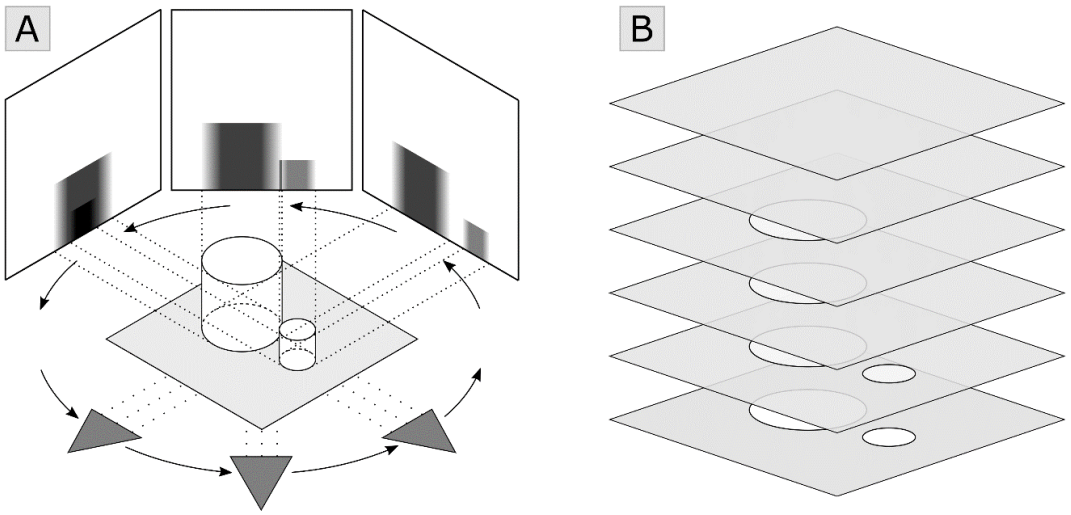

Figure 1-3. Computed tomography basics. CT scanners essentially work by taking X-ray images of an object from many directions and then triangulating the locations of thousands of points throughout the object based on differences in X-ray attenuation. A gantry holding the X-ray source and detector rotates around the object being imaged and takes images at set intervals (A). These projection images are transformed via the tomographic reconstruction process into image slices (B) which when combined with one another in series allow analysis in three dimensions. These slice images are constructed of multiple three-dimensional pixels which are termed voxels. Different density materials will show different levels of X-ray attenuation, represented in the slices as different shades of grey in the image.

X-ray CT vs microphotographic methods of foramina measurement

Some early studies of blood flow through foramina relied upon light microscopy (microphotographic) techniques to determine foramen dimensions (Seymour *et al.* 2012; Seymour *et al.* 2015). These measurements depend on the ability to obtain digital photographs of a perfect view through a foramen; however, this is often impractical. Foramina dimensions and orientation may not be uniform throughout their length; the carotid foramina curves inwards towards the braincase and flares out along its length. Obtaining an idealised view of foramina may furthermore be made difficult by the structures surrounding them; in diprotodont marsupials the mastoid process very nearly blocks the angle of the opening of the foramen such that classical microscopy techniques are disadvantaged. Computed tomography (CT) is a versatile, non-invasive technique which allows us to obtain detailed images of internal structures of the body (Figure 1-3). CT imaging is regularly used in biological studies (Rawson *et al.* 2020; Keklikoglou *et al.* 2021). The use of high-resolution X-ray computed tomography (CT) improves the accuracy of the foramen measurement technique (Figure 1-4). Software for CT image analysis makes it possible to obtain a perfect view of a foramen at the point

of its minimum diameter, often at a higher resolution than may be possible using standard microscopy techniques.

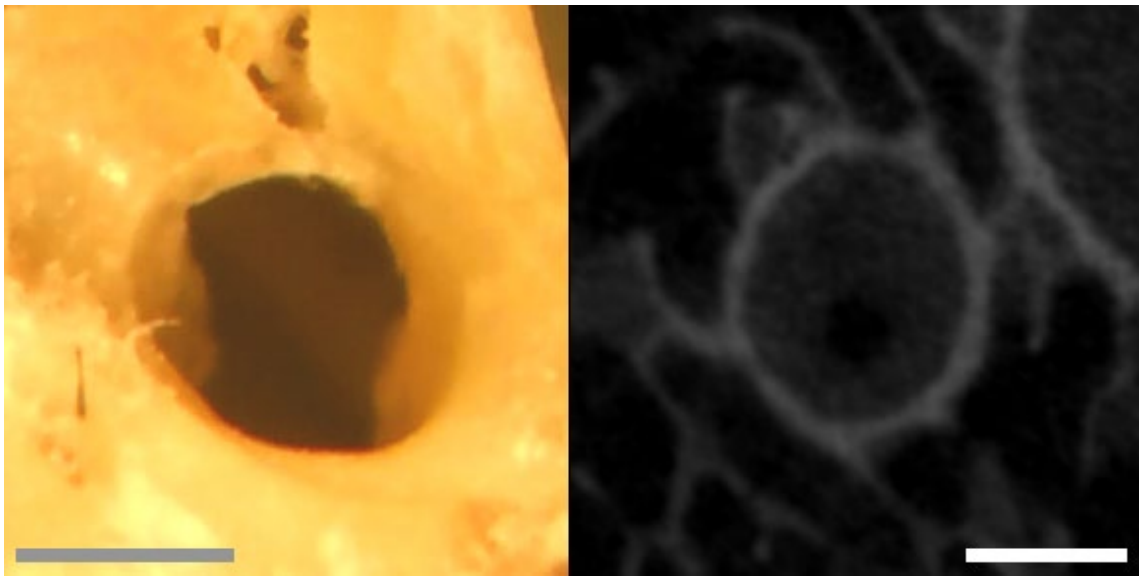

Figure 1-4. Different methods of foramen measurement offer distinct advantages and disadvantages. Left, a microphotograph of the exterior opening of the carotid foramen in a chicken. Right, computed tomography (CT) imagery of the same foramina further along the canal. Scale bars are both 0.5 mm. Photography of foramina is cheap and conceptually straightforward to do, but issues related to lighting, depth of field, and foramina shape can introduce difficulties in obtaining accurate measurements. CT imaging is more time consuming and expensive than photography but offers the ability to examine foramina dimensions in discrete locations that may not be possible with traditional photography. Consideration of all advantages and disadvantages is important when determining which technique is best for a given sample.

Equations of the foramen technique

Depending on the foramen being examined, different equations can be used to calculate blood flow estimates. The first equation developed for calculation of blood flow through an osteoforamina was the blood flow index. The blood flow index was developed from the Poiseuille-Hagen equation and operates under the same assumptions of the Poiseuille-Hagen equation (*Equation 4*), with vessel length assumed to be proportional to the length of the bone. The blood flow index was first applied to the blood flow into femoral bones of mammals, reptiles, and birds (Seymour *et al.* 2012; Allan *et al.* 2014). These early studies were the first to obtain blood flow estimations based on the size of a foramen through which an artery passes.

$$Q_i = r_o^4 \,/\, L$$

Equation 6 – The blood flow index.

where Q_i is the blood flow index in arbitrary units; r_f is foramen radius (cm); and L is femur length (cm).

To calculate blood flow rate rather than blood flow index the shear stress equation (*Equation 3*) was employed in examination of a type II foramina; the carotid foramen

(Seymour *et al.* 2015). The internal carotid artery – which passes through the carotid foramen – is the principal supply or blood to the brain in some mammal groups. In examining blood flow rate for the first time, several variables needed to be accounted for. Arterial walls have a thickness which is determined by the principle of Laplace (*Equation 2*). This thickness can be accounted for using a wall thickness to lumen radius conversion ratio. Seymour *et al.* (2015) relied upon a lumen size conversion ratio of *w* = 0.40, however recently this conversion ratio has been re-examined from 14 imaging studies on humans and is given as *w* = 0.30 (Seymour *et al.* 2019a). This gives the vessel lumen radius, or internal vessel radius. Blood viscosity was taken constant at 0.04 dynes s cm^{-2} in the large vessels of mammals (Schmid-Schönbein *et al.* 1969). Heart rate is not accounted for as cerebral perfusion in humans is largely independent of heart rate (Wilcox *et al.* 1970; Krejza *et al.* 2006). Calculation of wall shear stress was based on data from humans and rats to estimate blood flow rate through the internal carotid artery from the radius of the carotid foramen. This calculation provided the scaling equation $\tau_w = 167\ M_b^{-0.20}$. This scaling equation is supported by an earlier study which examined shear stress in the aorta of humans and rodents and found an exponent of -0.375 (Weinberg and Ethier 2007).

Seymour *et al.* (2016) applied the foramen technique to hominins using the lumen size conversion, the scaling exponent for shear stress, and the shear stress equation (*Equation 3*) of Seymour *et al.* (2015). Boyer and Harrington (2018) criticised the assumptions used for calculation of blood flow rate (particularly the scaling of shear stress), advocating instead for the use of foramina cross sectional area as a proxy for blood flow rate in order to avoid complex haemodynamic considerations. This suggestion was challenged by Seymour and Snelling (2019) in defence of their approach, with the argument that haemodynamics were vital to address due to the respective shortcomings of the use of blood flow proxies. This argument was accepted in a response by Boyer and Harrington (2019).

These discussions between Seymour and Snelling (Seymour *et al.* 2015; Seymour and Snelling 2019) and Boyer and Harrington (Boyer and Harrington 2018; Boyer and Harrington 2019) brought to the fore that ultimately the functional relationship between wall shear stress and body mass was imperfectly understood. Consequently, further equations were developed to sidestep this problem entirely. Seymour *et al.* (2019b) developed two new empirical equations. Blood flow rate and vessel dimensions were compared in the major systemic arteries of nine mammal species (*Bos taurus*, *Canis familiaris*, *Equus caballus*, *Felis catus*, *Homo sapiens*, *Macaca fascicularis*, *Mus musculus*, *Oryctolagus cuniculus*, and *Rattus norvegicus*) and a second order polynomial equation was established that describes the relationship;

$$log\ \dot{Q} = -0.20\ log\ r_i^2 + 1.91\ log\ r_i + 1.82$$

Equation 7 – The Seymour et al. (2019b) mammalian equation.

where $\dot{Q}$ is blood flow rate ($cm^3\ s^{-1}$); and r_i is the arterial internal lumen radius (cm).

Seymour *et al.* (2019b) further examined blood flow rate and vessel dimensions in a subset of data containing only the major cephalic arteries, where the following scaling relationship was determined;

$$\dot{Q} = 155\ {r_i}^{2.49}$$

Equation 8 – The Seymour et al. (2019b) cephalic arteries equation.

where $\dot{Q}$ is blood flow rate ($cm^3\ s^{-1}$); and r_i is the arterial internal lumen radius (cm).

The results from these empirical equations compare with those of the shear stress equation (*Equation 3*) favourably (Seymour *et al.* 2019b). *Equation 7* and *Equation 8* ultimately allow estimations of blood flow rate from mammalian artery dimensions alone without relying on the large number of assumptions of the previous equations. Using only these equations and foramen dimension measurements, the blood flow rate in any foramina enclosed artery of the body can be established. By pairing blood flow measurements with measurements of brain volume and body mass it is possible to examine cerebral perfusion, and thus brain metabolism, allometrically. Thus far, many of these blood flow studies have focused predominantly on mammals.

THESIS AIMS AND STRUCTURE

In the remainder of this introductory chapter, I seek to provide a brief outline of the body of the work and introduce the main aims of the thesis. The experimental work in this thesis focuses principally on two separate groups of taxa: birds and marsupials. Studies of animal cognition often revolve around highly encephalised taxa such as birds and mammals due to their prominence, reputation for intelligence, and relation to humans. Many comparisons have been drawn between the intelligence and cognition of mammals and birds, with some studies putting forth their shared intelligence as a case of convergent evolution (Emery and Clayton 2004b; Rattenborg *et al.* 2009; Roth 2015). Despite both being highly encephalised and renowned for their intelligence, birds and mammals are not particularly closely related. The most recent common ancestor of birds and mammals was a stem amniote, an early animal from the group of organisms defined by the series of fluid filled membranes that surround their young during early development. Amniotes first appeared over 300 million years ago, and through speciation have developed the wide variety of forms known today, including the extant mammals, birds, crocodiles, turtles, and squamates (lizards and snakes) (Shedlock and Edwards 2009; Kverková *et al.* 2022). Detail of the evolutionary relationships between some major amniote divisions is shown in Figure 1-5. Birds and mammals make

convenient candidates for study using the foramen technique as generally their circulatory patterns are better defined in the literature than other groups, and their brain cases are more well defined and enclosed than some groups. For this reason, birds and mammals are the principal groups of interest in the studies presented in this thesis.

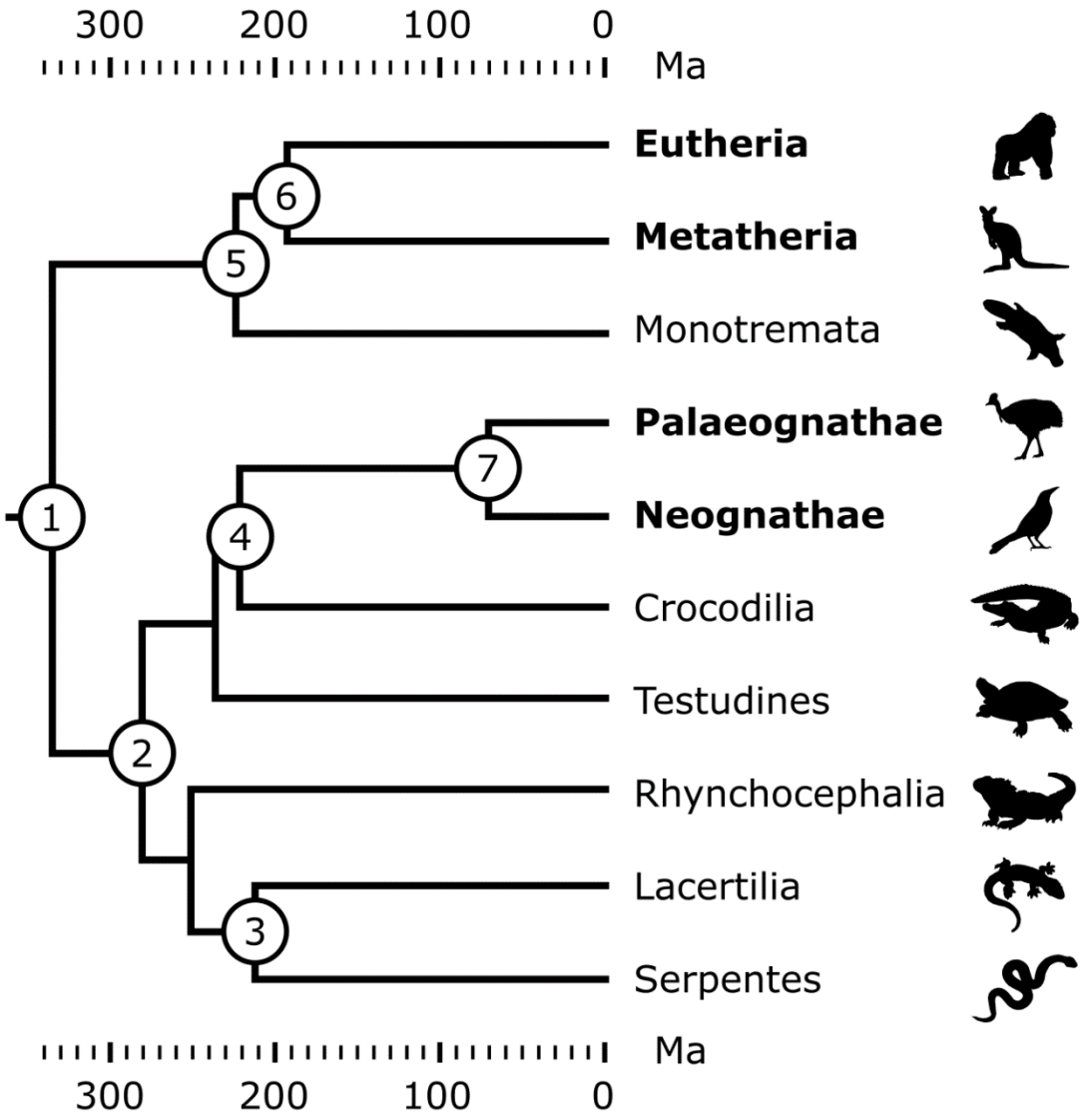

Figure 1-5. Simplified tree of life showing the evolutionary relationships of extant amniotes. Silhouettes of representative species are depicted by their lineages. The specific clades examined in this thesis are indicated with their names in bold. Branch length approximates length of time denoted by the scales at top and bottom of the image (Ma is millions of years). The indicated divisions are (1) Amniotes, (2) Reptiles, (3) Squamates, (4) Archosaurs, (5) Mammals, (6) Therians, and (7) Aves. Aves represents all birds, eutherians are placental mammals, metatherians are marsupial mammals, and monotrematans are monotreme mammals. Based upon trees by Warren *et al.* (2008), Castoe *et al.* (2011), Jones *et al.* (2013), Prum *et al.* (2015), and Kapusta *et al.* (2017).

The aim of this thesis is to examine cerebral metabolism of birds and mammals with the goal of exploring cognition and intelligence. Intelligence and cognition are closely related but distinct concepts. Intelligence is the general ability to learn, understand, and

apply knowledge and skills in order to adapt to new situations. Cognition, on the other hand, refers to the mental processes and mechanisms involved in acquiring, processing, storing, and using information. It encompasses a wide range of abilities such as perception, memory, attention, problem-solving, and decision-making. Cognition is the process that underlies intelligence, but it is not the same thing. Intelligence is complex and difficult to examine quantitatively, with studies largely relying on subjective, qualitative comparisons which evaluate characteristics of the physiology and behaviour of one species in the light of another. Cognition, on the other hand, is easier to quantify. To approach an objective, quantitative, and empirical measurement of cognition I examine brain metabolism through blood flow. The first portion of this thesis focuses upon the scaling relationships for brain metabolism in marsupial taxa across a range of species and their development. The second portion of this thesis seeks to elucidate the nature of brain metabolism in avian taxa across a range of species and their development. The main body of the thesis is divided into five chapters which are structured as follows:

In Chapter 2 of this thesis, I examine the relationship between anterior and posterior cerebral blood flow and brain metabolism in an ontogenetic sequence of the western grey kangaroo, *Macropus fuliginosus.* Blood flow rates through the internal carotid and vertebral arteries are calculated and some comparison is made to blood supply ratios in other mammals by way of reanalysis of specimens from Seymour *et al.* (2015).

Chapter 3 explores the relationship between cerebral blood flow and brain metabolism across a wide swath of avian taxa, ranging from ratites to passerines. Blood flow rates through the cerebral carotids (homologous to the cranial portion of the internal carotids of mammals) are calculated across the Aves and for individual clades and compared with those of the primates and marsupials from chapter 2.

In Chapter 4 I produce a description and anatomical map of the major arteries of the head in the domestic fowl, *Gallus gallus domesticus*. This compared with descriptions of other birds – principally Galliformes. A small artery supplying the cerebrum is identified and described for the first time.

Chapter 5 contains the results of investigations into the relationship between cerebral blood flow and regional brain metabolism in major life history stages and gender groups of the domestic fowl, *Gallus gallus domesticus.* The chapter seeks to provide justification for the methodology used in other chapters (foramen measurement) by contrasting foramen measurement with two other techniques of blood flow calculation – microsphere quantification and contrast assisted lumen measurement.

In Chapter 6 I discuss the major conclusions of the thesis. The use of the foramen technique in blood flow calculation is discussed. Difficulties in equating cerebral perfusion to intelligence are addressed, and future directions for research are proposed.

Three appendices are provided. Appendix A provides brief instructions for navigating an interactive 3D figure produced in Chapter 4. Appendix B provides supplementary material in the form of summary data tables from each study. Appendix C contains the settings and parameters relating to X-ray CT measurements for each chapter. Data relevant to this thesis is available on MorphoSource under project ID: 000445264.

CHAPTER 2

BRAIN PERFUSION IN THE WESTERN GREY KANGAROO

ABSTRACT

Ontogenetic studies of blood flow and brain metabolism are rare, and marsupials are especially important to study because of their distinctive development. This chapter aims to investigate the development of whole brain blood flow via the internal carotid and vertebral arteries in a large-bodied macropod marsupial, the western grey kangaroo (*Macropus fuliginosus*). I produce the first description of the cervical course of the vertebral arteries and examine the ontogenetic development of the lateral atlantal foramen, including blood flow quantification. Paired with additional measurements of carotid foramen dimensions, brain volume, and body mass, this chapter gives calculations of total cerebral blood supply in an ontogenetic series. To provide evolutionary context, haplorrhine primate and diprotodont marsupial specimens from Seymour *et al.* (2015) were reanalysed with the current best practice approach, allowing for comparison with the western grey life history sequence. Dissection revealed that the first cervical vertebrae (atlas) of kangaroos possess foramina that carry the vertebral arteries into the vertebral foramen where they pass into the braincase with the spinal cord via the foramen magnum. These paired foramina in the atlas are common in other animals but the literature lacks a standard nomenclature for this structure, hence I propose the use of the term 'lateral atlantal foramen' to distinguish this structure from other nearby structures and underscore its uniqueness to the first cervical vertebrae. Quantification of perfusion rates through 'preforaminal' vascular grooves was established as a valid technique. The brains of in-pouch joeys have rapidly increasing energy requirements when compared with their adult counterparts, likely driven by an increase in the thickness of the cortex and the formation of more synaptic connections. As western greys develop brain growth rates decreases, with a breakpoint at 620 g that coincides with the period immediately prior to first pouch exit. Brain perfusion increases constantly across the life history sequence, scaling according to $V_{br}^{1.14\pm0.07}$. Flow rate through the major cerebral feeder arteries were also compared and the proportion found to be constant across development, with internal carotid arteries supplying about 70-80% of the brains cerebral blood flow with the remaining 20-30% coming from the vertebral arteries. In marsupials and primates, brain perfusion $\dot{Q}$ scales to brain volume at rates that suggest primate brains may be more efficient than marsupial brains as a way of reducing the volumetric metabolic requirements of their larger, more neuron-dense brains.

INTRODUCTION

Marsupial development is distinctive when viewed through the lens of placental development in that a large proportion of development occurs post partition in the mother's pouch. Placental mammals carry young which receive nourishment during gestation from a placenta and are well relatively developed by parturition. Conversely, marsupial mammals are born at an extremely morphologically primitive stage of development. Generally in placental mammals endothermy is developed across the course of gestation (Tzschentke and Rumpf 2011), while marsupials are ectothermic at birth and progressively adjust their metabolism upward to endothermic levels towards the end of pouch life (Wilkes and Janssens 1986). The marsupial neonate has well-defined forelimbs, a sense of orientation, and separated feeding breathing passages via development of the secondary palate, features which allow the newborn to navigate its way from the birth canal to the mother's pouch, locate a teat, attach to it and begin to suckle (Cannon *et al.* 1976; Renfree 2006; Dawson 2012). Little else is possible for a newborn marsupial neonate. Aside from the forelimbs and part of the palate, future osseous structures are largely cartilaginous at birth, and even the skull of the marsupial neonate is largely unossified at parturition.

Despite the sensory and motor organisation requirements of the marsupial neonate immediately following birth, there is no accelerated shift in the development of the nervous system during gestation (Renfree *et al.* 1982; Nelson 1992). Although the marsupial neonate begins life outside of the pouch, at parturition the rhombencephalon is the primary region of the brain capable of function and thus the marsupial neonate has very limited senses (Cannon *et al.* 1976; Nelson 1988; Nelson 1992; Schneider *et al.* 2009). Most neural development occurs entirely postnatally in marsupials. The newborn marsupial neocortex is two-layered and largely resembles two- to six-week-old eutherian embryos. The final layer of the neocortex begins differentiation three to five days after birth, such that six layers of the neocortex are present at the time of weaning (ca. 10 – 12 kg) (Reynolds *et al.* 1985; Lee and Ward 1989; Saunders *et al.* 1989; Dawson 2012). Aside from the advanced development of the forelimb, jaw and palate, marsupial development progresses analogously to placental mammals – but in the pouch rather than womb. Here, characters that underwent accelerated development before parturition progress more slowly postnatally; these characters were only accelerated to be formed before birth (Nesslinger 1956; Nelson 1992). As the brain is a metabolically expensive organ, this delay in neural development may be an example of resource partitioning during development. However, examinations of how the metabolism of the brain changes across development are lacking in the literature.

Most previous work on brain metabolism and blood flow considers only adult specimens, with a study of human development by Harrington *et al.* (2019a) being the exception. Allometric scaling can be examined within a species across ontogenetic ranges

to determine how the organism develops morphologically and physiologically (Calder 1984). Most organisms change considerably over the course of their life and scaling relationships across a life history are not always the same as those across a taxonomy; in this sense, ontogeny does not necessarily recapitulate phylogeny. The development of the brain is associated with increasing metabolic rate that relies on an adequate supply of blood not only for brain function but also growth. The cost of building and maintaining a brain increases with brain size and composition and is closely related to synaptic activity (Attwell and Laughlin 2001; Herculano-Houzel 2011a). The metabolic rate of the brain is linearly proportional to cerebral blood flow rate (Hawkins *et al.* 1983; Lou *et al.* 1987; Changizi 2001; Turnquist and Minugh-Purvis 2012). Thus, by examining cerebral blood flow rate it is possible to determine cerebral metabolism.

In the absence of direct measurements of flow rates or arterial lumen size, cerebral blood flow can be examined by measurement of osteoforamnia – foramina in bones – which pass arteries that supply the brain. This approach is termed the foramen technique. That cortical brain blood flow rate might be measured by the size of the carotid foramen was independently recognised by Seymour *et al.* (2015) and Boyer *et al.* (2016). Seymour *et al.* (2015) examined the dimensions of the carotid foramina interspecifically in strepsirrhine primates (lemurs, bushbabies, pottos, and lorises), haplorrhine primates (tarsiers, monkeys, apes, and humans) and diprotodont marsupials (the largest marsupial group, including wombats, koalas, possums, gliders, and kangaroo relatives) for the purpose of investigating brain metabolism in these groups. Blood flow regimes are similar in haplorrhines and diprotodonts, where blood flow to the brain occurs via the internal carotid arteries, the vertebral arteries, and the spinal arteries (du Boulay *et al.* 1998). The internal carotid arteries are responsible for the largest proportion of cerebral perfusion and flow rate through the internal carotid arteries is representative of brain metabolism (Lou *et al*. 1987). The internal carotid arteries pass through the carotid foramina to reach the braincase. The spinal arteries provide the internal structures of the spinal cord with blood and do not pass through any distinct foramina. The vertebral arteries are responsible for the blood supply to much of the cerebellum.

Seymour *et al.* (2015) found that carotid supply of the brain increased most strongly in haplorrhine primates across the range of brain volumes with a scaling exponent of 0.95, while in diprotodonts carotid perfusion scales to brain volume with an exponent of 0.73. Blood flow rate through the internal carotid arteries increased with body mass in both groups. Cerebral perfusion in small diprotodonts appears to be similar to that of small primates – suggesting that there may be little difference between their respective cognitive abilities – however, this study did not examine the contribution of the vertebral arteries to whole brain perfusion (Seymour *et al.* 2015). In humans the internal carotid arteries supply about 80% of the brain's blood flow, with the remaining 20% coming from the vertebral arteries (Oktar *et al.* 2006). If the vertebral arteries supply the same

proportion of blood flow in the species examined by Seymour *et al.* (2015), the flow rates and hence brain metabolic rates presented may be four fifths of whole brain metabolism.

Blood flow rate through the vertebral arteries has been estimated in Boyer and Harrington (2018) using foramen measurements applied to the transverse vertebral foramen, however the transverse vertebral foramen contains a venous plexus and so the relationship between foramen size and arterial lumen size was not known (Boyer and Harrington 2019; Seymour and Snelling 2019). In order to accurately gauge whole brain perfusion and hence brain metabolism, it is necessary to first examine the course of the vertebral arteries and determine their size.

In some groups the path of the vertebral artery is well documented in the literature, and in some less so. Some of the earliest descriptions of the cephalic arterial system of mammals contain descriptions of the course of the vertebral arteries in kangaroos (Tandler 1898), however, in the past 120 or so years this aspect of the literature has been dormant. The vertebral arteries pass through the transverse foramen of the lower cervical vertebrae through to the second cervical vertebrae. However, after passing through the transverse foramen of the axis (C2) the precise course of the vertebral artery to the braincase has not been addressed in the literature for kangaroos. The transverse foramina are absent from the atlas (C1) of the kangaroo. In many species the vertebral artery enters a foramen in the lateral mass of the atlas which transports it to the inside of the vertebral foramen, where it then courses anteriorly and enters the braincase via the foramen magnum with the spinal cord. Nomenclature given for this structure varies between names such as alar foramen, atlantal foramen, intervertebral foramen, vertebrarterial [sic] foramen, and lateral vertebral foramen (De Iuliis 2007; Kear *et al.* 2007; König *et al.* 2007; Schaller 2007; Gingerich 2015; Mespoulhès-Rivière *et al.* 2016; Warburton and Prideaux 2021). This structure is present in kangaroos, and here is termed the lateral atlantal foramina to help distinguish the structure from other foramina of the vertebrae (i.e., the alar foramen, vertebral foramen, and transverse foramen).

This chapter examines the development of cerebral blood flow in a large-bodied marsupial, the western grey kangaroo (*Macropus fuliginosus*) with the aim of quantifying whole brain blood flow via the internal carotid and vertebral arteries. To begin with, this chapter provides a description of the upper cervical course of the vertebral arteries in a macropod marsupial for the first time. This chapter applies the foramen technique to both the internal carotid and vertebral arteries, with improved assumptions about wall thickness and the an empirical equation (*Equation 7*) that does not depend on theory (Seymour *et al.* 2019b). Further, this chapter examines the ontogenetic development of the lateral atlantal foramen and presents the first use of the foramen technique to quantify blood flow using the dimensions of pre-foraminal grooves – vascular grooves which

during growth are fully encompassed by bone to form osteoforamina. Finally microphotographs of specimens from Seymour *et al.* (2015) are reanalysed with the current best practices approach to provide for comparison.

METHODS

Sample collection and preparation

Nineteen western grey kangaroos of various ages were scavenged from planned conservation culls carried out on overpopulated properties in south-eastern South Australia. Each cull was carried out according to Australian legal requirements dictated by the Code of Practice for the Humane Shooting of Kangaroos (www.environment.gov.au). Approval to scavenge organ and tissue samples from animals euthanised for conservation or other non-research-related purposes was provided by the University of Adelaide Animal Ethics Committee (S-2011-223).

Initial assessment of specimens involved measurements of body mass and head length. Body mass of small juveniles was determined to a resolution of 1 mg using a 160 g capacity bench scale (Mettler-Toledo AE163, Mettler-Toledo, Switzerland). For large juveniles, body mass was determined to a resolution of 1 g using a 16 kg capacity bench scale (Sartorius QS16, Sartorius, Germany). Adult body mass was determined to a resolution of 10 g by suspending the carcass from a 300 kg capacity spring balance (PCE-CS 300, PCE Instruments, United Kingdom). The body mass of the specimens ranged from 52 g to 62,263 g. Body masses were determined after removal of gut food contents. Head length was determined to 1 mm using digital callipers. Specimens were then beheaded. Specimens with overall head lengths less than 130 mm were fixed in formalin to avoid damage to the cranial and vertebral bones as complete fusion was unlikely to have occurred. Four specimens with overall head lengths greater than 130 mm were also fixed in formalin for later dissection, while the remainder were skinned and hand cleaned in preparation for warm water maceration. Maceration took place at the South Australian Museum's world class facilities at the SA Water sewage treatment plant at Bolivar, South Australia. Following three months of maceration, specimens were cleaned and degreased using a commercially available sodium hydroxide-based cleaning product (Red Knight TruClean, Australia). In a number of cases, there was incomplete fusion of the bones of the crania or vertebrae and the maceration and degreasing processes resulted in disarticulation. In these cases, the disarticulated bones were glued back in place using a conservation grade adhesive (Paraloid B-72 resin Conservation Supplies Australia, Redfern New South Wales, Australia).

Specimens were imaged with X-ray computed tomography (CT scanning). Specimens with head lengths less than 135 mm were scanned intact. In specimens with head

lengths greater than 135 mm, vertebrae were disarticulated from the cranium via the maceration process. Specimens with head lengths less than 135 mm were imaged using the SkyScan-1076 Micro-CT scanner at Adelaide Microscopy. NRecon 1.6.9.4 (Bruker microCT, Kontich, Belgium) was used to reconstruct cross sectional images from tomography projection images and subsequent voxel dimensions were isometric. Specimens with head lengths greater than 135 mm were imaged using the Philips Ingenuity Core 128 scanner at Sound Radiology, Adelaide. Reconstruction was performed using paired software and voxels dimensions were anisometric. Files imaged at Sound Radiology were converted from DICOM format to bitmap format in Fiji (Open Source, www.fiji.sc) and voxel dimensions were corrected from anisometric to isometric using Fiji and DataViewer 1.5.1.2 (Bruker microCT, Kontich, Belgium). Imaging settings were optimised for each specimen in order to maximise image contrast and resolution (Appendix C). Data relevant to this chapter is available on MorphoSource under project ID: 000445264.

Carotid foramina and lateral atlantal foramina were examined in this study to determine internal carotid arterial and vertebral arterial blood flow rates respectively. In diprotodonts the internal carotid arteries pass through the carotid foramina in the posterior end of the basisphenoid (Turner 1848; Archer 1976; Wible 1986; Clark and Smith 1993). To my knowledge there are no studies that describe or identify the lateral atlantal foramina in macropods, nor the structures associated with the lateral atlantal foramina. I identified the lateral atlantal foramina in the kangaroo based upon similarities to descriptions of the cervical vertebrae of other mammals (Schaller 2004; König *et al.* 2007; Evans and de Lahunta 2013; Tobias and Johnston 2013), and from dissections of fresh and fixed specimens obtained from scavenging.

Approach to dissection

A vertical incision was made along the midline of the dorsal surface of the neck from the nuchal crest as far posteriorly as was possible with the decapitated specimens. The skin of the back of the neck was peeled back from this incision to reveal the musculature of the neck. Here the trapezius muscles cover the cervical vertebrae, attaching from the nuchal crest at the anterior end and to the scapula (not present in these specimens) at their posterior end (Dawson *et al.* 1989; Harvey and Warburton 2010). The layers of the postvertebral musculature were removed with care to reveal the dorsal surface of the atlas. A midline incision was made through the musculature from the back of the cranium to the decapitated neck. Lateral incisions were made following the curve of the back of the cranium until reaching the longitudinal ligament. From here, the incision was continued laterally until reaching the mandible where the incision was continued posteriorly. At this point the lateral atlantal foramina was able to be located and examined (Figure 2-3).

Measurement of foramina dimensions and braincase volume

Carotid foramina and lateral atlantal foramina dimensions were determined by analysing CT scans using Fiji. Measurement of foramina was carried out on datasets of pre-prepared images. Preparation involved rotating scans in DataViewer to obtain an idealised view of the path which the arteries take through each specific foramen and saving these idealised views as a reduced volume of interest (VOI) dataset. Reduced VOI datasets were then analysed in Fiji to determine and measure the point with the minimum cross-sectional area of the foramen across its length. This area was assumed to be circular in order for its radius to be inserted into equations to estimate the rate of blood flow. In juvenile specimens, the lateral atlantal foramina were found to be incompletely enclosed and presented as a notch; measurements were taken by measuring the area of the notch which it was perceived an artery would fill assuming a circular cross section (Figure 2-1, Figure 2-9). Although the notch is not closed, for simplicity, throughout the chapter this structure is referred to as a foramen. Carotid foramina were fully enclosed in all specimens examined.

Braincase volume (V_{br}) was measured via the creation of digital cranial endocasts in Avizo 9.0.0 (FEI SAS, Hillsboro, Oregon, USA) following the methodology outlined by Balanoff et al. (2015). In some cases TConv 2.1 (Bruker microCT, Kontich, Belgium) was used to resize datasets due computational memory restrictions (Appendix C). There is a strong correlation between braincase volume, brain volume, and brain mass in organisms which possess large brains relative to their body mass (Isler *et al.* 2008; Balanoff *et al.* 2015). The inside of the braincase is lined with soft tissues which comprise the dural meninges and cerebral vasculature. The presence of these soft tissues results in some discrepancy between the morphology and volume of a cranial endocast and that of the brain, however, in highly encephalised taxa such as birds and mammals the impact of these layers of tissue is regarded as negligible (Balanoff *et al.* 2015). Furthermore, brain case volume and brain mass are essentially interchangeable as the brain has a density of 1.04 g ml^{-1} (Isler *et al.* 2008).

Calculation of absolute cerebral perfusion rate

Absolute cerebral perfusion was estimated for the growth of the Western Grey Kangaroo based upon the measurements of the carotid foramina and lateral atlantal foramina in 19 specimens. Blood flow was calculated individually for left and right foramina and then added together to give a total cerebral blood flow rate. Blood flow rate was calculated using the mammalian interspecific blood flow rate equation from (Seymour *et al.* 2019b);

$$log\ \dot{Q} = -0.20\ log\ r_i^2 + 1.91\ log\ r_i + 1.82$$

Equation 7 – The Seymour et al. (2019b) mammalian equation.

where $\dot{Q}$ is blood flow rate ($cm^3\ s^{-1}$); and r_i is the arterial internal lumen radius (cm).

Arterial walls have a thickness, which is proportional to the internal radius at constant mean blood pressure, according to the principle of Laplace (*Equation 2*). The thickness of the arterial walls of the internal carotid arteries are accounted for by using a wall thickness to lumen radius conversion ratio $w = (r_o - r_i)/r_i$. This conversion ratio has been determined in humans from 14 imaging studies and is given as $w = 0.30$ (Seymour *et al.* 2019a). There is no data available on wall thickness ratios of macropods and the manner in which the kangaroo specimens were scavenged for this study meant that it was not possible to obtain this data myself (i.e. through pressurised fixation of freshly culled specimens in the field). This conversion ratio is not expected to vary much in mammals due to similarities in physiology (ie blood pressure, erythrocytes, hct, etc), and hence $w = 0.30$ is used here.

Reanalysis of specimens from Seymour *et al.* (2015)

Haplorrhine primate and diprotodont marsupial specimens from Seymour *et al.* (2015) were reanalysed with the current best practices approach to provide for comparison with the western grey life history sequence. This reanalysis was chiefly undertaken as the original approach used in the original Seymour *et al.* (2015) paper relied on measurements of minimum foramen radius only. However, diprotodonts possess foramina with cross sections which are quite elliptical rather than circular, and the cross sections of haplorrhine primate foramina – while much less elongated – are by no means perfectly circular. As arterial cross sections may be elliptical rather than circular (Zeina *et al.* 2007; Kamenskiy *et al.* 2012; Seddighi and Han 2021), it stands to reason that blood flow rates through these foramina may have been underestimated. Foramen radius was recalculated by remeasuring the original microphotographs produced for measurement in (Seymour *et al.* 2015); previously foramina size was measured taking minimum radius, where here I take an area measurement using a best fit ellipse. Foramen area measurements were then assumed to be circular to obtain a radius to substitute into equations to estimate the rate of blood flow. Values for body mass and brain volume were sourced from the original Seymour *et al.* (2015) paper. Lumen radius, total internal carotid blood flow rate, and volumetric carotid blood flow rate are calculated according to the updated approach outlined above.

Statistical analysis

Least squares regression was conducted to determine the allometric relationship between $\log_{10}$-transformed independent and dependent variables: M_b, body mass; V_{br}, brain volume; r_{CF}, carotid foramen radius; r_{LAF}, lateral atlantal foramen radius; $\dot{Q}_{ICA}$, internal carotid blood flow rate; $\dot{Q}_{VA}$, vertebral arterial blood flow rate; and $\dot{Q}_{ICA+VA}$ the sum of internal carotid and vertebral arterial blood flow rates. Ordinary least squares regressions on log-transformed data, 95% confidence intervals of regression means and

significant differences between life history stages were determined using analysis of covariance (ANCOVA) in GraphPad Prism 6.0 statistical software (GraphPad Software, La Jolla, CA, USA). Where ANCOVA revealed differences in the scaling exponents, a Johnson–Neyman (J–N) test was performed to determine the range of *X* values over which the individual data for *Y* were significantly different (White, 2003).

In some cases, log-transformed data were not linear, but appeared to be broken into segments. To determine whether biphasic or triphasic relationships existed in a dataset, a Davies' test and breakpoint analysis was performed on the data in the R Statistical Environment v 1.3.1073 (R Core Team 2021) using the segmented package (Muggeo 2008).

Figure 2-1. Development of the lateral atlantal foramen in kangaroos. Initially the path of the vertebral artery is visible as a small groove on the anterior fringe of the atlas termed the lateral atlantal groove. As ossification progresses the vertebral artery is subsumed into the bone, forming a lateral atlantal notch and eventually the lateral atlantal foramen. The structure formed by the path of the vertebral artery is circled or indicated with an arrow in each instance. Each vertebra is represented in lateral aspect (top) and anterior aspect (bottom). From left to right; 52 g, 381 g, 7,173 g, 47,299 g. Rendered images were produced by exporting segmented structures from Avizo into Blender 2.90.1 (Open Source, www.blender.org).

RESULTS

Dissection of the lateral atlantal foramina and vertebral artery

The C2 vertebrae was incomplete or absent in the scavenged specimens that were available for dissection, so the lower segments of the vertebral artery are not described here. In mammals the vertebral artery passes sequentially through the transverse foramina of the vertebrae on its path to the head. After passing through the transverse foramen of the axis (C2) vertebrae, the vertebral arteries pass ventrally under the transverse

process of atlas vertebra before turning medially to pass across the dorsal surface of the vertebrae and then enter the lateral atlantal foramen (Figure 2-2). In some specimens, the vertebral artery gives of a small anteriorly directed branch that appears to supply the musculature of the neck (Figure 2-3). The only identified structures entering the lateral atlantal foramen was the vertebral artery. The vertebral artery did not fill the entirety of the lateral atlantal foramen, but I attribute this to the fact that the arteries were not fixed under pressure. Arteries elastic walls passively cause them to collapse significantly from their natural pressurised calibre when pressure is no longer applied (Drzewiecki *et al.* 1997; Faury *et al.* 1999; Wang *et al.* 2017).

Lateral vertebral foramina in juvenile specimens were discovered to be incompletely enclosed and presented as a groove or notch in the anterior fringe of the atlas, dorsal to the articular facets (Figure 2-1, Figure 2-9, Figure 2-10). As growth and ossification progresses, the vertebral arteries are encompassed by the bone of the atlas, eventually progressing from being present as a groove in joeys, to a notch in juveniles, to a proper foramen as mature adults.

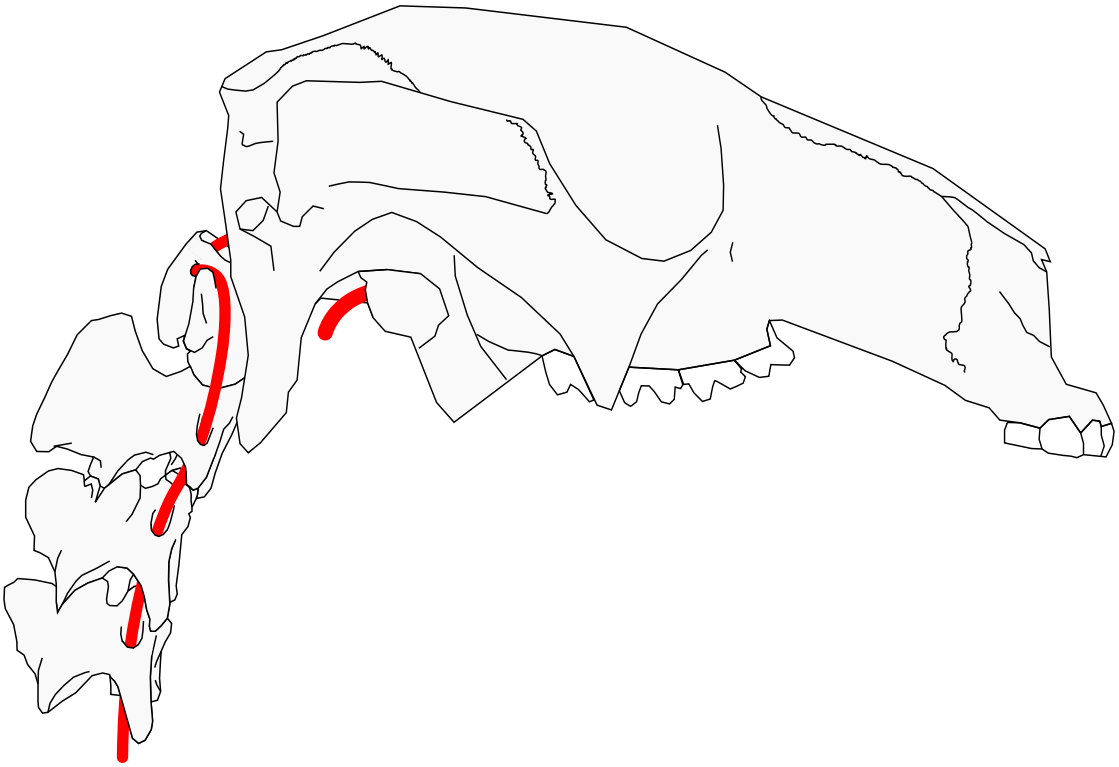

Figure 2-2. Simplified path of the vertebral artery in kangaroos. The vertebral artery is represented by the red line on the left side of the image. The vertebral artery passes as such: Transverse foramen C4, Transverse foramen C3, Transverse foramen C2 (axis), under ventral side of transverse process of atlas, laterally across dorsal surface of atlas, through lateral atlantal foramen in C1, and enters foramen magnum with nerve cord. Also note the relative position of the internal carotid artery, represented in red to the right of the vertebral artery. Spinal arteries pass through the vertebral foramina and into the braincase via the foramen magnum and are not pictured.

Figure 2-3. Dissection of the cervical region of the head of the western grey kangaroo. The top image is one specimen, and the middle and bottom images are from a second. Grey boxes on left images indicate position of enlarged insets on right. Arteries are visible entering the lateral atlantal foramen. The vertebral artery wraps around ventral side of the wing of the C1 vertebra before turning medially to pass across the dorsal surface of the vertebrae and then enter the lateral atlantal foramen. In the second specimen, immediately prior to the entry of the vertebral artery into the lateral atlantal foramen a small branch is given off dorsally which appears to supply the musculature of the neck.

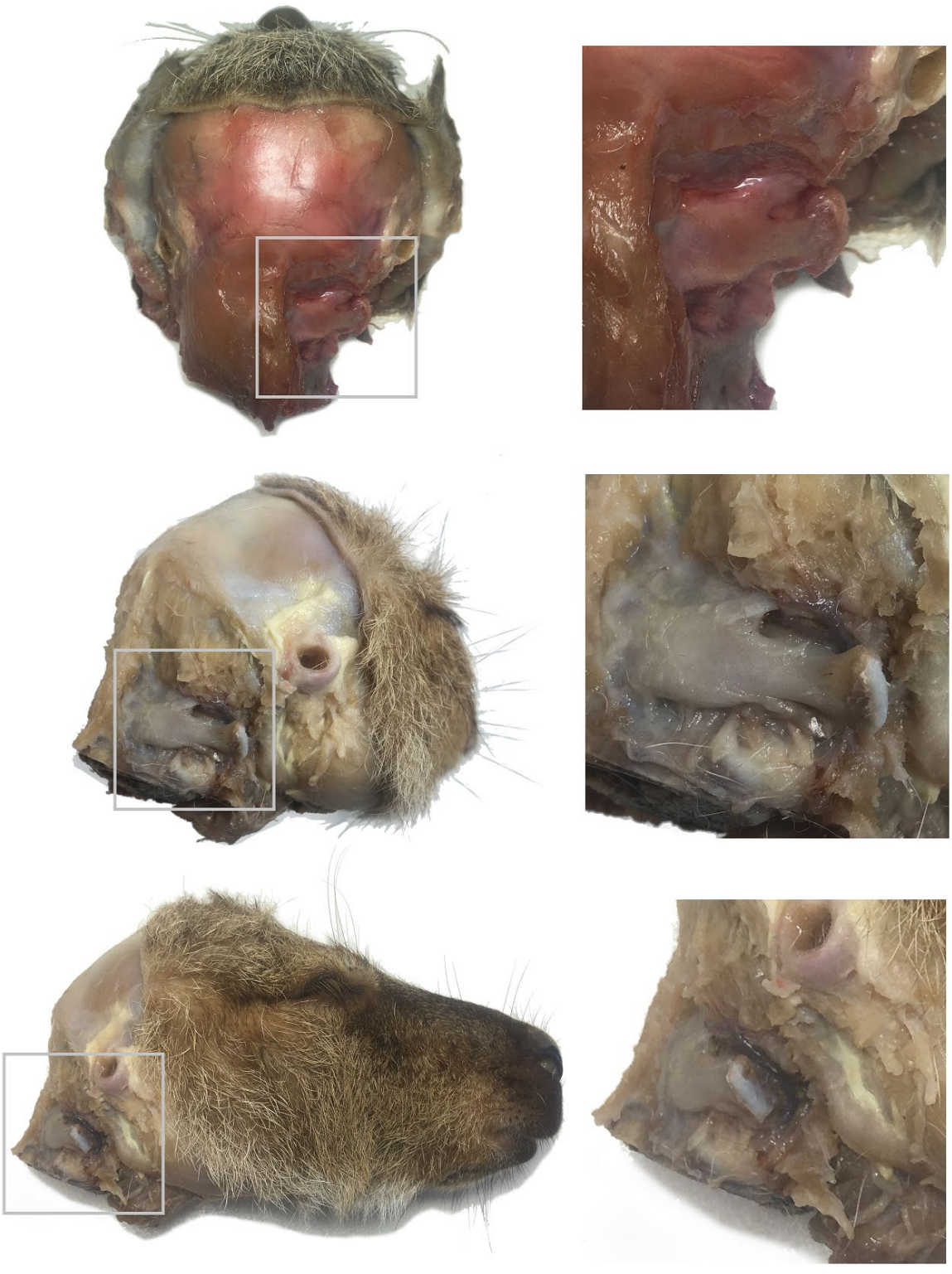
50 mm
25 mm

Reanalysis of Seymour et al. (2015)

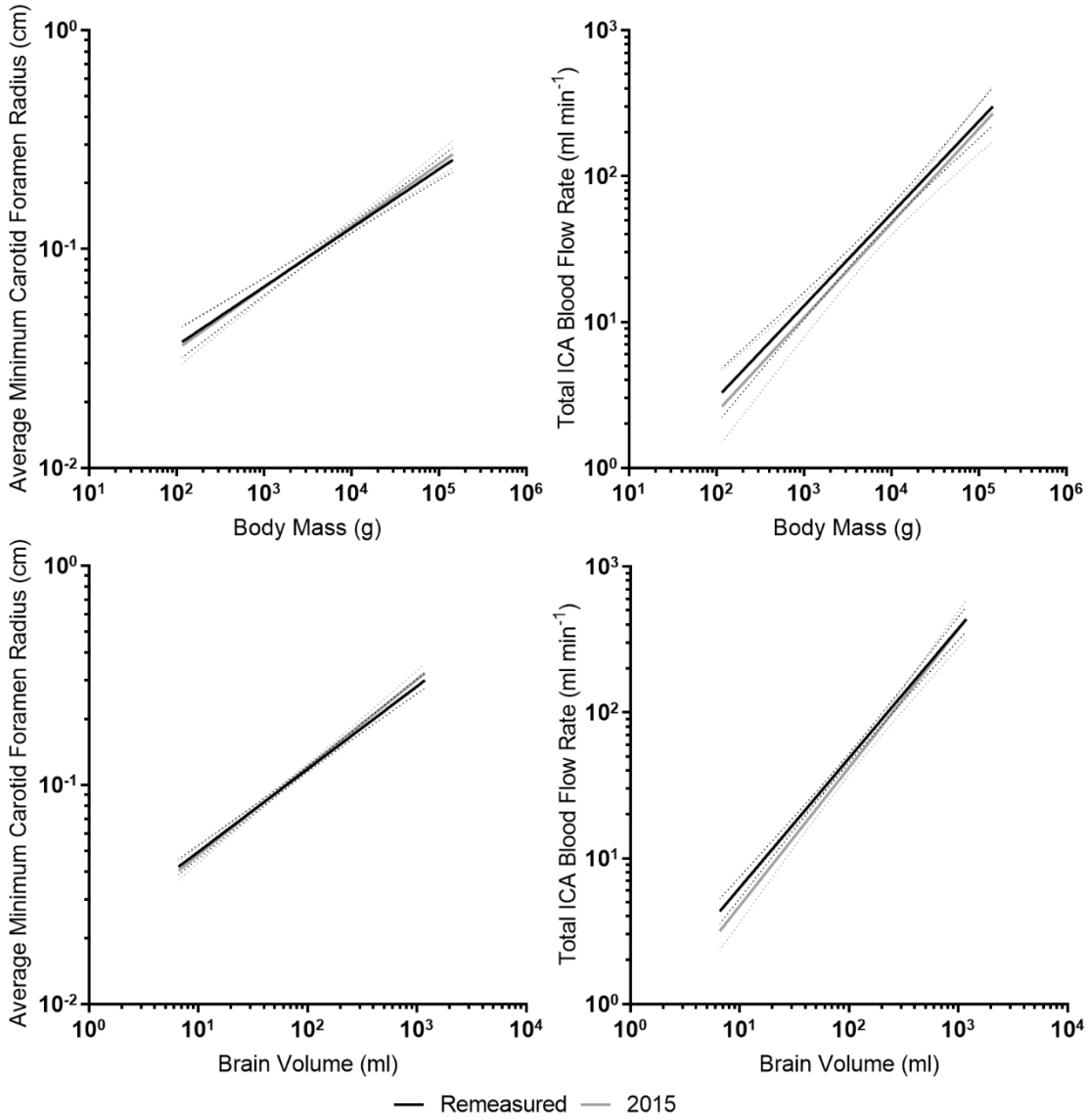

Figure 2-4. Comparison between regressions in haplorrhine primates from original Seymour et al. (2015) blood flow study compared with a remeasurement and analysis of the dataset using the most recent approaches. Haplorrhine primates possess foramina with highly circular cross sections, and hence there is minimal change in the remeasurement which uses a best fit ellipse rather than the minor radius of toe 2015 dataset.

Diprotodont carotid foramen – rather than being perfectly circular – have a distinct elliptical shape. In Seymour *et al.* (2015), the measurements of diprotodont carotid foramen calibre were obtained using optical microscopy and using an earlier approach where the minimum radius of the foramen was taken for blood flow calculations. The current best practices as established in dictate that instead the total area of the carotid foramen is measured, and that this area is converted to a simple radius regardless of whether the foramen is an imperfect ellipse or perfectly circular (Hu *et al.* 2020). The current best-practices' method established by Hu *et al.* (2020) is the approach that was

used in this thesis and thus direct comparison of foramen radius and arterial flow rates between the data produced for this thesis and the original Seymour *et al.* (2015) analysis is not technically rigorous. Figure 2-4 and Figure 2-5 present the differences in regressions from the original data from Seymour *et al.* (2015) and the reanalysed data from Chapter 2 (Table 2-1 and Table 2-2).

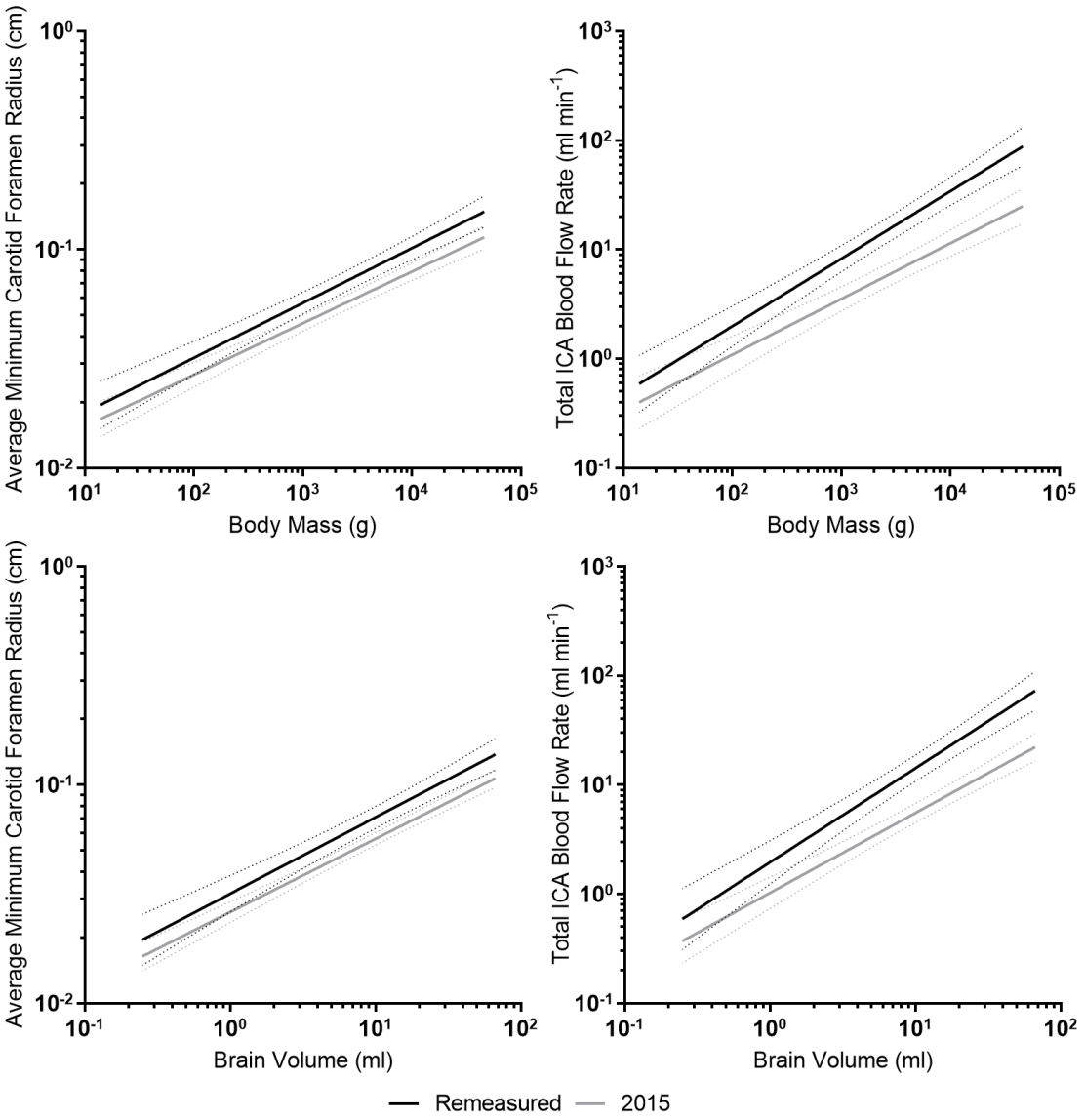

Figure 2-5. Comparison between regressions in diprotodont marsupials from original Seymour et al. (2015) blood flow study compared with a remeasurement and analysis of the dataset using the most recent approaches. Diprotodont foramina have an ellipsoid or oval cross section, hence the dramatically increased elevation in the remeasurement that uses a best fit ellipse rather than the minor radius of toe 2015 dataset.

To further demonstrate the difference between area and radii approaches, testing was performed comparing measurements for minimum radius and radius from area in the ontogenetic data to test if there was a significant difference between the approaches (Appendix B: Table S 2 - 2.). This was testing was performed on measurements from CT

imagery data as optical microscopy could not be performed on the half of the dataset, which was not macerated due to incomplete osteological development. Data were non-parametric and asymmetric, so paired-samples sign tests were conducted. The median radius in cm of the foramina obtained from the minimum radius measurement was significantly different from the median radius in cm of the foramina measured from area (paired-samples sign test, $p < 0.0001$). This result was true of both the CF and the LAF. Further, the median radius in cm of the lumen calculated from the 1.3 ratio was significantly different from the median radius in cm of the lumen calculated from the 1.4 ratio (paired-samples sign test, $p < 0.0001$). This result was true of both the ICAs and the VAs.

Biphasic development of brain volume and cerebral perfusion

Across the overall life history sequence, western grey kangaroo brain volume increased at a rate of $M_b^{0.40}$, carotid foramina and vertebral foramina radius both increased at a rate of $M_b^{0.19}$, carotid blood flow increased at a rate of $M_b^{0.45}$, vertebral artery flow increased at a rate of $M_b^{0.46}$, and the sum of carotid and vertebral artery blood flow increased at a rate $M_b^{0.45}$. Similarly, carotid foramina increased at a rate of $V_{br}^{0.48}$, vertebral foramina radius both increased at a rate of $V_{br}^{0.47}$, carotid blood flow increased at a rate of $V_{br}^{1.14}$, vertebral artery flow increased at a rate of $V_{br}^{1.15}$, and the sum of carotid and vertebral artery blood flow increased at a rate $V_{br}^{1.14}$. However, it was immediately clear that there was a growth curve present in the data when plotted against body mass, and so a breakpoint analysis was performed to determine any break in phase in the dataset.

Breakpoints in the data were identified using Davies' test, which revealed that data was biphasic. Various breakpoints were identified depending on the independent and dependent variable being examined. All breakpoints identified concerned body mass as the independent variable; no change in the slope was detected in the relationships of $\dot{Q}$ ($\dot{Q}_{ICA}$, or $\dot{Q}_{VA}$, or $\dot{Q}_{ICA+VA}$) versus V_{br} (Davies' test, $p > 0.05$). Breakpoints involving blood flow calculations had broad variability, and so were discarded. The remaining breakpoints (464 ± 133 for V_{br} on M_b, 860 ± 673 for r_{ICF} on M_b, and 532 ± 904 for r_{LAF} on M_b) all fall between the same two datapoints for body mass, hence a rounded average of 620 g is used as the breakpoint throughout the analysis. For ease of comparison slopes for in-pouch, post-pouch, and overall life history sequence are presented in tables regardless of independent variable (Table 2-3, Table 2-4, Table 2-5, Table 2-6).

Brain volume in the in-pouch growth phase increased at a rate which had some overlap with isometry ($V_{br} \propto M_b^{1.0}$)., while brain volume in the post-pouch phase increased at a rate much lower than isometry ($V_{br} = M_b^{0.24}$). Brain volume increased in regards to body mass with a steeper exponent for in-pouch individuals than for post-pouch individuals. Bonferroni corrected Johnson-Neyman post hoc testing revealed a with a narrow region of non-significance in the relationship of brain volume to body mass for the in-pouch and post-pouch groups which corresponded with the breakpoint region, at 335g to

785g. For in-pouch individuals, V_{br} scaled with M_b according to an exponent which was greater than but not significantly different from that of diprotodonts interspecifically. In-pouch V_{br} is 5.3-fold larger than in diprotodonts of equivalent body mass (Figure 2-6; Table 2-3). The lines for post-pouch and diprotodonts intersect at a point which is equivalent with the proposed measurements of brain volume and body mass of a typical adult western grey kangaroo (Figure 2-6). The post-pouch phase saw V_{br} scale with M_b according to an exponent (0.24 ± 0.30) which was lower than the in-pouch (0.87 ± 0.13), interspecific (0.70 ± 0.06), and haplorrhine (0.71 ± 0.09) exponents, with small regions of non-significance where the regressions intersected (Bonfer. J–N tests).

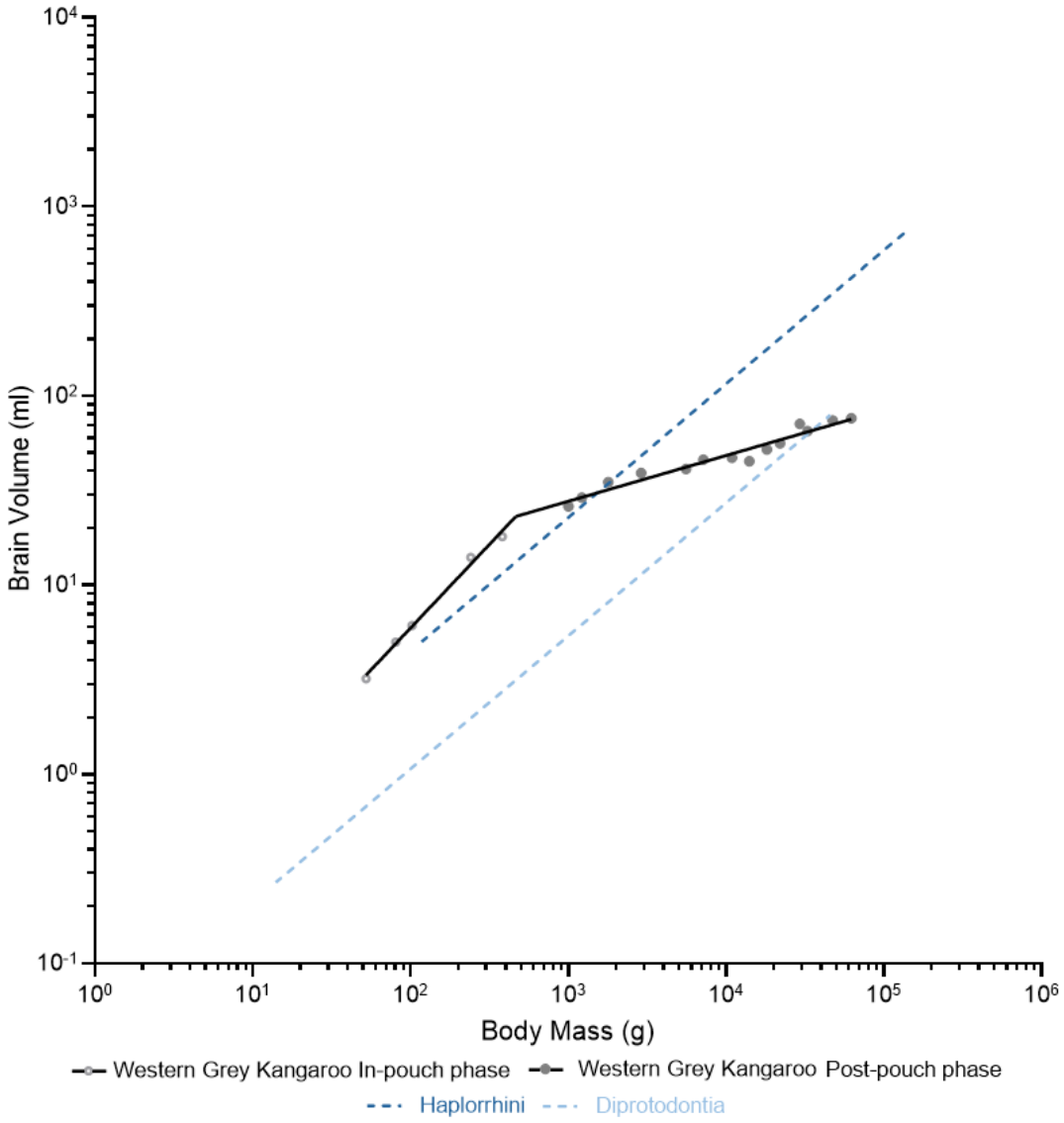

Figure 2-6. Brain volume compared with body mass across the development of the western grey kangaroo. This graph shows the dramatic change in the growth rate of the brain between the in-pouch and the post-pouch phases of development in the western grey kangaroo. Hollow grey dots represent the in-pouch phase while solid grey dots represent the post-pouch phase. The interspecific scaling relationships of haplorrhine primates and diprotodont marsupials (recalculated from Seymour *et al.* (2015)) are represented with dark and light blue dotted lines, respectively.

Figure 2-7. Graphs (A-D) of internal carotid foramen radius and carotid arterial blood flow rate across the development of the western grey kangaroo. As the foramen dimension measurement technique dictates, radius is used in conjunction with *Equation 7* and a wall thickness correction ratio to gauge blood flow. This graph shows how LAF radius changes with increasing body mass in the developing western grey kangaroo. Initially, radius increases at a rapid rate; this rate decreases in adults. Average minimum foramen radius refers to an average of left and right foramina, while total blood flow rate refers to the sum of flow through paired arteries.

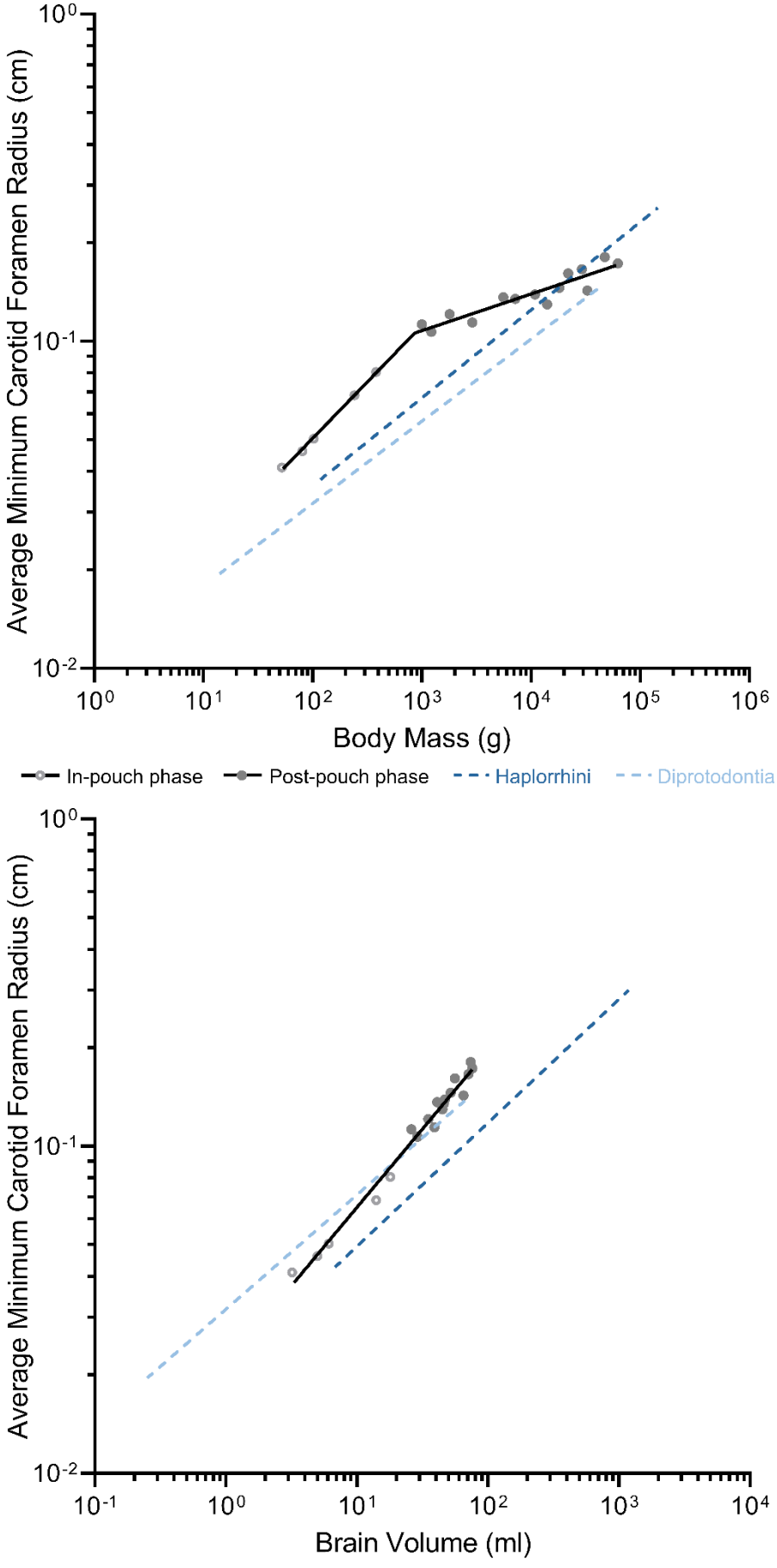
Average Minimum Carotid Foramen Radius (cm)
10^0
10^{-1}
10^{-2}
10^0 10^1 10^2 10^3 10^4 10^5 10^6
Body Mass (g)
In-pouch phase
Post-pouch phase
Haplorrhini
Diprotodontia
Average Minimum Carotid Foramen Radius (cm)
10^0
10^{-1}
10^{-2}
10^{-1} 10^0 10^1 10^2 10^3 10^4
Brain Volume (ml)

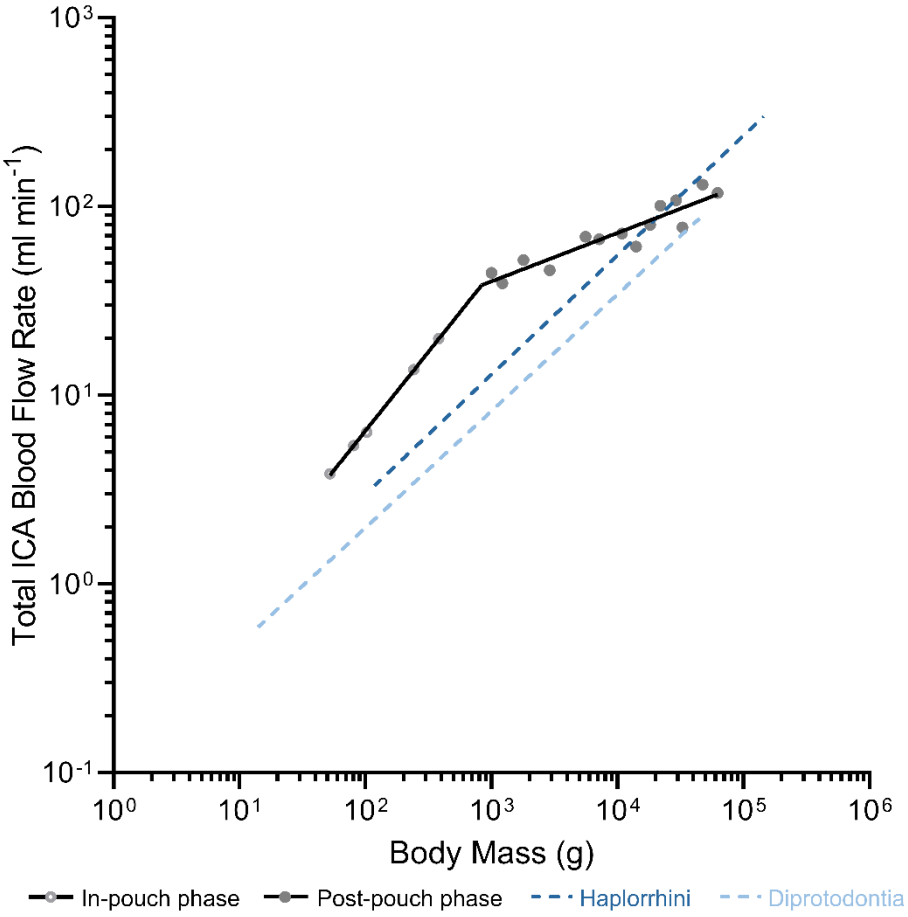
Total ICA Blood Flow Rate (ml min-1)
Body Mass (g)
In-pouch phase
Post-pouch phase
Haplorrhini
Diprotodontia

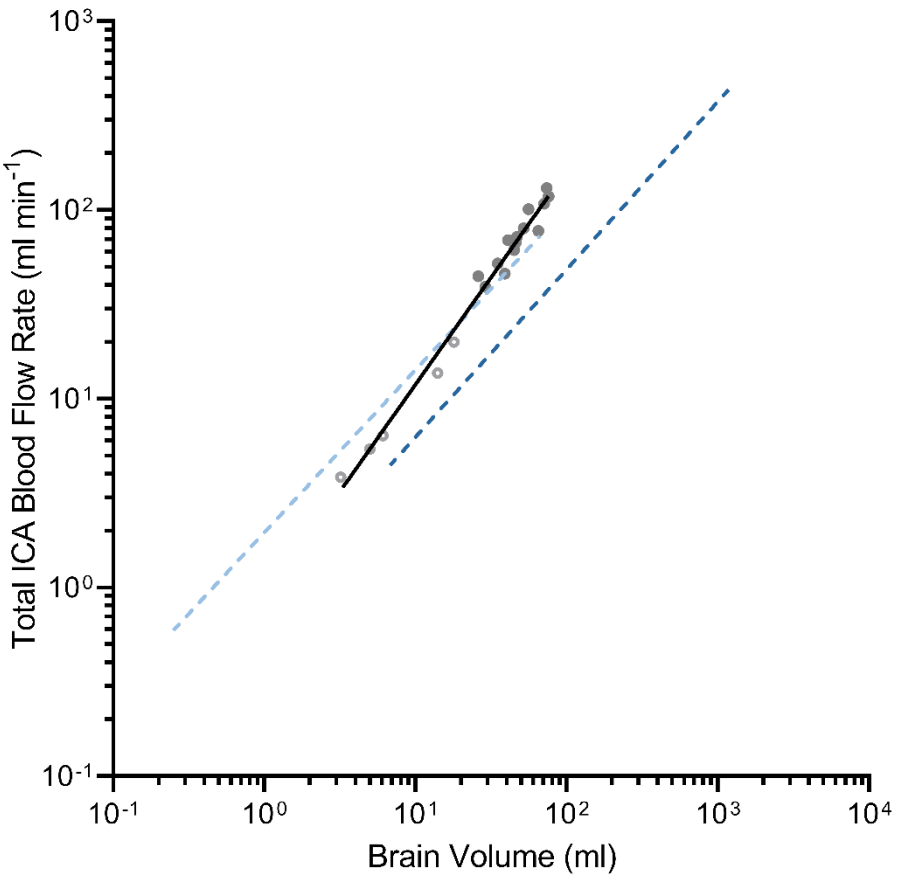
Total ICA Blood Flow Rate (ml min-1)
Brain Volume (ml)

During the in-pouch phase total internal carotid artery blood flow rate scales to body mass with an exponent (0.84 ± 0.05) which was significantly different from isometry ($\dot{Q}_{ICA} < M_b^1$) (Figure 2-7). During the post-pouch phase $\dot{Q}_{ICA}$ scales to M_b with a much shallower exponent (0.26 ± 0.06). The allometric equations for $\dot{Q}_{ICA}$ on M_b in the in-pouch phase and post-pouch phase are statistically significantly different with a region of non-significance around the breakpoint region, at 400 g to 3460 g (Bonfer. J–N tests) (Table 2-3). The exponent for the in-pouch phase (0.84 ± 0.05) was not significantly different from the interspecific exponent (0.62 ± 0.10) or that of haplorrhines (0.63 ± 0.09) but the difference between each of the elevations were significant (Table 2-3). The exponent for the post-pouch phase (0.26 ± 0.06) was lower than the interspecific and haplorrhine exponents, with a region of non-significance beginning at ca. 10000 g M_b (Bonfer. J–N tests).

For the scaling relationship of total internal carotid artery blood flow rate against brain volume, no breakpoint was detected in the western grey data and the exponents of the in-pouch and post-pouch datasets were not significantly different from one another. Across the overall western grey ontogeny total internal carotid artery blood flow rate scales to brain volume with an exponent (1.14 ± 0.07) which was steeper than isometry ($\dot{Q}_{ICA} > V_{br}^1$). The overall western grey scaling exponent for $\dot{Q}_{ICA}$ to V_{br} was not significantly different from the interspecific (0.86 ± 0.16) and haplorrhine (0.89 ± 0.07) exponents within the examined brain volume ranges (Bonfer. J–N tests). The elevation of the in-pouch and post-pouch regression lines for $\dot{Q}_{ICA}$ to V_{br} were lower than that of the haplorrhine line but not significantly different from the elevation of the interspecific (Table 2-4).

During the in-pouch phase total vertebral artery blood flow rate scales to body mass with an exponent (0.94 ± 0.76) which was not significantly different from isometry ($\dot{Q}_{VA} \propto M_b^1$). Post-pouch $\dot{Q}_{VA}$ scales to M_b according to an exponent (0.29 ± 0.13) which is significantly different from the in-pouch exponent. The in-pouch and post-pouch relationships both scaled at a rate which was not significantly different from the overall scaling relationship ($2.87 \times 10^{-1} M_b^{0.46 \pm 0.09}$) (Table 2-5). Total vertebral artery blood flow rate scales to brain volume with isometry in each group ($\dot{Q}_{VA} \propto V_{br}^1$). The in-pouch growth phase exponent was 1.07 ± 0.95, post-pouch phase was 1.12 ± 0.59, and overall life history sequence exponent 1.15 ± 0.17 (Table 2-5).

Total cerebral perfusion rate scaled to body mass in the in-pouch growth phase at a rate which was not significantly different from isometry. For $\dot{Q}_{ICA+VA}$ on M_b, the in-pouch phase scaled with an exponent (0.86 ± 0.16) that was significantly different from the post-pouch phase (0.26 ± 0.05) and the overall exponent (0.45 ± 0.07) (Table 2-6). There was no significant difference detected in the relationships of total cerebral perfusion rate scaled to brain volume between the in-pouch, post-pouch, or overall life history

sequence. All exponents scaled at a rate not significantly differently from isometry ($\dot{Q}_{ICA+VA} \propto V_{br}^{1.0}$) (Table 2-6).

Figure 2-8 compares the scaling relationships between different arteries and foramina. No difference is present between the slopes of any of the scaling relationships in different foramina or arteries from the same phase (Table 2-7). In-pouch blood flow rate scales to body mass with an exponent of 0.86, specifically, vertebral arteries scale $M_b^{0.94\pm0.76}$, carotids scale $M_b^{0.84\pm0.05}$, and combined cerebral feeders scale $M_b^{0.86\pm0.16}$. Post-pouch blood flow rate scales to body mass with an exponent of approximately 0.27; vertebral arteries scale $M_b^{0.29\pm0.13}$, carotids scale $M_b^{0.26\pm0.06}$, and combined cerebral feeders scale $M_b^{0.26\pm0.05}$. Across the entire life history sequence, blood flow rate scales to brain volume with an exponent of approximately 1.14; vertebral arteries scale $V_{br}^{1.15\pm0.17}$, carotids scale $V_{br}^{1.14\pm0.07}$, and combined cerebral feeders scale $V_{br}^{1.14\pm0.07}$ (Figure 2-8, Table 2-7).

Elevations of the scaling relationships are significantly different between each group of arteries and foramina. For $\dot{Q}$ on V_{br}, internal carotid artery elevations are 3.6 times greater than vertebral arteries and cerebral feeder artery elevations are 1.29 times greater than internal carotid arteries. The internal carotids contribute 78% and the vertebral arteries 22% of total arterial supply. For $\dot{Q}$ on M_b, in-pouch internal carotid artery elevations are 5.7 fold higher than vertebral arteries and cerebral feeder artery elevations are 1.18 times higher than internal carotid arteries. Post-pouch internal carotid artery elevations are 4.76 times higher than vertebral arteries and cerebral feeder artery elevations are 1.2 times higher than internal carotid arteries (Figure 2-8, Table 2-7). The proportion of blood flow contributed to the brain by each artery remains essentially constant across development (Figure 2-8, Table 2-7). Comparisons for scaling relationships from different phases are provided in Table 2-3, Table 2-4, Table 2-5, and Table 2-6.

Figure 2-8. Blood flow rate across the development of the western grey kangaroo.These graphs (A-D) show the dramatic difference between the volume of blood which is supplied to the brain via the vertebral arteries and the volume of blood which is supplied to the brain via the internal carotids. Combined, these graphs show the allometric relationships of the rate of flow provided by the cerebral feeder arteries and the growth of the brain.

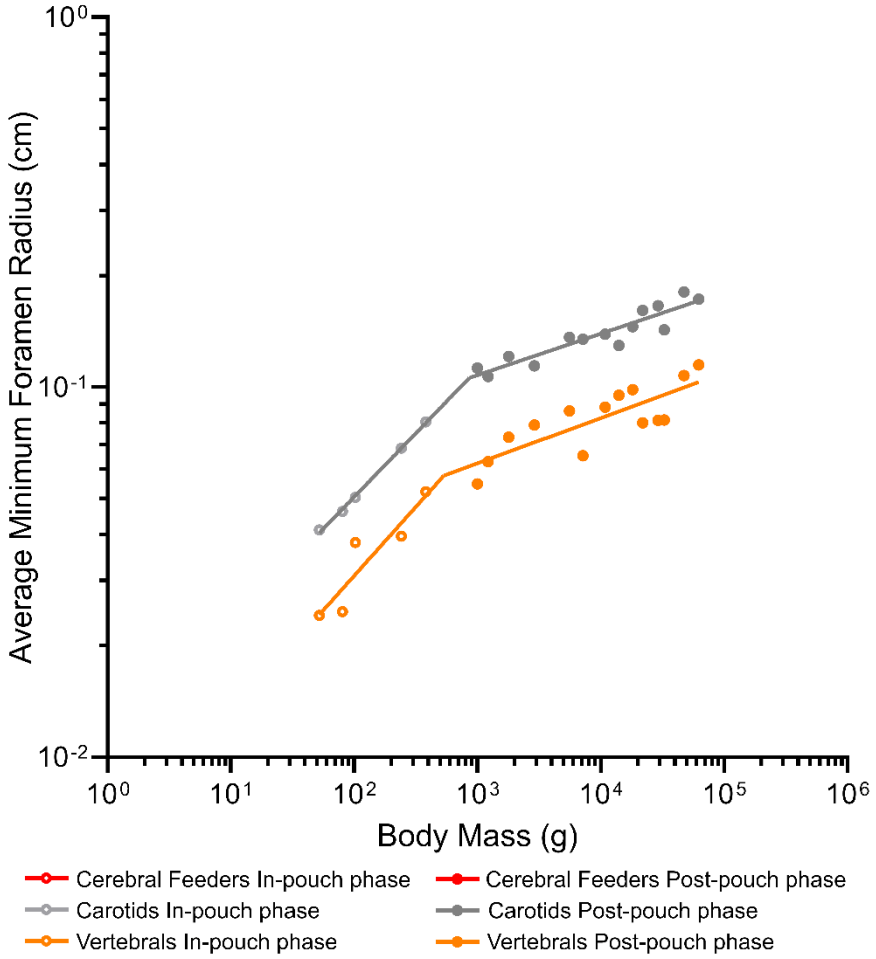
Average Minimum Foramen Radius (cm)
10^0
10^-1
10^-2
10^0
10^1
10^2
10^3
10^4
10^5
10^6
Body Mass (g)
Cerebral Feeders In-pouch phase
Cerebral Feeders Post-pouch phase
Carotids In-pouch phase
Carotids Post-pouch phase
Vertebrals In-pouch phase
Vertebrals Post-pouch phase

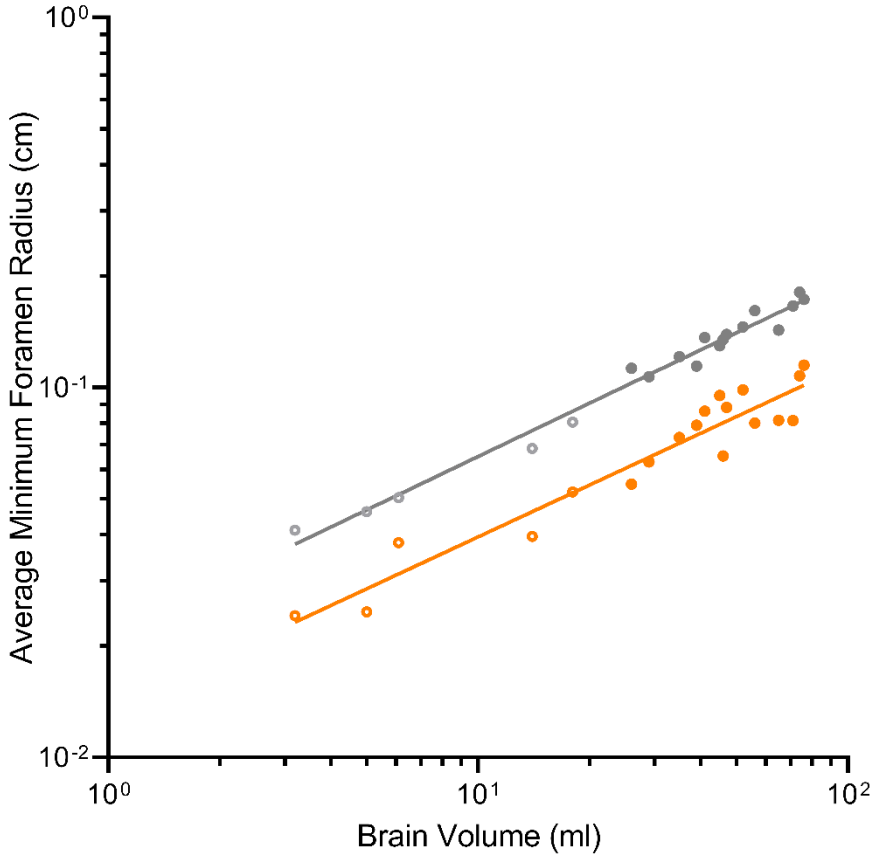
Average Minimum Foramen Radius (cm)
10^0
10^-1
10^-2
10^0
10^1
10^2
Brain Volume (ml)

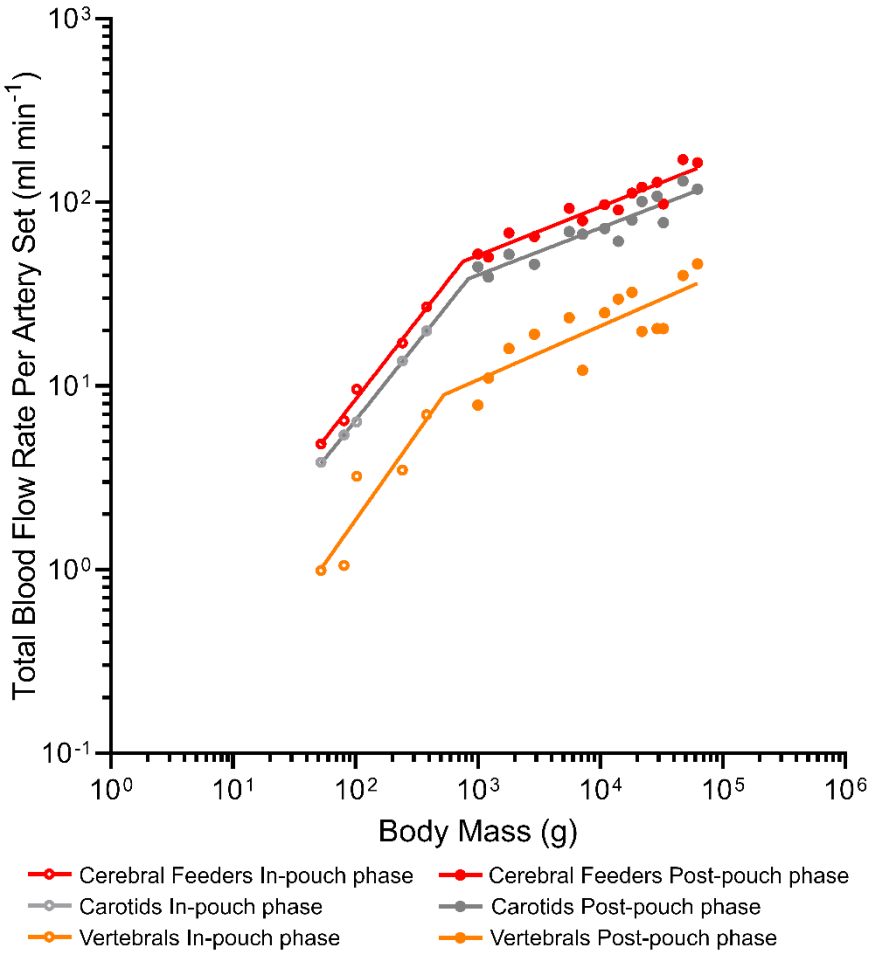
Total Blood Flow Rate Per Artery Set (ml min-1)
10^3
10^2
10^1
10^0
10^-1
10^0
10^1
10^2
10^3
10^4
10^5
10^6
Body Mass (g)
Cerebral Feeders In-pouch phase
Cerebral Feeders Post-pouch phase
Carotids In-pouch phase
Carotids Post-pouch phase
Vertebrals In-pouch phase
Vertebrals Post-pouch phase

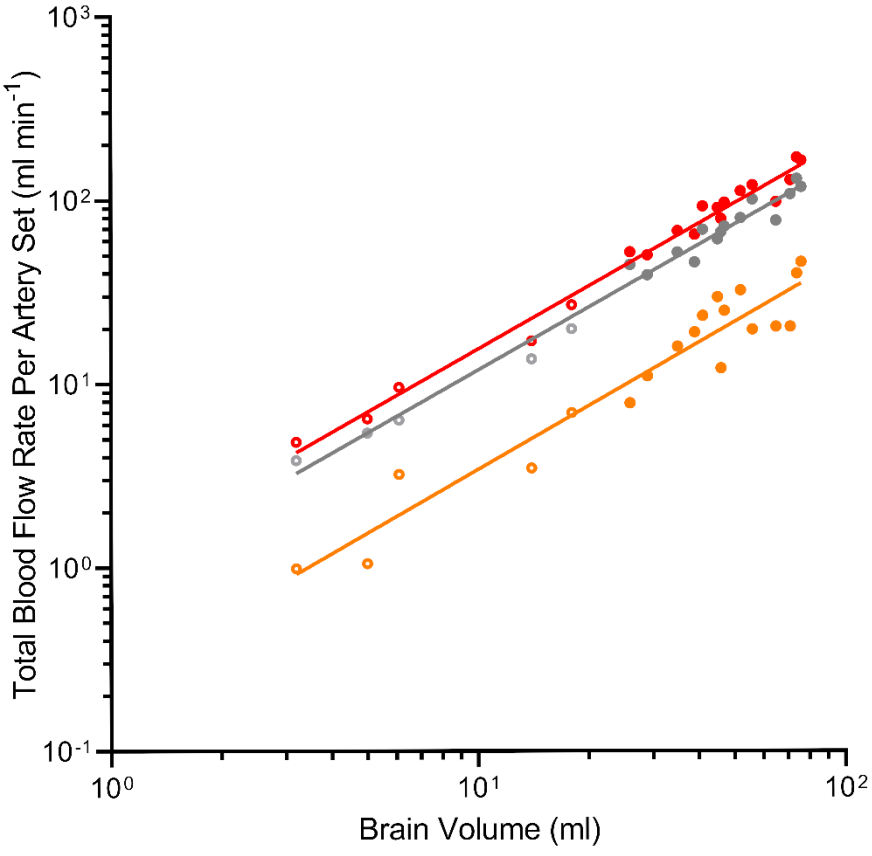
Total Blood Flow Rate Per Artery Set (ml min-1)
10^3
10^2
10^1
10^0
10^-1
10^0
10^1
10^2
Brain Volume (ml)

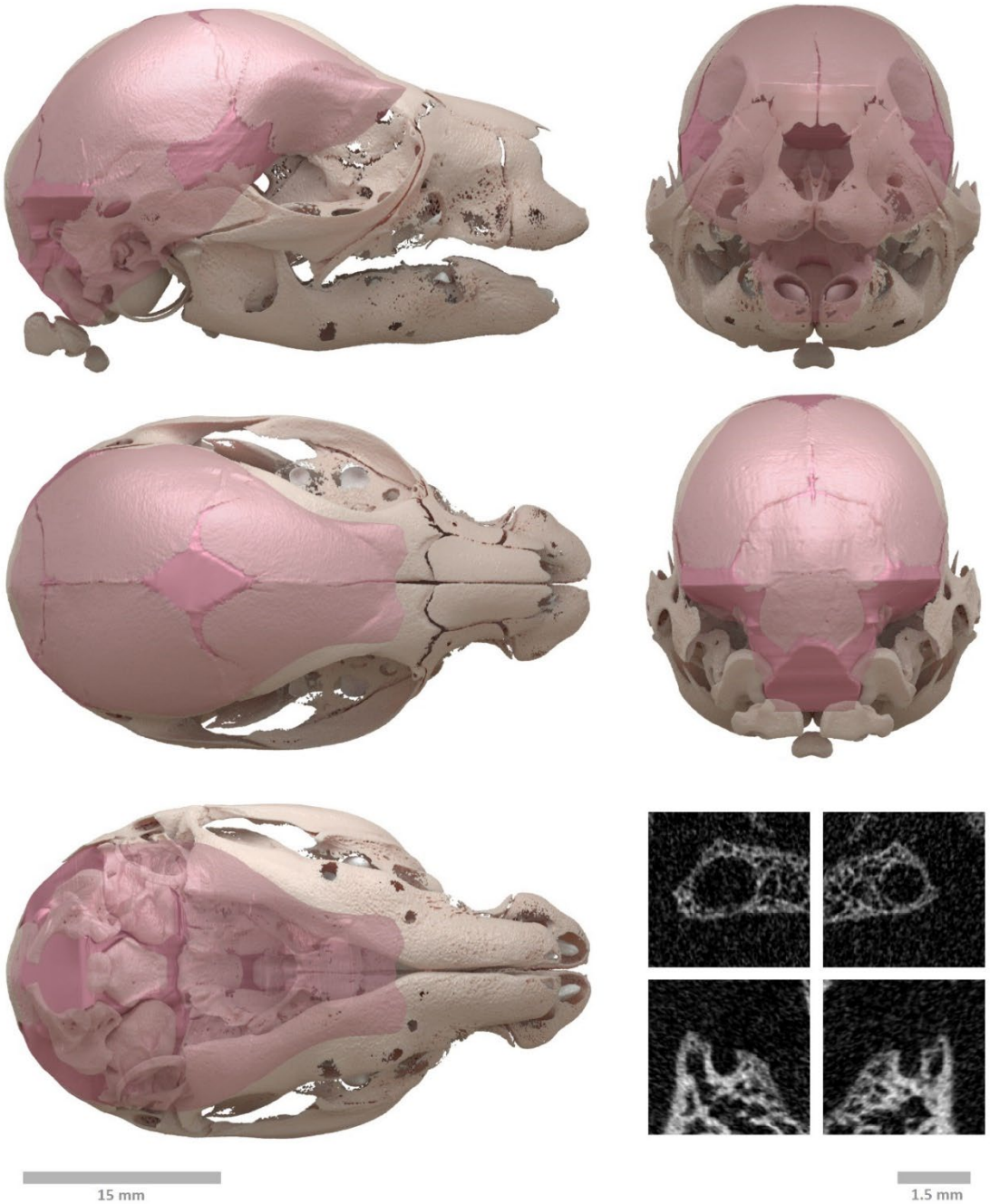

Figure 2-9. Digital cranial endocasts and foramina of cerebral feeder arteries in an 80 g western grey kangaroo joey. The cranial bones and atlas vertebrae have been made transparent such that the endocast shape can be better visualised. On bottom right are the left and right carotid foramina (top) and left and right lateral atlantal foramina (bottom). Note distinct scale bars for three-dimensional renders and two-dimensional foramina images. By this stage of development the carotid foramina is fully enclosed, while the lateral atlantal foramina are osseous grooves across the anterior fringe of the atlas. Rendered images were produced by exporting segmented structures from Avizo into Blender 2.90.1 (Open Source, www.blender.org).

Figure 2-10. Digital cranial endocasts and foramina of cerebral feeder arteries in a 62 kg adult male western grey kangaroo. The cranial bones and atlas vertebrae have been rendered transparent such that the endocast shape can be better visualised. On bottom right are the left and right carotid foramina (top) and left and right lateral atlantal foramina (bottom). Note distinct scale bars for three-dimensional renders and two-dimensional foramina images. Both the carotid foramina and the lateral atlantal foramina are fully enclosed osteoforamina by the time western greys reach adulthood. Rendered images were produced by exporting segmented structures from Avizo into Blender 2.90.1 (Open Source, www.blender.org).

Table 2-1. Allometric equations in haplorrhine primates from the original Seymour et al. (2015) blood flow study compared with a remeasurement and analysis of the dataset using the most recent approaches. The regression of brain volume on body mass did not change but is included (greyed out) for comparison.

Independent	Dependent	Clade	Power Equation	(r^2)	Slope	Elev.
M_b (g)	V_{br} (ml)	Haplorrhini Remeasured	$1.73x10^{-1}M_b^{0.71±0.09}$	0.89	A	A
		Haplorrhini 2015	$1.73x10^{-1}M_b^{0.71±0.09}$	0.89	A	A
M_b (g)	$\dot{Q}_{ICA}$ (cm^3 min^{-1})	Haplorrhini Remeasured	$1.62x10^{-1}M_b^{0.63±0.09}$	0.87	A	A
		Haplorrhini 2015	$1.21x10^{-1}M_b^{0.65±0.13}$	0.76	A	A
M_b (g)	r_{CF} (cm)	Haplorrhini Remeasured	$1.05x10^{-2}M_b^{0.27±0.04}$	0.87	A	A
		Haplorrhini 2015	$9.46x10^{-3}M_b^{0.28±.0.04}$	0.84	A	A
V_{br} (ml)	$\dot{Q}_{ICA}$ (cm^3 min^{-1})	Haplorrhini Remeasured	$8.08x10^{-1}V_{br}^{0.89±.0.07}$	0.95	A	A
		Haplorrhini 2015	$5.29x10^{-1}V_{br}^{0.95±.0.11}$	0.91	A	B
V_{br} (ml)	r_{CF} (cm)	Haplorrhini Remeasured	$2.07x10^{-2}V_{br}^{0.38±.0.03}$	0.96	A	A
		Haplorrhini 2015	$1.91x10^{-2}V_{br}^{0.40±.0.03}$	0.95	A	A
V_{br} (ml)	$\dot{Q}_{ICA}$ (cm^3 min^{-1}) / V_{br} (ml)	Haplorrhini Remeasured	$1.24x10^{0}V_{br}^{0.11±.0.07}$	0.25	A	-
		Haplorrhini 2015	$5.29x10^{-1}V_{br}^{-0.05±.0.11}$	0.03	B	-

Ordinary least squares regression equations are given with 95% confidence intervals for the exponent, coefficients of determination (r^2) and significant differences between the three groups according to ANCOVA. Exponents of the allometric equations are significantly different ($P < 0.05$) if the letters A or B differ. If exponents are not different, then the elevation is significantly different if the letters are different. For full statistical results see Appendix A.

Table 2-2. Allometric equations in diprotodont marsupials from the original Seymour et al. (2015) blood flow study compared with a remeasurement and analysis of the dataset using the most recent approaches.

Independent	Dependent	Clade	Power Equation	(r^2)	Slope	Elev.
M_b (g)	V_{br} (ml)	Diprotodontia Remeasured	$4.19x10^{-2}M_b^{0.70\pm0.06}$	0.98	A	A
		Diprotodontia 2015	$4.19x10^{-2}M_b^{0.70\pm0.06}$	0.98	A	A
M_b (g)	$\dot{Q}_{ICA}$ (cm^3 min^{-1})	Diprotodontia Remeasured	$1.15x10^{-1}M_b^{0.62\pm0.10}$	0.90	A	A
		Diprotodontia 2016	$1.04x10^{-1}M_b^{0.51\pm0.10}$	0.88	A	B
M_b (g)	r_{CF} (cm)	Diprotodontia Remeasured	$1.00x10^{-2}M_b^{0.25\pm0.04}$	0.90	A	A
		Diprotodontia 2017	$8.97x10^{-3}M_b^{0.24\pm0.03}$	0.93	A	B
V_{br} (ml)	$\dot{Q}_{ICA}$ (cm^3 min^{-1})	Diprotodontia Remeasured	$1.95x10^{0}V_{br}^{0.86\pm0.16}$	0.89	A	A
		Diprotodontia 2019	$1.03x10^{0}V_{br}^{0.73\pm0.11}$	0.92	A	B
V_{br} (ml)	r_{CF} (cm)	Diprotodontia Remeasured	$3.18x10^{-2}V_{br}^{0.35\pm0.07}$	0.88	A	A
		Diprotodontia 2020	$2.61x10^{-2}V_{br}^{0.34\pm0.04}$	0.95	A	B
V_{br} (ml)	$\dot{Q}_{ICA}$ (cm^3 min^{-1}) / V_{br} (ml)	Diprotodontia Remeasured	$5.12x10^{-1}V_{br}^{0.14\pm0.16}$	0.17	A	-
		Diprotodontia 2021	$1.03x10^{0}V_{br}^{-0.27\pm0.27}$	0.59	B	-

Ordinary least squares regression equations are given with 95% confidence intervals for the exponent, coefficients of determination (r^2) and significant differences between the three groups according to ANCOVA. Exponents of the allometric equations are significantly different ($P < 0.05$) if the letters A or B differ. If exponents are not different, then the elevation is significantly different if the letters are different. For full statistical results see Appendix A.

Table 2-3. Allometric equations and ANCOVAs relating body mass, brain volume, total flow through both internal carotid arteries and carotid foramen radius across two phases of a western grey kangaroo life history sequence, and in diprotodonts and haplorrhine primates interspecifically for comparison.

				Post-Pouch		Overall		Interspecific		Haplorrhines		1	0
Variables (units)		**Group**	**Power Equation**	**(r^2)**	**Slope**	**Elevation**	**Slope**	**Elevation**	**Slope**	**Elevation**	**Slope**	**Elevation**	**Slope**	**Slope**
M_b (g)	V_{br} (ml)	In-Pouch	$1.10x10^{-1}M_b^{0.87\pm0.13}$	0.99	Y*	-	N*	N	N	Y	N	N	N	Y
		Post-Pouch	$5.17x10^{0}M_b^{0.24\pm0.3}$	0.95			Y*	-	Y*	-	Y*	-	Y	Y
		Overall	$1.2210^{0}M_b^{0.40\pm0.06}$	0.92					Y*	-	Y*	-	Y	Y
		Interspecific	$4.19x10^{-2}M_b^{0.70\pm0.06}$	0.98							N	Y	Y	Y
		Haplorrhine	$1.73x10^{-1}M_b^{0.71\pm0.09}$	0.89									Y	Y
M_b (g)	r_{CF} (cm)	In-Pouch	$1.04x10^{-2}M_b^{0.34\pm0.03}$	1.00	Y*	-	N	Y	N	Y	N	Y	Y	Y
		Post-Pouch	$4.97x10^{-2}M_b^{0.11\pm0.03}$	0.86			Y*	-	Y*	-	Y*	-	Y	Y
		Overall	$2.34x10^{-2}M_b^{0.19\pm0.03}$	0.92					N*	Y	Y*	-	Y	Y
		Interspecific	$1.00x10^{-2}M_b^{0.25\pm0.04}$	0.90							N	Y	Y	Y
		Haplorrhine	$1.05x10^{-2}M_b^{0.27\pm0.04}$	0.87									Y	Y
M_b (g)	$\dot{Q}_{ICA}$ (ml min^{-1})	In-Pouch	$1.38x10^{-1}M_b^{0.84\pm0.05}$	1.00	Y*	-	N	N	N	Y	N	Y	Y	Y
		Post-Pouch	$6.81x10^{0}M_b^{0.26\pm0.06}$	0.86			Y*	-	Y*	-	Y*	-	Y	Y
		Overall	$1.06x10^{0}M_b^{0.45\pm0.07}$	0.92					N*	Y	Y*	-	Y	Y
		Interspecific	$1.15x10^{-1}M_b^{0.62\pm0.10}$	0.90							N	Y	Y	Y
		Haplorrhine	$1.62x10^{-1}M_b^{0.63\pm0.09}$	0.87									Y	Y

See bottom of Table 2-4 for descriptive information.

Table 2-4. Allometric equations and ANCOVAs relating body mass, brain volume, total flow through both internal carotid arteries and carotid foramen radius across two phases of a western grey kangaroo life history sequence, and in diprotodonts and haplorrhine primates interspecifically for comparison.

				Post-Pouch		Overall		Interspecific		Haplorrhine		1	0
Variables (units)		**Group**	**Power Equation**	**(r^2)**	**Slope**	**Elevation**	**Slope**	**Elevation**	**Slope**	**Elevation**	**Slope**	**Elevation**	**Slope**	**Slope**
V_{br} (ml)	r_{CF} (cm)	In-Pouch	$2.51x10^{-2}V_{br}^{0.39\pm0.08}$	0.99	N	Y	N	N	N	N	N	Y	Y	Y
		Post-Pouch	$2.37x10^{-2}V_{br}^{0.46\pm0.10}$	0.88			N	N	N	N	N	Y	Y	Y
		Overall	$2.16x10^{-2}V_{br}^{0.48\pm0.03}$	0.98					Y*	-	Y*	-	Y	Y
		Interspecific	$3.18x10^{-2}V_{br}^{0.35\pm0.07}$	0.88							N	Y	Y	Y
		Haplorrhine	$2.07x10^{-2}V_{br}^{0.38\pm0.03}$	0.96									Y	Y
V_{br} (ml)	$\dot{Q}_{ICA}$ (ml min^{-1})	In-Pouch	$1.18x10^{0}V_{br}^{0.96\pm0.16}$	0.99	N	Y	N	N	N	N	N	Y	N	Y
		Post-Pouch	$1.25x10^{0}V_{br}^{1.05\pm0.24}$	0.89			N	N	N	N	N	Y	N	Y
		Overall	$8.72x10^{-1}V_{br}^{1.14\pm0.07}$	0.98					N*	N	Y*	-	Y	Y
		Interspecific	$1.95x10^{0}V_{br}^{0.86\pm0.16}$	0.89							N	Y	N	Y
		Haplorrhine	$8.08x10^{-1}V_{br}^{0.89\pm0.07}$	0.95									Y	Y

Ordinary least squares regression equations are given with 95% confidence intervals for the exponent, coefficients of determination (r2) and significant differences between the three groups according to ANCOVA. Exponents of the allometric equations are significantly different ($P<0.05$) if the letter Y appears in the relevant cell and not significantly different if the letter N appears in the relevant cell. If exponents are not different, then the elevation is significantly different if the letter Y appears in the relevant cell and not significantly different if the letter N appears in the relevant cell. When exponents are significantly different it is not possible to test whether the elevations differ significantly and a - appears in the cell. If a significant difference was detected in the ANCOVA comparisons of slope, these groups were subjected to a post hoc Johnson–Neyman (J–N) test with Bonferroni correction. Groups for which slope and elevation were subjected to post hoc testing are denoted with an asterisk (*) in the slope column, and the result of their testing. Significances without post hoc testing were $P=0.05$; significances with post hoc Bonferroni correction can be calculated by dividing 0.05 by the number of cells for a set of variables which show an asterisk. For full statistical results see Appendix A.

Table 2-5. Allometric equations and ANCOVAs relating body mass, brain volume, total flow through both vertebral arteries and lateral atlantal foramina radius across two phases of a western grey kangaroo life history sequence.

Variables (units)		Group	Power Equation	(r^2)	Post-Pouch		Overall		1	0
					Slope	Elevation	Slope	Elevation	Slope	Slope
M_b (g)	r_{LAF} (cm)	In-Pouch	$5.53\times10^{-3}M_b^{0.37\pm0.29}$	0.85	Y	-	N	N	Y	Y
		Post-Pouch	$2.68\times10^{-2}M_b^{0.12\pm0.06}$	0.65			N	N	Y	Y
		Overall	$1.44\times10^{-2}M_b^{0.19\pm0.04}$	0.88					Y	Y
M_b (g)	$\dot{Q}_{VA}$ (ml min^{-1})	In-Pouch	$2.42\times10^{-2}M_b^{0.94\pm0.76}$	0.84	Y	-	N	N	N	Y
		Post-Pouch	$1.43\times10^{0}M_b^{0.29\pm0.13}$	0.65			N	N	Y	Y
		Overall	$2.87\times10^{-1}M_b^{0.46\pm0.09}$	0.87					Y	Y
V_{br} (ml)	r_{LAF} (cm)	In-Pouch	$1.46\times10^{-2}V_{br}^{0.42\pm0.36}$	0.82	N	N	N	N	Y	Y
		Post-Pouch	$1.35\times10^{-2}V_{br}^{0.47\pm0.25}$	0.59			N	N	Y	Y
		Overall	$1.35\times10^{-2}V_{br}^{0.47\pm0.07}$	0.92					Y	Y
V_{br} (ml)	$\dot{Q}_{VA}$ (ml min^{-1})	In-Pouch	$2.78\times10^{-1}V_{br}^{1.07\pm0.95}$	0.81	N	N	N	N	N	Y
		Post-Pouch	$2.78\times10^{-1}V_{br}^{1.12\pm0.59}$	0.59			N	N	N	Y
		Overall	$2.43\times10^{-1}V_{br}^{1.15\pm0.17}$	0.92					N	Y

See bottom of Table 2-6 for descriptive information.

Table 2-6. Allometric equations and ANCOVAs relating body mass, brain volume, and total flow through cerebral feeding arteries across two phases of a western grey kangaroo life history sequence.

Variables (units)		Group	Power Equation	(r^2)	Post-Pouch		Overall		1	0
					Slope	Elevation	Slope	Elevation	Slope	Slope
M_b (g)	$\dot{Q}_{ICA+VA}$ (ml min^{-1})	In-Pouch	$1.63x10^{-1}M_b^{0.86\pm0.16}$	0.99	Y*	-	N*	N	N	Y
		Post-Pouch	$8.25x10^{0}M_b^{0.26\pm0.05}$	0.90			Y*	-	Y	Y
		Overall	$1.36x10^{0}M_b^{0.45\pm0.07}$	0.92					Y	Y
V_{br} (ml)	$\dot{Q}_{ICA+VA}$ (ml min^{-1})	In-Pouch	$1.48x10^{0}M_b^{0.98\pm0.28}$	0.98	N	N	N	N	N	Y
		Post-Pouch	$1.54x10^{0}M_b^{1.06\pm0.23}$	0.89			N	N	N	Y
		Overall	$1.13x10^{0}M_b^{1.14\pm0.07}$	0.99					Y	Y
V_{br} (ml)	$\dot{Q}_{ICA+VA}$ / V_{br} (ml min^{-1}) / (ml)	In-Pouch	$1.48x10^{0}V_{br}^{0.98\pm0.28}$	0.98	N	N	N	N	Y	N
		Post-Pouch	$1.54x10^{0}V_{br}^{1.06\pm0.23}$	0.89			N	N	Y	N
		Overall	$1.13x10^{0}V_{br}^{1.14\pm0.07}$	0.99					Y	Y

Ordinary least squares regression equations are given with 95% confidence intervals for the exponent, coefficients of determination (r2) and significant differences between the three groups according to ANCOVA. Exponents of the allometric equations are significantly different ($P<0.05$) if the letter Y appears in the relevant cell and not significantly different if the letter N appears in the relevant cell. If exponents are not different, then the elevation is significantly different if the letter Y appears in the relevant cell and not significantly different if the letter N appears in the relevant cell. When exponents are significantly different it is not possible to test whether the elevations differ significantly and a - appears in the cell. If a significant difference was detected in the ANCOVA comparisons of slope, these groups were subjected to a post hoc Johnson–Neyman (J–N) test with Bonferroni correction. Groups for which slope and elevation were subjected to post hoc testing are denoted with an asterisk (*) in the slope column, and the result of their testing. Significances without post hoc testing were $P=0.05$; significances with post hoc Bonferroni correction can be calculated by dividing 0.05 by the number of cells for a set of variables which show an asterisk. For full statistical results see Appendix A.

Table 2-7. Significant differences between cerebral feeding arteries and their foramina in different life history stages according to ANCOVA.

Variables (units)		Groups		Slope	Elevation
M_b (g)	$r_{Foramen}$ (cm)	LAF in-pouch	CF in-pouch	N	Y
		LAF post-pouch	CF post-pouch	N	Y
V_{br} (ml)	$r_{Foramen}$ (cm)	LAF overall	CF overall	N	Y
M_b (g)	$\dot{Q}$ ($cm^3\ min^{-1}$)	VA in-pouch	ICA in-pouch	N	Y
		VA post-pouch	ICA post-pouch	N	Y
V_{br} (ml)	$\dot{Q}$ ($cm^3\ min^{-1}$)	VA overall	ICA overall	N	Y
M_b (g)	$\dot{Q}$ ($cm^3\ min^{-1}$)	VA in-pouch	ICA in-pouch	N	Y
		VA in-pouch	Cerebral Feeders in-pouch	N	Y
		ICA in-pouch	Cerebral Feeders in-pouch	N	Y
		VA post-pouch	ICA post-pouch	N	Y
		VA post-pouch	Cerebral Feeders post-pouch	N	Y
		ICA post-pouch	Cerebral Feeders post-pouch	N	Y
V_{br} (ml)	$\dot{Q}$ ($cm^3\ min^{-1}$)	VA overall	CF overall	N	Y
		VA overall	Cerebral Feeders overall	N	Y
		ICA overall	Cerebral Feeders overall	N	Y

$r_{Foramen}$ = radius of respective foramen; $\dot{Q}$ = Blood flow in respective arteries; LAF = Lateral Atlantal Foramen; CF = Carotid Foramen; VA = Vertebral Arteries; ICA = Internal Carotid Arteries; Cerebral Feeders = Sum of Vertebral Arteries and Internal Carotid Arteries. Ordinary least squares regression equations with statistical information are provided in Table 2-3, Table 2-4, Table 2-5, and Table 2-6. Exponents of the allometric equations are significantly different ($P<0.05$) if the letter Y appears in the relevant cell and not significantly different if the letter N appears in the relevant cell. If exponents are not different, then the elevation is significantly different if the letter Y appears in the relevant cell and not significantly different if the letter N appears in the relevant cell. When exponents are significantly different it is not possible to test whether the elevations differ significantly and a - appears in the cell. For full statistical results see Appendix A.

DISCUSSION

Brain development and perfusion

The scaling of cerebral perfusion $\dot{Q}$ with body mass M_b or brain volume V_{br} is parallel in arteries from the same pouch phase (Figure 2-6). The contributions to brain perfusion from the VA and ICA keep a constant ratio across both the rapid and adult phases of growth, indicating that the somatic and integrative parts of the brain are developing at the same rates rather than one before the other (potential for transfer of blood between caudal and rostral parts of brain circulation notwithstanding). It is perhaps surprising that the vertebral artery is not relatively more important early on given the marsupial neonates extremely altricial stage of development. In tammar wallabies – a small bodied diprotodont – the cerebellum grows faster than the cerebrum in both growth phases (Renfree *et al.* 1982). Assuming that western grey brains experience the same regional growth patterns as tammar wallabies, the similar perfusion exponents for the forebrain and hindbrain represents a greater increase in the cerebral energy use on a mass-specific basis, possibly related to disproportionate increasing synapses in the cerebrum. In humans the internal carotid arteries supply about 70% of the brain's total blood flow in children but 80% in adults, with the remaining proportions almost entirely coming from the vertebral arteries (Schöning and Hartig 1998; Oktar *et al.* 2006). In western grey kangaroos across growth the internal carotid arteries supply about 70-80% of the brains cerebral blood flow, with the remaining 20-30% coming from the vertebral arteries regardless of age (post parturition at least). Human and diprotodont brain proportions are not dissimilar, with diprotodont cerebellum taking up 12% of the brain volume compared to human 10% (Renfree *et al.* 1982). Marsupial cerebella even have similar neurons densities to primate cerebella (Dos Santos *et al.* 2017). Harrington *et al.* (2019b) suggest differences in diprotodont and haplorrhine cognitive capacities are related to differences in the efficiencies of cerebral tissue, however the driver of this difference is not immediately evident.

The overall scaling of total brain perfusion ontogeny has an exponent which is much higher than interspecific studies and even isometry. This means that ontogeny does not recapitulate phylogeny, but rather there is an exponentially increasing energy cost to the developing brain. Certain physical traits develop rapidly before birth to allow the crawl from the birth canal to the pouch, but there is no accelerated shift in the development of the nervous system during gestation (Renfree *et al.* 1982; Nelson 1992). The newborn marsupial neocortex is two-layered and largely resembles two- to six-week-old placental embryos. The final layer of the neocortex begins differentiation three to five days after birth and proceeds from there such that six layers of the neocortex are present at the time of weaning (ca. 10 – 12 kg) (Reynolds *et al.* 1985; Lee and Ward 1989; Saunders *et al.* 1989; Dawson 2012). Aside from the advanced development of the features required to traverse to the pouch, marsupial development

progresses analogously to placental mammals – but in the pouch rather than womb (Nesslinger 1956; Nelson 1992). This delay in neural development is surely due to the sheer expense of brain tissue to grow and maintain. The marsupial neonate has all of the characteristics it requires for its short journey, and no more.

The large energy inputs in the western grey in-pouch growth phase are required to fund the ongoing neural development that occurs postnatally in the marsupial pouch. The elevated requirements for energy during early brain development stem from two main factors; the proportionally larger number of energetically expensive synapses, and the large quantities of ATP required in order to synthesise cellular components (Harris *et al.* 2012). The cost of building and maintaining a brain increases with brain size and composition, as the metabolic rate of the brain is proportional to number of neurons and related to neural activity (Attwell and Laughlin 2001; Herculano-Houzel 2011a). Most brain energy is used on synaptic transmission which makes up roughly 50-90% of the metabolic rate of the brain across development. Despite this, the energy metabolism required by a singular synapse remains constant across an animal's lifespan; high energy requirements in younger brains is driven by massive neuronal and synaptic development (Karbowski 2012). Brains that are younger and undergoing development have higher energy requirements than adult brains, driven by an increase in the thickness of the cortex and the formation of more and more synaptic connections. Synaptic failures from synaptic pruning become desirable as animals develop to reduce the proportion of total metabolic energy required to maintain brain function (Harris *et al.* 2012). Beyond adolescence brain energy requirements are seen to decrease; adult brains undergo cortical thinning as superfluous synaptic connections are pruned and the brain reaches its mature state (Harris *et al.* 2012). Furthermore, the rate of synaptic firing decreases with growth, suggesting that brains become more efficient as they become larger (Karbowski 2012).

Cerebral perfusion scales to body mass according to the same pattern of biphasic allometry as seen for brain volume on body mass. Across the in-pouch growth phase, cerebral perfusion increases rapidly in order to meet the demands of the developing brain. This period of rapidly increasing cerebral perfusion ends where the allometric trajectory of brain growth decreases (Figure 2-7). This pattern of biphasic allometry disappears when cerebral perfusion is graphed against brain volume (Figure 2-7). The rate of change in volumetric perfusion is constant across brain development. The scaling exponent for total cerebral blood flow rate on brain volume (1.14 ±0.07) shows that total perfusion to the brain increases disproportionately with brain size during development. This indicates that the synaptic activity is increasing on a volume-specific basis.

The driver of the biphasic relationships seen here across western grey ontogeny seems to be linked to a shift from brain development to locomotory development. Critical periods are well known in developmental biology as a stage in an organism's lifespan when

the nervous system is particularly sensitive to environmental stimulus and have been associated with the onset of synaptic pruning (Bock and Braun 1999; Knudsen 2004; Tzschentke and Plagemann 2006). In this study the allometric trajectory of cerebral development decreases at ca. 620 g M_b. This breakpoint aligns between a 380 g specimen and a 1000 g specimen. This stage of development coincides with the period immediately prior to first pouch exit in western greys which occurs at around 1000 g M_b (Dawson 2012). During the critical period preceding pouch exit the juvenile kangaroo experiences an enormous amount of novel environmental sensory stimulation as it begins to become aware of its environment. As the neonate approaches pouch exit its senses develop and the marsupial joeys begins to experience its first tangible exposure to life outside the pouch, including the requirements of locomotion. Numerous studies into growth rates across mammalian ontogenies have revealed biphasic developmental rates, with initial growth phases more rapid than later growth phases; the timing of phase shifts within biphasic allometric relationships are generally related to a sudden shift in development, physiology, or other dynamics (Munn and Dawson 2003; Mitchell and Skinner 2009; Snelling *et al.* 2015a; Snelling *et al.* 2015b). Snelling finds a biphasic relationship in cardiac development with the breakpoint occurring at approximately 5-6 kg M_b, which aligns with the point at which western grey joeys tend to leave the pouch (Snelling *et al.* 2015a; Snelling *et al.* 2015b). Hu *et al.* (2019) found biphasic relationships in the scaling of femur volume with body mass, blood flow index (Q_i) with body mass, and blood flow index with femur volume, with breakpoints all circa 1-5 kg M_b. The differences between the breakpoints for the brain, heart, and femora are likely owed to the way this locomotory pressure is enacted upon the different organs.

There is a significant difference between the interspecific diprotodont relationships reported in this chapter and those reported by Seymour *et al.* (2015), in terms of how they relate to the haplorrhine primates. This difference is caused by the approach used in each study, with minor radius used in Seymour *et al.* (2015) and area here. It is unclear what the implications are of the reanalysis of specimens from Seymour *et al.* (2015) elevating the diprotodont lines to be higher than the haplorrhine lines for both foramen radius and blood flow rate on a given brain volume (Figure 2-7). In their original analysis, Seymour *et al.* (2015) expressed curiosity at the large difference between the elevations of the diprotodonts and haplorrhines for the relationship between V_{br} on M_b (Figure 2-6). Diprotodonts and haplorrhines share similarities in diet, locomotion, and arboreal habitat, but primates outstrip diprotodonts in terms of social interaction and cognitive ability, with a correlation between brain size, innovation, and social learning (Reader and Laland 2002). Hence, that diprotodonts should present cerebral volumetric perfusion rates elevated above much of the haplorrhine taxa seems contradictory (Figure 2-7). Harrington *et al.* (2019b) in a study of $\dot{Q}_{ICA+VA}$ in marsupials and euarchontans (tree-shrews, colugos, and primates) similarly found that in regards to V_{br} marsupial brain blood flow rates scaled at greater exponents ($V_{br}^{1.05}$) than their euarchontans

counterparts ($V_{br}^{0.88}$). Harrington *et al.* (2019b) postulate that marsupials and euarchontans may have faced differing selective pressures with regards to brain metabolism and suggest that euarchontans brains may be more energetically efficient than marsupial brains – requiring less blood flow for the same purpose – as a way of reducing the volumetric metabolic requirements of their larger more neuron dense brains. This notion is supported by my analysis here.

The lateral atlantal foramina

The internal carotid arteries are responsible for the largest proportion of cerebral perfusion and flow rate through the internal carotid arteries is representative of brain metabolism (Lou *et al*. 1987). The vertebral arteries are responsible for the blood supply to much of the cerebellum. These arteries pass through type II foramina on their course into the braincase.

The lateral atlantal foramen in kangaroos has been overlooked for nearly 125 years (Tandler 1898). This structure is by no means unique to kangaroos, with homologous structures appearing in dogs, pigs, horses, ruminants, and carnivorans where it carries the vertebral artery prior to its entrance into the braincase via the foramen magnum (De Iuliis 2007; Kear *et al.* 2007; König *et al.* 2007; Schaller 2007; Gingerich 2015; Mespoulhès-Rivière *et al.* 2016; Spataru 2016; Warburton and Prideaux 2021). Nomenclature presented for this structure is confused in the literature, with a variety of names given including alar foramen, atlantal foramen, vertebrarterial [sic] foramen, and lateral vertebral foramen (De Iuliis 2007; Kear *et al.* 2007; König *et al.* 2007; Schaller 2007; Gingerich 2015; Warburton and Prideaux 2021).This confusion in the literature is understandable due to the number of foramina present in the first cervical vertebrae in some cases. For instance, in horses the vertebral arteries pass through three distinct canals on their path past the atlas; first the transverse foramen, emerging and turning dorsally to pass through the alar foramen, before finally turning laterally to pass through the lateral atlantal foramen and into the vertebral foramen (Mespoulhès-Rivière *et al.* 2016).

To add complexity to the matter, a recorded mutation may occur in humans where an analogous foramen forms around the vertebral artery via ossification of soft tissues. In humans the vertebral arteries pass over the superior aspect of the posterior vertebral arch of the atlas after passing through the transverse foramina of the atlas before penetrating the posterior atlantooccipital membrane and passing into the braincase via the foramen magnum. A foramen can form around the vertebral artery on the superior aspect of the atlas where the vertebral arteries pass into the posterior atlantooccipital membrane. When a foramen forms from soft tissues in this location it has been is variously termed ponticulus posticus (Pyo and Lowman 1959), arcuate foramen (Stubbs 1992) retroarticular superior foramen, or Kimerle anomaly (Tubbs *et al.* 2007).

Human medical studies notwithstanding, the most consistent nomenclature for the lateral atlantal foramen seems to be that of Schaller (2007),where it is termed the lateral vertebral foramen. However, due to the common place misidentification of the structure in the literature, I advance the use of the proposed term of lateral atlantal foramen to help distinguish it from other structures and underscore its uniqueness to the first cervical vertebrae.

Methodological validation and critique

No empirical data on the rate of macropod cerebral perfusion exists, and hence some difficulties were encountered when attempting to validate these perfusion calculations. Here, I arrived at cerebral blood flow rate by relying upon a number of assumptions which may or may not fail to account for changes across development. The principal assumption the mammalian interspecific blood flow rate equation from Seymour *et al.* (2019b) (*Equation 7*) appropriate to use across an ontogenetic sequence. For instance, problems may arise if the enclosed artery does not occupy the same proportion of the bony foramen at all body sizes or developmental stages. However, until empirical data is available with which to test this chapter's calculations against, this assumption is difficult to address.

An assumption was made that the wall thickness ratio correction used is constant across the ontogenetic sequence. Certainly, blood pressure changes in humans across life (Sarkola *et al.* 2012), one would assume the same of macropods. A study of human arteries from infancy to adulthood found that ratios of wall thickness to lumen radius increase in major arteries from w = 0.20 at birth to w = 0.30 at 18 years of age (Sarkola *et al.* 2012). This change corresponds well with the increase in blood pressure from around 55 mm Hg at birth to 75 mm Hg at 18 years of age (Sarkola *et al.* 2012). A search of the literature for any information on arterial wall structure across development in macropods found no relevant studies. Snelling finds a biphasic relationship in cardiac development with the breakpoint occurring at approximately 5-6 kg M_b, which aligns with the point at which western grey joeys tend to leave the pouch (Snelling *et al.* 2015a; Snelling *et al.* 2015b). Pressurised or in vivo measurements of major macropod arteries would reveal more about the scaling of arterial dimensions across a life history and help improve the blood flow estimates provided herein.

Another factor which may impact flow rates is that of blood viscosity. Simmonds *et al.* (2011) find that blood viscosity in adult eastern greys is about 0.04 dynes s cm^{-2} (the value used by Seymour *et al.* (2015) in their original interspecific analysis of primate and diprotodont brain perfusion) and plasma viscosity is about 0.014 dynes s cm^{-2}. No values in the literature describe the ontogeny of blood viscosity in macropods, however Basden *et al.* (1996) shows that haematocrit (Hct) increases across Tammar development from approximately 32% in a day old 44 g joey to 50% in a one-year-old 2,326 g adult (masses from Runciman *et al.* (1998)). The relationship between haematocrit and whole blood

viscosity is complex and several conversion equations exist. According to Einstein (Westerhof 2006);

$$\eta_{whole\ blood} = \eta_{plasma}\ (1 + 2.5\ Hct)$$

Equation 9 – Einstein's blood viscosity formula.

where $\eta_{whole\ blood}$ = whole blood viscosity; η_{plasma} = plasma viscosity; and *Hct* = hematocrit value.

Application of this formula to Tammar wallabies – assuming an independent plasma viscosity across development – yields whole blood viscosity values which increase from a value of 0.025 dynes s cm^{-2} at birth to 0.032 dynes s cm^{-2} at adulthood. The mammalian interspecific blood flow rate equation from Seymour *et al.* (2019b) (*Equation 7*) does not rely on blood viscosity values in its calculation, but is derived from blood flow values in adults of nine species of mammal (*Bos taurus*, *Canis familiaris*, *Equus caballus*, *Felis catus*, *Homo sapiens*, *Macaca fascicularis*, *Mus musculus*, *Oryctolagus cuniculus*, and *Rattus norvegicus*). An alternative blood flow calculation equation – the shear stress equation (*Equation 3*) – accounts for changes in blood viscosity but also involves calculation of shear stress. The scaling relationship of vascular shear stress across an ontogenetic sequence remains undefined.

The interspecific and ontogenetic data series were collected using different methods (interspecific via microphotography (Seymour *et al.* 2015), ontogenetic via CT). In this chapter at the upper bounds of the body mass range there is an intersection between the western grey post-pouch and the interspecific lines. This represents the point at which mature adult western greys occur in each dataset (Figure 2-6). Similarly, there are near intersections the measurements of both foramen radius and blood flow rate on either body mass or brain volume (Figure 2-7, Figure 2-8). Hence, this chapter supports the assertions of (Hu *et al.* 2020) that microphotographic and CT approaches are comparable.

This chapter presents the first time that blood flow quantification was performed through measurement of the size of 'preforaminal' vascular grooves. These preforiminal vertebral measurements had more variation than in the carotids of the same body mass range, however, the variation in the vertebral in-pouch phase (where foramina were not enclosed) is similar to the variation in the vertebral post-pouch phase (where foramina were closed). I take this as indicative that the use of preforiminal grooves for measurement is valid, at least on this occasion. I feel the correlation of the scaling relationships for r_{LAF} and $\dot{Q}_{VA}$ with those for r_{CF} and $\dot{Q}_{ICA}$ ultimately validates these measurements. I caution researchers that the 'preforaminal' vascular grooves measured in this chapter were well defined or otherwise "deep enough" such that I felt it was possible to visually determine the space which may be occupied by a vessel passing through (Figure 2-1, Figure 2-9); this approach may not necessarily prove valid in all other cases.

CONCLUSION

That the lateral atlantal foramen has been overlooked in kangaroos nearly 125 years is unsurprising as it represents a niche area of study (Tandler 1898). However, the presence of this structure in so many groups of taxa (at least dogs, pigs, horses, ruminants, and carnivorans) presents an issue when the nomenclature presented for this structure is confused in the literature. Niche subjects can be difficult to broach when terminology is ambiguous. The more specific and distinct term 'lateral atlantal foramen' which I propose should help distinguish this structure from others and underscore its uniqueness to the first cervical vertebrae.

The volume-specific metabolic rate of the brain increases significantly and uniformly in western grey kangaroos across development. The cerebral perfusion rates of diprotodonts are paradoxical. Despite similarities in diprotodonts and haplorrhines diets, locomotion, and habitats, primates outstrip diprotodonts in terms cognitive ability. Hence, that diprotodonts should present cerebral volumetric perfusion rates elevated above much of the haplorrhine taxa seems contradictory. In marsupials and primates $\dot{Q}$ scales to V_{br} at rates that suggest primate brains may be more efficient than marsupial brains as a way of reducing the volumetric metabolic requirements of their larger more neuron dense brains (Harrington *et al.* 2019b).

In the western grey kangaroo growth series, the internal carotid arteries supply about 70-80% of the brains cerebral blood flow with the remaining 20-30% coming from the vertebral arteries. Blood flow quantification through measurement of the size of 'preforaminal' vascular grooves appears to be valid although there existed lots of variation in my measurements of LAF in general. This approach may not necessarily prove valid in other cases. Further, at the present stage of development of this technique there is no perfect blood flow equation; each equation has its own drawbacks. The current foramina blood flow quantification equation (*Equation 7*) is based upon flow in adult mammals and may not be directly applicable to a growth series as haemodynamic variables change across development. The shear stress equation (*Equation 3*) allows us to incorporate blood viscosity and shear stress scaling rates, but how these change across ontogenetic sequences is complex and remains to be fully understood.

CHAPTER 3

BIRD BRAINED? CEREBRAL BLOOD FLOW IN THE AVES

ABSTRACT

Many comparisons have been drawn between the intelligence and cognition of primate and avian species, with some studies putting forth primate and avian intelligence as a case of convergent evolution. Both birds and mammals developed large brains in spite of the extreme metabolic demands of neural tissue. Neural metabolic demands must be met through an adequate supply of blood. This chapter aims to calculate cerebral perfusion from the dimensions of the cerebral carotid canal, measured in skulls of numerous avian clades and compares these rates with those of the carotid canal of haplorrhine primates and diprotodont marsupials from Chapter 2. I use phylogenetic generalized least squares analysis (PGLS) to test how total cerebral carotid blood flow rate increases with brain volume and body mass while accounting for the statistical dependence of related species due to their common ancestral history. Aves as a clade possess scaling exponents for brain volume and cerebral blood flow rate on body mass which are shallower than the mammal groups, but scaling exponents and elevations for blood flow rate on brain volume ($V_{br}^{0.77\pm0.12}$) similar to haplorrhine primates ($V_{br}^{0.95\pm0.08}$). Relationships noted in Aves as a whole do not hold when taxa are divided into their separate lineages, where a wide variety of scaling rates are resolved. Some avian clades exhibit scaling rates in line with those of the mammal groups, while others exhibit scaling rates which are significantly and dramatically different from the mammal groups and other avian clades. Scaling relationships of psittacine and passerine birds were not dissimilar from the those of the mammalian groups, with passerine birds bearing the most similarities to haplorrhine primates of all clades examined. Palaeognaths presented the shallowest scaling exponents for all relationships examined, with palaeognath brain perfusion almost independent of body mass ($M_b^{0.19\pm0.16}$) and palaeognath carotid canal radius almost independent of brain volume ($V_{br}^{0.18\pm0.12}$). Birds that have altricial young have steeper scaling exponents than birds have precocial young, indicating this may be part of an adaptation towards higher cognition. Overall, this study lends credence to the assertion that cognition in primates and some groups of birds evolved convergently.

INTRODUCTION

Many comparisons have been drawn between the intelligence and cognition of primate and avian species, with some studies putting forth primate and avian intelligence as a case of convergent evolution (Emery and Clayton 2004b; Rattenborg *et al.* 2009; Roth 2015). The corvid forebrain has a relative size which is significantly larger than those of other birds (with the exception of some parrots) and this enlargement of the "avian prefrontal cortex" may indicate a parallel primate-like intelligence (Emery and Clayton 2004b). Corvid brains are significantly larger than would be predicted for their body size (Jerison 1973), relatively the same size as those of chimpanzees (Emery and Clayton 2004a). However, the belief that enhanced cognitive abilities stem from higher degrees of encephalisation has been questioned in light of recent data showing that intelligence is instead contingent on the absolute number of cerebral neurons and their connections (Herculano-Houzel 2011a).

Both birds and mammals developed large brains in spite of the extreme metabolic demands of neural tissue. In mammals, the energy budget of the whole brain is proposed to be largely determined by total neuron number rather than neuron size, neuron density, or brain mass (Herculano-Houzel 2011a). Mammals which possess a larger number of brain neurons for a given body size would be expected to have a higher metabolic rate of the brain than those with a smaller number of brain neurons for a given body size (Herculano-Houzel 2011b). Recent research shows that some birds have a significantly higher number of neurons in their brains than primates or other mammals (Olkowicz *et al.* 2016). This would imply that the metabolic rate of the brain may be even higher in some birds than in mammals assuming that avian neurons are as expensive as those in primates. However, few studies have examined the energy use of the avian brain in detail, and no studies exist which have calculated the metabolic rate of avian brains (Braun *et al.* 1985a; Braun *et al.* 1985b).

Mammalian cerebral energetics have received much attention recently owing to new developments in perfusion quantification techniques. Principally, the ability to obtain reliable estimates of cerebral metabolic rate through measurements of bony foramina has led to papers examining cerebral metabolism in several groups including marsupials, primates, and hominins (Seymour *et al.* 2015; Seymour *et al.* 2016; Boyer and Harrington 2018; Boyer and Harrington 2019; Harrington *et al.* 2019b; Seymour *et al.* 2019a; Seymour and Snelling 2019). However, this technique is yet to be applied to avian taxa.

Several arteries connect with the avian endocranial region. In order of magnitude (calibre), these are the cerebral carotid, ethmoid, orbital, ventral spinal arteries (Figure 4-7). There is disagreement in the literature regarding the direction of flow in the ethmoid and orbital arteries, with some authors suggesting they form a collateral supply of perfusion to the brain, while others state that this is unlikely based upon the

orientation of the arteries and the pressure gradient of blood reaching the brain (Richards 1970; Midtgård 1984a; Midtgård 1984b; Arad *et al.* 1987; Arad 1990; Porter and Witmer 2016). The role of the ventral spinal arteries in supplying the brain is certain, and these arteries pass through the vertebral foramen with the spinal cord before entering the braincase via the foramen magnum. However, in connecting to the braincase the ethmoid, orbital, and ventral spinal arteries pass through large foramina which pass other structures such as veins or nerves (type I foramina), and hence the foramen technique cannot easily be applied to these arteries. The cerebral carotid arteries are large arteries which represent the principal supply of blood to the brain, and these pass through the cranial carotid canal – a type II foramina (Hu *et al.* 2020).

Considering how varied avian taxa are, the carotids path to the brain is largely conserved. The common carotid divides into its internal and external portions, with the external carotid continuing rostrally while the extra-cranial segment of the internal carotid moves dorsally towards the carotid foramen in the parabasal fossa. Upon entering the carotid foramen the nomenclature of the internal carotid artery changes to cerebral carotid artery (unlike in mammals where the term internal carotid is also used for the length of the cerebral carotid) (Baumel 1993; Porter and Witmer 2016). The cerebral carotid artery can be divided into five sections along its path: the cervical segment; intrasphenoid segment; intrasellar segment; anastomotic segment; and intracranial segment (Baumel and Gerchman 1968). These divisions describe the position of the artery as it travels along its elongated canal – the cranial carotid canal. The largest degree of variation amongst taxa is seen in the anastomotic segment, where the left and right cerebral carotid arteries anastomose with one another immediately before reaching the endocranial cavity. This anastomosis can be in many forms, generally described by their shape as Type X, H, or I (Baumel and Gerchman 1968) (Figure 3-1). Immediately prior to the intercarotid anastomosis two small arteries arise from the cerebral carotid and exit the canal in a rostral direction. These are the sphenopalatine and sphenomaxillary arteries. In some taxa these arteries are represented by a joint artery referred to as the sphenomaxillary palatine artery. From the intercarotid anastomosis, the cerebral carotid arteries continue along their canal and enter the braincase at the pituitary fossa (Baumel and Gerchman 1968) (Figure 3-1).

Aves are a complex and varied taxon, with several thousand avian species worldwide. Although it may be possible to answer some questions regarding overall cerebral metabolic rate of certain groups, it is important to keep the diversity of avian taxa in mind when interpreting results. The regional distribution of cerebral perfusion is important to consider, as the brains sensory regions may effectively counterbalance the metabolism used for higher processing and cognition, disguising how much energy is actually dedicated towards intelligent behaviour. This comparison may become further obfuscated when comparisons are made to mammalian groups.

Recent work including targeted next generation DNA sequencing has developed near comprehensive avian life trees (Prum *et al.* 2015). Figure 3-2 presents one such avian tree of life in condensed form, with silhouettes representative of bird species in each major branch of the tree. This chapter examines 46 species of bird from seven clades, and these are mapped onto the tree.

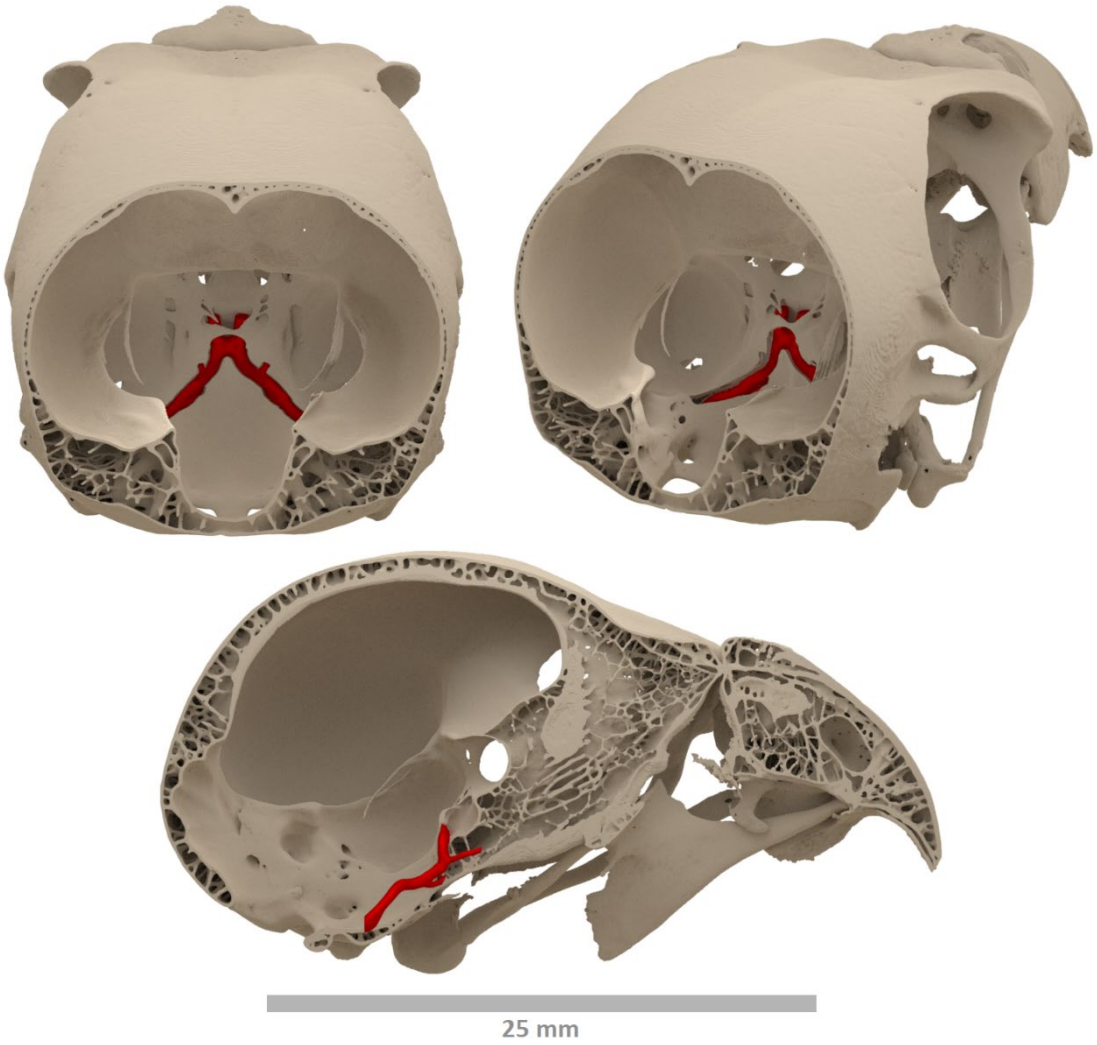

Figure 3-1. The intracranial course of the cerebral carotid artery in a cockatiel (*Nymphicus hollandicus*). Clockwise from top left: Caudodorsal aspect; Twenty degrees off centre right lateral posterior coronal aspect of cranial cavity with the caudal section of the calvaria and inferior part of dorsum sellae and inner table of bone of posterior cranial fossa digitally removed; Carotid canal opened to show arteries; right lateral aspect of cranium digitally sectioned down the sagittal midline. Carotid canal presented as it appears in situ. Scale bar is 25 mm. Note type-x intercarotid anastomosis immediately caudal to hypophyseal fossa. The sphenomaxillary and sphenopalatine arteries are visible branching off from the carotids prior to the intercarotid anastomosis. The areas of the left and right carotid canals were measured at a point between the branching of the sphenomaxillary artery and the intercarotid anastomosis. Rendered images were produced by exporting segmented structures from Avizo into Blender 2.90.1 (Open Source, www.blender.org). Based on figure by Baumel and Gerchman (1968).

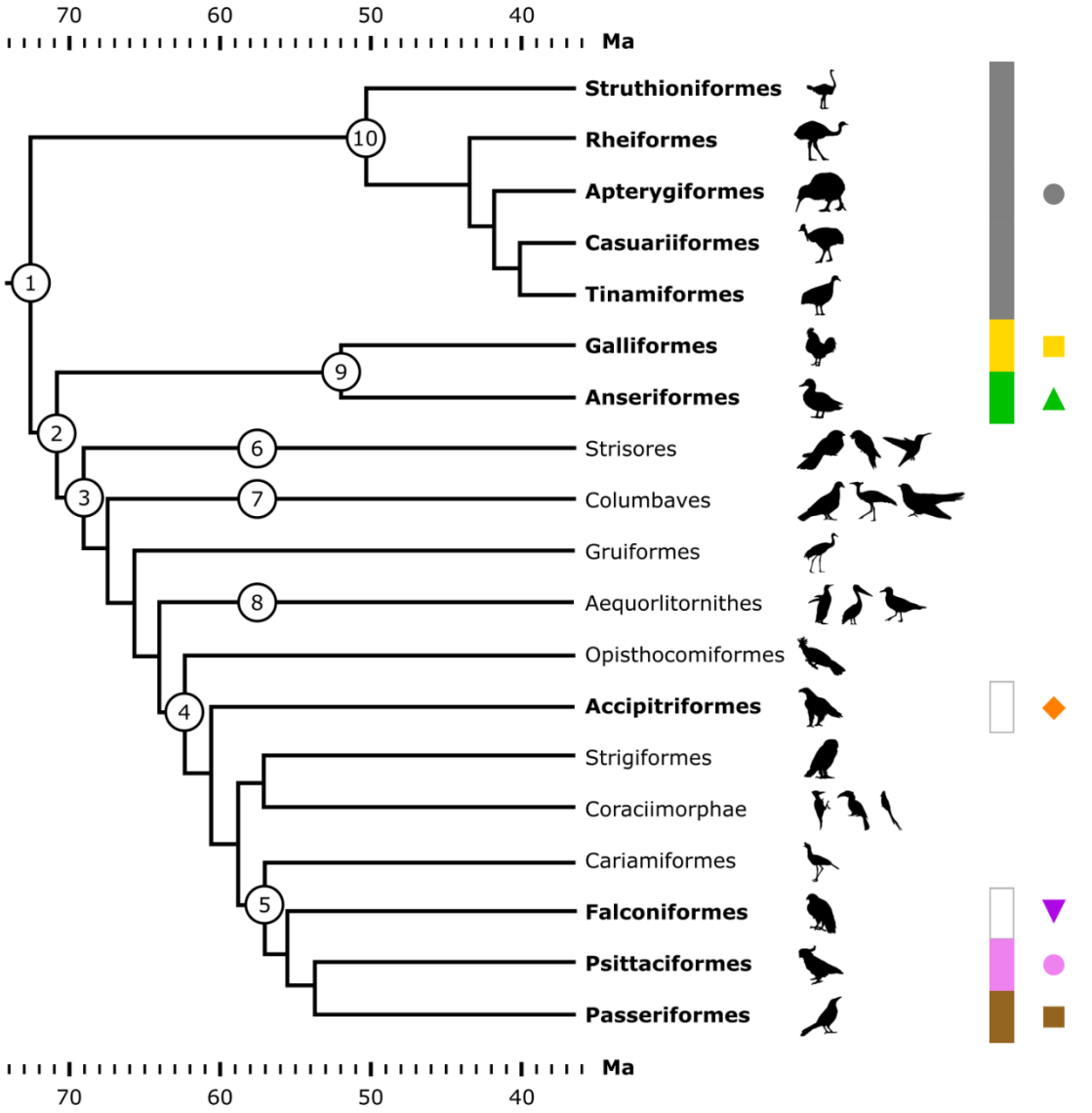

Figure 3-2. Avian evolutionary tree simplified from Prum *et al.* (2015). Silhouettes of representative bird species are depicted by their lineages. The specific clades examined in this chapter are indicated with their names in bold – coloured boxes and shapes next to these clades indicate their representative colours throughout the chapter. Branch length approximates length of time denoted by the scales at top and bottom of the image (Ma is millions of years). The numbered nodes designate the (1) Aves, (2) Neognathae, (3) Neoaves, (4) Inopinaves, (5) Australaves, (6) Strisores, (7) Columbaves, (8) Aequorlitornithes, (9) Galloanserae, (10) Palaeognathae. Branches terminate at order level divisions, aside from the Strisores, Columbaves, Aequorlitornithes, and Coraciimorphae which are higher level divisions and are here truncated for the sake of simplification.

The present study aims to compare avian cerebral perfusion rates with those of mammals for the purpose of commenting on the cerebral metabolism and cognition of each group. Cerebral perfusion in Aves is determined from the radius of the cranial carotid canal, measured in skulls of numerous avian clades. Subsequent to this, data characterising the cerebral perfusion rates in haplorrhine primates and diprotodont marsupials were utilised for comparison (Chapter 2). The body sizes of birds, haplorrhine primates,

and diprotodont marsupials overlap, with large ratites equivalent to primates and kangaroos. I use phylogenetically-informed generalised least-squares regression analysis (PGLS) to test how total cerebral carotid blood flow rate increases with brain volume and body mass while accounting for the statistical dependence of related species due to their common ancestral history. Finally, life history traits of the clades are examined in relation to brain perfusion.

METHODS

Sample collection and preparation

Specimens for this chapter were obtained for the South Australian Museum's Ornithology Collection. Morphometric data, including brain case volume and carotid foramen cross-sectional area, were collected from X-ray computed tomography (CT) scans of 46 species of birds from seven clades. The clades examined are the Palaeognathae (Figure 3-7), Galliformes (Figure 3-8), Anseriformes (Figure 3-9), Accipitriformes (Figure 3-10), Falconiformes (Figure 3-10), Psittaciformes (Figure 3-11), and the Passeriformes (Figure 3-12). Specimens with overall head widths less than 68 mm were imaged using a Sky-Scan-1076 Micro-CT scanner (Adelaide Microscopy, Adelaide, South Australia) while specimens with overall head widths greater than 68 mm were imaged using a Philips Ingenuity Core 128 CT system (Sound Radiology, Adelaide, South Australia). Imaging and reconstruction settings were optimised for each specimen in order to maximise image contrast and resolution (full settings available in Appendix C). The intactness of the cranial cavity and nearby structures took priority when assessing candidate specimens for scanning. Some specimens were articulated and scanned in their entirety including lower jaw. Some specimens were disarticulated, damaged, or otherwise missing bones and in these cases only the relevant parts of the cranium were scanned. Unfortunately, this study could not differentiate between genders as this was intermittently indicated in the available museum specimens. Imagery was post processed using DataViewer 1.5.1.2 (Bruker microCT, Kontich, Belgium) to obtain desired rotations. Files imaged at Sound Radiology were converted from DICOM format to bitmap format in Fiji (Open Source, www.fiji.sc) and voxel dimensions were corrected from anisometric to isometric using DataViewer and Fiji. Adult body mass of each species as well as life history traits were obtained from the literature (Billerman *et al.* 2020). Data relevant to this chapter is available on MorphoSource under project ID: 000445264.

Braincase volume (V_{br}) was measured via the creation of digital cranial endocasts in Avizo 9.0.0 (FEI SAS, Hillsboro, Oregon, USA) following the methodology outlined by Balanoff et al. (2015). In some cases TConv 2.1 (Bruker microCT, Kontich, Belgium) was used to resize datasets due computational memory restrictions (Appendix C). There is a strong correlation between braincase volume, brain volume, and brain mass in

organisms which possess large brains relative to their body mass (Isler *et al.* 2008; Balanoff *et al.* 2015). The inside of the braincase is lined with soft tissues which comprise the dural meninges and cerebral vasculature. The presence of these soft tissues results in some discrepancy between the morphology and volume of a cranial endocast and that of the brain, however, in highly encephalised taxa such as birds and mammals the impact of these layers of tissue is regarded as negligible (Balanoff *et al.* 2015). Furthermore, brain case volume and brain mass are essentially interchangeable as the brain has a density of 1.04 g ml^{-1} (Isler *et al.* 2008).

I identified the carotid foramina from published anatomical illustrations of avian skulls (Baumel and Gerchman 1968). After entering the carotid foramen the left and right cerebral carotid arteries move rostrally through the cranial carotid canals and anastomose shortly before reaching the pituitary fossa (Baumel and Gerchman 1968) (Figure 3-1). Before the left and right cerebral carotids anastomose, they give rise to the sphenomaxillary and sphenopalatine arteries (Kilgore *et al.* 1976). For all specimens, I measured the cross-sectional area of the cranial carotid canals at the point immediately caudal to the sella turcica and carotid anastomosis, rostral of the branch of the sphenomaxillary and sphenopalatine arteries (Figure 6). This ensured that any blood flow being subtracted (or added) to the cerebral carotid by the sphenomaxillary and sphenopalatine arteries was accounted for. Cross-sectional areas of the cranial carotid canals were measured with image analysis software Fiji. These cross-sectional area measurements were then converted to radii (referred to from here as foramen radii) by assuming the area was that of a circle. To calculate the lumen radius of the artery passing through the canal from the foramen radius, the effective thickness of the arterial walls needs to be known. Arterial walls have a thickness which is determined by the principle of Laplace. I account for the thickness of the arterial walls of the cerebral carotid arteries by using a wall thickness to lumen radius conversion ratio. Early publications utilising this technique relied upon a lumen size conversion ratio of w = 0.40 for mammals (Seymour *et al.* 2015; Seymour *et al.* 2016). Recently this conversion ratio has been re-examined from 14 imaging studies on humans and is given as w = 0.30 (Seymour *et al.* 2019a). Avian mean arterial blood pressures are around 1.3 times higher than mammalian values Seymour *et al.* (2004). Hence, a wall thickness to lumen radius conversion ratio of w = 0.40 is used for avian taxa. This lumen radius was then subjected to blood flow rate calculation using the mammalian interspecific blood flow rate equation from (Seymour *et al.* 2019b);

$$log\ \dot{Q} = -0.20\ log\ r_i^2 + 1.91\ log\ r_i + 1.82$$

Equation 7 – The Seymour et al. (2019b) mammalian equation.

where $\dot{Q}$ is blood flow rate ($cm^3\ s^{-1}$); and r_i is the arterial internal lumen radius (cm).

This equation is derived using measurements of blood flow rates and lumen size data from 20 named systemic arteries of mammals (Seymour *et al.* 2019b). Birds exhibit several differences from mammals in terms of blood properties including possession of larger (nucleated) red blood cells and a whole blood viscosity around half that of mammals (Maxwell *et al.* 1992; Zhou *et al.* 1999; Scanes 2015). However, as the haemodynamic principles which dictate the relationship between blood flow rate and vascular calibre are the same in all vertebrates, and in the absence of an equation specifically formulated for avian taxa, I use this mammalian equation here to calculate flow rates in birds. Blood flow was calculated individually for left and right foramina and then added together to give a total cerebral carotid blood flow rate. Data from Chapter 2 of this thesis were used allowing comparison between the Aves, haplorrhine primates, and diprotodont marsupials.

Statistical analysis

Least squares regression was conducted to determine the allometric relationship between $\log_{10}$-transformed independent and dependent variables: M_b, body mass; V_{br}, brain volume; r_{CF}, carotid foramen radius; and $\dot{Q}_{CA}$, blood flow rate in homologous carotid arteries (internal carotid blood flow rate in mammals, or cerebral carotid blood flow rate in birds). Ordinary least squares regressions on log-transformed data, 95% confidence intervals of regression means and significant differences between groups were determined using analysis of covariance (ANCOVA) in GraphPad Prism 6.0 statistical software (GraphPad Software, La Jolla, CA, USA). Where ANCOVA revealed differences in the scaling exponents a Johnson–Neyman (J–N) test was performed to determine the range of *X* values over which the individual data for *Y* were significantly different. Error correction was performed by performing a Bonferroni post hoc test following analysis of co-variance for each set of variables (White 2003).

Because the dataset was thought to be phylogenetically influenced, statistical analysis was performed to test for phylogenetic autocorrelation. One thousand avian phylogenetic trees were constructed online (http://birdtree.org/) using the 'Ericson All Species set of 10000 trees with 9993 OTUs each' with the associated taxonomy from GenBank (Arnold *et al.* 2010; Rubolini *et al.* 2015). A consensus tree was rooted, and no outgroup was designated. The tree contained polytomies which were broken in a random order to make the tree binary (see Figure 3-3). The phylogenetic signal present in body mass, brain volume, cerebral carotid blood flow rate, and carotid foramina radius was measured using Pagel's lambda (λ) (Pagel 1999). Pagel's lambda indicates the strength of the phylogenetic relationship, where values lie between 0 and 1. Lambda values of or near 0 are indicative of phylogenetic independence and values of or near 1 indicate that the variable is related to evolutionary history (Kamilar and Cooper 2013). Phylogenetic generalised least squares (PGLS) models were constructed to test the association between $\log_{10}$-transformed values of the response variables V_{br}, r_{CF}, and $\dot{Q}_{CA}$ in the Aves, using an

optimised Pagel's lambda. PGLS models were constructed using the 'pgls' function in the package 'caper' (Orme *et al.* 2013) in the R Statistical Environment v 1.3.1073 (R Core Team 2021). Using the 'pgls' function in 'caper', the covariance between related taxa was incorporated into the calculation of estimated coefficients from a PGLS model. The covariance matrix of the expected covariance between each pair of tips was calculated using the branch lengths of an estimated phylogeny. PGLS models were assessed using Akaike Information Criterion (AICc) corrected for small sample sizes (Burnham and Anderson 2001), running univariate models which included either M_b and V_{br}, and a model which incorporated both. No phylogenetic analysis was performed on individual avian clades as the number of species within each clade was insufficient.

RESULTS

Phylogenetic effect on variables

The best supported phylogenetic model for explaining $\dot{Q}_{CA}$ variability in the Aves includes both M_b and V_{br}. This model ranked first ahead of models with only V_{br} or only M_b, with a relative model weight of 0.972 versus 0.026 for V_{br} only and 0.001 for M_b only (Table 3-1). Values for Pagel's lambda are indicative that all variables examined are significantly related to avian evolutionary history (Table 3-2). The highest phylogenetic signals (λ values) were obtained in M_b (0.9999, P = 4.04×10^{-11}) and V_{br} (0.994, P = 3.17×10^{-07}), followed by r_{CF} (0.901, P = 1.05×10^{-03}). $\dot{Q}_{CA}$ had a λ value of 0.648 (P = 2.22×10^{-02}), the least of any of the examined variables but still indicative of a strong phylogenetic signal. Volumetric brain perfusion, a blend of the carotid blood flow and brain volume variables expressed as $\dot{Q}_{CA} \cdot V_{br}^{-1}$ presented a phylogenetic signal between that of $\dot{Q}_{CA}$ and V_{br} (0.807, P = 2.00×10^{-08}) (Table 3-2).

PGLS modelling in the Aves did not have a dramatic impact on the pattern witnessed in the standard GLM models (Table 3-3). All PGLS relationships were substantially similar to their GLM relationship counterparts, with the PGLS and GLM relationships of r_{CF} versus V_{br} and $\dot{Q}_{CA}$ versus V_{br} being virtually identical (Figure 3-4). Being highly phylogenetically influenced (high lambda) does not necessarily indicate that one should expect a different trend, just that trends are influenced by their phylogenetic history. This can be because of group clustering, or for any reason.

Comparing the Aves to primates and diprotodonts

For V_{br} on M_b, Aves scale with an exponent ($M_b^{0.47}$) which is lower than that of the haplorrhine ($M_b^{0.71}$) or diprotodont ($M_b^{0.70}$) mammals (Figure 3-4, Table 3-4). Haplorrhine V_{br} scaled to M_b with an exponent which was not significantly different from that of diprotodonts, but with a higher elevation. Johnson–Neyman (J–N) tests reveal the difference in V_{br} on M_b between the data for Aves and Haplorrhini is significant except for

at the lowest extremes of haplorrhine M_b. For V_{br} on M_b, avian and diprotodont slopes were not significantly different for body masses above 206 g (J–N test).

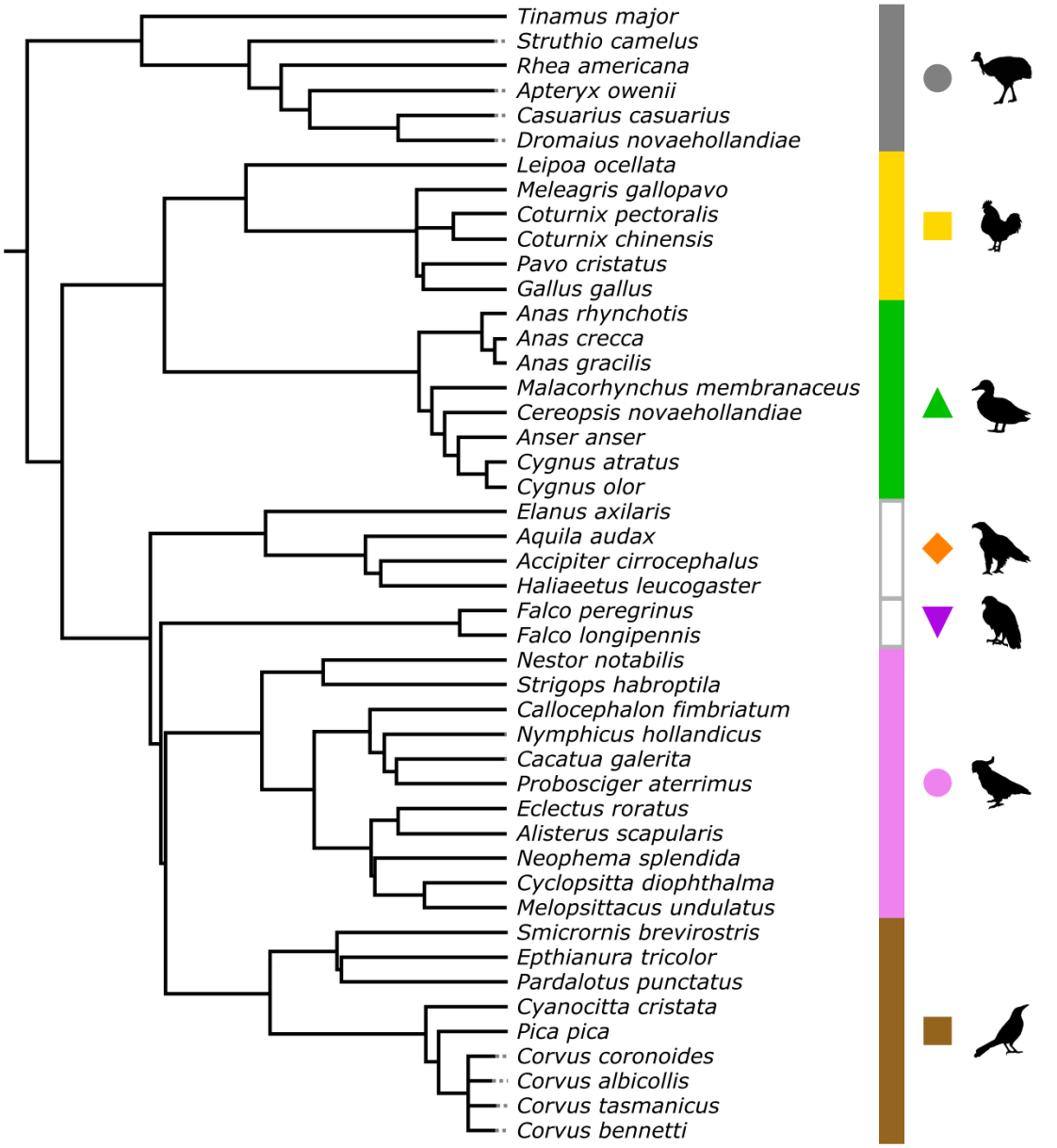

Figure 3-3. Phylogeny of the avian species examined in this chapter. Silhouettes of representative bird species are depicted by their lineages – coloured boxes and shapes next to these clades indicate their representative colours throughout the chapter. Branch length indicates relatedness. The clades examined, top to bottom, are the Palaeognathae, Galliformes, Anseriformes, Accipitriformes, Falconiformes, Psittaciformes, and the Passeriformes.

An identical trend is noted for $\dot{Q}_{CA}$ on M_b, with Aves scaling with a lower exponent of $M_b^{0.41}$ as compared to haplorrhine's $M_b^{0.67}$ and diprotodont's $M_b^{0.59}$ (Table 3-4). Again, the difference between the data for Aves and Haplorrhini is significant except for at the lowest extremes of haplorrhine M_b (J–N test). For $\dot{Q}_{CA}$ on M_b, avian and diprotodont slopes were not significantly different for body masses below 4,105 g (J–N test).

Haplorrhine and diprotodont $\dot{Q}_{CA}$ scale to M_b with non-significantly different exponents but significantly different elevations.

Haplorrhine r_{CF} on V_{br} scales with an exponent and elevation which is not significantly greater than that of Aves after post hoc testing (J–N test). Diprotodonts and Aves scale with similar allometric equations, with no significant difference detected between their exponents and a slight but significant difference between their elevations. Haplorrhine primates and diprotodont marsupial an exponent which is not steeper than that of Aves after post hoc testing, but with significantly different elevations (Figure 3-4, Table 3-5).

Haplorrhine $\dot{Q}_{CA}$ on V_{br} scales isometrically, with an elevation which is not significantly different than that of Aves. Haplorrhine and avian exponents for $\dot{Q}_{CA}$ on V_{br} were both not significantly different than that of diprotodonts but the three groups had significantly different elevations from one another (Figure 3-4, Table 3-4). Haplorrhine $\dot{Q}_{CA} \cdot V_{br}^{-1}$ on V_{br} scales with an exponent and elevation which is not significantly different than that of Aves after Bonferroni correction (P>0.0083). Haplorrhine and avian exponents for $\dot{Q}_{CA}$ on V_{br} were both not significantly different than that of diprotodonts but had significantly different elevations. Haplorrhine $\dot{Q}_{CA} \cdot V_{br}^{-1}$ on V_{br} scaled at a rate which was not significantly different from independence.

Comparing avian lineages to primates and diprotodonts

Relationships noted above comparing mammals to Aves do not hold when Aves are divided into their separate lineages, where a wide variety of scaling relationships are resolved (Table 3-4, Table **3-5**). Some avian clades exhibit scaling in line with those of the mammal groups, while others exhibit scaling which are significantly and dramatically different from the mammal groups and other avian clades (Figure 3-5).

Scaling relationships of psittacine and passerine birds were similar to those of the mammalian groups, with passerine birds bearing the most similarities to haplorrhine primates of all clades examined. No difference was detected between the psittacine, passerine, haplorrhine, or diprotodont groups for the scaling exponents of V_{br} versus M_b, though there were significant differences in elevations with psittacine and passerine elevations sitting somewhere between the two mammalian groups.

Passerines scaling for $\dot{Q}_{CA}$ on M_b was steeper than that of haplorrhines, but this difference was not statistically significant. Conversely, psittacine scaling for $\dot{Q}_{CA}$ on M_b was shallower than haplorrhines. For $\dot{Q}_{CA}$ on M_b psittacine birds had significantly different elevations from haplorrhines, while passerine birds were not significantly different from haplorrhines. Passerine $\dot{Q}_{CA}$ on M_b exponents were not statistically different than diprotodonts and passerine elevations were lower. Psittacine and passerine scaling relationships for $\dot{Q}_{CA}$ on M_b were not significantly different from one another after Bonferroni correction (P>0.0036).

Passeriform and haplorrhine $\dot{Q}_{CA}$ on V_{br} scale at rates which are not significantly different from isometry. The same is not true for psittacine and diprotodont scaling for $\dot{Q}_{CA}$ on V_{br}, though there is no detectable difference in the exponents of the four groups for this relationship. Psittacine and passerine scaling elevations were lower than those of diprotodonts. Psittacine and passerine scaling relationships for $\dot{Q}_{CA}$ on V_{br} were not significantly different from one another after Bonferroni correction (P>0.0083).

For r_{CF} on V_{br}, the psittacine scaling exponent was lower than the haplorrhine scaling exponent after Bonferroni correction (P>0.0063), though this was not true across the range where psittacine and haplorrhine V_{br} overlap (J–N test). Passerine and haplorrhine scaling for r_{CF} on V_{br} were not statistically distinguishable. Diprotodont scaling exponents were not significantly different than either passerines or psittacines. Psittacine and passerine scaling relationships for r_{CF} on V_{br} were not significantly different from one another after Bonferroni correction (P>0.0063).

Psittaciform and haplorrhine scaling for $\dot{Q}_{CA} \cdot V_{br}^{-1}$ on V_{br} were indistinguishable from one another following Bonferroni correction (P>0.0083). Passeriform and haplorrhine exponents for $\dot{Q}_{CA} \cdot V_{br}^{-1}$ on V_{br} were not statistically significantly different, but elevations were significantly different following Bonferroni correction. Diprotodont scaling exponents were not significantly different from those of psittaciformes, passeriformes, or haplorrhines, but elevations were all statistically significantly different.

Scaling relationships for other avian groups were disparate and varied compared to the relatively close similarities noted between the scaling relationships of psittacine and passerine birds and the mammalian groups. The distribution of 95% CI's across the data was not uniform. Passeriformes tended to have the tightest 95% CI's of the avian groups across the data, though it is important to note that the number of replicates (*n*) was not equivalent across all clades examined. Due to their broad 95% CI's, galliform and anseriform exponents were not significantly different from any of the scaling exponents of any of the avian or mammal groups examined across the data set – whether for V_{br} on M_b, $\dot{Q}_{CA}$ on M_b, $\dot{Q}_{CA}$ on V_{br}, r_{CF} on V_{br}, or $\dot{Q}_{CA} \cdot V_{br}^{-1}$ on V_{br}. Galliform and Anseriform $\dot{Q}_{CA}$ on V_{br} are both not significantly different from isometry but have a broad 95% CI ($\approx M_b^{0.74\pm0.40}$); the same variability is seen in the relationships for $\dot{Q}_{CA} \cdot V_{br}^{-1}$ on V_{br} as this is effectively the inverse of $\dot{Q}_{CA}$ on V_{br}. The broad 95% CI's and overlapping brain volumes and body masses make teasing apart the traits of different clades difficult. Individual significances can be found in Table 3-4 and Table **3-5**.

Palaeognathae presented the shallowest scaling exponents for all relationships examined (aside from $\dot{Q}_{CA} \cdot V_{br}^{-1}$ on V_{br} as this effectively the inverse of $\dot{Q}_{CA}$ on V_{br}). Palaeognath $\dot{Q}_{CA}$ is almost independent of body mass ($M_b^{0.19\pm0.16}$), and palaeognath r_{CF} is almost independent of brain volume ($V_{br}^{0.44\pm0.29}$). Removing *Tinamus major* – the single tinamidae replicate – from the data results in even shallower exponents for the palaeognaths. For all equations in which V_{br} was the independent variable ($\dot{Q}_{CA}$ on V_{br}, r_{CF} on V_{br}, and

$\dot{Q}_{CA} \cdot V_{br}^{-1}$ on V_{br}), palaeognath scaling exponents were statistically lower than those of passerines or haplorrhines. After Bonferroni correction, passeriformes scale with greater exponents for V_{br} on M_b (P<0.0033) and $\dot{Q}_{CA}$ on M_b (P<0.0036) than in palaeognaths, galliformes, or anseriformes.

Scaling of avian taxa with precocial or altricial young

Generally, birds which have altricial young have brain masses which are greater than birds which have precocial young when scaled to M_b (Figure 3-6, Table 3-6). Altricial birds have higher V_{br} in relation to M_b, while birds with precocial young have higher blood flow rates at the lower end of the range for V_{br} than is seen in altricial birds. The scaling exponent of V_{br} to M_b was greater in birds with altricial young ($M_b^{0.68}$) than in birds with precocial young ($M_b^{0.52}$). $\dot{Q}_{CA}$ scaled to M_b with a steeper exponent in birds with altricial young ($M_b^{0.48}$) than in birds with precocial young ($M_b^{0.29}$). Further, r_{CF} on V_{br} scaled with an exponent which was again steeper in birds with altricial ($V_{br}^{0.33}$) than precocial life histories ($V_{br}^{0.22}$). $\dot{Q}_{CA}$ scaled to V_{br} with a steeper exponent in birds with altricial young ($V_{br}^{0.74}$) than in birds with precocial young ($V_{br}^{0.5}$) although this difference was non-significant at brain masses above 17.20 ml (Figure 3-6, Table 3-6).

Figure 3-4. Graphs (A-D) of the relationships between M_b, V_{br}, r_{CF}, and $\dot{Q}_{CA}$ for the avian taxa examined compared with two mammalian clades. Note log–log axes. The black line is the uncorrected avian GLM line, and the grey dots are datapoints for individual avian species. The red line is that of the PGLS analysis. The mammalian clades are represented with dotted lines (Haplorrhini, dark blue, Diprotodontia light blue). See Appendix B for the full list of species.

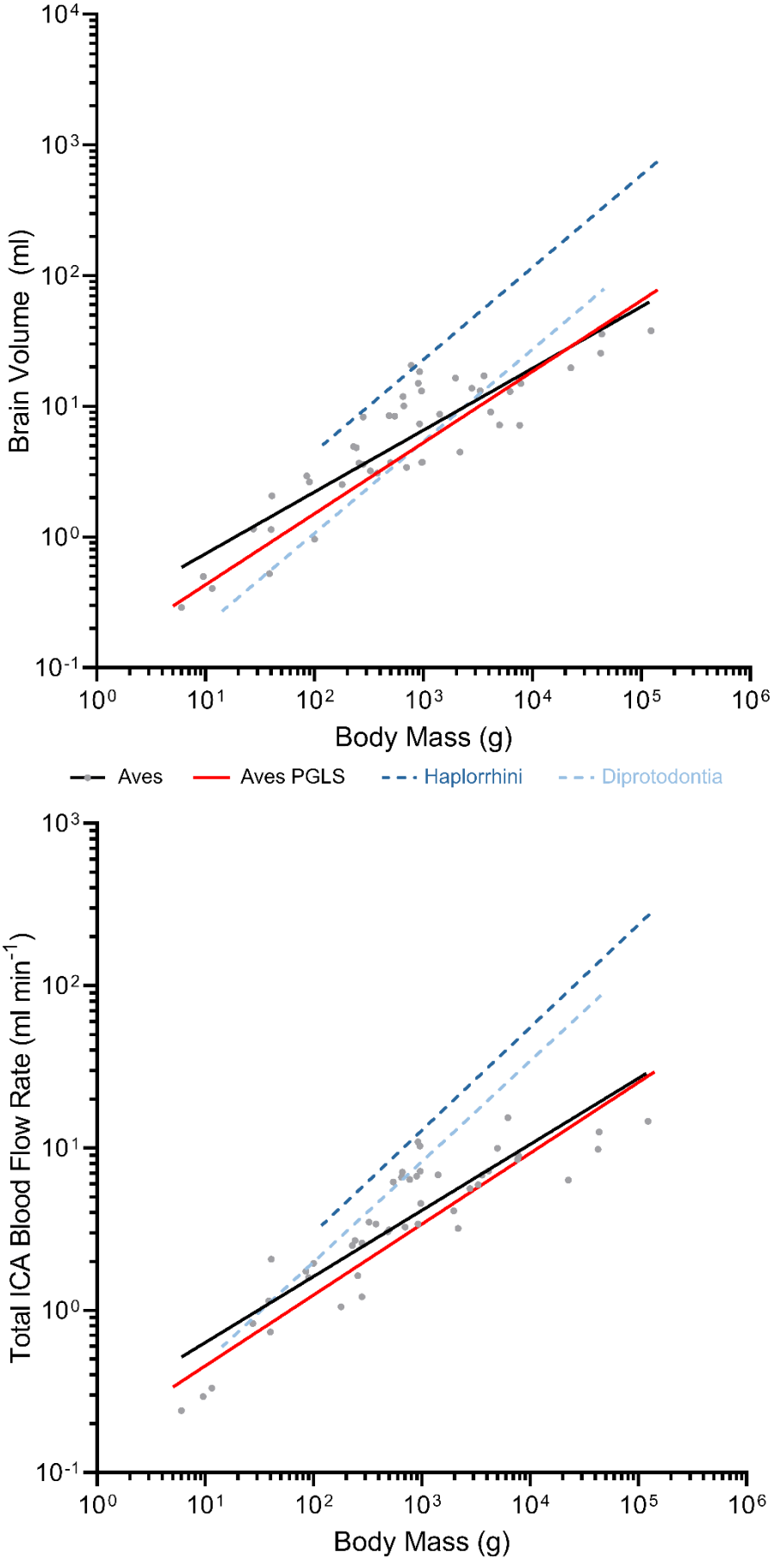
Brain Volume (ml)
Body Mass (g)
Aves
Aves PGLS
Haplorrhini
Diprotodontia
Total ICA Blood Flow Rate (ml min-1)
Body Mass (g)

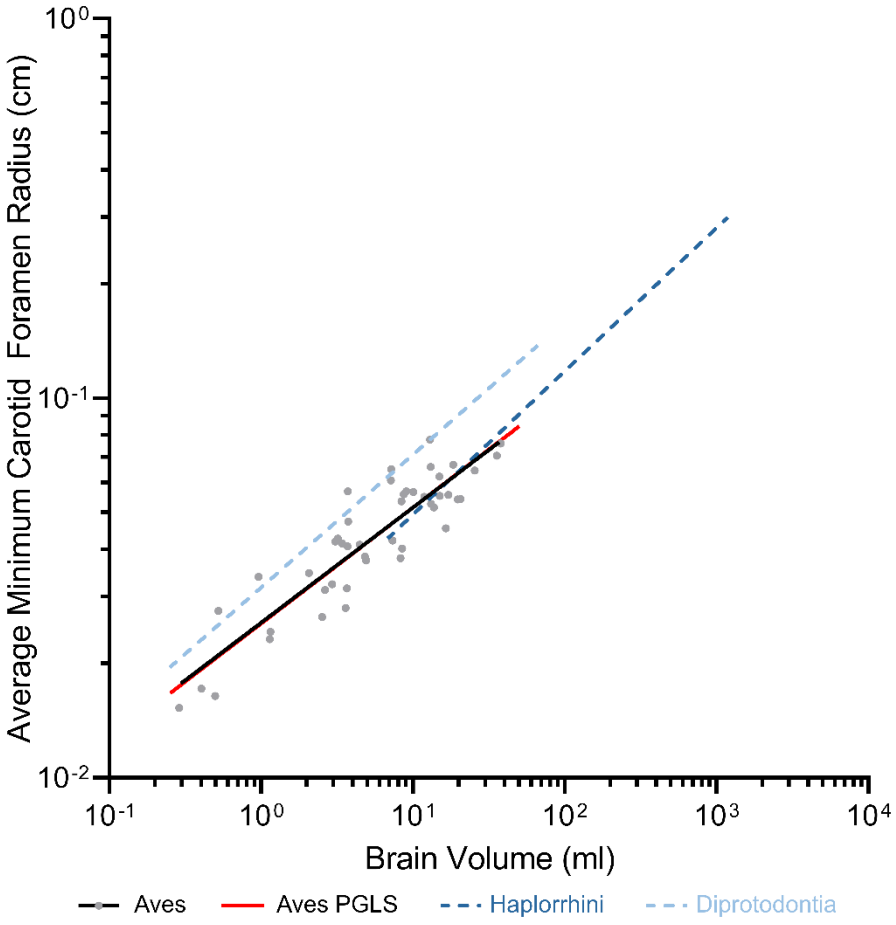
Average Minimum Carotid Foramen Radius (cm)
10^0
10^-1
10^-2
10^-1
10^0
10^1
10^2
10^3
10^4
Brain Volume (ml)
Aves
Aves PGLS
Haplorrhini
Diprotodontia

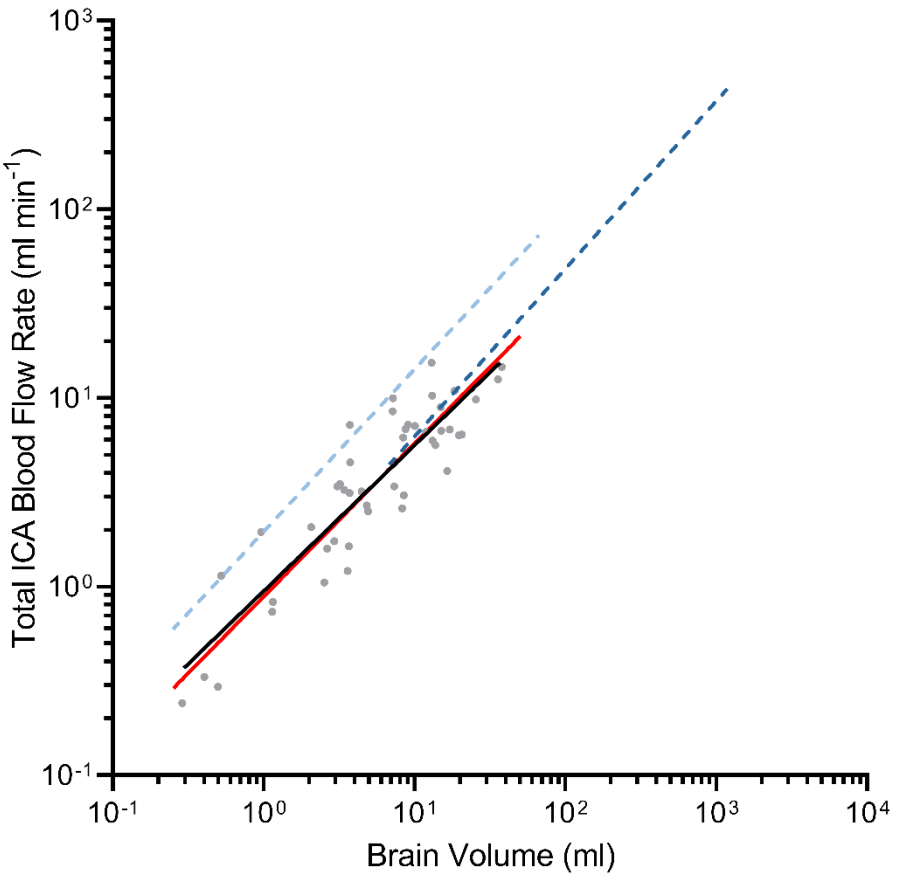
Total ICA Blood Flow Rate (ml min^-1)
10^3
10^2
10^1
10^0
10^-1
10^-1
10^0
10^1
10^2
10^3
10^4
Brain Volume (ml)

Figure 3-5. Graphs (A-D) of the relationships between M_b, V_{br}, r_{CF}, and $\dot{Q}_{CA}$ for the avian clades examined compared with two mammalian clades. Note log–log axes. Each dot is a datapoint for an individual avian species. The colour scheme is consistent with other parts of the chapter; Palaeognathae grey dots; Galliformes yellow boxes; Anseriformes green triangles; Accipitriformes orange diamonds; Falconiformes purple triangles; Psittaciformes pink dots; Passeriformes brown boxes. The mammalian clades are represented with dotted lines (Haplorrhini, dark blue, Diprotodontia light blue). See Appendix B for the full list of species.

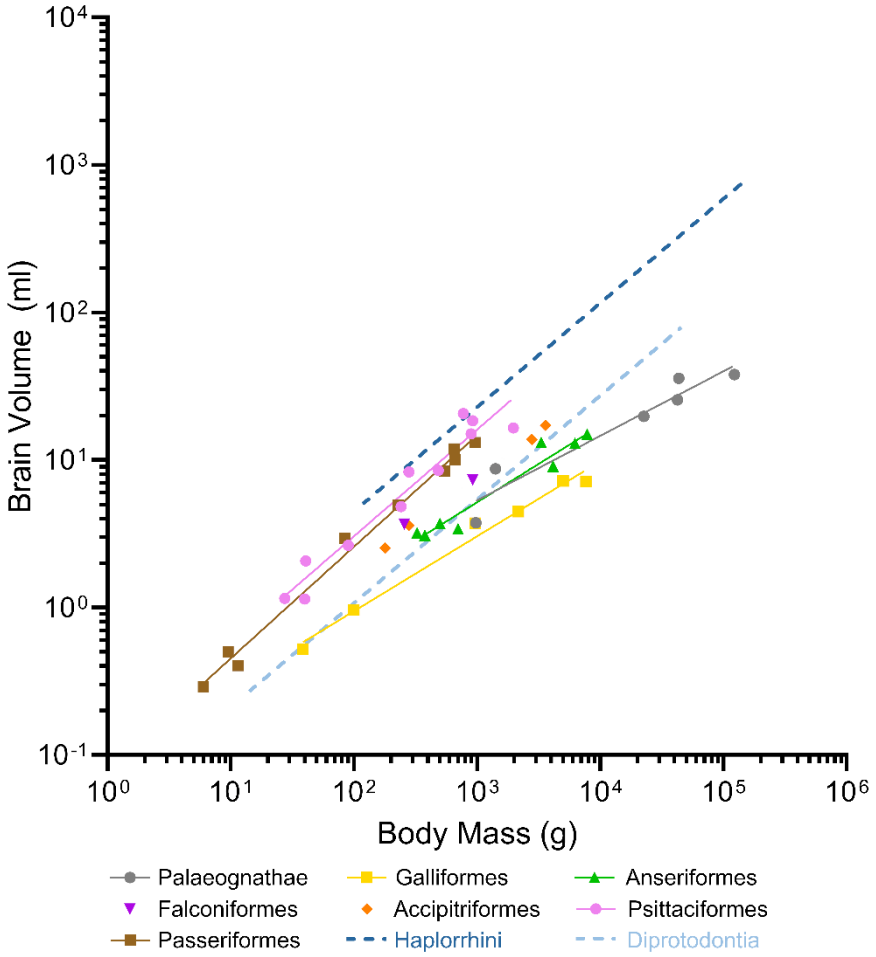
Brain Volume (ml)
Body Mass (g)
Palaeognathae
Galliformes
Anseriformes
Falconiformes
Accipitriformes
Psittaciformes
Passeriformes
Haplorrhini
Diprotodontia

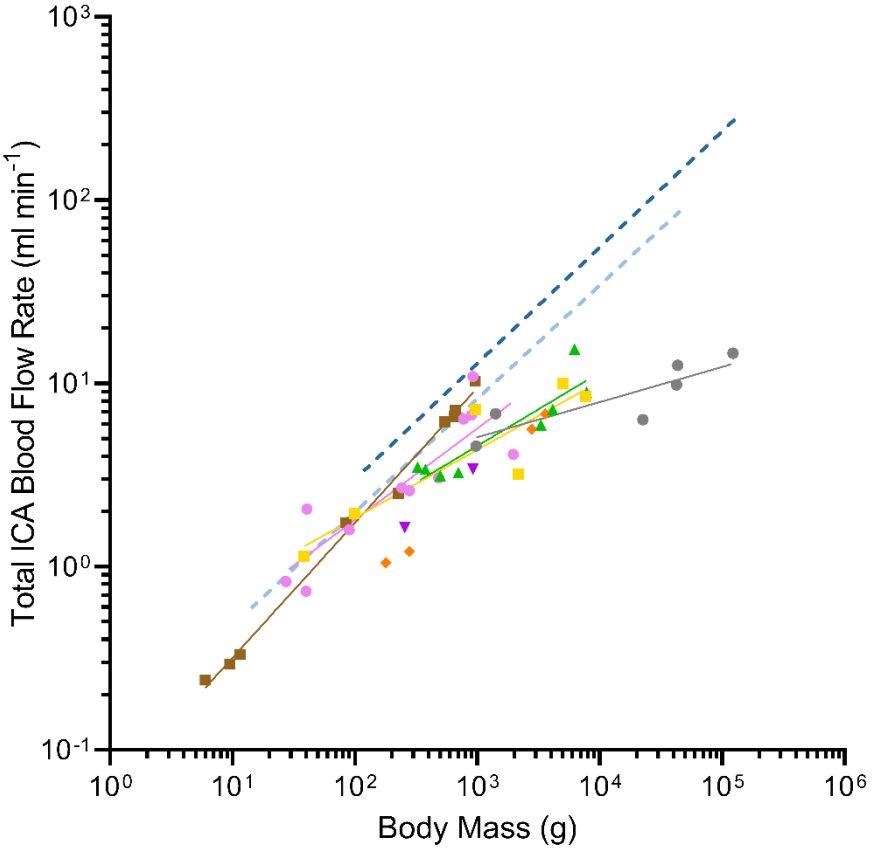
Total ICA Blood Flow Rate (ml min-1)
Body Mass (g)

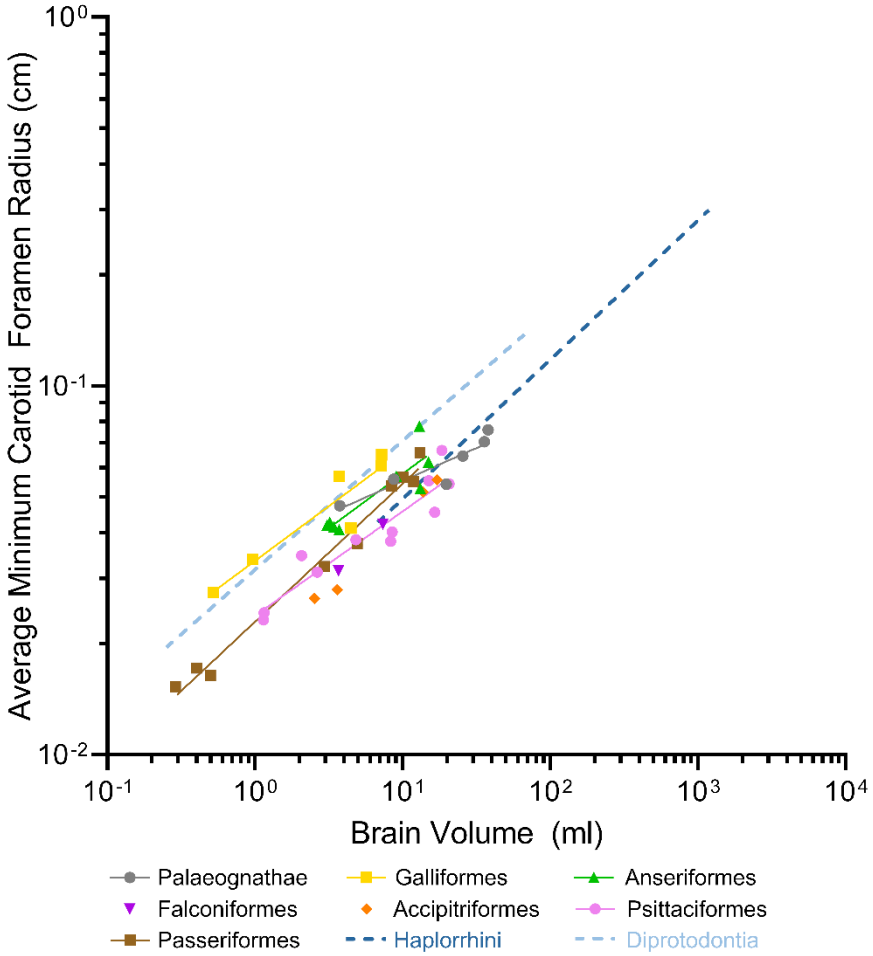
Average Minimum Carotid Foramen Radius (cm)
10^0
10^{-1}
10^{-2}
10^{-1}
10^0
10^1
10^2
10^3
10^4
Brain Volume (ml)
Palaeognathae
Galliformes
Anseriformes
Falconiformes
Accipitriformes
Psittaciformes
Passeriformes
Haplorrhini
Diprotodontia

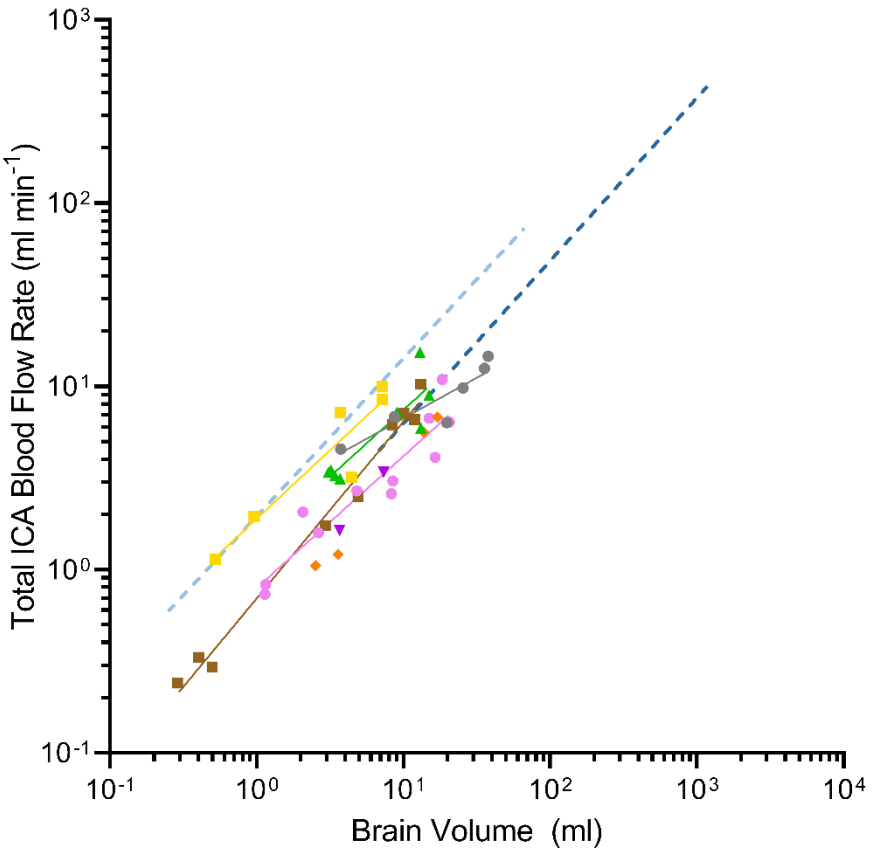
Total ICA Blood Flow Rate (ml min^{-1})
10^3
10^2
10^1
10^0
10^{-1}
10^{-1}
10^0
10^1
10^2
10^3
10^4
Brain Volume (ml)

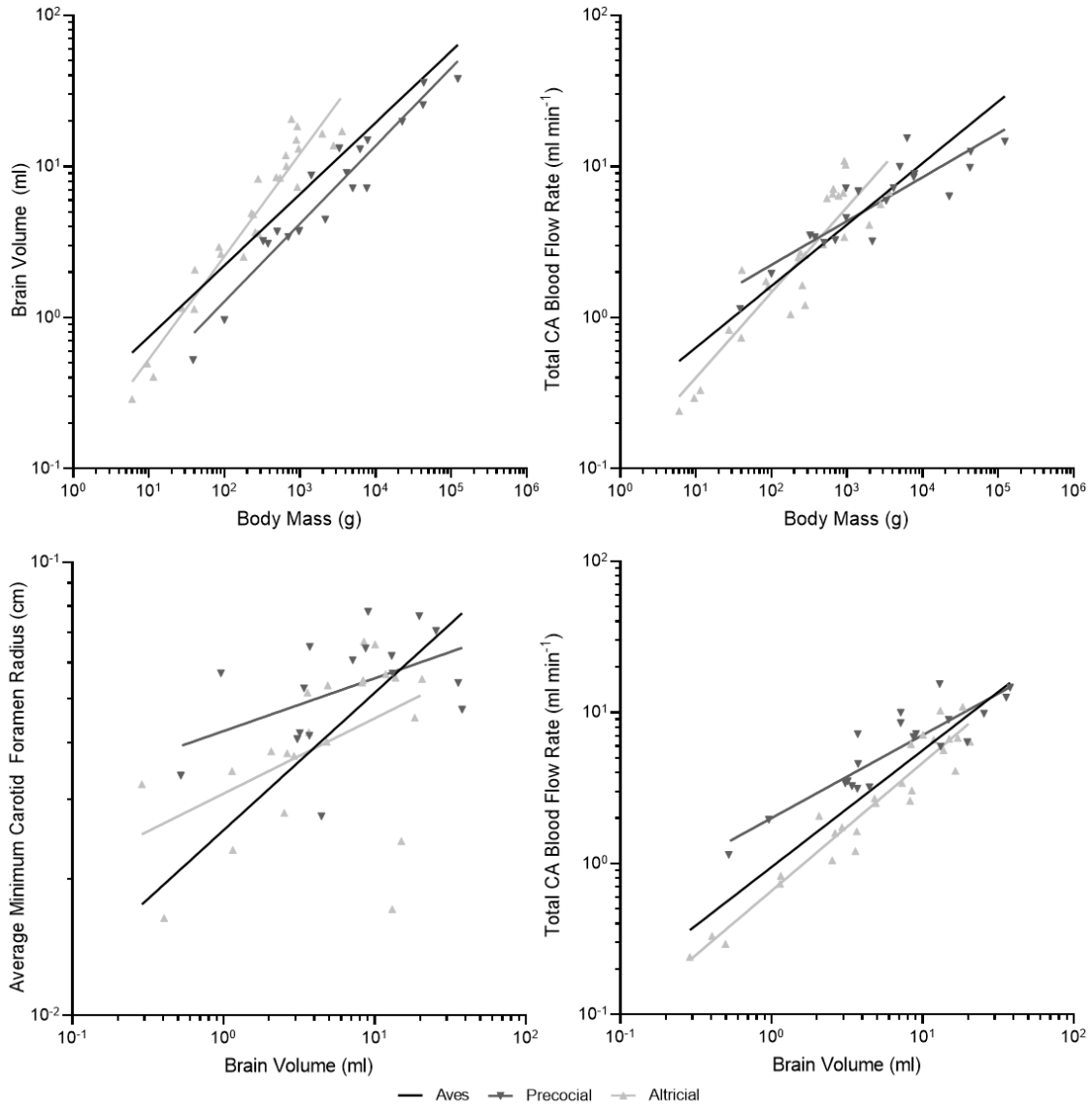

Figure 3-6. Comparing relationships between M_b, V_{br}, r_{CF}, and $\dot{Q}_{CA}$ for Aves with precocial and altricial young. Note log–log axes. Each dot is a datapoint for an individual avian species. The black lines represent the GLM for Aves as a whole. Aves which have precocial young are represented with dark grey inverted triangles, while Aves which have altricial young are represented with light grey triangles. See Appendix B for the full list of species.

Table 3-1. Model support for phylogenetic least squares models of total cerebral carotid blood flow rate in the Aves.

Intercept	Adult body mass $\log_{10}$ (g)	Braincase volume $\log_{10}$ (ml)	Δ AICc	Relative model weight	R^2	P	Model Rank
-0.327 [0.107]	0.188 [0.059]	0.464 [0.111]	0.00	0.972	0.8419	2.2×10^{-16}	1st
-0.024 [0.051]	-	0.773 [0.057]	7.21	0.026	0.8051	2.2×10^{-16}	2nd
-0.605 [0.097]	0.407 [0.033]	-	13.28	0.001	0.7776	5.836×10^{-16}	3rd

Predictor variables (median estimate [standard error]) are provided for the four models of cerebral carotid blood flow rate using the variables adult body mass and braincase volume. Model ranks and median relative model weights are also provided. ΔAICc, Akaike's information criterion; median AICc is provided.

Table 3-2. Support for phylogenetic signal in the examined variables in the Aves.

Variable	Symbol (units)	Pagel's lambda (λ)	logL (lambda)	LR (lambda=0)	P-value (based on LR test)
Adult Body Mass	M_b (g)	0.9999	-498.836	43.60	4.04×10^{-11}
Braincase Volume	V_{br} (ml)	0.994	-151.371	26.14	3.17×10^{-07}
Carotid Foramina Radius	r_{CF} (cm)	0.901	130.587	10.74	1.05×10^{-03}
Cerebral carotid Blood Flow Rate	$\dot{Q}_{CA}$ (ml min^{-1})	0.648	-124.192	5.23	2.22×10^{-02}
Volumetric Brain Perfusion	$\dot{Q}_{CA} \cdot V_{br}^{-1}$ (ml min^{-1} ml^{-1})	0.807	-10.8641	31.49	2.00×10^{-08}

Measures relating to phylogenetic signal are provided for five variables relating to brain perfusion. Pagel's lambda (λ) signifies the strength of the phylogenetic relationship with a value between 0 and 1; lambda values of 0 indicate phylogenetic independence while values of 1 indicate a strong phylogenetic signal in the variable. Confidence (P) values are provided.

Table 3-3. Allometric equations relating body, relating body mass, brain volume, total flow through left and right cerebral carotid arteries and carotid foramen radius in the Aves following PGLS correction.

Independent	Dependent	Power Equation	Adjusted R^2
M_b (g)	V_{br} (ml)	$1.23x10^{-1}M_b^{0.54\pm0.04}$	0.87
M_b (g)	$\dot{Q}_{CA}$ (ml min^{-1})	$1.66x10^{-1}M_b^{0.44\pm0.07}$	0.67
V_{br} (ml)	$\dot{Q}_{CA}$ (ml min^{-1})	$8.84x10^{-1}M_b^{0.81\pm0.06}$	0.77
V_{br} (ml)	r_{CF} (cm)	$2.47x10^{-2}M_b^{0.32\pm0.02}$	0.76
V_{br} (ml)	$\dot{Q}_{CA} \cdot V_{br}^{-1}$ (ml min^{-1} ml-1)	$8.85x10^{-1}M_b^{-0.19\pm0.06}$	0.14

Table 3-4. Allometric equations and ANCOVAs relating body mass, brain volume, total flow through both cerebral carotid arteries and carotid foramen radius in the Aves and two groups of mammals.

Variables		Clade	Power Equation	(r^2)	Palaeognathae		Galliformes		Anseriformes		Psittaciformes		Passeriformes		Haplorrhini		Diprotodontia		1	0
					Slope	Elev.	Slope	Elev.	Slope	Elev.	Slope	Elev.	Slope	Elev.	Slope	Elev.	Slope	Elev.	Slope	Slope
M_b (g)	V_{br} (ml)	Aves	$2.51x10^{-1}M_b^{0.47\pm0.08}$	0.78	N	N	N	Y	N	N	N*	N	N*	N	Y*	-	Y*	-	Y	Y
		Palaeognathae	$2.59x10^{-1}M_b^{0.44\pm0.18}$	0.92			N	Y	N	N	N*	Y	Y*	-	N*	Y	Y*	-	Y	Y
		Galliformes	$9.09x10^{-2}M_b^{0.51\pm0.09}$	0.98					N	Y	N*	Y	Y*	-	N*	Y	N*	Y	Y	Y
		Anseriformes	$1.42x10^{-1}M_b^{0.52\pm0.12}$	0.95							N*	Y	Y*	-	N	Y	N*	N	Y	Y
		Psittaciformes	$1.09x10^{-1}M_b^{0.72\pm0.14}$	0.94									N	N	N	Y	N	Y	Y	Y
		Passeriformes	$7.89x10^{-2}M_b^{0.76\pm0.06}$	0.99											N	Y	N	Y	Y	Y
		Haplorrhini	$1.73x10^{-1}M_b^{0.71\pm0.09}$	0.89													N	Y	Y	Y
		Diprotodontia	$4.19x10^{-2}M_b^{0.70\pm0.06}$	0.98															Y	Y
M_b (g)	$\dot{Q}_{CA}$ (ml min^{-1})	Aves	$2.48x10^{-1}M_b^{0.41\pm0.07}$	0.78	N	N	N	N	N	N	N	N	Y*	-	Y*	-	Y*	-	Y	Y
		Palaeognathae	$2.26x10^{0}M_b^{0.19\pm0.16}$	0.74			N	N	N*	N	N*	N	Y*	-	Y*	-	Y*	-	Y	Y
		Galliformes	$3.32x10^{-1}M_b^{0.37\pm0.24}$	0.82					N	N	N	N	Y*	-	N*	Y	N*	N	Y	Y
		Anseriformes	$2.87x10^{-1}M_b^{0.40\pm0.18}$	0.83							N	N	Y*	-	N*	Y	N	N	Y	Y
		Psittaciformes	$1.81x10^{-1}M_b^{0.50\pm0.21}$	0.76									N*	N	N	Y	N	N	Y	Y
		Passeriformes	$5.83x10^{-2}M_b^{0.74\pm0.05}$	0.99											N	N	N	Y	Y	Y
		Haplorrhini	$1.26x10^{-1}M_b^{0.67\pm0.10}$	0.87													N	Y	Y	Y
		Diprotodontia	$8.22x10^{-2}M_b^{0.59\pm0.08}$	0.90															Y	Y
V_{br} (ml)	$\dot{Q}_{CA}$ (ml min^{-1})	Aves	$9.46x10^{-1}V_{br}^{0.77\pm0.12}$	0.81	N	N	N	Y	N	N	N	N	N	N	N	Y	N	Y	Y	Y
		Palaeognathae	$2.41x10^{0}V_{br}^{0.44\pm0.29}$	0.82			N	N	N	N	N	Y	Y*	-	Y*	-	N	Y	Y	Y
		Galliformes	$1.89x10^{0}V_{br}^{0.75\pm0.41}$	0.87					N	N	N	Y	N	Y	N	Y	N	Y	N	Y
		Anseriformes	$1.39x10^{0}V_{br}^{0.73\pm0.38}$	0.79							N	Y	N	N	N	Y	N	Y	N	Y
		Psittaciformes	$7.94x10^{-1}V_{br}^{0.72\pm0.20}$	0.88									N*	N	N*	Y	N	Y	Y	Y
		Passeriformes	$6.96x10^{-1}V_{br}^{0.97\pm0.10}$	0.99											N	Y	N	Y	N	Y
		Haplorrhini	$6.65x10^{-1}V_{br}^{0.95\pm0.08}$	0.95													N	Y	N	Y
		Diprotodontia	$1.19x10^{0}V_{br}^{0.85\pm0.09}$	0.89															Y	Y

See bottom of Table 3-5 for descriptive information.

Table 3-5. Allometric equations and ANCOVAs relating body mass, brain volume, total flow through both cerebral carotid arteries and carotid foramen radius in the Aves and two groups of mammals.

Variables	Clade	Power Equation	(r^2)	Palaeognathae		Galliformes		Anseriformes		Psittaciformes		Passeriformes		Haplorrhini		Diprotodontia		1	0
				Slope	Elev.	Slope	Elev.	Slope	Elev.	Slope	Elev.	Slope	Elev.	Slope	Elev.	Slope	Elev.	Slope	Slope
V_{br} (ml) r_{CF} (cm)	Aves	$2.56x10^{-2}V_{br}^{0.30\pm0.05}$	0.80	N	N	N	Y	N	N	N	N	N	N	N*	N	N	Y	Y	Y
	Palaeognathae	$3.67x10^{-2}V_{br}^{0.18\pm0.12}$	0.82			N	N	N	N	N	Y	Y*	-	Y*	-	N	Y	Y	Y
	Galliformes	$3.35x10^{-2}V_{br}^{0.30\pm0.16}$	0.86					N	N	N	Y	N	Y	N	Y	N	N	Y	Y
	Anseriformes	$2.93x10^{-2}V_{br}^{0.29\pm0.16}$	0.78							N	Y	N	N	N	Y	N	N	Y	Y
	Psittaciformes	$2.38x10^{-2}V_{br}^{0.28\pm0.08}$	0.88									N*	N	Y*	-	N	Y	Y	Y
	Passeriformes	$2.29x10^{-2}V_{br}^{0.37\pm0.04}$	0.99											N	N	N	Y	Y	Y
	Haplorrhini	$1.91x10^{-2}V_{br}^{0.40\pm0.03}$	0.96													N	Y	Y	Y
	Diprotodontia	$2.61x10^{-2}V_{br}^{0.34\pm0.04}$	0.88															Y	Y
V_{br} (ml) $\dot{Q}_{CA} \cdot V_{br}^{-1}$ (ml min^{-1} ml^{-1})	Aves	$9.46x10^{-1}V_{br}^{-0.23\pm0.23}$	0.26	N	N	N	Y	N	N	N	N	N	N	N*	N	N*	Y	Y	Y
	Palaeognathae	$2.41x10^{0}V_{br}^{-0.56\pm0.56}$	0.88			N	N	N	N	N	Y	Y*	-	Y*	-	N*	Y	Y	Y
	Galliformes	$1.89x10^{0}V_{br}^{-0.25\pm0.41}$	0.43					N	N	N	Y	N	Y	N*	Y	N	Y	Y	N
	Anseriformes	$1.39x10^{0}V_{br}^{-0.27\pm0.38}$	0.34							N	Y	N	N	N*	N	N	N	Y	N
	Psittaciformes	$7.94x10^{-1}V_{br}^{-0.28\pm0.28}$	0.54									N*	N	N*	Y	N*	Y	Y	Y
	Passeriformes	$6.96x10^{-1}V_{br}^{-0.04\pm0.10}$	0.09											N*	N	N	N	Y	N
	Haplorrhini	$1.24x10^{0}V_{br}^{0.11\pm0.07}$	0.25													N	Y	Y	N
	Diprotodontia	$5.12x10^{-1}V_{br}^{0.14\pm0.16}$	0.17															Y	Y

All equations are standard GLM. Ordinary least squares regression equations are given with 95% confidence intervals for the exponent, coefficients of determination (r2) and significant differences between the three groups according to ANCOVA. Exponents of the allometric equations are significantly different (P<0.05) if the letter Y appears in the relevant cell and not significantly different if the letter N appears in the relevant cell. If exponents are not different, then the elevation is significantly different if the letter Y appears in the relevant cell and not significantly different if the letter N appears in the relevant cell. When exponents are significantly different it is not possible to test whether the elevations differ significantly and a - appears in the cell. If a significant difference was detected in the ANCOVA comparisons of slope, these groups were subjected to a post hoc Johnson–Neyman (J–N) test with Bonferroni correction. Groups for which slope and elevation were subjected to post hoc testing are denoted with an asterisk (*) in the slope column, and the result of their testing. Significances without post hoc testing were P=0.05; significances with post hoc Bonferroni correction can be calculated by dividing 0.05 by the number of cells for a set of variables which show an asterisk. For full statistical results see Appendix A.

Table 3-6. Allometric equations and ANCOVAs relating body, relating body mass, brain volume, total flow through both cerebral carotid arteries and carotid foramen radius in the Aves by degree of developmental maturity at hatching.

Variables		Clade	Power Equation	(r^2)	Precocial		Altricial		1	0
					Slope	Elev.	Slope	Elev.	Slope	Slope
M_b (g)	V_{br} (ml)	Aves	$2.51\times10^{-1}M_b^{0.47\pm0.08}$	0.78	N	Y	Y	-	Y	Y
		Precocial	$1.19\times10^{-1}M_b^{0.52\pm0.07}$	0.93			Y	-	Y	Y
		Altricial	$1.11\times10^{-1}M_b^{0.68\pm0.08}$	0.93					Y	Y
M_b (g)	$\dot{Q}_{CA}$ (ml min^{-1})	Aves	$3.01\times10^{-1}M_b^{0.38\pm0.08}$	0.67	N	N	N	N	Y	Y
		Precocial	$5.86\times10^{-1}M_b^{0.29\pm0.08}$	0.78			Y	-	Y	Y
		Altricial	$1.75\times10^{-1}M_b^{0.48\pm0.17}$	0.59					Y	Y
V_{br} (ml)	$\dot{Q}_{CA}$ (ml min^{-1})	Aves	$1.05\times10^{0}M_b^{0.71\pm0.15}$	0.68	N	Y	N	N	Y	Y
		Precocial	$2.00\times10^{0}M_b^{0.55\pm0.14}$	0.80			Y	-	Y	Y
		Altricial	$7.74\times10^{-1}M_b^{0.74\pm0.20}$	0.71					Y	Y
V_{br} (ml)	r_{CF} (cm)	Aves	$2.56\times10^{-2}M_b^{0.30\pm0.05}$	0.80	Y	-	N	Y	Y	Y
		Precocial	$3.41\times10^{-2}M_b^{0.22\pm0.06}$	0.79			Y	-	Y	Y
		Altricial	$2.23\times10^{-2}M_b^{0.33\pm0.04}$	0.92					Y	Y
V_{br} (ml)	$\dot{Q}_{CA} \cdot V_{br}^{-1}$ (ml min^{-1} ml^{-1})	Aves	$9.43\times10^{-1}M_b^{-0.23\pm0.12}$	0.26	Y	-	N	Y	Y	Y
		Precocial	$2.00\times10^{0}M_b^{-0.45\pm0.14}$	0.73			Y	-	Y	Y
		Altricial	$1.12\times10^{0}M_b^{-0.15\pm0.10}$	0.27					Y	Y

All equations are standard GLM. Ordinary least squares regression equations are given with 95% confidence intervals for the exponent, coefficients of determination (r2) and significant differences between the three groups according to ANCOVA. Exponents of the allometric equations are significantly different (P<0.05) if the letter Y appears in the relevant cell and not significantly different if the letter N appears in the relevant cell. If exponents are not different, then the elevation is significantly different if the letter Y appears in the relevant cell and not significantly different if the letter N appears in the relevant cell. When exponents are significantly different it is not possible to test whether the elevations differ significantly and a - appears in the cell. For full statistical results see Appendix A.

DISCUSSION

Trends in avian cerebral perfusion

Aves exhibit lower exponents for brain size to body mass than either of the mammal groups examined, equivalent to what is reported elsewhere. The scaling exponent for brain mass to body weight has been shown as $M_b^{0.75}$ for mammals (Martin 1981; Bennett and Harvey 1985a), while values for birds have been given variously as $M_b^{0.56}$ (Martin 1981), $M_b^{0.53}$ (Bennett and Harvey 1985a) or $M_b^{0.58}$ (Font *et al.* 2019). These values coincide with this chapter's exponent for avian adult brain volume on adult body weight ($M_b^{0.47}$) (Figure 3-4, Table 3-4). In comparison, non-avian reptiles have a scaling exponent of around $M_b^{0.56}$ (Martin 1981), or $M_b^{0.58}$ (Font *et al.* 2019), but a ten-fold smaller brain mass than birds for the same body mass. Font *et al.* (2019) have suggested that this difference between birds and non-avian reptiles could simply be attributed to birds' evolutionary adaptations towards lightness, with highly pneumatised bones and the reduction of their tail. Regardless, the allometric scaling relationship for brain size on body size found in aves as a whole differs among finer taxonomic groupings in birds (Figure 3-5, Table 3-4). Indeed the exponent is higher for some parts of the brain than others, irrespective of taxonomic level (Bennett and Harvey 1985b). The literature reflects the allometric relationships of relative brain size I have presented here for avian clades, with palaeognaths $M_b^{0.59}$ (Corfield *et al.* 2008), galliforms $M_b^{0.60}$ (Boire and Baron 1994), anseriforms $M_b^{0.51}$, psittaciforms $M_b^{0.76}$, and passeriforms $M_b^{0.71}$ (Franklin *et al.* 2014) (Figure 3-5, Table 3-4). Franklin *et al.* (2014), in a large study on Australian bird's relative brain size found that patterns of brain-size differed among different orders, noting that there is possible variation in relative brain size among passerine families depending on data treatment. Large relative brain sizes are noted in parrots, cockatoos and owls, and particularly small relative brain sizes in galliforms, dromaiids, grebes, swifts, and swallows, with identical allometric patterns as recorded for birds outside Australia (Franklin *et al.* 2014). Franklin *et al.* (2014) suggest that that because small relative brain size is a trait seen in unrelated aerial foragers there may be similar physical constraints influencing the evolution of brain size across these taxa.

Birds exhibit a lower exponent for cerebral perfusion against body mass than either of the mammal groups examined here. However, this relationship does not hold when the Aves are divided into their separate lineages, where a wide variety of exponents are resolved (Figure 3-5, Table 3-4). Some avian clades exhibit exponents in line with those of the mammal groups, while others exhibit exponents which are significantly and dramatically different from the mammal groups and other avian clades. Avian groups which are considered 'older' (branched off earlier in the avian phylogenetic history) exhibit lower exponents for brain size to body mass than younger groups. Palaeognaths (oldest group) and the galloanseres (oldest Neognathae group) cluster together with lower

brain size to body mass exponents. The two most modern groups – the psittaciformes and the Passeriformes – have exponents which are equal to the haplorrhines, with elevations just shy of the haplorrhine group. This indicates a trend towards increasing brain sizes across avian phylogenetic history and is supported by the literature (Ksepka *et al.* 2020).

Avian volume-specific brain perfusion appears to decrease as body mass and brain volume grow larger. However, this trend may be due to the statistical weight which the palaeognath group exerts upon the dataset at higher body masses. Palaeognaths exhibit a perfusion rate that is largely independent of body mass and brain volume – across a 126-fold increase in body mass, brain volume increases by 10-fold and blood flow by 1.8-fold. In comparison, the parrots experience a 71-fold change in body mass, 18-fold increase in brain volume and 12.6-fold increase in blood flow. In the palaeognath group, cerebral blood flow remains largely constant across their body mass and brain volume ranges. This group is perhaps the most unique among those examined.

Palaeognaths possess a large degree of brain structural variation (Picasso *et al.* 2010). Differences in brain structure, the activity of different brain regions, and an animal's behaviour all relate to one another. The endocasts of rheas are similar to those of ostriches and emus but differ from tinamous and kiwis. Kiwis' brains have large olfactory lobes which give their brain a bulbous shape and reflect the kiwi's reliance on their sense of smell, while rhea, ostriches and emus have a larger hindbrain relative to their forebrain than kiwis (Picasso *et al.* 2010). Tinamous – the only flighted palaeognaths – possess brains that are similar to the other palaeognaths in terms of proportions but are much more compact and arguably more similar to pigeons (Columbidae) (Picasso *et al.* 2010). The cerebral perfusion exponents of palaeognaths determined in this chapter are very low (Table 3-4, Table 3-5, Figure 3-5). However, removing the single tinamidae replicate from the data results in even shallower exponents for the palaeognaths. The brain sizes of larger palaeognaths such as moa fit the line for V_{br} on M_b in Palaeognathae (Ashwell and Scofield 2008). In this chapter, Palaeognaths represent the most evolutionary diverse clade presented as they cover an entire infraclass of diversity while the other clades examined are at the 'order' level of taxonomic division. Aves as a whole possess an exponent which is different to those of the individual clades which make up the class. This difference between exponents at different taxonomic levels could be a form of Simpson's paradox. It is possible that palaeognaths are experiencing a similar kind of effect and would have different scaling exponents if there were enough taxa to examine each palaeognath order individually. As it stands, the most remarkable thing about the palaeognaths is their low cerebral perfusion exponents.

Galliform birds – especially the quail – have an elevated blood flow rate relative to their brain size, with small brained galliform birds possessing a higher rate of cerebral perfusion than any of the other groups with similar brain sizes (Figure 3-5). The significance

of this trend decreases as brain size increases. A wild turkey has approximately the same brain volume and cerebral perfusion rate as a pygmy marmoset, despite a 65-fold greater body mass (Figure 3-5, Appendix B). That two seemingly disparate animals would have the same volumetric perfusion rate is interesting as one may anticipate a primate possessing more complex cognition. However, similarities between the two certainly exist. Turkeys are known to live in large social groups that are somewhat complex, with many vocalisations and intricate mating rituals (Watts and Stokes 1971; Williams 1984; Buchwalder and Huber-Eicher 2003). Pygmy marmosets live in social groups that are around six individuals and exhibit the ability for complex communication (Soini 1982; Snowdon 2001; De la Torre and Snowdon 2009). Perhaps viewing marmosets as more cognitively developed is simply a form of anthropocentrism.

Parrot and songbird scaling bore significant similarities to haplorrhine primates in terms of brain perfusion (Table 3-4, Table 3-5, Figure 3-5). Songbirds were almost indistinguishable from higher primates in terms of the allometric brain perfusion. Parrots follow the songbirds, with a similar brain size scaling to higher primates but some statistical differences in the elevations of their allometric equations for brain metabolic rate (Table 3-4, Table 3-5, Figure 3-5). These similarities are unsurprising given parrots and songbirds have been shown to exhibit similarities to primates in the scaling of their neuronal densities (Olkowicz *et al.* 2016). Across the aves, different lineages exhibit differences in their scaling relationships, with metabolic energy use in the brain likely due to the different neuronal scaling rules exhibited by each lineage (Olkowicz *et al.* 2016). Furthermore, Olkowicz *et al.* (2016) show that more basal lineages including ratites and fowl share a lower degree of encephalisation and generally lower neuronal densities, such that their brains host significantly smaller neuron numbers than those of an equivalently sized songbird or parrot. Yet even basal birds possess pallial neuronal densities which are comparable to those found in the primate cerebral cortex. Pallial neuronal densities in primates are matched by those of galliforms and palaeognaths, but surpassed by those of psittaciforms and passeriforms (Olkowicz *et al.* 2016).

Life history traits

The impact of life history on relative brain size is of interest in the literature due to the uncertain relationships between the two. Researchers have alternatively found support (Bennett and Harvey 1985b) or a lack of support (Iwaniuk *et al.* 2004) for flightless birds possessing smaller relative brain sizes than volant birds. An attempt was made at dividing the taxa examined into groups based on life history traits such as locomotion (cursorial or volant) or developmental maturity (precocial or altricial) to investigate their relationship to cerebral perfusion. However, for the chosen taxa the divisions of locomotion and young essentially recapitulated one another; the cursorial group contained the same individuals as the precocial group and the volant group contained the same individuals as the altricial (with the two exceptions of the volant tinamous and cursorial

kakapo). Furthermore, these groupings were largely reflective of taxonomic position due to the tight clumping of clades at either end of the phylogenetic tree, with the palaeognaths and galloanseres trending cursorial/precocial and the neoaves trending volant/altricial. As there is a strong correlation between locomotion and developmental maturity (Dial 2003), only the developmental maturity (precocial/altricial) is analysed and referred to here and in the results (Figure 3-6, Table 3-6).

Precocial birds exist higher on the body mass and brain volume ranges, however altricial birds have steeper exponents for $\dot{Q}_{CA}$ on M_b and $\dot{Q}_{CA}$ on V_{br} (Figure 3-6, Table 3-6). Altricial birds have a low volumetric blood flow rate at smaller brain volumes, but their volumetric blood flow is larger than cursorial birds at higher brain volumes (Table 3-6). The developmental maturity spectrum strongly correlates with brain size relative to body mass. Adults of precocial species have significantly smaller relative brain sizes than adults of altricial species (Bennett and Harvey 1985a; Bennett and Harvey 1985b; Starck 1993). However, in hatchlings the opposite is true; precocial hatchlings possess significantly larger relative brain sizes (Bennett and Harvey 1985a). In precocial birds, most neural growth occurs during incubation, while in altricial birds most neural growth occurs post hatching (Iwaniuk and Nelson 2003). Embryologically, blood supply does not vary based on encephalisation or behavioural complexity in avian embryos; there is no difference in the scaling of carotid calibre in avian embryos of different groups (Yu *et al.* 2020). Hence, the established differences between clades in adults must develop after the embryonic stage of life. Increasing degree of parental care is associated with low developmental maturity at hatching and flightedness in adults (Dial 2003). Indeed, increasing the length of development through parental care is associated with increasing relative brain volume, whether this care occurs in the form of the incubation, fledging, or post-fledging periods (Iwaniuk and Nelson 2003). Additional brain power may be required for special cognition by volant birds processing three-dimensional perception whilst flying. However, the directionality of the association between developmental maturity, locomotion, and relative brain size is unclear. In this chapter altricial birds have steeper scaling exponents for foramen size and cerebral perfusion on brain volume than precocial birds (Figure 3-6, Table 3-6). However, the precocial birds generally exhibited higher perfusion rates for a given brain value than the precocial birds (Figure 3-6, Appendix B). Basal bird lineages have been demonstrated as showing generally lower neuronal densities, and larger glia/neuron ratios than songbirds or parrots (Olkowicz *et al.* 2016). This incongruency between neuron density and perfusion is somewhat puzzling, perhaps implying more efficient brain energetics in the altricial group.

As the clades in this study are tightly grouped at either end of the avian taxonomic tree (Figure 3-2), the allometric equations for the life history groupings may be offset by particular groups. Ultimately, the degree of development at hatching and degree of flightedness are not categorical data, but rather exist across a spectrum. Hence, categorisation into altricial/precocial or cursorial/volant here may be somewhat invalid regardless.

Phylogenetic influence

Brain volume and body mass were two main correlates with blood flow rate (Table 3-1). That brain volume correlates with blood flow rate is perfectly logical because the size of the brain and its metabolic processes is directly related to the rate of blood flow required. However, brain volume has an intrinsic link to body mass as it makes up a proportion of an animal's body mass, and so body mass is also an important variable to consider when attempting to examine and explain cerebral blood flow rates.

Obtaining an indication that a result is highly phylogenetically influenced indicates that trends are influenced by their phylogenetic history, but not that the trend is incorrect. Blood flow rate was less phylogenetically influenced than foramen radius. That r_{CF} should be more phylogenetically influenced than $\dot{Q}_{CA}$ is somewhat perplexing as one is calculated from the other. As $\dot{Q}_{CA}$ can be expressed as a function of several other variables such as shear stress (τ), blood viscosity (η), differential pressure (ΔP) across a vessels length (L) (*Equation 3*, *Equation 4*) I suspect that these variables may be subject to less phylogenetic signal than r_{CF} itself and are thus decreasing λ values for $\dot{Q}_{CA}$. Blood viscosity is complex, depending upon many factors including plasma constituents, haematocrit percentage, and erythrocyte size, shape, and haematological characteristics. Few direct measurements of avian in vivo whole blood viscosity exist in the literature. The greatest influence upon avian blood viscosity appears to come from haematocrit and plasma protein content (Viscor *et al.* 1984). Blood viscosities in pigeons and gulls are similar at values of 0.04-0.07 dyne s cm^{-2} depending on shear rate, while chicken viscosities are relatively constant at about 0.03 dyne s cm^{-2} (Viscor *et al.* 1984; Fedde and Wideman Jr 1996). Rheological properties in some birds can change depending on environmental thermal conditions and adjustment (Clarke and Nicol 1993; Niedojadlo *et al.* 2018). In Adélie and little penguins blood viscosities have been measured ranging from 0.03-0.04 dyne s cm^{-2} at 38 °C to 0.1-0.2 dyne s cm^{-2} at 8 °C (Clarke and Nicol 1993). Investigation into the relationship between avian blood properties and phylogenetic history would be informative.

Methodological critique

Some shortcomings are evident through the selection of specimens for use in this chapter. Disagreement exists regarding the specific relationships of some branches of the avian evolutionary tree (Hackett *et al.* 2008; Jarvis *et al.* 2014; Prum *et al.* 2015). The broad positioning of groups at either end of the phylogenetic tree generally appears to be more certain. This chapter examines groups located at either end of the phylogenetic tree; this chapter does not examine all orders of birds. Neither does this chapter examine such a quantity of birds to allow separation of all clades into individual family groups. Some clades contained members from only one suborder (i.e., passeri in Passeriformes) whist others presented more variation (i.e., many ratite orders in Palaeognathae). Falconiformes (Falco) and Accipitriformes (Accipitridae) make up part of the overall avian

allometric equation presented here, but are not examined as individual monophyletic clades, nor as a singular paraphyletic group. Removing the Falconiformes and Accipitriformes from the overall avian analysis does not cause any significant change in the avian allometric equation. Falconiformes and Accipitriformes appear to exhibit similar traits on the graphs, however proper analysis of these groups is not statistically sound due to the small number of individuals in each group. The taxa examined in this chapter tend to possess body mass ranges which exemplify broad ranges of their clades. Therefore, the best way to address weaknesses in statistical power in future work would be by increasing the sample sizes of the groups examined. This would be advantageous for other reasons, such as allowing investigation of interesting taxa, identifying outlying groups, and identifying patterns among lower-level groups, such as the corvids, or breaking up passerines in general. As it stands, the broad 95% CI's and overlapping brain volumes and body masses make teasing apart the traits of different clades difficult.

Avian cephalic circulation is complex, and although the general anatomy of blood vessels in the heads of birds is well known, the finer details of vascular pathways are much less so. In birds, the head is the site of a number of vascular heat exchangers which are used to regulate the temperature of the blood either heading to the brain or to the rest of the body. The number and location of these varies between species (Burgoon *et al.* 1987; Arad *et al.* 1989; Porter and Witmer 2016; Tattersall *et al.* 2017; Eastick *et al.* 2019). One key vascular heat exchanger found in birds is the ophthalmic rete. This vascular heat exchanger has been substantially investigated in regard to its role in the maintenance of a temperature differential between the brain and the body (Richards 1970; Pettit *et al.* 1981; Midtgård *et al.* 1983; Peltonen *et al.* 1989; Caputa 2004; Porter and Witmer 2016). However, although the role and to some degree the structure of the rete is well documented, the anatomy of the connections between the ophthalmic rete and the brain have often been poorly described. The number of arteries in the ophthalmic rete varies greatly across different species, with (Midtgård 1983) reporting a 100-fold variation artery counts, with the largest number (500) in large falconiformes and the fewest (<5) in small passerines. Vessels from the ophthalmic rete supply or drain blood directly from the orbital region (Hossler and Olson 1984). If blood does flow towards the brain via this route, it must travel through connections with the orbital or ethmoid arteries. Porter and Witmer (2016) point out that this route would entail blood flow to the brain to move in a retrograde direction, against the pressure gradient produced by the heart. Blood pressure would decrease after passing through the ophthalmic rete due to resistance, and so it is difficult to reconcile that blood flow could be going into the brain. The direction of flow, flow volume, and number of connections to the cephalic tissue is of key importance to studies in this area.

CONCLUSION

The evolution of intelligence has traditionally focused on primates. However, the prevalent assumption that complex cognition is restricted to primates has no reasonable basis. More recently, other animals have been recognised as intelligent. These animals are usually large brained, social, and have understanding of their physical worlds. Emery and Clayton (2004b) set forth an idea that complex cognition depends on the possession of a specific set of traits which consists of causal reasoning, flexibility, imagination, and prospection. Cognitive abilities have clearly evolved multiple times in species which are only distantly related and possess vastly different brain structures. It seems likely that disparate groups would develop these cognitive tools to solve similar socioecological problems. Birds which have altricial young have steeper scaling exponents than birds which have precocial young, indicating this may be part of an adaptation towards higher cognition. This study lends credence to the assertion that cognition in primates and some groups of birds evolved convergently. Some groups of birds seem to essentially be smaller primates in terms of their rates of cerebral perfusion and brain sizes – although classifying birds in terms of primates must be a different form of the anthropocentricism which led to the reputation of birds as being cognitively uncomplex.

Figure 3-7. Digital renderings of the skulls of two palaeognath birds examined in this study, with endocranial casts overlain. Top, Southern Cassowary (*Casuarius casuarius*); bottom, Emu (*Dromaius novaehollandiae*). Rendered images were produced by exporting segmented structures from Avizo into Blender 2.90.1 (Open Source, www.blender.org).

Figure 3-8. Digital renderings of the skulls of two galliform birds examined in this study, with endocranial casts overlain. Top, Turkey (*Meleagris gallopavo*); bottom, Malleefowl (*Leipoa ocellata*). Rendered images were produced by exporting segmented structures from Avizo into Blender 2.90.1 (Open Source, www.blender.org).

Figure 3-9. Digital renderings of the skulls of two anseriform birds examined in this study, with endocranial casts overlain. Top, Australian Shoveler (*Anas rhynchotis*); bottom, Cape Barren Goose (*Cereopsis novaehollandiae*). Rendered images were produced by exporting segmented structures from Avizo into Blender 2.90.1 (Open Source, www.blender.org).

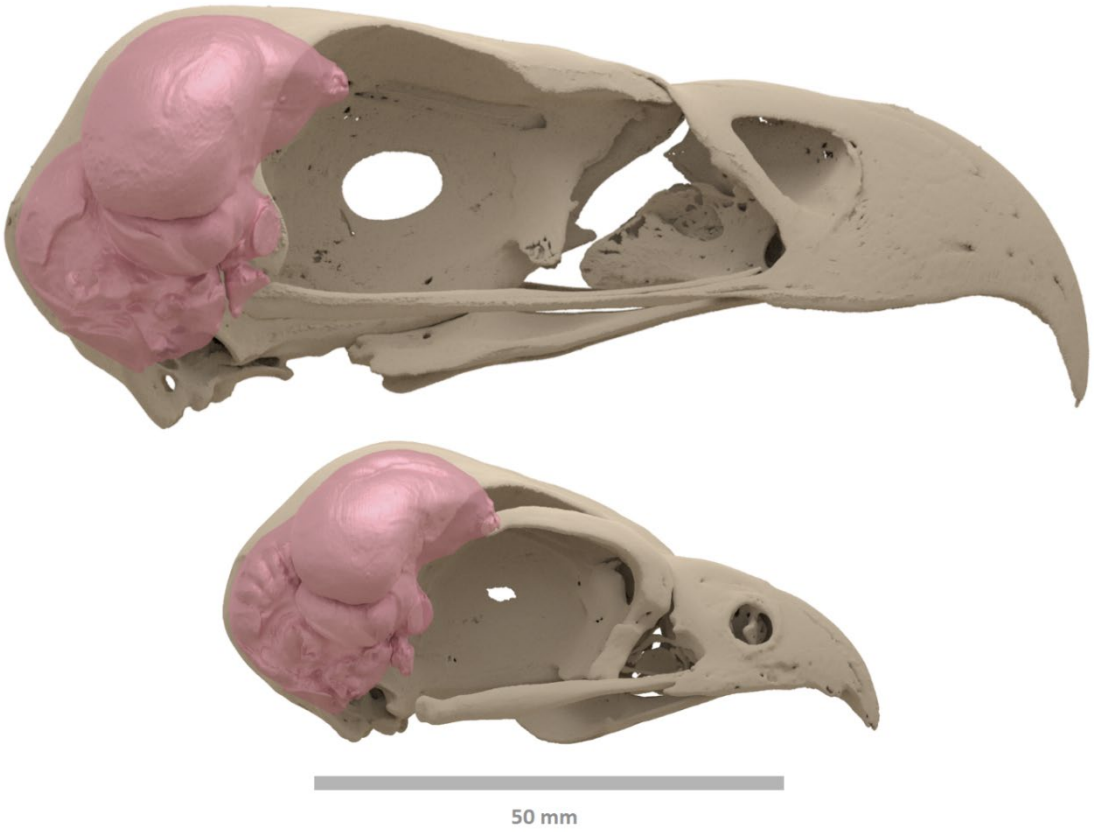

Figure 3-10. Digital renderings of the skulls of two birds of prey examined in this study, with endocranial casts overlain. Top, Wedge-Tailed Eagle (*Aquila audax*), an accipitriform; bottom, Peregrine Falcon (*Falco peregrinus*), a falconiform. Rendered images were produced by exporting segmented structures from Avizo into Blender 2.90.1 (Open Source, www.blender.org).

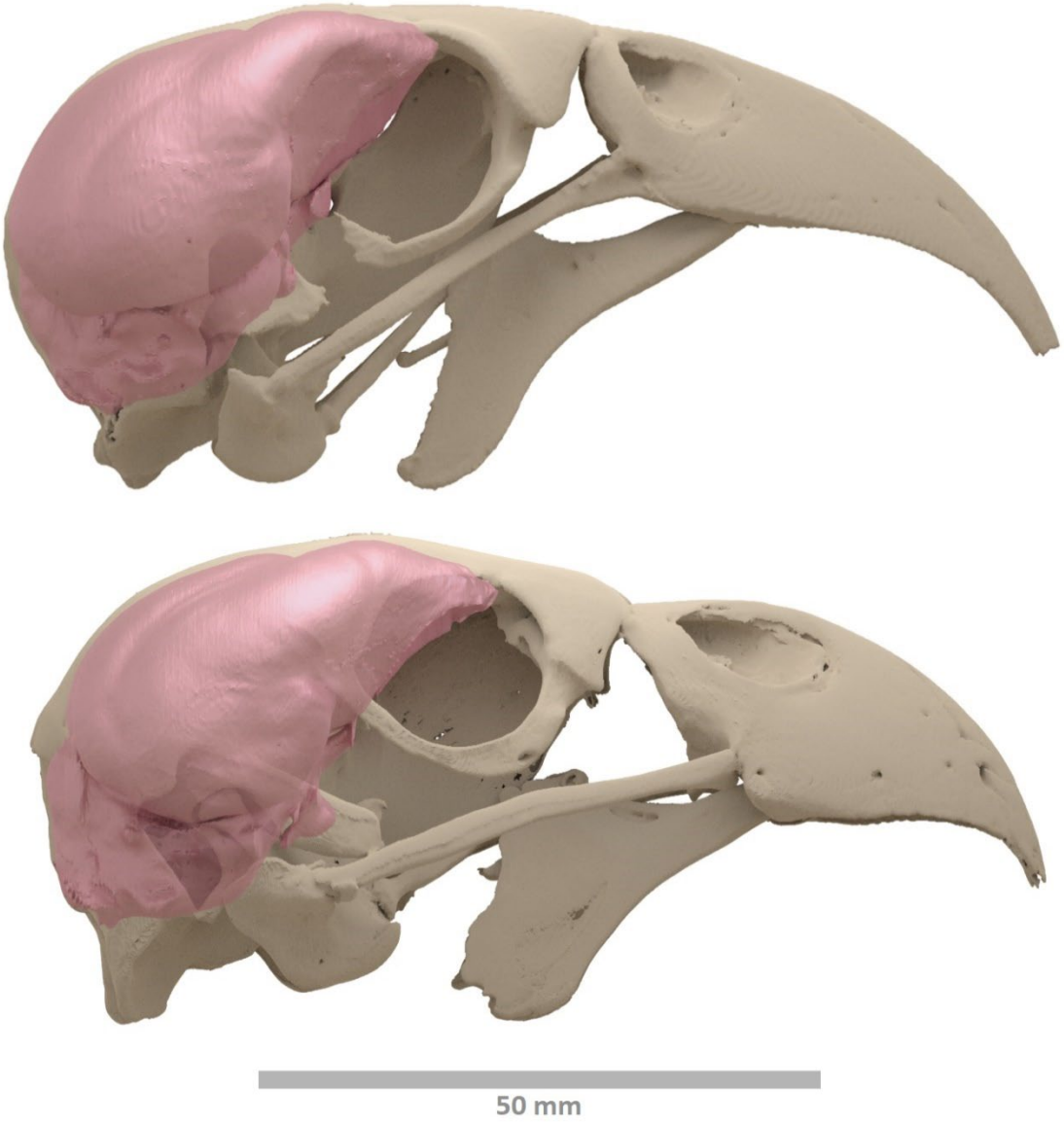

Figure 3-11. Digital renderings of the skulls of two psittaciform birds examined in this study, with endocranial casts overlain. Top, Kea, (*Nestor notabilis*); bottom, Kakapo, (*Strigops habroptilus*). Rendered images were produced by exporting segmented structures from Avizo into Blender 2.90.1 (Open Source, www.blender.org).

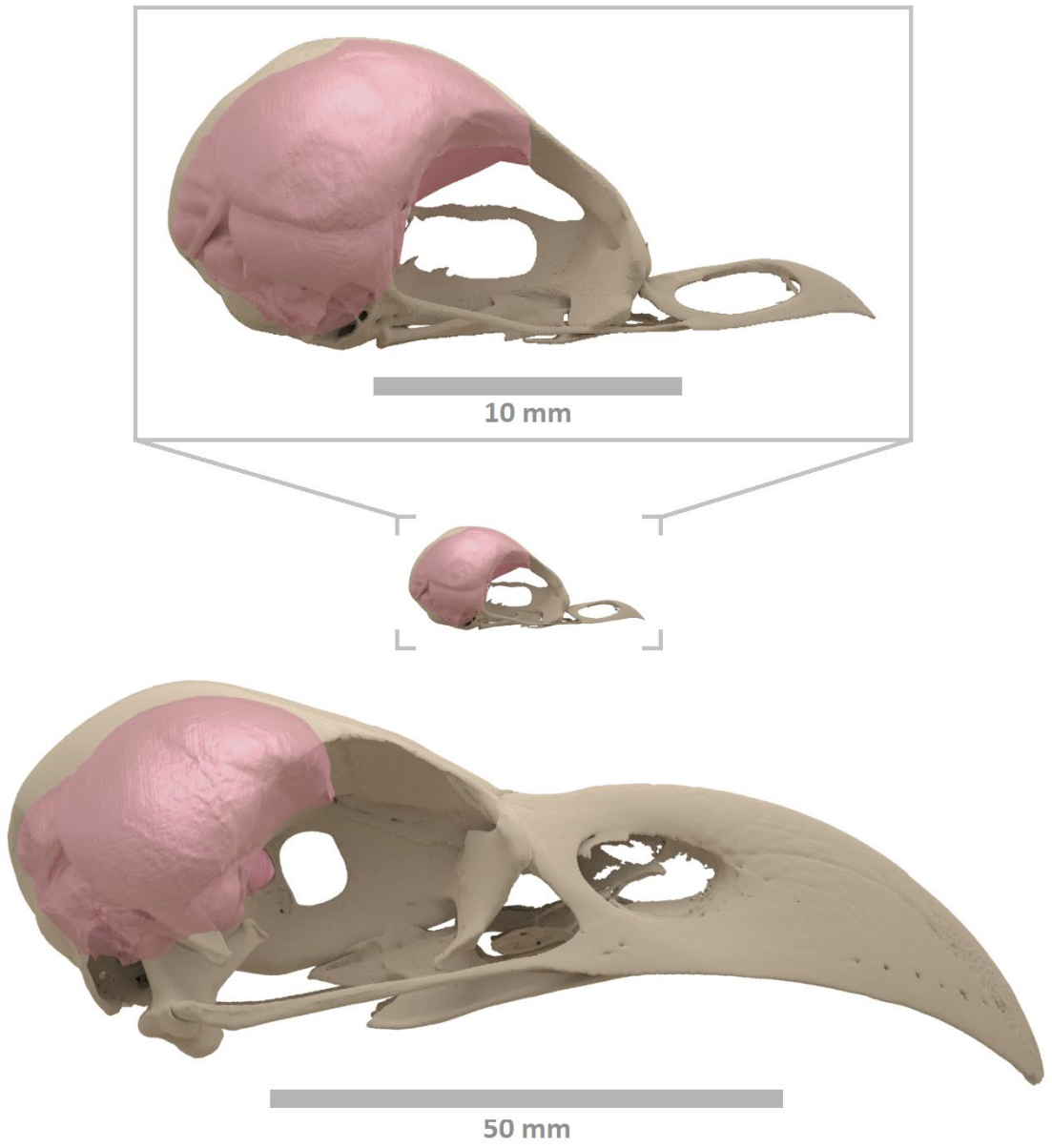

Figure 3-12. Digital renderings of the skulls of two passeriform birds examined in this study, with endocranial casts overlain. Top, Spotted Pardalote (*Pardalotus punctatus*); bottom, White Necked Raven (*Corvus albicollis*). Rendered images were produced by exporting segmented structures from Avizo into Blender 2.90.1 (Open Source, www.blender.org).

CHAPTER 4

CEPHALIC ARTERIAL ANATOMY OF THE DOMESTIC FOWL (*GALLUS GALLUS DOMESTICUS)*

ABSTRACT

Despite more than 175 years of research into the vasculature of birds, many important details of the avian cephalic circulation remain unexplored. In order to better comprehend the complexities of cerebral blood flow (and thus metabolism) of birds, clearer descriptions of the arteries in the cephalic region are essential. This chapter aims to investigate the cephalic arterial blood flow patterns in chickens (*Gallus gallus domesticus*), which have historic descriptions but have not had a modern comprehensive interpretation. Here I use the vascular contrast perfusion to produce a modern anatomical description in three dimensions of the cephalic arteries of the chicken in relation to one another and relevant osseous landmarks. I produce the first easily navigable three-dimensional map of the cephalic arteries of the chicken. The ethmoid and orbital arteries have been suggested as an important source of collateral flow, which is indeed a possibility, but here the mapping of the blood flow pattern is inconclusive in determining the role of these arteries in supplying the braincase during normal circulation. The major supply to the braincase ultimately comes from a branch of the common carotid artery – the cerebral carotid artery. Secondary supply comes from the ventral spinal artery. Three other arteries connect to the inside of the braincase – these are the ethmoid, orbital, and minor temporal cerebral artery. The minor temporal cerebral artery likely heads into the braincase but is minuscule and would provide negligible supply. The paths of the ethmoid and orbital arteries continue out of the brain, rostrally towards the beak. The discovery of the temporal cerebral artery after more than 175 years of study of this system illustrates the need for further, modern studies in this field.

INTRODUCTION

Avian gross anatomy and taxonomy is generally well described in the literature. However, despite more than 175 years of research into the vasculature of birds (Neugebauer 1845), many important details of the avian circulation remain unexplored. Avian cephalic vasculature is of particular interest due to the complex relations of vessels in the head and their role in heat exchange and supplying the brain. In particular, the presence of several cephalic rete mirabile, and many vessels that traverse between the extracranial and endocranial regions, make this field ripe for modern examination. The temporal region of galliform birds holds one such rete mirabile – the ophthalmic rete – to which many arteries connect. Several papers suggest that some supply of cerebral blood flow comes as an indeterminate contribution from collateral flows via the ophthalmic rete, although the actual use of these pathways has been disputed in more recent literature (Richards 1970; Midtgård 1984a; Midtgård 1984b; Arad *et al.* 1987; Arad 1990). Due to the position of the ophthalmic rete and its related arteries relative to the brain, Porter and Witmer (2016) state that for blood to flow from the rete into the endocranial cavity would require retrograde flow, suggesting that it is more plausible that blood exits the braincase via these pathways. Many aspects of avian vasculature have been shown to be conserved across taxa (Pettit *et al.* 1981; Holliday *et al.* 2006; Porter and Witmer 2016). However, much of the finer detail regarding cephalic-encephallic connectivitiy is in want of further investigation. In order to better comprehend the complexities of cerebral blood flow (and thus metabolism) in birds, better descriptions of the arteries in the cephalic region are essential. By using modern approaches to vascular imaging it is possible to produce three-dimensional reconstructions that are high quality and enhance the ability of researchers to understand cephalic vascular architecture.

This chapter aims to investigate the cephalic arterial blood flow pattern in chickens (*Gallus gallus domesticus*), which although communicated in the literature (Richards 1967; Richards 1970; Baumel 1975; Arad and Midtgård 1984; Baumel 1993; Verduzco Mendoza *et al.* 2009) has not been investigated using modern techniques which allow more comprehensive descriptions of the cephalic arterial architecture. Here I use vascular contrast perfusion to produce a modern anatomical description of the cephalic arteries of the chicken in relation to one another and relevant osseous landmarks. Vascular contrast perfusion allows three-dimensional reconstruction of the course of an animal's vasculature based upon the filled lumen volumes following the same principles as vascular corrosion casting. I produce for the first time an easily navigable three-dimensional map of the cephalic arteries of the chicken. Finally, I describe for the first time the presence of a temporal cerebral artery which connects the ophthalmic rete and the cerebrum of the brain in chickens and other galliform birds, a description which has been absent from the literature for more than 175 years.

METHODS

Animals and imaging

This study describes cerebral blood flow patterns in Isa Brown domestic chickens. The Isa Brown breed is a high egg production sex-linked crossbreed commonly used in both private and commercial egg production. Bird specimens in this chapter were salvaged from work undertaken in Chapter 5 of this thesis. Four domestic chickens with body masses ranging from 883 g to 2659 g were used for the study. Body masses were determined to a resolution of 1 g using a 16 kg capacity bench scale (Sartorius QS16, Sartorius, Germany). Chickens were obtained locally from grain and fodder stores in metropolitan Adelaide, South Australia. Animals were housed in an indoor holding facility under a 14 to 16 h daylight cycle with a constant temperature of 23°C, and with access to tap water and food pellets *ad libitum* (Red Hen premium layer and breeder pellets, Laucke Mills, Daveyston, South Australia, Australia) prior to euthanasia. Euthanasia was carried out humanely via intravenous administration of ketamine and xylazine. Approval to euthanise animals for research-related purposes was provided by the University of Adelaide Animal Ethics Committee (S-2017-058). Specimens in this section of the study were shared with another study (Hu 2021; Hu *et al.* 2022), and with Chapter 5 of this thesis.

Following euthanasia specimens were rapidly processed in preparation for contrast perfusion. Specimens were decapitated and the left and right common carotid arteries were cannulated. Vessels were flushed of blood with heparinised saline (125 IU ml^{-1}) mixed with a small amount of detergent via the cannulated arteries. BriteVu (Scarlet Imaging, Murray, Utah, United States) was the selected vascular contrast agent used in this study. During specimen exsanguination the contrast medium mixture of 1-part BriteVu and 3-parts water, with 1.5% BriteVu enhancer (Scarlet Imaging, Murray, Utah, United States) was prepared. This mixture was heated to a temperature between 70°C and 80°C and maintained at this temperature for 10 min. The contrast medium mixture was continually stirred and a temperature of 70°C was maintained while it was perfused. The BriteVu vascular contrast medium was perfused into the cannulated common. Contrast perfusion was carried out until the excess contrast draining from the severed vessels in the neck began to solidify. Specimens were then packed in ice and refrigerated for up to 24 h until imaging could take place. Refrigeration was necessary to allow the BriteVu solution to solidify prior to CT scanning. Specimens were not fixed with formalin prior to contrast injection or imaging. One specimen was perfused with the vascular contrast agent using hand pressure applied to a syringe plunger, while in the other three specimens the contrast agent was perfused into arteries under approximately systemic arterial physiological pressures (150 mm Hg).

Specimens were scanned using the SkyScan-1276 X-ray micro-CT scanner at Adelaide Microscopy (Appendix C). NRecon 1.6.9.4 (Bruker microCT, Kontich, Belgium) was used to reconstruct cross sectional images from tomographic projection images and

subsequent voxels were cubic (isometric). Imaging settings were optimised for each specimen in order to maximise image contrast and resolution (Appendix C). Imagery was post processed using DataViewer 1.5.1.2 (Bruker microCT, Kontich, Belgium) to obtain desired rotations. Creation of digital cranial endocasts was performed in Avizo 9.0.0 (FEI SAS, Hillsboro, Oregon, USA). Data relevant to this chapter is available on MorphoSource under project ID: 000445264.

Model construction

Segmentation of structures was performed in Avizo 9.0.0 (FEI SAS, Hillsboro, Oregon, USA). Bones and contrast perfused arteries were segmented into their individual structures. Delineating between bone and arterial structures relied upon a difference in contrast of the structures, rather than the pre-injection and post-injection scanning technique employed by Porter and Witmer (2016). However, in some cases the difference in contrast was not sufficient to allow automatic delineation between the contrast material and osseous structures, and arteries had to be traced in manually.

Segmented structures were exported from Avizo into Blender 2.90.1 (Open Source, www.blender.org). In Blender, arterial structures from the segmentations of different chickens were composited to fill any areas of incomplete perfusion present in individual birds. The resulting unified structures were simplified and split down the midline. The structures present on the right side were preserved to show the vessels as they appeared in the perfusions. Arterial structures present on the left side were then overlain with 3D surfaces, using the segmented blood vessels as templates. More than 60 unique vascular structures were delineated and overlain on the left side. FinalMesh 2.1 (Pelikan Software Kft., Nagykovácsi, Hungary) was used to compose the final resultant 3D model and organise the Model Tree. This 3D model was then imported into Adobe Acrobat Pro DC 2021 (Adobe, San Jose, California, United States) during preparation of the 3D PDF document.

I encountered the same issue reported by Verduzco Mendoza *et al.* (2009) and Porter and Witmer (2016) of a lack of standardised nomenclature. Vascular nomenclature follows Porter and Witmer's paper on turkeys. Descriptions of arterial patterns are separated into five delineated regions of the head: the cervical region, orbital region, oral region, nasal region, and the encephalic region.

RESULTS

Arterial anatomy will be described within five delineated regions of the head. Arteries will be described in terms of anastomotic connections with other blood vessels, arterial plexuses, and the brain. Arteries are generally described in a caudal – rostral direction. Except where noted, arteries are described for one side of the head and can be assumed to have a symmetrical partner on the other side.

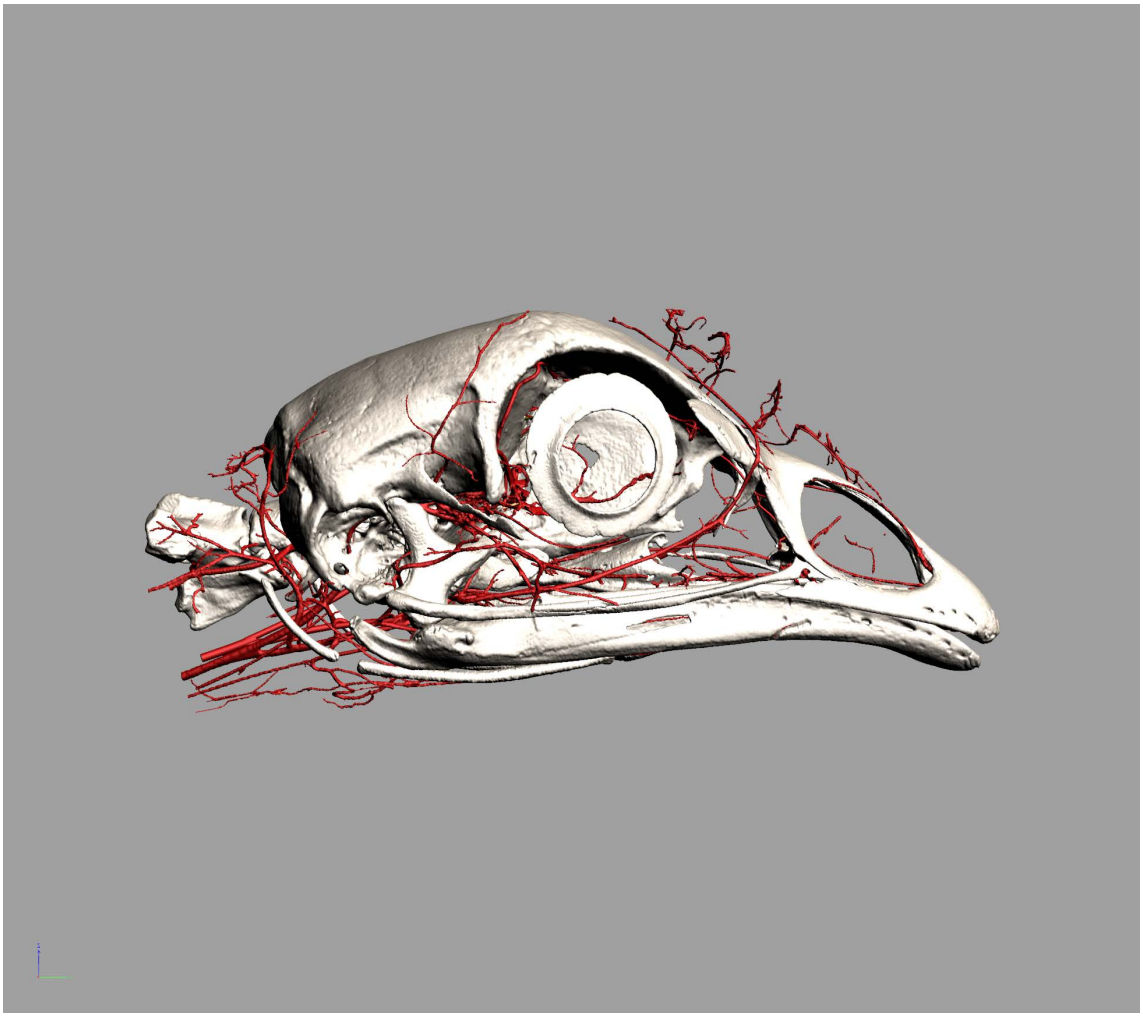

Figure 4-3D. An interactive three-dimensional model of the skull and blood vessels of an ISA Brown chicken (*Gallus gallus domesticus*). Arteries on the right side of the model are as reconstructed from a scan, while arteries on left side of the model are simplified. Of the simplified arteries, arteries external to the brain-case are coloured red, arteries inside the brain-case are green, and arteries connecting the two are blue. Arterial calibres have been exaggerated during model creation. Click on the chicken skull in the centre of the page to activate the 3D PDF. The model can then be freely rotated and zoomed, and structures can be visible, invisible, or transparent by right clicking the object. The names of structures can be found by clicking on them and reading the indicated name at left in the model tree. Below the model tree are a list of clickable views that will orient the model to some preselected positions. Opening the model in a floating window (right click, View in Floating Window) will allow the model to remain open in a separate window for reference as pages are read. See Appendix A: 3D Figure Instructions for diagrammatical instructions on navigating this figure.

Cervical region

The arteries providing the overall cephalic blood supply are the common carotid arteries, the vertebral arteries, and the spinal arteries (Figure 4-3D, Figure 4-3D / 1, Figure 4-7). The common carotid has the largest calibre of these three sources of cephalic blood. The common carotid is located superficially in the neck. As the common carotid passes the midpoint of the axis (C2) vertebrae it divides into the internal carotid and external carotid arteries. The internal carotid continues rostrally towards the back of the cranium where it enters the parabasal fossa – here the internal carotid divides into the cerebral carotid artery and the stapedial artery. The external carotid continues rostrally and meets the occipitovertebral artery.

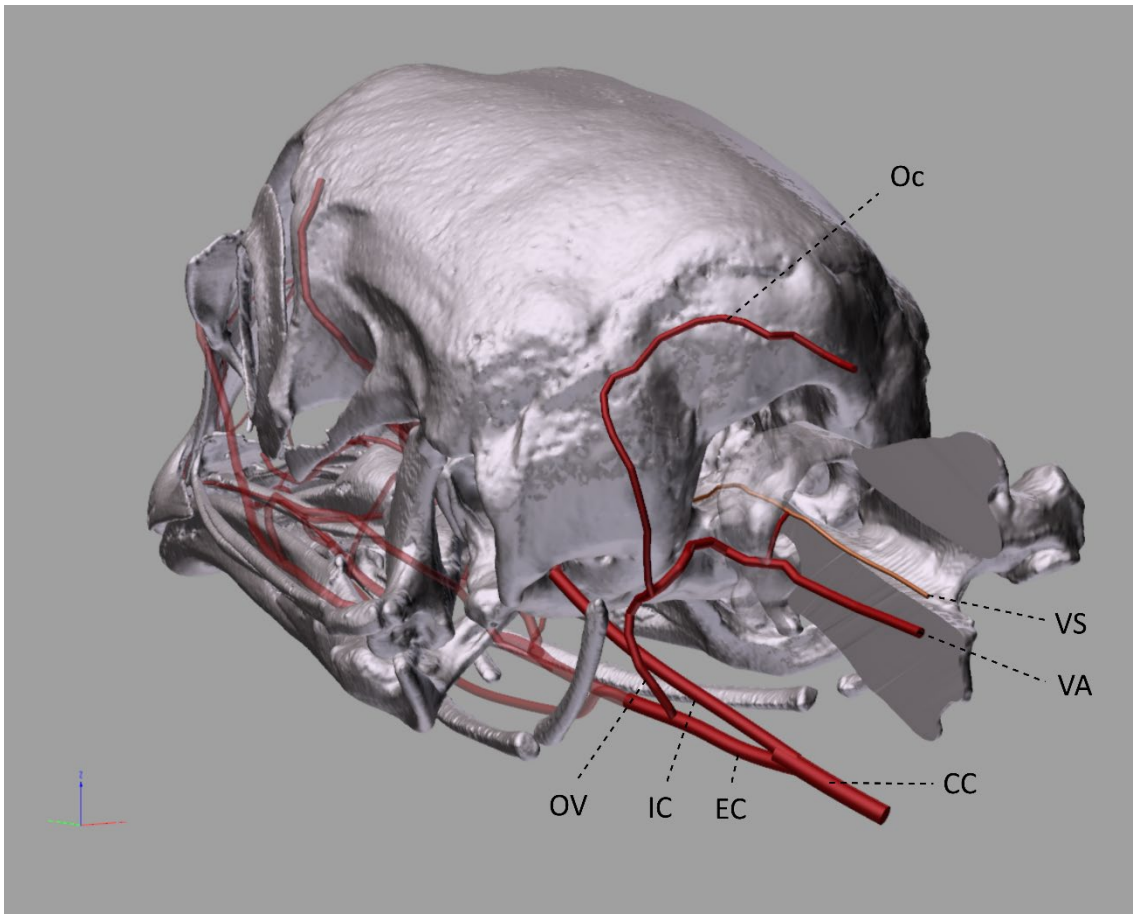

Figure 4-3D / 1. Three-dimensional model of the cephalic arteries of the domestic chicken, lateral posterior aspect with arteries of the cervical region highlighted. Here the carotid, vertebral, spinal, and related arteries can be seen in relation to each other and osseus structures. Arteries outside of the cervical region are rendered semitransparent. Arteries connecting to or in direct proximity to the braincase are coloured in orange. Arteries exterior to the braincase are coloured in red. Arteries wholly internal to the braincase are coloured in yellow. CC, common carotid artery; EC, external carotid artery; IC, internal carotid artery; Oc, occipital artery; OV, occipitovertebral artery; VA, vertebral artery; VS, ventral spinal artery.

The vertebral arteries are situated deep in the neck, passing close to the dorsolateral wall of the atlas vertebrae (C1) on its path towards the base of the cranium. A small artery is given off from the vertebral artery and passes through the intervertebral

foramen of the atlas (C1) and axis (C2) to connect to the ventral spinal artery. The vertebral artery continues further towards the base of the cranium before turning more than 90 degrees laterally and travelling outward where it anastomoses with the occipital artery, becoming the occipitovertebral artery. The occipitovertebral artery continues ventrally where it joins with the external carotid artery. The spinal arteries traverse the neck inside the vertebral foramen. The ventral spinal arteries are the first (most caudal) structures to enter the braincase, via the foramen magnum (Figure 4-3D, Figure 4-3D / 1, Figure 4-7).

Endocranial region

Five sets of arteries make the traverse between the inside and outside of the braincase. These arteries are the ventral spinal arteries, common encephalic arteries, minor temporal cerebral arteries, orbital arteries, and ethmoid arteries (Figure 4-3D, Figure 4-3D / 2, Figure 4-7).

At the parabasal fossa, the cerebral carotid artery passes into the carotid foramen and continues in this canal rostrodorsolaterally towards the midline of the head. Shortly before reaching the pituitary fossa two small arteries are given off in a rostral direction – the sphenomaxillary artery and the sphenopalatine artery. After the branching of the sphenomaxillary and the sphenopalatine arteries the cerebral carotid artery becomes the common encephalic artery, reaching the hypophyseal fossa of the pituitary fossa, entering the braincase. Upon reaching the pituitary fossa the left and right common encephalic arteries anastomose via a short lateral artery – this structure is the intercarotid anastomosis and is H-shaped. From here, the common encephalic arteries move vertically to move out of the pituitary fossa. Just ventral to the lip of the depression of the pituitary fossa the common encephalic arteries are linked to the outside of the braincase via the orbital artery which connects to the braincase through the internal ophthalmic foramen ventrolateral to the optic foramen. From here the encephalic artery continues dorsally a short distance until it has vacated the depression of the pituitary fossa. On the lip of the pituitary fossa, the common encephalic artery is connected to arteries which supply the hind, mid, and forebrain.

The principal arteries of the hindbrain are the ventral spinal arteries, the posterior ventral cerebellar arteries, and the singular basilar artery (the caudal encephalic basilar artery of Porter and Witmer (2016)). The ventral spinal arteries enter the braincase via the foramen magnum and anastomose with one another to form the singular medial ventral spinal artery. Continuing rostrally, there is a junction between the medial ventral spinal artery, the basilar artery, and the left and right posterior ventral cerebellar arteries. From its source, each posterior ventral cerebellar artery moves within a groove caudolaterally along the ventral surface of the cranial cavity until it reaches the wall of the cranial cavity directly below the floccular fossa. From here, the posterior ventral cerebellar artery moves caudodorsally into the floccular fossa and terminates at its deepest point.

The basilar artery connects the ventral spinal artery and the left and right posterior ventral cerebellar arteries to the common encephalic artery via the caudal encephalic artery, which it meets immediately caudal to the lip of the pituitary fossa. Along its path between these two junctures, the basilar artery gives off numerous small lateral branches which are rapidly unresolvable. The caudal encephalic artery is usually present on only one side of the braincase.

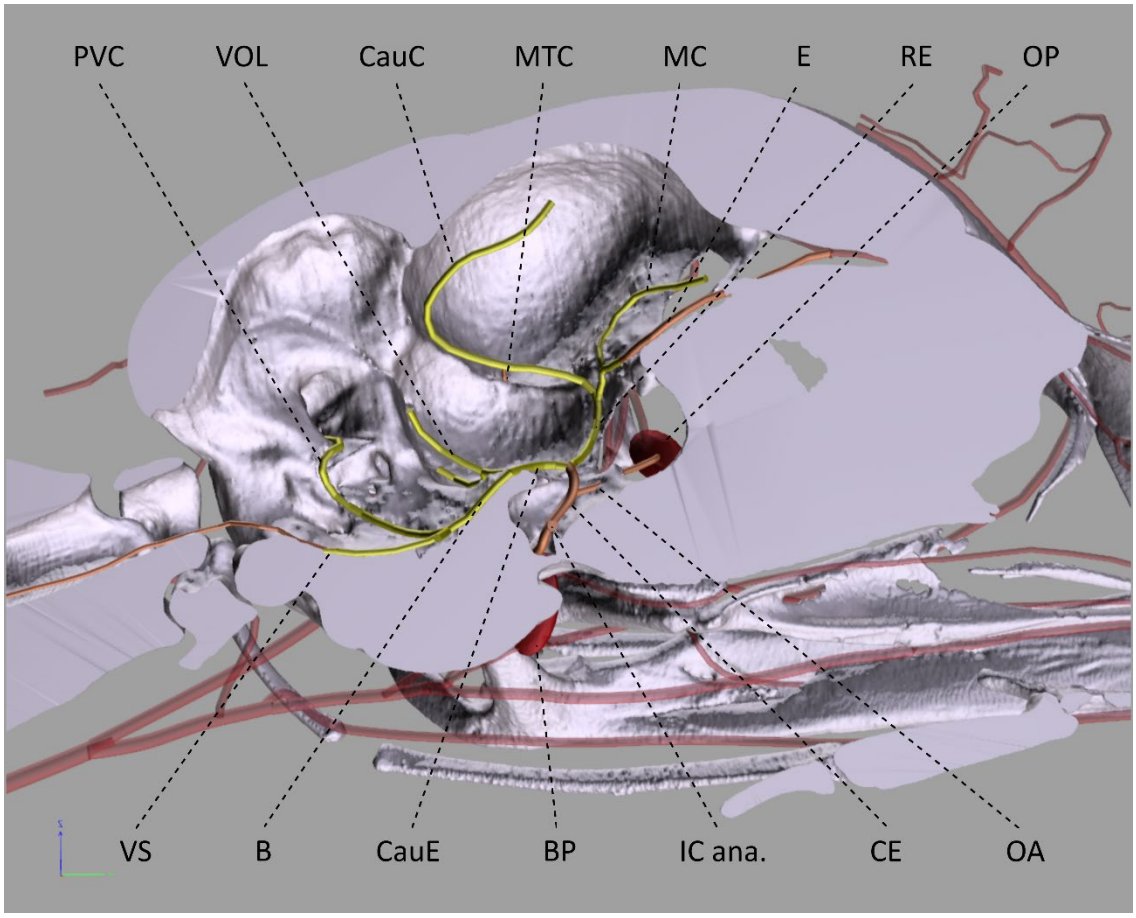

Figure 4-3D / 2. Three-dimensional model of the cephalic arteries of the domestic chicken, lateral aspect cut away at the midline with arteries of the endocranial region highlighted. Here the major arteries of the braincase can be seen in relation to each other and osseus structures. The right side of the cranium has been removed in this image and complex trabeculae structures have been removed from the cutaway surfaces for simplicity. Arteries connecting to or in direct proximity to the braincase are coloured in orange. Arteries exterior to the braincase are coloured in red. Arteries wholly internal to the braincase are coloured in yellow. B, basilar artery; BP, basisphenoid plexus; CauC, caudal cerebral artery; CauE, caudal encephalic artery; CE, common encephalic artery; E, ethmoid artery; IC ana., intercarotid anastomosis; MTC, minor temporal cerebral artery; OA, orbital artery; OP, orbital plexus; PVC, posterior ventral cerebellar artery; RE, rostral encephalic artery; VOL, ventral optic lobe artery; VS, ventral spinal artery.

The optic tecta are supplied by the ventral optic lobe artery which arises from the common encephalic artery at the same location as the caudal encephalic artery. The ventral optic lobe artery passes along the ventral floor of the fossa of the optic tectum, before dividing into a medial and lateral branch. The lateral branch follows the ventral floor

laterally past the foramen for the trigeminal nerve while the medial branch moves caudodorsally to wrap around the optic lobe.

The forebrain is supplied by the rostral encephalic artery which again arises from the common encephalic artery at the same location as the caudal encephalic artery. The rostral encephalic artery moves rostrodorsally along the internal fringe of the optic foramen, giving off the caudal cerebral artery before becoming the cerebroethmoid artery. The caudal cerebral artery is the largest artery of the forebrain, giving off many small lateral branches along its path. The caudal cerebral artery moves first caudally through the fissure between the telencephalon and optic tectum, before wrapping around on itself rostrodorsally as it moves slightly towards the midline of the brain. The cerebroethmoid artery continues dorsally from its juncture with the caudal cerebral artery and gives off the middle cerebral artery. The middle cerebral artery initially flows dorsolaterally, follows a smooth arc rostrally, and terminates near the centre of the orbitocranial fonticulus. After giving off the middle cerebral artery, the caudal cerebral artery moves gradually towards the midline of the brain and becomes ethmoid artery, traversing to the outside of the braincase via a notch in the medial edge of the orbitocranial fonticulus.

A separate artery connects to the braincase via a foramen which begins in the temporal fossa, passes mediodorsally through the squamous wall of the temporal fossa, and exits into the braincase between the telencephalon and optic tectum. This small artery, the minor temporal cerebral artery, has no resolvable connections to the other major arteries of the braincase (Figure 4-3D, Figure 4-3D / 2, Figure 4-7).

Orbital region

The principal root arterial supply to the orbit comes via the stapedial artery which branches from the internal carotid artery when it enters the parabasal fossa (Figure 4-3D, Figure 4-3D / 4, Figure 4-7). The stapedial artery continues dorsally, turns rostrally becoming the temporoorbital artery, then continues rostrally where it becomes the profundus artery shortly before reaching the ophthalmic rete (Porter and Witmer 2016).

The ophthalmic rete is a rete mirabile which is located in the temporal region caudodorsal to the orbit, spanning the region beneath the temporal fossa rostromedial of the quadrate bone. Several large arteries are associated with to the ophthalmic rete including the superficial temporal, supraorbital, and ophthalmotemporal arteries. A small artery moves rostromedially from the caudoventromedial fringe of the ophthalmic rete to communicate with the maxillary artery.

The superficial temporal artery exits the ophthalmic rete along its caudodorsal verge and travels dorsally through the temporal fossa along a tortuous route. Here it gives off the minor temporal cerebral artery which passes mediodorsally through the squamous

wall of the temporal fossa and enters into the braincase (Figure 4-3D). The superficial temporal artery continues dorsally out of the temporal fossa, towards the scalp behind the caudal fringe of the orbit.

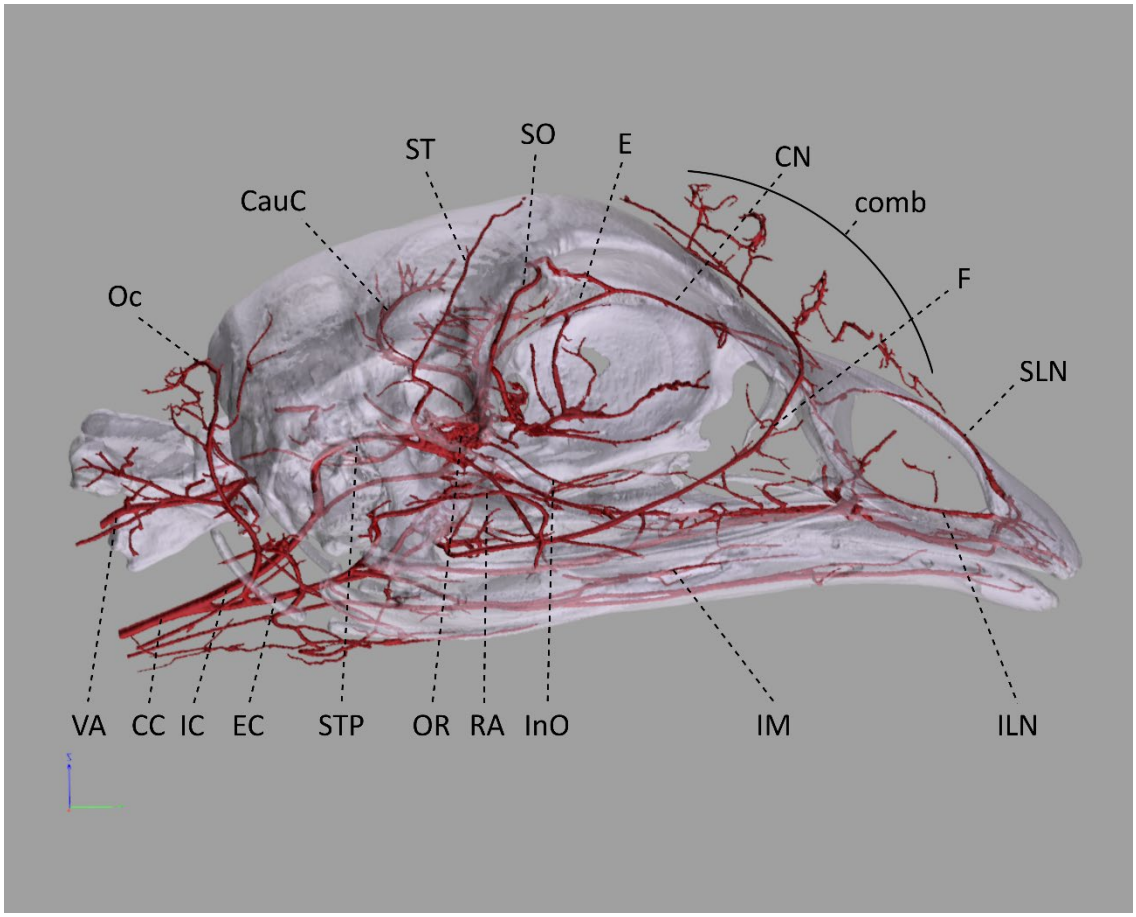

Figure 4-3D / 3. Three-dimensional model of the cephalic arteries of the domestic chicken, lateral aspect with arteries as they appeared before simplification. The cranium is rendered semitransparent. The dense mesh of arteries left of centre in the temporal fossa is the ophthalmic rete. To the right of and slightly obscured by the ophthalmic rete is the orbital plexus. The basisphenoid plexus sits beneath and slightly behind the ophthalmic rete and is obscured by the quadrate and other bones. CauC, caudal cerebral artery; CC common carotid artery; CN, common nasal artery; comb, various arteries supplying the comb; E, ethmoid artery; EC, external carotid artery; F, facial artery; IC internal carotid artery; ILN, inferior lateral nasal artery; IM, intramandibular artery; InO, infraorbital artery; Oc, occipital artery; OR, ophthalmic rete; RA, rostral auricular artery; SLN, superior lateral nasal artery; SO, supraorbital artery; ST, superficial temporal artery; STP, stapedial, temporoorbital, and profundus arteries; VA, vertebral artery.

The ophthalmotemporal artery leaves the ophthalmic rete along its rostrodorsal verge, first heading in a dorsal direction along the caudal wall of the orbit. The ophthalmotemporal artery quickly curves medially and then ventrally to connect to a small orbital plexus, distinct from the ophthalmic rete. The orbital artery exits the braincase via the internal ophthalmic foramen ventrolateral to the optic foramen and anastomoses with this orbital plexus. The ophthalmotemporal artery is the major artery of this small plexus and continues directly rostrally out of the plexus. Rostrally to the orbital plexus the ophthalmotemporal artery connects to a small artery which communicates between itself

and the ethmoid artery, outside the orbitocranial fonticulus. The ophthalmotemporal artery continues rostrally along the interorbital septum but neither gives off nor anastomoses with any further arteries of note.

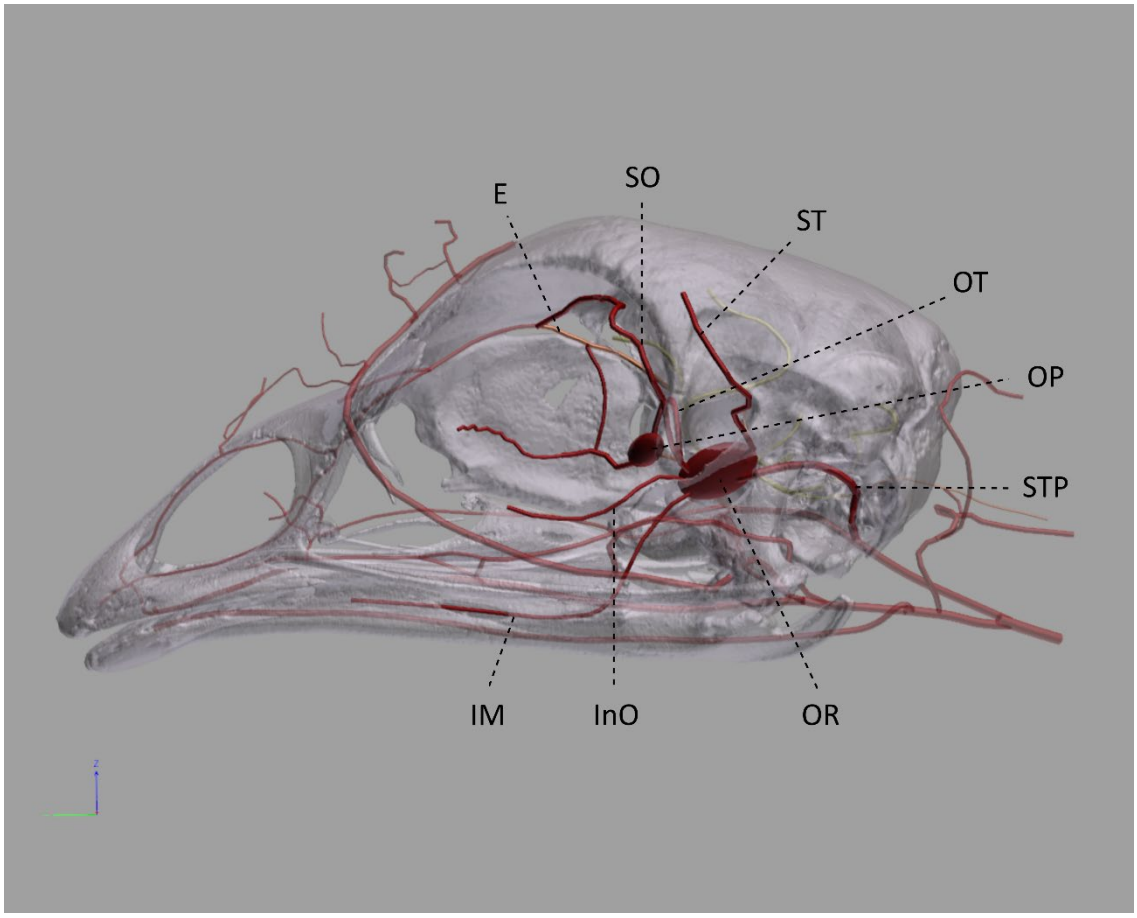

Figure 4-3D / 4. Three-dimensional model of the cephalic arteries of the domestic chicken, lateral aspect with arteries of the orbital region highlighted. The cranium and arteries outside of the orbital region are rendered semitransparent. Arteries connecting to or in direct proximity to the braincase are coloured in orange. Arteries exterior to the braincase are coloured in red. Arteries wholly internal to the braincase are coloured in yellow. The two large oblate shapes visible are the orbital plexus (left) and ophthalmic rete (right). E, ethmoid artery; IM, intramandibular artery; InO, Infraorbital artery; OP, optic plexus; OR, ophthalmic rete; OT, opthalmotemporal artery; SO, supra orbital artery; ST, superficial temporal artery; STP, stapedial, temporoorbital, and profundus arteries.

The supraorbital artery exits the ophthalmic rete along its rostrodorsal verge in the same vicinity as the ophthalmotemporal artery and traces a path dorsally along the inside edge of the orbit before turning in a rostrodorsomedial direction and anastomosing with the ethmoid artery after its exit from the braincase. After traversing from the braincase via the orbitocranial fonticulus, the ethmoid artery anastomoses with an artery connecting to the ophthalmotemporal artery. The ethmoid artery continues rostrally and anastomoses with the supraorbital artery to form the nasal artery which leaves the orbital region rostrally (Figure 4-3D, Figure 4-3D / 4, Figure 4-7).

Oral region

The root source of blood supply to the oral region comes from the external and internal carotids (Figure 4-3D, Figure 4-3D / 5). The sphenomaxillary and sphenopalatine arteries arise from the cerebral carotid artery immediately prior to the entrance of the cerebral carotid artery into the hypophyseal fossa of the pituitary fossa. The sphenomaxillary and sphenopalatine arteries depart the cerebral carotid artery and move rostrally into the floor of the orbit to course out via the caudal orbital canal (Porter and Witmer 2016), an opening of the carotid canal immediately lateral to the Eustachian foramen and directly caudal to the orbital process of the quadrate bone and the pterygoid bone. The sphenopalatine artery branches off from the cerebral carotid artery caudoventrally to the sphenomaxillary artery and connects to the anterior reach of the basisphenoid plexus. From here, the sphenopalatine travels rostrally along the parasphenoid rostrum, leaving a groove where it passes beneath the pterygoid ventrolateral to the palatobasal joint (where the parasphenoid rostrum and pterygoid connect). The sphenopalatine continues rostrally on the dorsal surface of the palatine bone. The sphenomaxillary artery branches off from the cerebral carotid artery rostrodorsally to the sphenopalatine artery and bypasses the basisphenoid plexus, moving rostrolaterally past the parasphenoid rostrum and passing dorsally over the pterygoid bone. Here the sphenomaxillary anastomoses with an artery which communicates rostromedially from the ophthalmic rete. The sphenomaxillary continues over the pterygoid, moving rostroventrolaterally, until it reaches its branching communication with the maxillary artery, lateral to the midpoint of the palatine bone.

Following the path of the external carotid rostrally from its anastomosis with the occipitovertebral, the first major branching encountered is the oromandibular and rostral auricular arteries. The oromandibular artery branches off rostrodorsolaterally before quickly curving rostroventrally and then finally turning rostrally. The oromandibular artery travels at the level of the mandible on a more or less direct rostromedial course until it reaches the mandibular symphysis. The rostral auricular artery branches rostrodorsally from the external carotid artery and passes rostrodorsolaterally beneath the tympanic cavity until coming into contact with the caudal wall of the quadrate. The rostral auricular artery then curves in a rostral direction around the quadrate and continues rostrally until reaching the tip of the postorbital process where it curves ventrally and anastomoses with the facial artery. From its juncture with the oromandibular and rostral auricular arteries, the external carotid continues rostrally as the temporomandibular artery until, reaching a point ventral to the basitemporal, it divides into the maxillary and facial arteries. From this junction there arises the temporomandibular basisphenoid artery, which moves rostromedially to connect to the basisphenoid plexus.

The facial artery stems from the temporomandibular artery. From its source, the facial artery moves rostrodorsally between the parasphenoid and the medial process of the

articular (bone of the mandible), before turning rostrolaterally under the pterygoid, crossing the rostroventral face of the quadrate bone. Upon meeting the jugal arch the facial artery turns again to flow rostrodorsally until it reaches the nasal. From here the facial artery turns caudodorsally and curves back along the frontal, moving slightly medially.

The basisphenoid plexus is a small arterial plexus which sits rostrolateral to the basisphenoid, caudolateral of the opening of the Eustachian foramen. The plexus is formed out of several small arteries which connect to one another between the mandibular and sphenopalatine arteries. This basisphenoid plexus is moderately larger than the aforementioned orbital plexus but much smaller than the ophthalmic rete. A small artery communicates between the basisphenoid plexus and the facial artery, passing ventrolaterally behind the pterygoid and meeting the facial artery on its course between the medial process of the articular (bone of the mandible) and the pterygoid.

The maxillary artery continues rostrally until it reaches a point ventral to the midpoint of the palatine bone where it has a branching communication with the sphenomaxillary. From this point the sphenomaxillary continues rostrolaterally as the lateral palatine artery, while the maxillary artery continues rostrally as the medial palatine artery. From here the artery continues until it anastomoses with its partner artery (the medial palatine anastomosis) ventral to the midpoint of the premaxillary bone to form the rostromedial palatine artery. The medial palatine artery communicates with branches of the medial nasal artery just caudal to the palatine anastomosis via the caudal dorsal nasal artery. The caudal dorsal nasal artery connects between the medial palatine and superior lateral nasal, passing rostrodorsally between the left and right palatine processes of the premaxillae.

The rostromedial palatine artery has some small lateral communications with the lateral palatine artery. The rostromedial palatine artery continues rostrally until the tip of the beak where it divides again into two small arteries which curve caudodorsally and anastomose with the inferior and superior lateral nasal arteries.

The lateral palatine artery is a continuation of the sphenomaxillary artery rostral to its communication with the maxillary. The lateral palatine artery continues rostrally until it passes ventral to the maxillary bone where it gives off a smaller rostral branch before turning rostromedially. The lateral palatine straightens to move rostrally for the remainder of its journey under the maxilla, before finally anastomosing with its smaller branch and then finally with the inferior and superior lateral nasal arteries (Figure 4-3D, Figure 4-3D / 5).

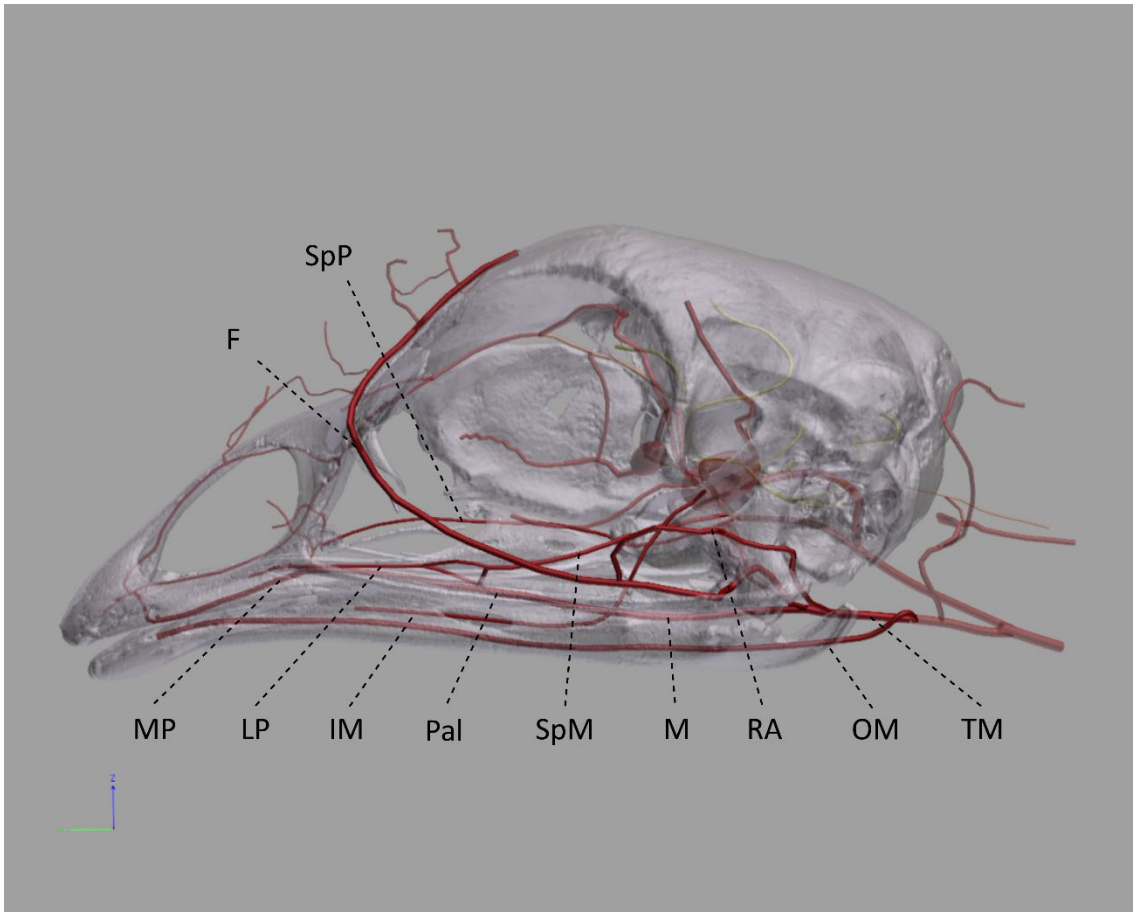

Figure 4-3D / 5. Three-dimensional model of the cephalic arteries of the domestic chicken, lateral aspect with arteries of the oral region highlighted. The cranium and arteries outside of the oral region are rendered semitransparent. Arteries connecting to or in direct proximity to the braincase are coloured in orange. Arteries exterior to the braincase are coloured in red. Arteries wholly internal to the braincase are coloured in yellow. The large oblate shape visible toward the bottom right of the figure is the basisphenoid plexus. F, facial artery; IM, intramandibular artery; LP, lateral palatine artery; M, maxillary artery; MP, medial palatine artery; OM, oromandibular artery; Pal, palatine artery; RA, rostral auricular artery; SpM, sphenomaxillary artery; SpP, sphenopalatine artery; TM, temporomandibular.

Nasal region

The nasal region of the chicken is supplied almost entirely via the ethmoid and supraorbital arteries, with potential collateral supply from the palatine arteries, and the facial artery via the comb (Figure 4-3D, Figure 4-3D / 6). The common nasal artery arises from the junction of the ethmoid and supraorbital arteries and moves in a rostral and then rostroventral direction along the ethmoid bone on the inside wall of the orbit. Slightly caudal to the juncture of the ethmoid bone and the prefrontal bone, the common nasal artery bifurcates into the medial and lateral nasal arteries. The medial nasal artery continues rostrally from this bifurcation along the ventral surface of the prefrontal bone and then nasal bone, before becoming unresolvable. The lateral nasal artery flows rostroventrolaterally along the medial side of the maxillary process of the nasal bone where it branches into the superior and inferior lateral nasal arteries.

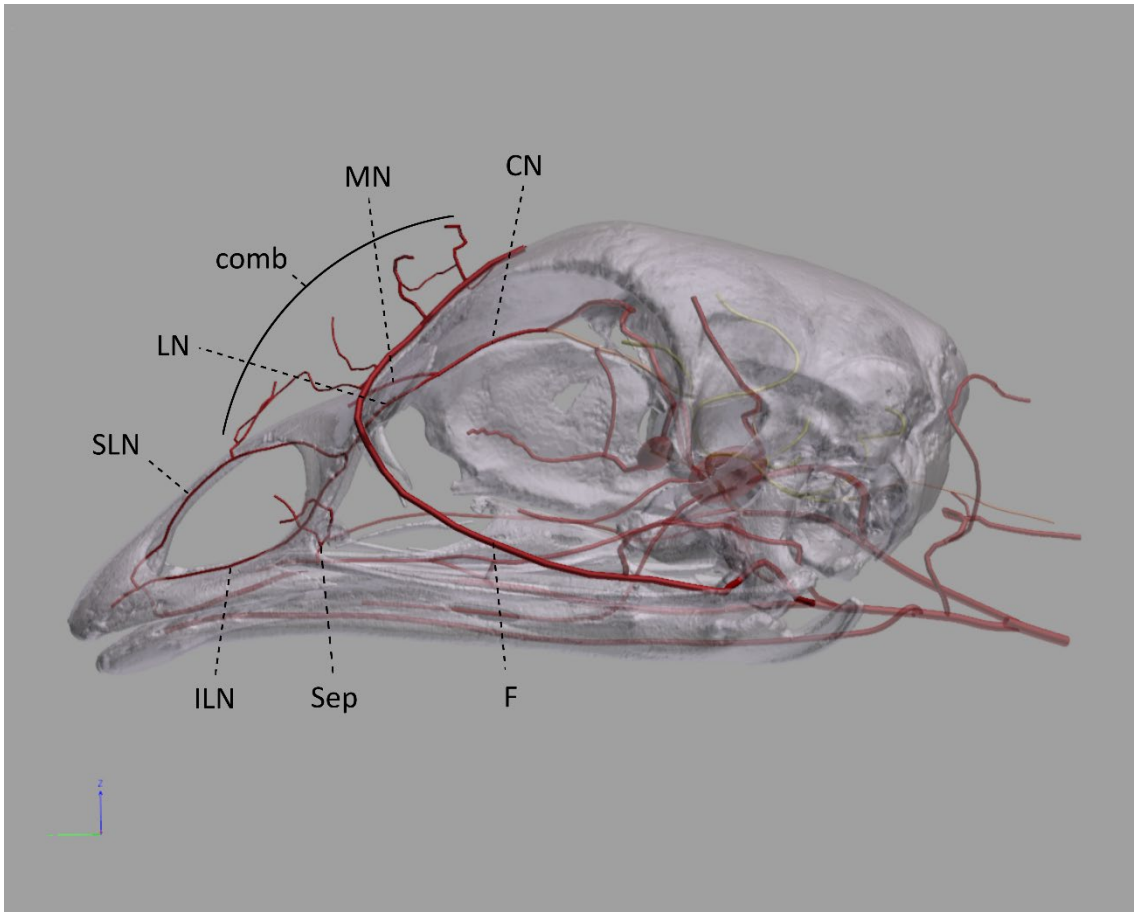

Figure 4-3D / 6. Three-dimensional model of the cephalic arteries of the domestic chicken, lateral aspect with arteries of the nasal region highlighted. The cranium and arteries outside of the nasal region are rendered semitransparent. Arteries connecting to or in direct proximity to the braincase are coloured in orange. Arteries exterior to the braincase are coloured in red. Arteries wholly internal to the braincase are coloured in yellow. CN, common nasal artery; comb, various arteries supplying the comb; F, facial artery; ILN, inferior lateral nasal artery; LN, lateral nasal artery; Mn, medial nasal artery; Sep, septum arteries; SLN, superior lateral nasal artery.

The superior lateral nasal artery moves in a rostroventral direction along the dorsal lip of the nares until reaching the rostral most extent of the opening, where it moves ventrally towards the tip of the beak. The inferior lateral nasal artery moves ventrally until it reaches the dorsal floor of the palatine process of the premaxilla, from where it flows rostrally along the ventral lip of the nares until it reaches the tip of the beak. The inferior and superior lateral nasal arteries anastomose with the palatine arteries at the tip of the beak. A widely dispersed mesh of minor arteries in the comb connects between the facial artery and the superior lateral nasal artery at the lip of the nares (Figure 4-3D, Figure 4-3D / 6).

DISCUSSION

Conservation of arterial patterns

Previous published studies report that arterial perfusion patterns of birds seem highly conserved (Porter and Witmer 2016). Here, cephalic arterial patterns in chickens were found to be largely the same to that observed in turkeys (Porter and Witmer 2016). This is not to say that cerebral perfusion patterns were identical. A number of differences are observed between turkeys (Porter and Witmer 2016), guineafowl (Crowe and Crowe 1979), ducks and chickens (Richards 1967). Many of these differences concern slight variations in arterial connections or patterns but are yet worth describing.

In the cervical region the major deviation from other avian arterial patterns concerns the occipital artery. In chickens the occipital artery is supplied by the vertebral artery and moves dorsally to supply the musculature in the back of the head and top of the neck. This is different from that seen in ducks by Sedlmayr and Witmer (2002) where the occipital artery arises from the stapedial artery, and different again from what is observed in the turkey by Porter and Witmer (2016) where the occipital arises from the external carotid artery. The functional significance of this difference is uncertain.

The endocranial region is largely the same as what has been reported elsewhere in the literature. The chicken lacks the rostral cerebral artery seen in the turkey (Porter and Witmer 2016), with the middle cerebral artery in the chicken arising from the same location as in the turkey but curving farther forward towards the front of the brain along its course, effectively fulfilling the role of both arteries. The endocranial region has generally been of greater interest than other regions so that the arterial pattern here is well established should come as no surprise.

In the orbital region, the ophthalmic rete gives off the superficial temporal artery which supplies the scalp. This is not reported in turkeys by Porter and Witmer (2016), guineafowl by Crowe and Crowe (1979), or previous studies of chickens (Richards 1967). It seems likely that this artery is present in some form in these species but is overlooked or not reported due to a focus on other areas of circulation. Further, the ethmoid artery is here reported as crossing the boundary from endocranium to exocranium. Rather than passing through an ethmoid foramen as in the turkey in Porter and Witmer (2016) here the ethmoid artery passes through more of a semi enclosed notch, which while well contained/delineated, is open to the larger orbitocranial fonticulus.

In the oral region of the helmeted guineafowl, Crowe and Crowe (1979) report the helmeted three maxillary arteries – an upper, middle, and lower – which arise in quick sequence from the external carotid artery shortly from its origin. In contrast, in the turkey Porter and Witmer (2016) observe only one maxillary artery. Here in chickens, I observe only one maxillary artery arising from the external carotid artery.

The nasal region of chickens is largely similar to that observed in turkeys (Porter and Witmer 2016). In Porter and Witmer (2016) the medial nasal artery continues its rostral course far forward enough into the beak to anastomose with the caudal ventral nasal artery. Here, the medial nasal artery halts its rostral course in the nasal region and no connection is observed to the rostral circulation. The caudal ventral nasal artery in chickens, moves in a caudodorsal direction and will be referred to as the caudal dorsal nasal artery.

The presence of retia and vascular plexuses in the cephalic circulation of birds is commonly reported in the literature. However, the arrangement of these plexuses do not align with those reported in this study. In chickens the small basisphenoid plexus lies either side of the basisphenoid bone. This structure is not reported in turkeys by Porter and Witmer (2016), guineafowl by Crowe and Crowe (1979), or previous studies of chickens (Richards 1967). This lack of presence in the literature is likely due to the size of the basisphenoid plexus. The basisphenoid plexus is a relatively small web of arteries which connect the caudal extent of the facial artery to the sphenopalatine artery. Porter and Witmer (2016) also report a large auricular rete in turkeys which does not appear to be present in the chickens of this study, perhaps due to a failure of the contrast agent to sufficiently penetrate the rostral auricular artery. The ophthalmic rete reported in a wide variety of birds (Kilgore *et al.* 1979; Bech and Midtgård 1981; Kilgore *et al.* 1981; Arad *et al.* 1987; Ninomiya 2002; Porter and Witmer 2016) was observed in chickens of this study in much the same arrangement as in turkeys (Porter and Witmer 2016). However, a small intermeshing of arteries deep in the orbit next to the orbital foramen which connects the orbital and ophthalmotemporal arteries is not reported elsewhere in the literature. This orbital plexus is the smallest significant intermeshing of arteries observed in our specimens. Further investigation into the relationship between these plexuses and the venous circulation would help inform on the how these structures relate to one another.

Endocranial blood supply and circulation

The core concern of this study was determining the pattern of blood circulation which supplies the chicken brain. To that end – supply is complex. Five sets of arteries make the traverse between the inside and outside of the braincase. These arteries are the ventral spinal arteries, common encephalic arteries, minor temporal cerebral arteries, orbital arteries, and ethmoid arteries (Figure 4-3D). However, in the assessment endocranial blood supply the direction of blood flow is more pertinent than just knowing which arteries traverse the braincase.

The cerebral carotid arteries principally supply the mid brain and forebrain via the encephalic, ventral optic lobe, cerebral, and ethmoid arteries. Based entirely upon the orientation of the arteries, the ethmoid and orbital arteries appear to flow *out* of the brain, rostrally towards the beak. The directionality of flow in these arteries has recently been

a source of contention in the literature, with many past authors suggesting they form part of a collateral source of flow into the brain (Richards 1970; Kilgore *et al.* 1976; Kilgore *et al.* 1979; Midtgård 1984a; Midtgård 1984b; Arad *et al.* 1987; Arad 1990), while more recently it has been asserted that this would involve flow against the physiological pressures generated by the heart (Porter and Witmer 2016).

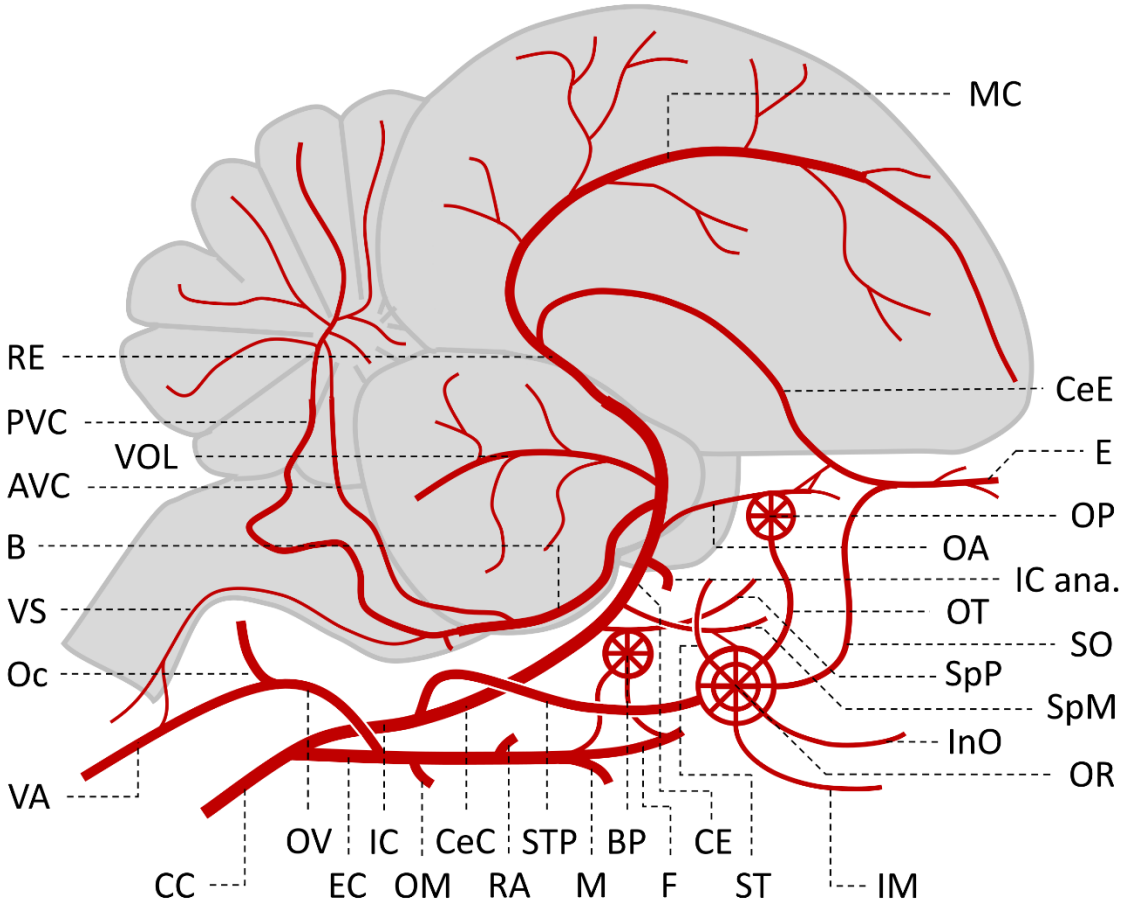

Figure 4-7. Simplified diagram illustrating the arrangement of the major arteries of the chicken head with respect to the brain. The principal source of blood flow to the brain comes via the cerebral carotid arteries, with a small amount supplied by the spinal arteries, and an indeterminate contribution from collateral flows via the complex arrangement of vessels surrounding the braincase. Unlike primates, the vertebral arteries have no major communications with the brain, with only a small contribution via an anastomosis with the ventral spinal arteries. Some extracranial arteries leaving to supply other regions of the head are not depicted. Not all arteries of the brain are depicted. AVC, anterior ventral cerebellar artery; B, basilar artery; BP, basisphenoid plexus ; CC, common carotid artery; CE, common encephalic artery; CeC, cerebral carotid artery; CeE, cerebroethmoid artery; E, ethmoid artery; EC, external carotid artery; F, facial artery; IC, internal carotid artery; IC ana., intercarotid anastomosis ; IM, intramandibular artery; InO, infraorbital artery; M, maxillary artery; MC, middle cerebral artery; OA, orbital artery; Oc, occipital artery; OM, oromandibular artery; OP, orbital plexus; OR, ophthalmic rete; OT, opthalmotemporal artery; OV, occipitovertebral artery; PVC, posterior ventral cerebellar artery; RA, rostral auricular artery; RE, rostral encephalic artery; SO, supra orbital artery; SpM, sphenomaxillary artery; SpP, sphenopalatine artery; ST, superficial temporal artery; STP, stapedial, temporoorbital, and profundus arteries; VA, vertebral artery; VOL, ventral optic lobe artery; VS, ventral spinal artery.

Blood supply to the hindbrain must also be sourced from the carotid arteries as the calibres of the ventral spinal arteries are small relative to the basilar artery and posterior ventral cerebellar arteries. However, it is difficult to comment further on what proportion of blood flow to the hind brain is supplied by each source. Hence, although the arteries of the hindbrain are described here in a caudal – rostral direction, it may be more accurate to describe them in reverse; caudal encephalic artery to basilar artery, to posterior ventral cerebellar arteries and medial ventral spinal artery (Figure 4-3D, Figure 4-3D / 2, Figure 4-7).

No major arteries appear to connect the external carotid artery to the arteries supplying the braincase. The vertebral artery – a supply of endocranial blood in other amniotes – anastomoses with the occipital artery (becoming the occipitovertebral artery) which then connects to the external carotid artery. The ventral spinals and vertebral arteries have a small communication before the ventral spinals reach the foramen magnum (Figure 4-3D, Figure 4-3D / 1, Figure 4-7). Aside from this, small communication, the vertebral arteries do not directly supply the braincase.

Following the path of the external carotid rostrally, no major arteries appear to connect to the arteries supplying the braincase. All arteries are oriented directionally indicating that the blood would flow rostrally towards the beak rather than dorsally towards the braincase (Figure 4-3D, Figure 4-7). Only two small branches along the perceived direction of flow approach the vicinity of the braincase – the temporomandibular basisphenoid artery, and the basisphenoid plexus facial communicating artery – but again flow appears oriented against the possibility of their providing perfusion to the braincase (Figure 4-3D). The temporomandibular basisphenoid artery and the basisphenoid plexus facial communicating artery connect to the basisphenoid plexus which lies either side of the basisphenoid bone. The basisphenoid plexus is connected to the sphenopalatine artery millimetres rostral of the sphenopalatine's diversion from the cerebral carotid artery. Supply to the braincase by this route would again require blood flow in a caudal direction (and from a smaller calibre artery to a larger calibre artery) (Figure 4-3D, Figure 4-7).

The presence of what is here termed the minor temporal cerebral artery has not previously been reported in the literature – however the foramina through which it passes is present in scans of other birds including all Galliformes examined (mallee fowl, king quail, stubble quail, chicken, peafowl, turkey), and some Anseriformes (Eurasian teal, grey teal, Australian shoveler, mute swan, teals, shovelers, some swans), and some passeriformes (there seems to be two similar foramina in the crimson chat, *Epthianura tricolor*) (pers. obs., scans from Chapter 3). Further, the foramen of the minor temporal cerebral artery is often present in depictions in other papers, though never named (Baumel 1993; Porter and Witmer 2016). The foramen of the minor temporal cerebral artery is absent in Palaeognathae, Accipitriformes, Falconiformes, Psittaciformes, and

many Passeriformes) (pers. obs., scans from Chapter 3). Functionally, the minor temporal cerebral artery would appear to be of negligible significance. Here the minor temporal cerebral artery has no resolvable connections to the other major arteries of the braincase, although I suspect connections do exist and are simply of too small a calibre to be adequately perfused by the contrast media used. Any contribution to the cerebral blood supply must be miniscule due to the arteries small calibre (Figure 4-3D), however, the prevalence of the foramina of the minor temporal cerebral artery in other aves suggests that there may be some significance to the structure. Further studies may shed light on this question.

Contrast perfusion quality

One notable deficiency in this study was identified during the production of the three-dimensional arterial map, in that there was an inability to 'disentangle' individual arteries in arterial plexuses. For instance, Porter and Witmer (2016) list the supraorbital artery as stemming from the profundus artery, the major artery of the ophthalmic rete. Here, I was unable to detach the profundus within the rete and so by an abundance of caution simply consider the supraorbital artery to have stemmed from somewhere within the rete itself, with the profundus artery a constituent artery of that rete (Figure 4-3D, Figure 4-3D / 3).

In some regions perfusion was superb, while in other regions perfusion was of much lower quality. Porter and Witmer (2016) describe many smaller arteries branching from the supraorbital artery which perforate the frontal bone to supply the skin. These arteries are surely present in the specimens of this study but are unresolved in imaging and segmentations. Here perfusion of the nasal region produced fewer resolvable arteries than observed by Porter and Witmer (2016), and hence I present fewer vessels and relationships in this model. Of the spinal arteries, the ventral spinal arteries are the only ones reported here, likely the only ones with sufficient calibre to be perfused with the contrast material. Further, I suspect the minor temporal cerebral artery has connections to the other major arteries of the braincase which are simply of too small a calibre to be adequately perfused by the contrast media used.

Similarly, the auricular rete (postorbital plexus) is a significant rete reported sitting lateral to the body of the quadrate, being supplied by the rostral auricular artery in Galliformes; Porter and Witmer (2016) describe the auricular rete in Turkeys, and Sedlmayr (2002) describes this structure as the postorbital plexus in their paper on chickens. However, despite this I did not observe the auricular rete/postorbital plexus arising from the rostral auricular artery in specimens in this study (Figure 4-3D, Figure 4-3D / 3, Figure 4-7). Once again, this may be due to a failure of the contrast to perfuse the area.

CONCLUSION

It seems like the cerebral carotid and the common encephalic artery are the major source of blood flow to the braincase, with small secondary and negligible tertiary supplies from the ventral spinal arteries and the minor temporal cerebral artery respectively. The ethmoid and orbital arteries may play a role in supplying collateral blood supply but based upon their orientations direct supply to the braincase seems odd as blood supplied via this route would have to travel much further towards the beak before having a chance of entering the braincase. The ethmoid and orbital arteries have been suggested as an important source of collateral flow which is indeed a possibility, but here mapping of the blood flow pattern has encountered the same issue as other studies in that the map can demonstrate the position and orientation of the arteries but not direction of flow. Hence, this arterial map is otherwise inconclusive regarding the role of these arteries in supplying the braincase during normal circulation. Studies of blood flow are required to answer this question.

The major supply to the braincase ultimately comes from a branch of the common carotid artery – the cerebral carotid artery. Secondary supply comes from the ventral spinal artery. Three other arteries connect to the inside of the braincase – these are the ethmoid, orbital, and minor temporal cerebral artery. The minor temporal cerebral artery likely heads into the braincase but is minuscule and would provide minuscule supply. The paths of the ethmoid and orbital arteries continue out of the brain, rostrally towards the beak.

The discovery of the temporal cerebral artery after more than 175 years of study in this area illustrates the need for further, modern studies in this field. The prevalence of the foramina of the minor temporal cerebral artery in a large number of other avian taxa suggests that there may be some functional role for the structure. Further studies should aim to improve upon the pressurised contrast perfusion technique. This method paired with Porter and Witmer's (2016) differential contrast dual vascular injection (DCDVI) to identify and attempt to quantify venous drainage could allow a complete picture of individual vessels contributions to endocranial flow.

CHAPTER 5

CEREBRAL BLOOD FLOW RATE IN THE DOMESTIC FOWL (*GALLUS GALLUS DOMESTICUS)*

ABSTRACT

Recently, avian and mammalian brains have been recognised as sharing many structural and cognitive qualities and capacities. The domestic chicken (*Gallus gallus domesticus*) is a model organism for avian research. This chapter aims to determine the metabolic rate of the brain of chickens in relation to sex and life stage. Measurement of cerebral metabolism relies upon calculation or estimation of cerebral perfusion rate. Three methods are used for cerebral perfusion quantification: 1) The microsphere perfusion method utilises fluorescently tagged microspheres injected into the left ventricle of anaesthetised chickens to quantify regional cerebral perfusion rates; 2) The foramen dimension measurement technique estimates whole brain perfusion through the examination of the dimensions of osteoforamina through which cerebral feeder arteries pass; 3) Vascular contrast perfusion allows three-dimensional reconstruction of the course of an animal's vasculature based upon the filled lumen volumes following the same principles as vascular corrosion casting and is here performed under physiological pressures to obtain measurements of arterial lumens. These three methods were applied to different sexes in three groups of chicken life stages: adolescent hens before point of lay, mature hens after point of lay, and mature roosters. Perfusion rates obtained from microsphere perfusion matched those obtained from foramen measurement calculations in immature hens and roosters, but not in laying hens where the microsphere perfusion technique resulted in statistically greater values for blood flow rate for the laying hens. This divergence relates to a higher volumetric perfusion rate in the forebrain of laying hens than either roosters or immature hens. I hypothesise that this is due to an increased role of collateral cerebral circulation in mature laying hens, which is not seen in roosters or immature hens. Regardless of the routes of perfusion, the role and triggers of cerebral metabolic increase at point-of-lay are as yet poorly understood. Adult hens take on the responsibilities of raising chicks, which requires a significant change in cognitive behaviour. I suggest that the capacity for this change in cognitive behaviour seems to be established at sexual maturity rather than upon motherhood, resulting in hens that have reached point of lay receiving a higher level of blood flow than either immature hens or roosters of a similar age. I conclude that while arteries perfused with contrast media underestimate flow rate and thus is not recommended, microsphere perfusion supports the use of foramina measurements as a method of estimation of cerebral metabolism as measurements correlate in most cases.

INTRODUCTION

Although long thought to be structurally and cognitively dissimilar, more recently avian and mammalian brains have been recognised as sharing many qualities and capacities. Numerous studies have demonstrated the similarities between the complexities of intelligence in different groups of animals including mammals, birds, and fish (Emery 2006; Brown 2015). The often-stark differences in physiology and behaviour between different animal groups, due to evolutionary histories and adaptations, make direct cognitive comparisons difficult. This investigation involves measurement of brain blood flow rates in chickens (*Gallus gallus domesticus*), which should reflect brain metabolic rates and shed light on possible cognitive differences between birds and mammals.

The brain is a metabolically expensive organ and the cost of building and maintaining a brain increases with brain size and composition. For example, in terms of tissue-mass-specific measurements, the metabolic rate of the brain in a resting mammal is about two-thirds of the rates of the most active organs (heart, liver, kidney) and more than 10-times higher than that of the rest of the body (Wang *et al.* 2001). The metabolic rate of the brain is thought to be proportional to number of neurons and related to neural activity (Attwell and Laughlin 2001; Herculano-Houzel 2011a). However, synapses require energy to maintain ion gradients across cell membranes and to synthesise neurochemical transmitters (Harris *et al.* 2012). Brain metabolism is not uniform across all structures; some brain structures have higher energy requirements than others (Karbowski 2007). In particular, synapse-rich grey matter has an approximately 80 times higher density of synapses than white matter (Harris and Attwell 2012) and four times greater volume-specific energy use (Harris *et al.* 2012). Continuous cerebral perfusion is required because of the brains inability to store glucose or glycogen and its aerobic nature (Weisbecker and Goswami 2010; Karbowski 2011).

Studies of mammals have demonstrated that blood flow rates in the internal carotid arteries correlate with the levels of brain metabolism as these arteries supply a large proportion the blood required by the brain. Cerebral blood flow via the internal carotid arteries is considered proportional to the metabolic rate of the cerebral cortex (Hawkins *et al.* 1983; Lou *et al.* 1987; Changizi 2001; Turnquist and Minugh-Purvis 2012). The rate of blood supply to the brain and the brains metabolic rate are intrinsically linked due to simple rules of supply and demand, demonstrated by similar allometric exponents for brain oxygen consumption rate, glucose utilisation rate and cerebral perfusion rate in relation to brain volume. In mammals the rate of oxygen uptake and glucose metabolism of the brain scale with brain volume with matching exponents of 0.86 (Karbowski 2007), while cortical blood flow rate and cortical brain volume varies with exponents between 0.81 and 0.87 (Karbowski 2011). These exponents show that there is a close correlation between brain metabolic rate and blood flow rate, and ergo, measurement of one of these variables can provide information on the other. The proportionality

between cerebral perfusion and metabolic rate indicates that the extraction of oxygen from the cerebral blood is constant, and thus it is not necessary to know variables associated with O_2 delivery in order to make conclusions on brain metabolism based on blood flow measurements. However, the regional distribution of this perfusion is important to consider, as the metabolic requirements of the brains sensory systems may effectively offset the metabolism used for higher processing and cognition, obfuscating how much energy is actually 'invested' in intelligence.

Measurement of cerebral blood flow rates and indeed cerebral metabolism in living organisms has proved to be technically difficult and often invasive. Beginning in 2012 a methodology was developed allowing calculation of the rate of blood flow through arteries based upon the application of haemodynamic principles to measurements of osteoforamina (Seymour *et al.* 2012). This approach – the foramen dimension measurement technique – can be applied to allow calculation of whole brain perfusion through the examination of the dimensions of osteoforamina through which cerebral feeder arteries pass (Seymour *et al.* 2012; Allan *et al.* 2014; Seymour *et al.* 2015; Seymour *et al.* 2016; Hu *et al.* 2019). This approach has since been used in the study of cerebral blood flow of haplorrhine primates, diprotodont marsupials, and hominins (Seymour *et al.* 2015; Seymour *et al.* 2016; Boyer and Harrington 2018; Seymour *et al.* 2019a), as well as femoral blood flow of mammals, birds, reptiles, and dinosaurs (Seymour *et al.* 2012; Allan *et al.* 2014; Hu *et al.* 2019). For best practices see Hu *et al.* (2020).

Chickens possess a number of qualities indicative of a greater level of intelligence than has traditionally been recognised (Marino 2017). Existing studies of chicken cognition are primarily focused around ethology and physiology rather than metabolism, in part due to the difficult and often destructive nature of performing focused metabolic studies. Few studies from the literature have measured or reported regional cerebral blood flow rates in chickens. Part of the difficulty in determining chicken cerebral blood flow rates can be traced to the lack of adequate understanding of cerebral blood flow patterns in chickens and Aves more broadly. Despite the common use of birds as models, the difference between avian vasculature and mammalian vasculature is under-appreciated due to under-documentation. With a few vital exceptions (Holliday *et al.* 2006; Porter and Witmer 2016), there is little modern material satisfactorily describing the cephalic and neuroanatomical vasculature of birds (Verduzco Mendoza *et al.* 2009).

In Chapter 4 of this thesis, I investigated the anatomy of chicken cephalic and encephalic blood supply. In the domestic fowl blood reaches the head via the paired common carotid, vertebral, and spinal arteries. The common carotids divide into its internal and external portions, with the external carotids continuing rostrally while the internal carotid moves dorsally towards the carotid foramen in the parabasal fossa. Immediately prior to its entry into the carotid foramen the internal carotid artery gives off the external ophthalmic artery which passes outward around the tympanic cavity and towards

the orbit (Richards 1967). Upon its entry into the carotid foramen the internal carotid becomes the cerebral carotid. Here the cerebral carotid moves rostrally though the cranial carotid canal. Within the cranial carotid canal the cerebral carotid gives off the sphenopalatine and sphenomaxillary arteries which arise from the cerebral carotid caudal to the hypophyseal fossa. The cerebral carotids move rostrally through the carotid canals and anastomose in a type H pattern shortly before reaching the sella turcica and the pituitary gland (Richards 1967; Richards 1970). Upon exiting the carotid canals, the cerebral carotids become the common encephalic arteries, which quickly give rise to both the basilar artery and internal ophthalmic arteries. In the domestic fowl the circle of Willis is incomplete such that the anterior cerebral arteries do not unite, and the basilar artery usually originates more from one side of the carotid anastomoses than the other (Richards 1967; Richards 1970). The basilar artery is further supplied by the spinal arteries which enter the braincase along with the spinal cord. In the domestic fowl the vertebral arteries have no major communications with the brain, instead anastomosing with the occipital arteries (Figure 4-7) (Richards 1967; Richards 1970).

The brain receives blood directly from the cerebral carotid artery, however, several authors have suggested the brain also receives blood indirectly via extensive extracranial-cerebral anastomoses (Richards 1967; Richards 1970; Midtgård 1984a; Midtgård 1984b; Arad *et al.* 1987; Arad 1990). In the temporal region caudodorsal to the orbit exists a rete mirabile called the ophthalmic rete. This complex mesh of arteries has several connections from the interior and exterior of the braincase; in particular the external ophthalmic, orbital, and ethmoid arteries all connect with the rete mirabile. It has been frequently suggested that a further supply of cerebral blood flow comes as an indeterminate contribution from collateral flows via the ophthalmic rete, although the actual use of these pathways has been disputed in more recent literature (Porter and Witmer 2016). Arterial blood flow from the ophthalmic rete towards the brain would require retrograde flow via the ethmoid and orbital arteries; in order for blood to flow from the rete into the endocranial cavity there would need to be a pressure greater than the pressure of the cerebral carotid artery, despite dropping pressures across the rete mirabile (Figure 4-7) (Porter and Witmer 2016).

This chapter aims to determine the perfusion rate of the brain of the chicken in relation to sex and life stage. Three methods are used for cerebral perfusion quantification. These techniques are the microsphere perfusion method, the foramen dimension measurement technique, and the pressurised vascular contrast perfusion method. The microsphere perfusion method has been used to calculate regional blood flow rates in different tissues based upon the application of the indicator dilution method (Anetzberger *et al.* 2004). Here I utilise fluorescently tagged microspheres injected into the left ventricle to quantify regional cerebral perfusion rates. The foramen dimension measurement technique estimates whole brain perfusion through the examination of the dimensions of osteoforamina through which cerebral feeder arteries pass. Vascular contrast

perfusion allows three-dimensional reconstruction of the course of an animal's vasculature based upon the filled lumen volumes following the same principles as vascular corrosion casting. I hypothesise that perfusion of vascular contrasts under physiological pressure would allow direct measurement of vascular lumens and, via these measurements, calculation of cerebral perfusion rates.

METHODS

Animals

This study examined cerebral blood flow rates in Isa Brown domestic layer chickens. The Isa Brown breed is a high egg production sex-linked crossbreed commonly used in both private and commercial egg production. Thirty-eight domestic chickens with body masses ranging from 883 g to 2659 g were used for the study. Body masses were determined to a resolution of 1 g using a 16 kg capacity bench scale (Sartorius QS16, Sartorius, Germany). Chickens were obtained locally from grain and fodder stores in metropolitan Adelaide, South Australia. The animals were housed in an indoor holding facility under a 14 to 16 h daylight cycle with a constant temperature of 23°C. Chickens had access to tap water and food pellets *ad libitum* (Red Hen premium layer and breeder pellets, Laucke Mills, Daveyston, South Australia, Australia). Animals were divided into three distinct groupings for this study: hens before point of lay (16 to 24 weeks old), hens after point of lay (24 to 32 weeks old) and roosters (22 to 32 weeks old). Half of each group was used for microsphere analysis and the other half for contrast perfusion and carotid foramen measurement. Classification as before or after point of lay was determined by monitoring of egg laying and confirmed during final dissection based upon the development of the reproductive organs. Birds were anaesthetised by intramuscular injection of a mixture of ketamine (40 µg kg^{-1}) and xylazine (4 µg kg^{-1}). Euthanasia was carried out humanely via intravenous administration of ketamine and xylazine. Approval to euthanise animals for research-related purposes was provided by the University of Adelaide Animal Ethics Committee (S-2017-058). Specimens in this section of the study were shared with another study (Hu 2021; Hu *et al.* 2022), and with Chapter 5 of this thesis.

Fluorescent microsphere infusion technique

The fluorescent microsphere infusion technique uses injected microspheres to determine the proportion of blood flow leaving the heart and reaching a particular tissue of interest. This technique is based on the principle that microspheres injected into the left ventricle will become homogeneously distributed in the arterial blood leaving the heart (Anetzberger *et al.* 2004; Anetzberger and Birkenmaier 2016). These microspheres flow through the large arteries of the body and become lodged in the arteriolar or capillary system, with the number of spheres lodged in a tissue being proportional to its blood

flow. During the microsphere perfusion the arterial blood is sampled using a Harvard pump with a known withdrawal rate, and the respective number of microspheres in this reference sample can be compared with the number of microspheres in a tissue sample to determine an absolute flow rate according to the equation (Anetzberger and Birkenmaier 2016);

$$\textit{Blood flow in tissue sample } (cm^3\ s^{-1}) = \frac{\textit{Harvard Pump Withdrawal Rate } (cm^3\ s^{-1}) \times \textit{Number of MS in tissue sample}}{\textit{Number of MS in reference sample}}$$

Equation 10 – Microsphere deposition and blood flow.

The number of spheres deposited in a tissue is measured indirectly by quantification of an indicator labelling the spheres (Serrat 2009). In this study, green polystyrene fluorescent (450/480) 15 µm microspheres (Thermo Fisher Scientific, Oregon) were used to gauge blood flow to the brain in a group of anaesthetised chickens.

The measurement of cerebral blood flow using perfused microspheres requires surgical intervention to inject microspheres into the left ventricle of the heart and to obtain arterial blood samples at a measured rate to calibrate flow rate to selected organs. Animals were placed under anaesthesia, and an incision was made into the ventral side of the left upper wing the using the basilic vein as a guide. The biceps brachii muscle was gently separated from the humerus to allow access to the brachial artery which was then cannulated with heparinised vinyl tubing (Dural Plastics & Engineering, New South Wales, Australia, Cat. No. SV. 31, od 0.8 mm, id 0.5 mm). Following cannulation of the brachial artery, an incision was made into the left side of the chest and the fibres of the left pectoralis major muscle were separated to expose the first three ribs and the edge of the breastbone. The intercostal muscles between the second and third rib were cut, and the ribs were separated using a self-retaining Weitlaner retractor, revealing the pericardium.

A 20-gauge Venocan Pencil style IV catheter (Kruuse, Denmark, Cat. No. 121931) connected to heparinised vinyl tubing was inserted into the left ventricle through the pericardium and ventricle wall. This needle was connected to a Grass Instruments 79D EEG Preamplifier & Polygraph Data Recording System (Grass Instruments, Quincy, Massachusetts, United States) calibrated with a water manometer to provide a blood pressure readout. Blood pressure values of between 50 mmHg and 150 mmHg were recorded, indicating correct placement of the needle inside the left ventricle. A 5 ml syringe-pump (Harvard Universal Infusion Pump, Harvard Apparatus, Kent, United Kingdom), modified for withdrawal, was connected to the cannulated brachial artery (Figure 5-1). This pump functioned as a reference organ by withdrawing a sample of blood at a rate of 0.46 or 0.283 ml min^{-1} as the microspheres entered circulation and became lodged in the tissues. A 1.5 ml volume of uniformly mixed microsphere suspension was injected into the left ventricle via the catheter tubing over a period of 20 s, with any remaining trace microspheres immediately rinsed into circulation with saline solution (Figure 5-1).

Euthanasia was performed 2.5 min after the completion of the microsphere injection and the bird was autopsied to verify correct placement of the cardiac catheter.

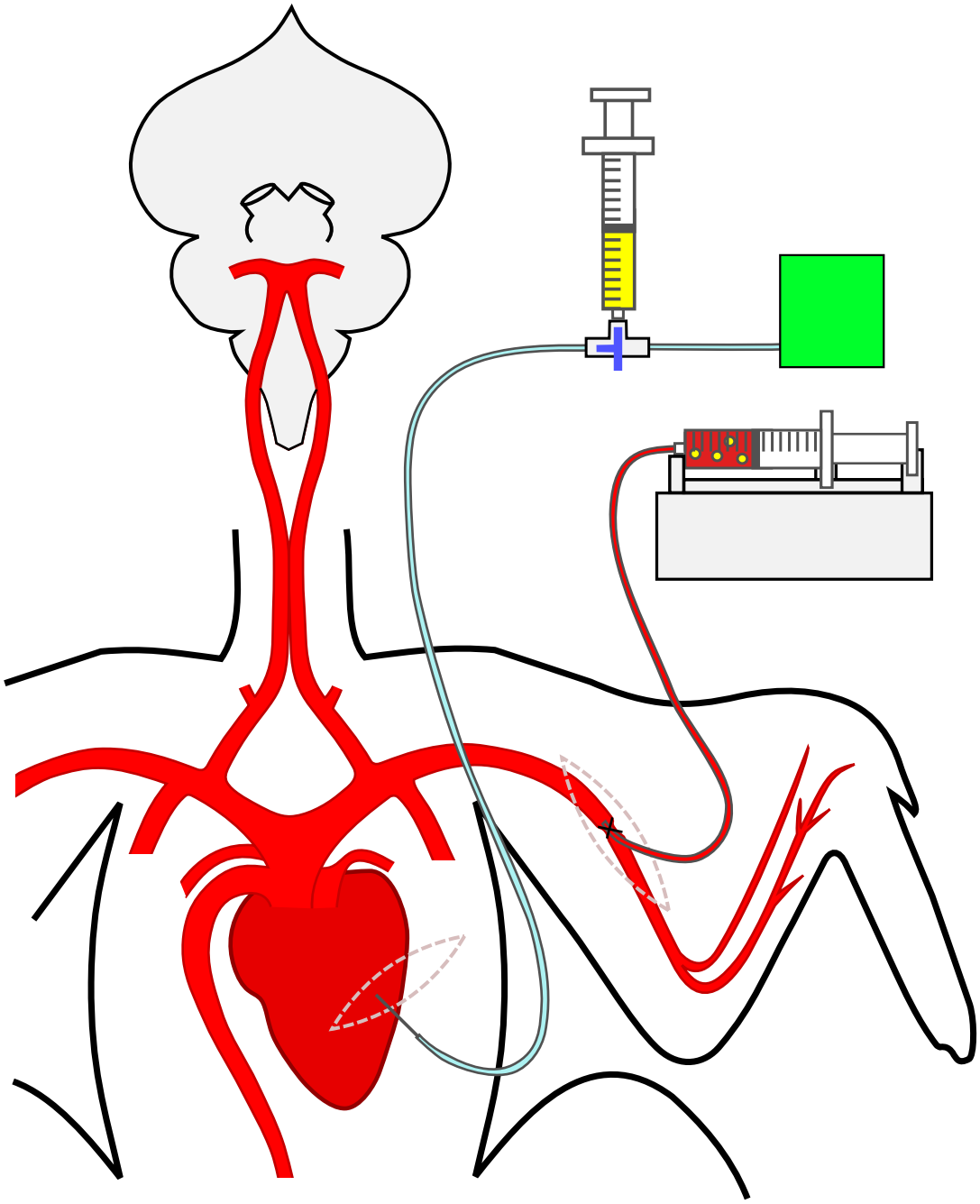

Figure 5-1. A simplified diagram of the surgical procedure involved in the microsphere perfusion approach. Two sites are incised in this technique, at the locations denoted by the dotted lines. The green box represents the Preamplifier & Polygraph Data Recording System used to verify correct placement of the cardiac puncture needle in the left ventricle. Once the cardiac needle is in place the three-way stopcock is switched to allow the microspheres to be injected. Microspheres circulate and are deposited into the body's tissues, including the brain. The cannulated brachial artery is connected to a syringe mounted on a Harvard pump which withdraws a reference blood sample.

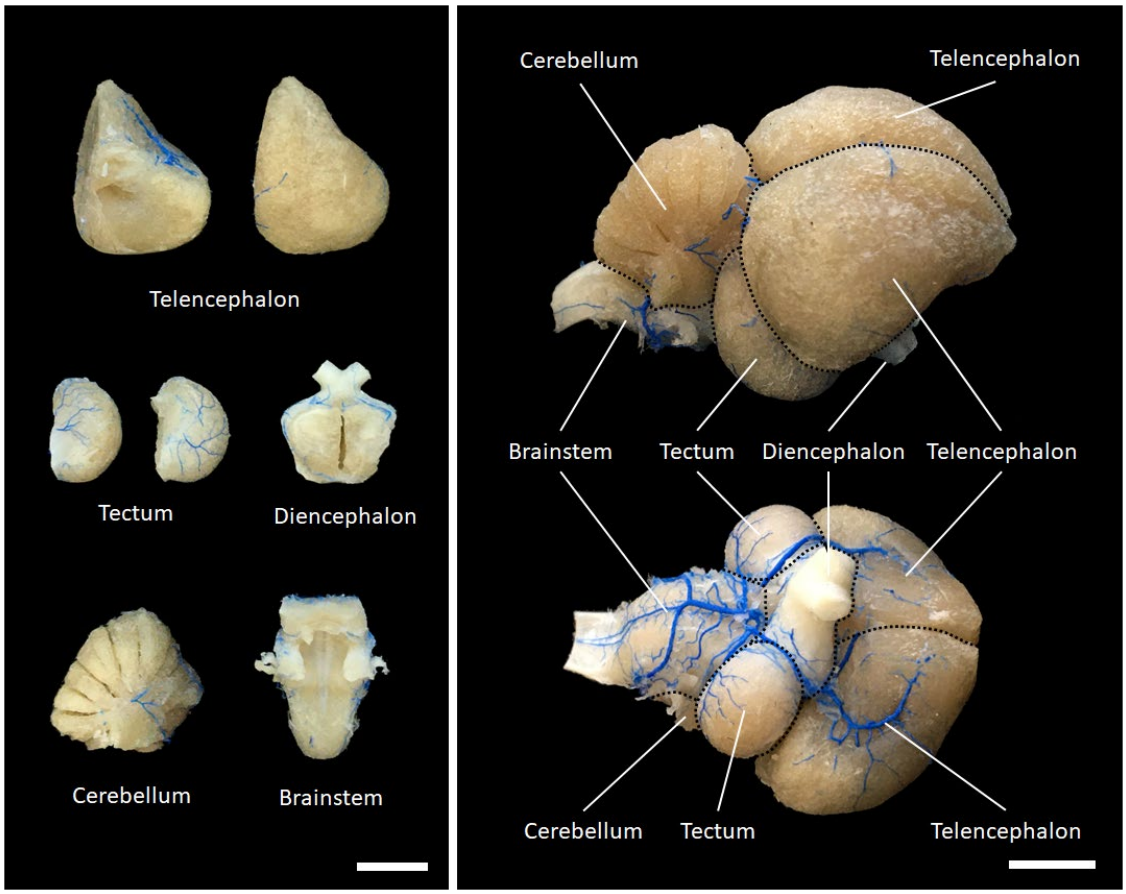

Figure 5-2. Brain regions of the chicken. The brain of the chicken was divided into seven regions for this study – the left and right telencephalon, left and right tectum, diencephalon, cerebellum, and brain stem. Dotted lines are used to highlight the divisions between regions. Arteries perfused with blue coloured liquid barium latex are visible. Scales are 10 mm.

The brain was removed and dissected into the cerebral hemispheres, cerebellum, diencephalon (including the hypothalamus and base of the optic nerves), tecta, and brainstem (Figure 5-2) following the approach of Olkowicz *et al.* (2016), with the exception that the difference between pallial and subpallial blood flow was not examined in this study. Each of the brain sections were weighed before being placed in a solution of 2 M ethanolic KOH with 2% Tween 80 (Thermo Fisher, cat. no. AJA2510-500ML) for dissolution (Figure 5-2, Figure 5-4). After 48 h, the solution was filtered through a glass microfiber filter (Grade 333, 47 mm DIA, Filtech, New South Wales, Australia, pore size 1.2 µm) using a vacuum pump. Filter paper containing the fluorescent microspheres was placed into a solution of Cellosolve acetate (2-ethoxyethyl acetate, 98%, Sigma Aldrich, cat. no. 109967) which dissolved the polystyrene microspheres, releasing their fluorescence into solution. Fluorescence measurements were made using a Cary Eclipse Fluorescence Spectrophotometer (Varian Australia Pty Ltd, Victoria, Australia) (excitation wavelength of 450 nm, slit width: 10 nm). Solutions of a known microsphere content were produced from the original microsphere stock and diluted with Cellosolve acetate to produce a standard curve. Standard curves were used to calculate the number of

spheres in each tissue. Fluorescence measurements were converted into flow rate measurements using the reference organ according to *Equation 10* and *Equation 11* (Anetzberger and Birkenmaier 2016).

$$Cardiac\ Output\ (cm^3\ s^{-1}) = \frac{Harvard\ Pump\ Withdrawal\ Rate\ \ (cm^3\ s^{-1}) \quad \times \quad Number\ of\ MS\ injected}{Number\ of\ MS\ in\ reference\ sample}$$

Equation 11 – Microsphere deposition and cardiac output.

Pressurised contrast perfusion technique

In the pressurised contrast perfusion technique, a radiopaque vascular contrast agent was perfused into arteries under physiological pressures with the aim that arterial cast dimensions measured from CT imagery would reflect in-life arterial lumen sizes. Following euthanasia specimens were rapidly processed in preparation for contrast perfusion. Specimens were decapitated and the left and right common carotid arteries were cannulated. Vessels were flushed of blood with heparinised saline (125 IU ml^{-1}) mixed with a small amount of detergent via the cannulated arteries.

BriteVu (Scarlet Imaging, Murray, Utah, United States) was the selected vascular contrast agent used in this study. During specimen preparation I prepared the contrast medium mixture of 1-part BriteVu and 3-parts water, with 1.5% BriteVu enhancer (Scarlet Imaging, Murray, Utah, United States). This mixture was heated to a temperature between 70°C and 80°C and maintained at this temperature for 10 min. The contrast medium mixture was continually stirred and a temperature of 70°C was maintained while it was perfused. The BriteVu vascular contrast medium was perfused into the common carotid arteries via the cannulas at physiological pressures (Figure 5-3). Contrast perfusion was carried out until the excess contrast draining from the severed vessels in the neck began to solidify. Specimens were then packed in ice and refrigerated for up to 24 h until imaging could take place. Refrigeration was necessary to allow the BriteVu solution to solidify prior to CT scanning. Specimens were not fixed with formalin prior to contrast injection or imaging.

Specimens were scanned using the SkyScan-1276 X-ray micro-CT scanner at Adelaide Microscopy (Appendix C). NRecon 1.6.9.4 (Bruker microCT, Kontich, Belgium) was used to reconstruct cross sectional images from tomographic projection images and subsequent voxels were cubic (isometric). Imaging settings were optimised for each specimen in order to maximise image contrast and resolution (Appendix C). Imagery was post processed using DataViewer 1.5.1.2 (Bruker microCT, Kontich, Belgium) to obtain desired rotations. Creation of digital cranial endocasts was performed in Avizo 9.0.0 (FEI SAS, Hillsboro, Oregon, USA). Data relevant to this chapter is available on MorphoSource under project ID: 000445264.

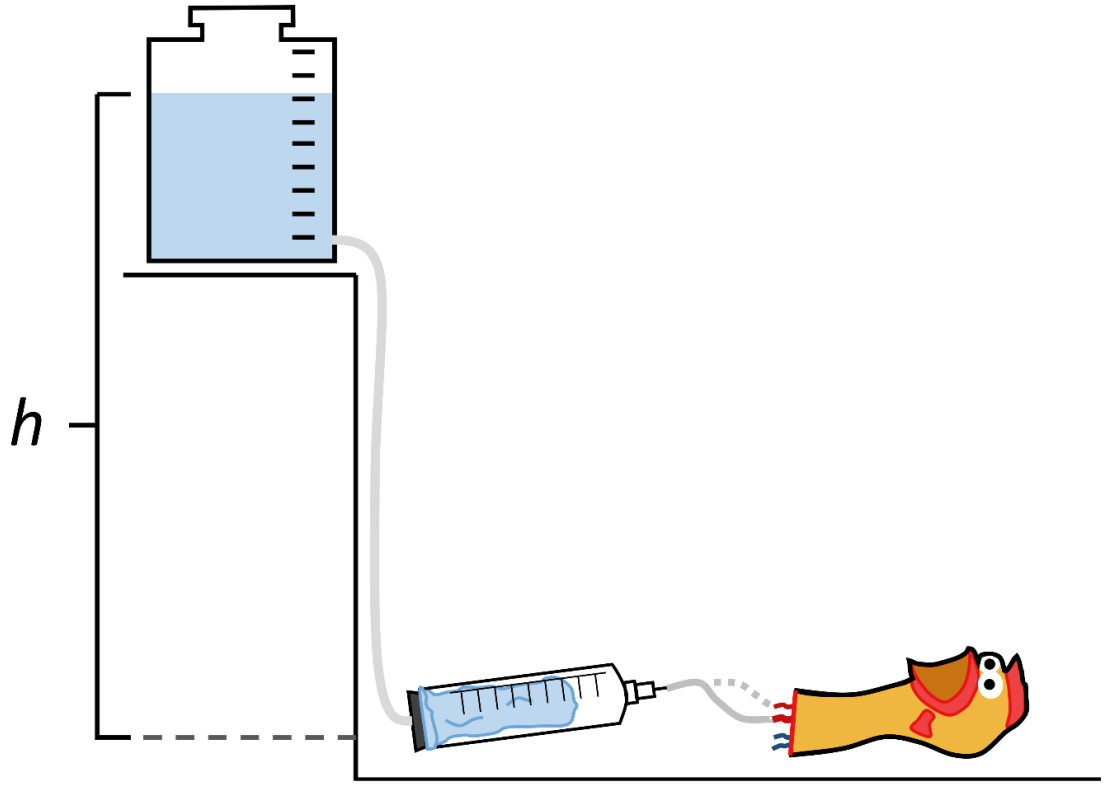

Figure 5-3. Diagram of the apparatus used to perfuse contrast media into specimens at a desired pressure. The beaker in the diagram is filled with water which feeds a column of fluid of height *h*. By adjusting the height, it is possible to increase or decrease the pressure exerted at the bottom of the column according to the hydrostatic pressure equation *(Equation 5)*. The bottom of the column of fluid is attached to a syringe where contrast media is separated from the water via a non-elastic, flexible diaphragm. The column of fluid exerts a pressure on the diaphragm which pushes the contrast fluid through cannula into the specimen at the desired pressure. Both carotids were cannulated contrast was perfused through each simultaneously.

For all specimens, I measured the cross-sectional area of the lumen of the cerebral carotid artery at the point immediately caudal to the sella turcica and carotid anastomosis, rostral of the branch of the sphenomaxillary and sphenopalatine arteries (Figure 6). This ensured that any blood flow being subtracted (or added) to the cerebral carotid by the sphenomaxillary and sphenopalatine arteries was accounted for. The cross-sectional area of the cerebral carotid artery lumen was measured with image analysis software Fiji (Open Source, www.fiji.sc). These cross-sectional area measurements were then converted to radii (referred to from here as lumen radii) by assuming the area was that of a circle. This lumen radius was then subjected to blood flow rate calculation using the mammalian interspecific blood flow rate equation from (Seymour *et al.* 2019b);

$$log\ \dot{Q} = -0.20\ log\ r_i^2 + 1.91\ log\ r_i + 1.82$$

Equation 7 – The Seymour et al. (2019b) mammalian equation.

where $\dot{Q}$ is blood flow rate ($cm^3\ s^{-1}$); and r_i is the arterial internal lumen radius (cm).

This equation is derived using measurements of blood flow rates and lumen size data from 20 named systemic arteries of mammals (Seymour *et al.* 2019b). Birds exhibit several differences from mammals in terms of blood properties including possession of larger (nucleated) red blood cells and a whole blood viscosity around half that of mammals (Maxwell *et al.* 1992; Zhou *et al.* 1999; Scanes 2015). However, as the haemodynamic principles which dictate the relationship between blood flow rate and vascular calibre are the same in all vertebrates, and in the absence of an equation specifically formulated for avian taxa, I use this mammalian equation here to calculate flow rates of birds. Blood flow was calculated individually for left and right foramina and then added together to give a total cerebral carotid blood flow rate.

Foramen dimension measurement technique

In the foramen dimension measurement technique blood flow rate through the cerebral carotid arteries was gauged from the dimensions of the cranial carotid canal of the same set of euthanised birds as were used in the pressurised contrast perfusion technique. The cross-sectional area of the cranial carotid canal was measured at the same point as the contrast perfused lumen in the pressurised contrast perfusion technique – immediately caudal to the sella turcica and carotid anastomosis, and rostral of the branch of the sphenomaxillary and sphenopalatine arteries. The cross-sectional area of the cranial carotid canal was measured with image analysis software Fiji (Open Source, www.fiji.sc). These cross-sectional area measurements were then converted to radii (referred to from here as foramen radii) by assuming the area was that of a circle.

To calculate the lumen radius of the artery passing through the canal from the foramen radius, the effective thickness of the arterial walls needs to be known. Arterial walls have a thickness which is determined by the principle of Laplace. Here, the thickness of the arterial walls of the cerebral carotid arteries is accounted for by using a wall thickness to lumen radius conversion ratio. Early publications utilising this technique relied upon a lumen size conversion ratio of w = 0.40 for mammals (Seymour *et al.* 2015; Seymour *et al.* 2016). Recently this conversion ratio has been re-examined from 14 imaging studies on humans and is given as w = 0.30 (Seymour *et al.* 2019a). Avian mean arterial blood pressures are around 1.3 times higher than mammalian values Seymour *et al.* (2004). Hence, a wall thickness to lumen radius conversion ratio of w = 0.40 is used for avian taxa.

Statistical analysis

Each of the three approaches yielded a total cerebral perfusion rate for each group of birds. GraphPad Prism 6.0 statistical software (GraphPad Software, La Jolla, California, USA) was then used to compare the cerebral perfusion rates according to each of the

approaches with one another using multiple one-way Analysis of Variance (ANOVA) to determine any if statistical significances existed.

The fluorescent microsphere infusion technique resulted in blood flow rates for seven brain regions. The blood flow rates for these regions were compared to each other and to corresponding brain regions in each of the groups of birds using GraphPad Prism and examined using Two-way Analysis of Variance (ANOVA) with age and brain region as the two factors to determine any if statistical significances existed. Post-hoc testing was performed using post-hoc testing using Tukey's HSD for two-factor ANOVA.

RESULTS

Fluorescent microsphere infusion technique

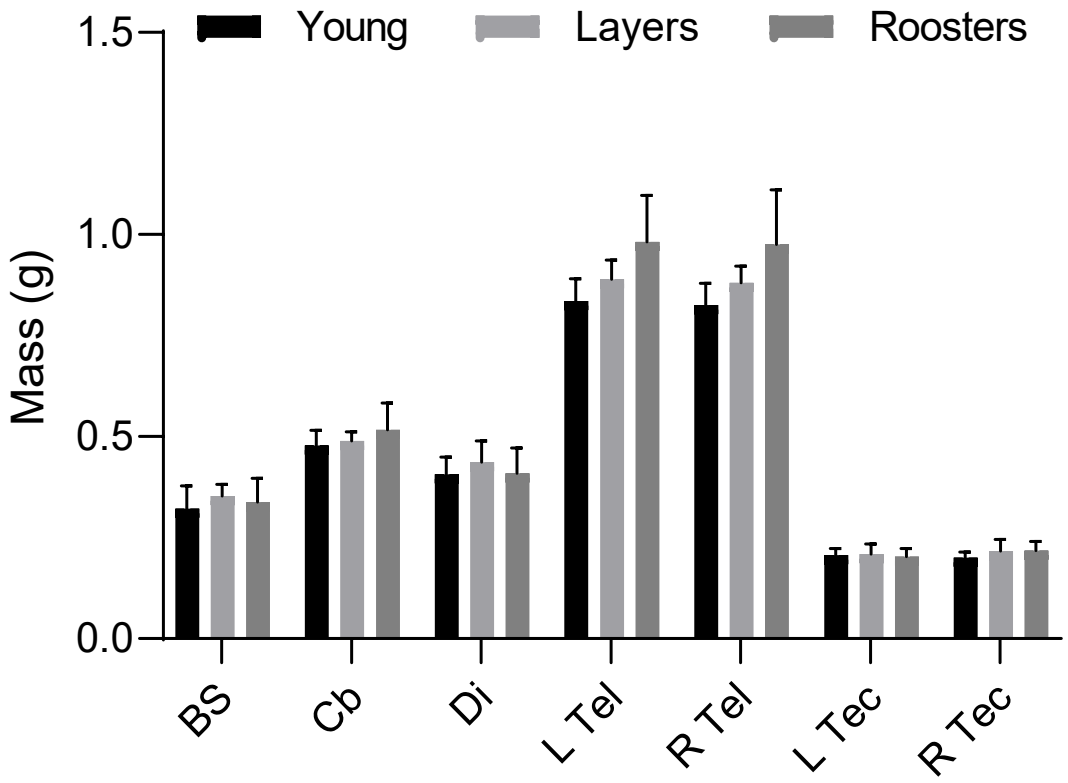

Figure 5-4. Masses of seven brain regions in pre-point-of-lay hens, post-point-of-lay hens, and roosters. Error bars represent 95% confidence intervals. Before POL body mass = 1246.17 (109) g, n = 6; After POL body mass = 1786.14 (157) g, n = 7; Rooster body mass 1963.00 (535) g, n = 6. BS, brainstem; Cb, cerebellum; Di, diencephalon; L Tel, left telencephalon; R Tel, right telencephalon; L Tec, left tectum; R Tec, right tectum.

Age, brain segment, and the interaction all had highly significant effects for brain mass. Brain segment accounted for the largest degree of variance by far at 95.23%, compared

to 0.56% for age and 0.87% for the interaction (Table 5-1). Age and brain segment had highly significant effects for blood flow rate, while the interaction was not significant. Brain segment again accounted for the largest degree of variance at 69.45%, compared to 9.41% for age and 2.99% for the interaction (Table 5-1). Age and brain segment also had highly significant effects for volumetric blood flow rate, while the interaction was not significant. For volumetric blood flow rate, age was responsible for the largest degree of variance at 33.52%, compared to 15.26% for brain segment and 2.56% for the interaction (Table 5-1).

Our microsphere perfusion results demonstrate no significant difference between the brain masses amongst the three groups in the brainstem, cerebellum, diencephalon, left tectum, or right tectum. Roosters had larger left and right telencephala than young hens, but there was no significant difference in telencephalon mass between the young hens and the layers, or between the layers and the roosters. A variety of significant differences existed between the other regions and amongst the groups (see Appendix B).

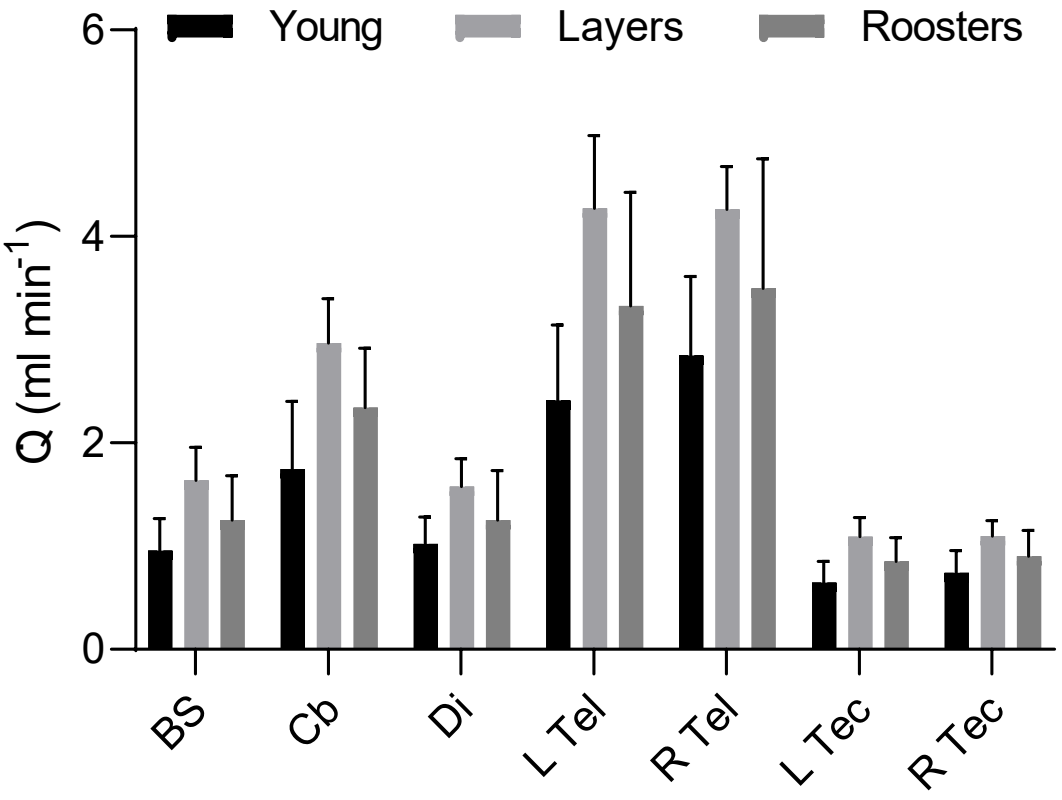

Figure 5-5. Absolute blood flow rate to seven brain regions in pre-point-of-lay hens, post-point-of-lay hens, and roosters determined by microsphere perfusion. There was no significant difference between the blood flow across the three groups in the brainstem, diencephalon, left tectum, or right tectum, but a variety of significant differences between the other regions and amongst the groups (see Appendix B). Error bars represent 95% confidence intervals. BS, brainstem; Cb, cerebellum; Di, diencephalon; L Tel, left telencephalon; R Tel, right telencephalon; L Tec, left tectum; R Tec, right tectum.

Across all brain regions, roosters had absolute brain blood flow values which were not statistically significantly different than the two groups of hens (Figure 5-7). However, across all brain regions, immature hens had absolute brain blood flow values smaller than laying hens (Figure 5-7). Immature hens had regional volume specific brain blood flow values smaller than layers (P=0.05), while no significant difference existed between the regional volume specific brain blood flow values in the immature hens and the roosters (P=0.24). The telencephalon of laying hens had volume specific blood flow values which were higher than the roosters, but other brain regions were not significantly different between the two groups (Figure 5-7).

No significant difference existed between the left and right telencephalon and left and right tectum in any of the groups in terms of absolute blood flow, volumetric blood flow, or brain mass (Figure 5-4, Figure 5-5, Figure 5-6, Figure 5-7). Roosters had larger telencephala than immature hens (P=0.01). Otherwise, brain region masses were not significantly different across all groups (Figure 5-4, Figure 5-7).

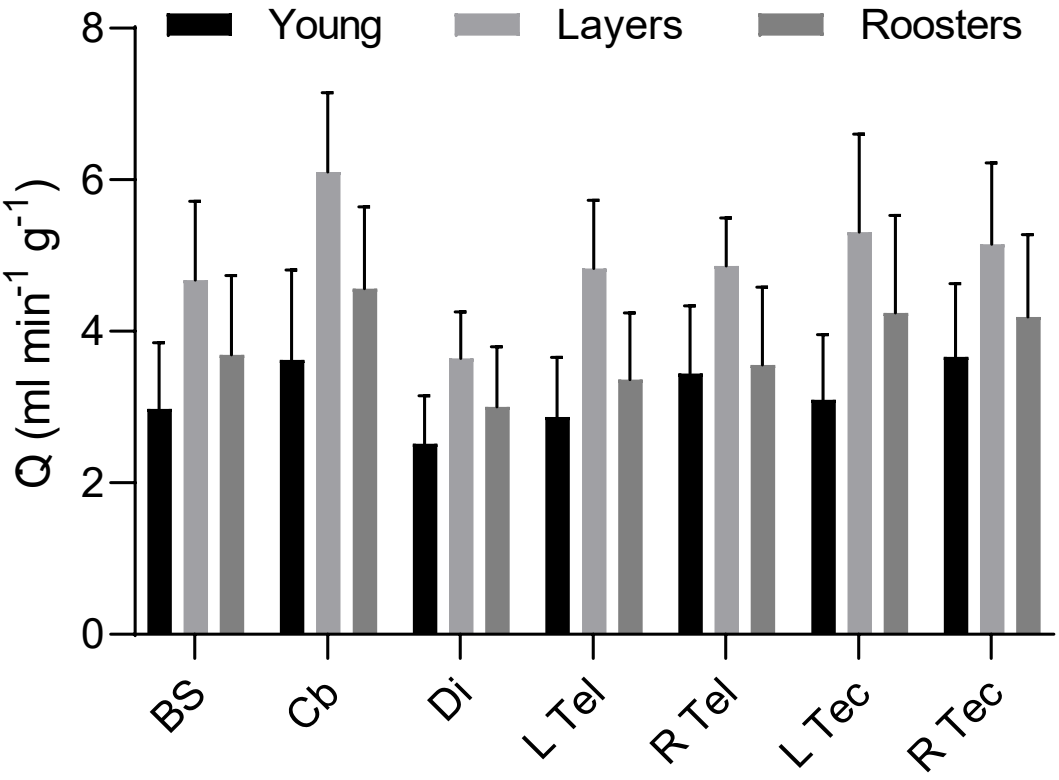

Figure 5-6. Volumetric blood flow rate to seven brain regions in pre-point-of-lay hens, post-point-of-lay hens, and roosters determined by microsphere perfusion. There was no significant difference between the volumetric blood flow across the three groups in the brainstem, diencephalon, left telencephalon, and right telencephalon, but a variety of significant differences between the other regions and amongst the groups (see Appendix B). Error bars represent 95% confidence intervals. BS, brainstem; Cb, cerebellum; Di, diencephalon; L Tel, left telencephalon; R Tel, right telencephalon; L Tec, left tectum; R Tec, right tectum.

Table 5-1. Results of two-way ANOVA for different variables from the microsphere infusion technique.

Variable	Source of Variation	SS	df	MS	F	p-value	% of total variation
Brain Volume (ml)	Brain Segment	9.808	6	1.635	562.1	<0.0001	95.23
	Age	0.05779	2	0.0289	9.937	0.0001	0.5611
	Interaction	0.08987	12	0.007489	2.575	0.0047	0.8725
	Residual	0.3257	112	0.002908			
	Total	10.28136	132				
$\dot{Q}_{ICL}$ (ml min^{-1})	Brain Segment	146.4	6	24.39	81.01	<0.0001	69.45
	Age	19.84	2	9.918	32.93	<0.0001	9.411
	Interaction	6.308	12	0.5257	1.746	0.0663	2.993
	Residual	33.73	112	0.3011			
	Total	206.278	132				
$\dot{Q}_{CF}/V_{Br}$ (ml min^{-1} g^{-1})	Brain Segment	33.58	6	5.597	5.929	<0.0001	15.26
	Age	73.77	2	36.88	39.07	<0.0001	33.52
	Interaction	5.636	12	0.4696	0.4975	0.9124	2.561
	Residual	105.7	112	0.944			
	Total	218.686	132				

See Appendix B for full multiple comparisons descriptive statistics table.

Figure 5-7. Two way ANOVA multi-comparison confidence interval plots for brain segment mass, brain segment blood flow rate, and volumetric blood flow rate in different life classes of chickens.

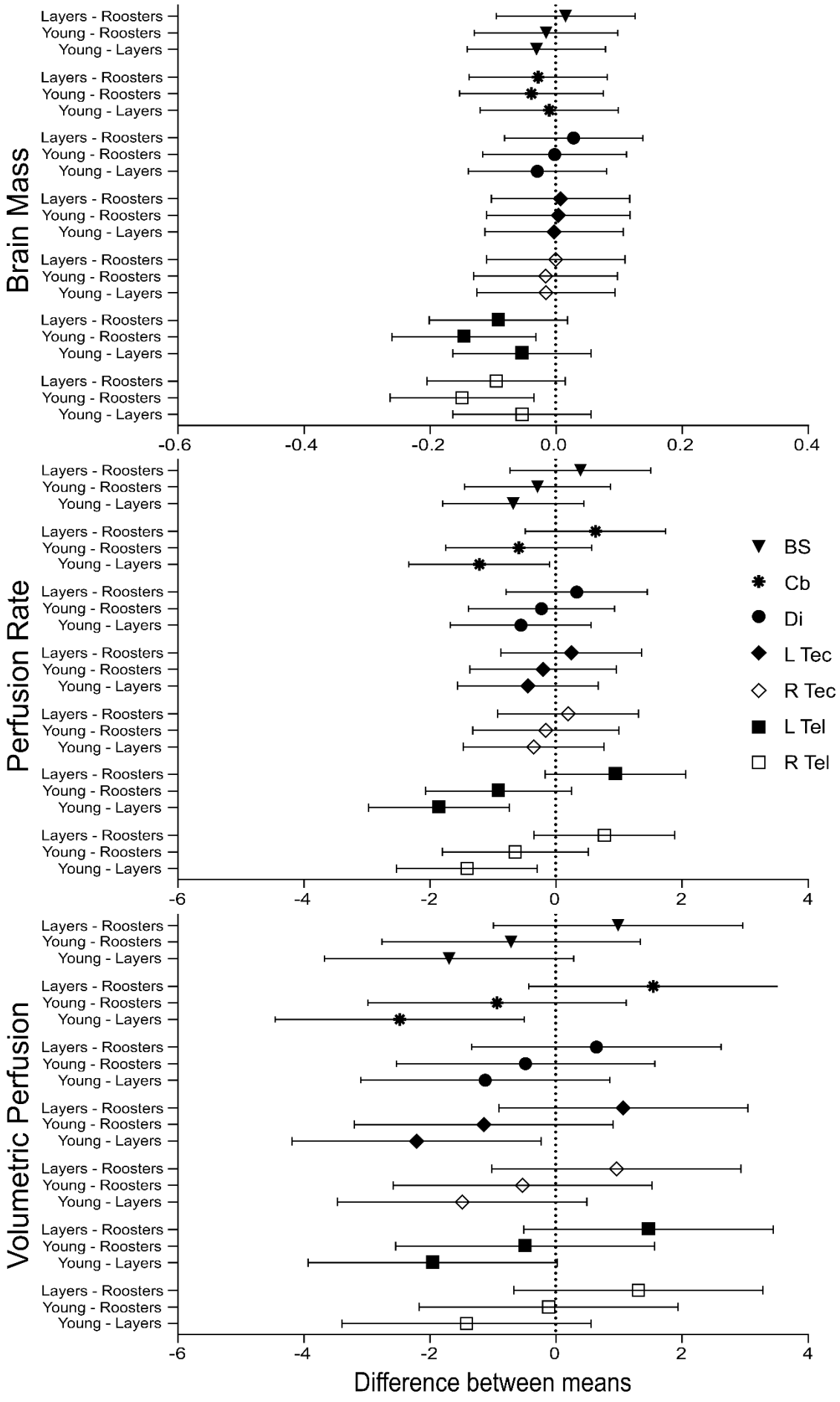
Brain Mass
Perfusion Rate
Volumetric Perfusion
Layers - Roosters
Young - Roosters
Young - Layers
-0.6
-0.4
-0.2
0.0
0.2
0.4
-6
-4
-2
0
2
4
BS
Cb
Di
L Tec
R Tec
L Tel
R Tel
Difference between means

Pressurised contrast perfusion technique

No significant difference in cerebral blood flow rate was detected between the three groups of birds using the pressurised contrast perfusion technique.

Table 5-2. Average whole brain perfusion rates of *Gallus gallus domesticus* calculated from the dimensions of the cerebral carotid lumen according to the lumen contrast dimension measurement technique.

Life Stage	Brain Volume (ml)	Measured r_{Lumen} (cm)	$\dot{Q}_{ICL}$ (ml min^{-1})	$\dot{Q}_{CF}$ / V_{Br} (ml min^{-1} g^{-1})
Before POL	3.59 (0.77)	0.024 (0.0028)	2.00 (0.53)	0.52 (2.61)
After POL	3.82 (1.30)	0.024 (0.0035)	2.03 (0.74)	0.64 (0.18)
Rooster	4.40 (0.40)	0.022 (0.0023)	1.58 (0.42)	0.45 (0.05)

Values in brackets represent 95% confidence intervals. Before POL body mass 1277.00 (262) g, n = 6; After POL body mass 1777.00 (158) g, n = 7; Rooster body mass 2247.00 (207.5) g, n = 6.

Foramen dimension measurement technique

No significant difference in cerebral blood flow rate was detected between the three groups of birds using the foramen dimension measurement technique. The brain volumes of the three groups of birds shared in the foramina dimension measurement and pressurised contrast perfusion techniques showed no statistical difference in brain volume.

Table 5-3. Average whole brain perfusion rates of *Gallus gallus domesticus* calculated from the dimensions of the cerebral carotid canal according to the foramen dimension measurement technique.

Life Stage	Brain Volume (ml)	Measured $r_{Foramen}$ (cm)	Calculated r_{Lumen} (cm)	$\dot{Q}_{CF}$ (ml min^{-1})	$\dot{Q}_{CF}$ / V_{Br} (ml min^{-1} g^{-1})
Before POL	3.59 (0.77)	0.065 (0.0068)	0.046 (0.0049)	9.91 (2.52)	2.89 (12.26)
After POL	3.82 (1.30)	0.065 (0.0048)	0.046 (0.0034)	10.04 (1.94)	3.08 (11.34)
Rooster	4.40 (0.40)	0.070 (0.0034)	0.050 (0.0024)	11.82 (1.43)	2.74 (4.76)

Values in brackets represent 95% confidence intervals. Before POL body mass 1277.00 (262) g, n = 6; After POL body mass 1777.00 (158) g, n = 7; Rooster body mass 2247.00 (207.5) g, n = 6.

Comparison of methods

When I compare cerebral blood flow values obtained via the microsphere method with cerebral blood flow values calculated based on foramina size, I find some degree of correlation (Figure 5-8). No statistical difference was found between the blood flow values obtained via the foramina dimension measurement and fluorescent microsphere infusion techniques for the whole brain across the immature hens and the roosters.

However, for the adult layers the fluorescent microsphere infusion technique yielded blood flow values which were higher than the foramen dimension measurement technique.

While no statistical difference was found between the blood flow values from the foramina dimension measurement and the microsphere perfusion method for the whole brain across the immature hens and roosters, in adult layers the fluorescent microsphere infusion technique yielded blood flow values which were higher than the foramen dimension measurement technique.

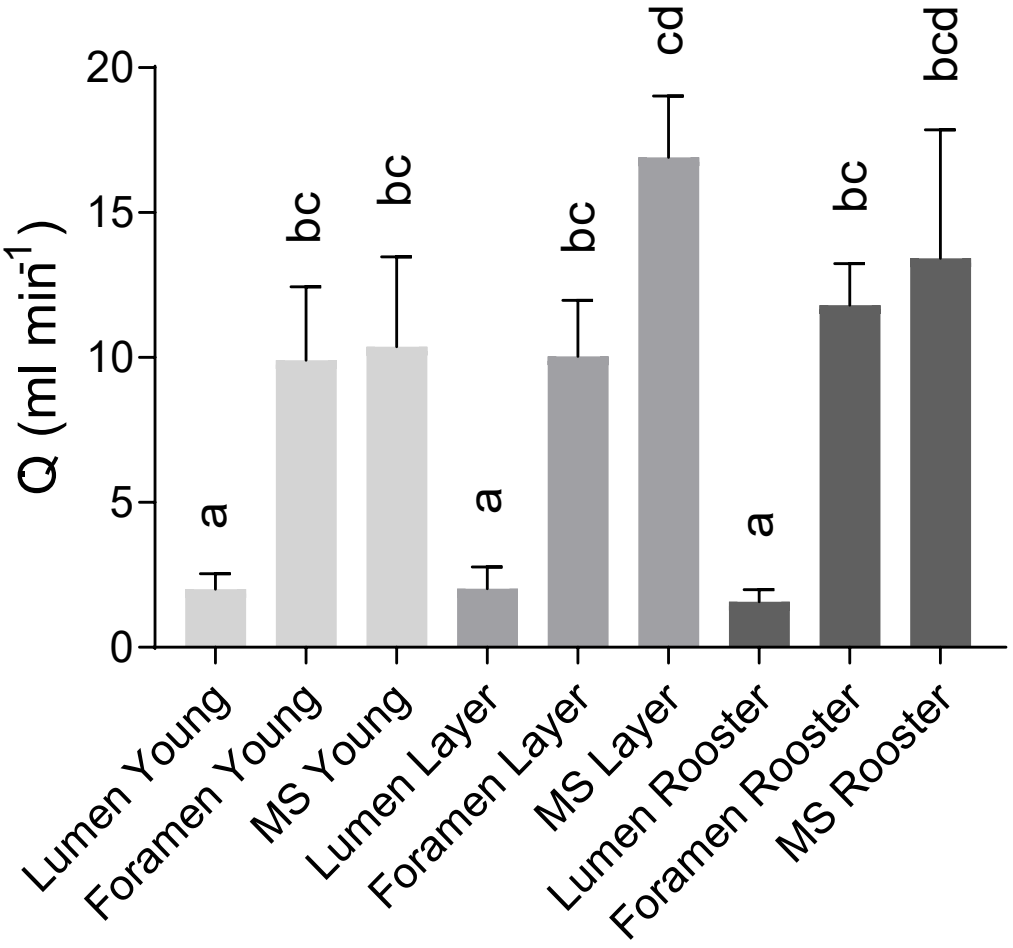

Figure 5-8. Comparison between whole brain absolute blood flow values calculated from the foramen dimension measurement technique, pressurised contrast perfusion technique, and fluorescent microsphere infusion technique. For all three groups of birds, whole brain blood flow values obtained via the pressurised contrast perfusion technique were statistically significantly lower than those obtained from both the foramina dimension measurement and fluorescent microsphere infusion technique s. Error bars represent 95% confidence intervals. Letters above error bars indicate groups which are significantly different at the level p=0.05.

For the pressurised contrast perfusion technique, I found that arteries perfused with contrast medium exhibit lumen sizes which are smaller than the predicted lumen sizes, and hence lower cerebral blood flow values (Figure 5-8, Figure 5-9, Table 5-3, Table 5-2).

In the fluorescent microsphere infusion technique, the body masses of the roosters and the layers were not statistically different from one another while those of the young hens were significantly different from both the layers and the roosters. The body masses of the three groups of birds shared in the foramina dimension measurement and pressurised contrast perfusion techniques were statistically significantly different from one another.

DISCUSSION

Cerebral blood flow rates in chickens

According to the microsphere perfusion technique, although there was a difference between the total amounts of blood flow to different regions of the brain (Figure 5-5, Figure 5-7), there were few statistically significant differences in volumetric blood flow across each of the different brain regions, with some notable exceptions (Figure 5-6, Figure 5-7). In particular the diencephalon had a lower volumetric blood flow than the cerebellum and the optic tecta. This is likely as the diencephalon is responsible for less intensive functions of the brain as one of its large tasks is as a sensory relay between other brain regions. However, because the diencephalon is also responsible for important autonomic functions and the management of emotion and memories, this dip is only slightly lower. In contrast to the diencephalon, the volumetric flow rate to the brain stem was not statistically significantly different than that of any other brain region, despite having the lowest neural cell count and neural cell density of any brain region (Olkowicz *et al.* 2016). The optic tectum is the primary visual centre of the avian brain and is central in many aspects visual and spatial processing, while also being an important site of sensory integration (Kloos *et al.* 2019). The optic tectum and telencephalon share a similar neural to glial cell ratio (Olkowicz *et al.* 2016). The brain stem and cerebellum, as in all vertebrates, are responsible for motor control, coordinating balance and movement by responding to commands from the forebrain. The brain stem also plays an important role hosting connections between other brain regions (Figure 5-5, Figure 5-6, Figure 5-7).

The telencephalon is the largest region of the avian brain and is the responsible higher thinking and voluntary actions. That the blood flow rate to the forebrain of laying hens increases above both the immature hens and mature roosters indicates that this increase cannot be explained as simply due to growth brain (Figure 5-5, Figure 5-7). Indeed, total brain size and regional brain sizes were statistically invariant across the

before-point-of-lay and after-point-of-lay groups (Figure 5-5, Figure 5-7). A study by Olkowicz *et al.* (2016) measuring counts of neural and non-neural (glial) cells in different regions of the avian brain determined that the telencephalon possesses the second highest neuron count after the cerebellum and the highest glial cell count of any of the brain regions examined. The telencephalon in all three groups examined received a far greater proportion of blood flow than any of the other brain regions, roughly equal to the flow rates to all other brain regions combined (Figure 5-5, Figure 5-7). Using neuron and non-neuron counts in the jungle fowl determined by Olkowicz *et al.* (2016) it can be seen that the blood flow per neuron plus non-neuron is greater in the telencephalon than that of any other brain region. The avian pallium comprises a similar proportion of the telencephalon as the mammalian pallium, at around 75%, and supports cognitive capabilities which are similar to or more advanced than those of many mammals (Jarvis *et al.* 2005). Although chicken brains have smaller absolute numbers of neurons than those of similarly sized songbirds or parrots, chicken pallial neuronal densities are still comparable to those of primates (Olkowicz *et al.* 2016).

No significant difference existed between the left and right telencephalon and left and right tectum in any of the groups in terms of absolute blood flow, volumetric blood flow, or brain mass (Figure 5-4, Figure 5-5, Figure 5-6, Figure 5-7). In humans, left or right handedness is associated with an increased size of some brain regions, in particular Broca's area in the frontal lobe and Wernicke's area in the temporal lobe. Although chickens have been shown to exhibit footedness (Rogers and Workman 1993; Tommasi 1999; Dharmaretnam *et al.* 2002), the relative sizes of any areas which reflect preferential footedness are likely to be quite small and thus the resolution of this study may be unable to detect any asymmetry based solely on the measurements of the left and right telencephalon and tectum.

The chicken brain is more metabolically intense than those of comparatively sized haplorrhine primates (Chapter 3). In haplorrhine primates cerebral blood flow rate is proportional to brain size, meaning that the metabolic intensity is nearly constant. Blood flow to the telencephalon of haplorrhine primates can be described by the allometric equation $\dot{Q}_{ICA} = 0.0103\ V_{tele}^{0.101}$ (Seymour *et al.* 2019a). When applied to an adult chicken this equation yields a prediction of a telencephalon perfusion rate of 1.15 ml min^{-1}, far lower than the actual chicken telencephalon perfusion rate of 7.75 ml min^{-1} demonstrated in this study. Furthermore, chicken forebrains are around eight times more metabolically intense than human brain tissue receiving 4.21 ml min^{-1} g^{-1} compared to humans 0.50 ml min^{-1} g^{-1} (Seymour *et al.* 2019a). The pygmy marmoset (which has the closest comparable telencephalon volume of any primate at 3.20 ml compared to a chickens 1.86 ml) has a volumetric telencephalon perfusion rate of 0.45 ml min^{-1} g^{-1} (Seymour *et al.* 2019a), a 4.88-fold difference from the chickens. The smallest difference in forebrain volumetric perfusion between a primate and a chicken exists with the crested black macaque, which has a 61 ml telencephalon and a volumetric

telencephalon perfusion rate of 1.18 ml min^{-1} g^{-1} (Seymour *et al.* 2019a), a 3.57-fold difference from chickens. If the assertion that cerebral perfusion rate and intelligence holds true, chicken intelligence seems to have been underestimated and overshadowed by other animals, particularly primates, cetaceans, and other aves (Marino 2017). This may indeed be a possibility, as studies of chicken cognitive abilities have regularly demonstrated that chickens possess several qualities indicating intelligence. The social intelligence of chickens has been recognised in some way for at least a century since the first description of the dominance hierarchy or pecking order of chicken social groups (Schjelderup-Ebbe 1921), and chicken communication and vocalisations have been recognised as having a level of complexity and sophistication previously thought to occur only in primate species (Nicol 2015).

It is difficult to specifically associate any changes in brain blood flow to changes in brain chemistry in chickens as they reach sexual maturity. Chickens reaching point of lay undergo a series of changes including immunosuppression (Johnston *et al.* 2012), increase in circulating oestrogen and progesterone concentrations (Joseph *et al.* 2003), and changes in body composition (Brody *et al.* 1984). The concentrations of circulating estrogens increase in laying hens as they approach sexual maturity, peaking around four weeks before the onset of point of lay, and decreasing after sexual maturity (Wilson and Sharp 1975). Maternal care behaviour in mammals is known to be regulated by oxytocin and mesotocin, the avian homologue of oxytocin, plays a similar role in native Thai chickens by regulating brooding behaviours. Neurons sensitive to mesotocin increase in number when hens enter a broody state and decrease again if chicks are removed from a broody mother (Chokchaloemwong *et al.* 2013). However, the hens in the present study were actively laying but had not reached or entered a state of broodiness. It seems likely that onset of sexual maturity would trigger changes in brain chemistry, which may relate to the observed changes in brain blood flow rate, however studies of the brain chemistry of hens before and after sexual maturity are lacking in the literature.

Roosters and hens exhibit different behaviours. Roosters are social of course, but it seems possible that their different social requirements might be responsible for some of the differences noted in their regional cerebral blood flow regimes. However, I could not find studies in the literature which provided enough information on the differences between the sociality of roosters and hens to allow us to reach concrete conclusions regarding this hypothesis. Adult hens take on the responsibilities of raising chicks which requires a significant change in cognitive behaviour. Mother hens express many different vocalisations specifically for communication with their young, which are not seen in juvenile hens. Maternal communication begins before hatching in response to embryonic vocalisations and so that incubating chicks will more easily be able to identify their mother upon hatching (Tuculescu and Griswold 1983). After hatching, maternal communication with their brood continues, playing important roles

in directing chicks towards profitable food items as well as in protecting them from harm (Nicol 2006). I suggest that the capacity for this change in cognitive behaviour seems to be established at sexual maturity rather than upon motherhood, resulting in hens which have reached point of lay receiving a higher level of blood flow than either immature hens or roosters of a similar age.

Critique and comparison of methods

The microsphere perfusion technique allows direct and accurate measurement of blood flow to tissues. The blood flow values from the microsphere perfusion technique and the foramen measurement method were similar in the before-point-of-lay-hens and the roosters, but significantly different in the after-point-of-lay-hens (Figure 5-8). In the before-point-of-lay-hens and the roosters, the microsphere perfusion and foramen dimension measurement methods yielded similar rates of total cerebral perfusion. This is indicative of the fact that the cerebral carotid arteries are the primary cerebral feeder arteries and are responsible for the vast majority of the cerebral perfusion. In the layer hens, whole brain cerebral blood flow values were higher under the microsphere approach than under the foramen dimension approach. This unlike the similarities exhibited between the other two groups (young hens and roosters). The cause of this discrepancy is uncertain; it is possible that as layers reach point of lay cerebral feeder arteries other than the cerebral carotid arteries take up a greater role in cerebral perfusion. Minor non-carotid sources of cephalic perfusion are not uncommon in the Aves and have been noted in several other studies. The Pekin duck exhibits a number of pathways for blood flow via anastomoses between the dorsal intercostal rami of the aorta and the descending vertebral arteries. Around 2.4% of the cephalic blood flow in the Pekin duck reaches the brain via non-brachiocephalic routes (Fedde *et al.* 1982), though it has been suggested that these anastomotic branches may be able to contribute more blood flow to the head if arterial pressure increases or these branches become dilated (Fedde and Guffy 1983). An ad hoc adjustment of 2.4% is not sufficient to make the difference in blood flow between the foramina dimension measurement and microsphere perfusion method insignificant (P=0.0001). Several papers (Richards 1970; Midtgård 1984a; Midtgård 1984b; Arad *et al.* 1987; Arad 1990) have report that blood from the ophthalmic rete flows to the brain, however, Porter and Witmer (2016) suggest that these connections would have to supply the brain via retrograde flow, against the pressure gradient produced by the heart (Porter and Witmer 2016). A study by McGinnis and Ringer (1965) involving complete ligation of both the common carotids and vertebral arteries resulted in a mortality rate of only 25%. Surviving chickens were reported to exhibit normal behaviours and levels of alertness, and McGinnis and Ringer (1965) concluded that carotid and vertebral occlusion must have little effect on the maintenance of normal cerebral function in the survivors. In many chickens there must exist a significant amount of collateral cerebral blood flow. As in mammals, the spinal arteries also supply a small amount of blood to the brain via the vertebral foramen and foramen magnum

with the nerve cord. I noted some variation in vascular pathways during the dissections, including one case of an early division of the common carotid artery into the external and internal carotids, with the carotid bulb positioned halfway down the length of the neck.

The fluorescent microsphere infusion technique is providing an estimation of the cerebral perfusion rate under anaesthesia and surgical intervention. The cerebral perfusion rate determined via this approach may be lower than the conscious cerebral perfusion rate because of a decreased cardiac output associated with the opening of the chest and cardiac puncture; chest opening and ventricular catheterisation is associated with a 20-25% fall in cardiac output (Boelkins *et al.* 1973). The anaesthetised cerebral perfusion rate may be lower than the non-anaesthetised cerebral perfusion rate because of the effect of ketamine anaesthesia on the body. Ketamine anaesthesia is known to be a circulatory stimulant, inducing increases in heart rate, blood pressure, and cardiac output (Tweed *et al.* 1972; Slupe and Kirsch 2018). Ketamine anaesthesia may also have a direct impact on cerebral circulation. A meta study of humans and 38 mammalian animal models demonstrate that ketamine anaesthesia may drive an increase in global and regional cerebral blood flow via vasodilation of medium-sized intracranial vessels (Zeiler *et al.* 2016). Within this meta study, five demonstrated a decrease in cerebral blood flow, seventeen an increase, and eight no effect. The impact on blood flow ranged from a decrease of 30% to an increase of 165% (Zeiler *et al.* 2016). I found no studies in the literature detailing the effect of ketamine anaesthesia on cerebral blood flow in chickens or birds in general and it is difficult suppose what effect the ketamine anaesthesia would have on these measurements. The foramen dimension measurement technique estimates a flat cerebral perfusion rate which can be assumed to be about the maximum cerebral perfusion rate if the lumen to wall ratio calculations are correct. Because of these variables it is possible that the microsphere perfusion quantification technique and foramen dimension measurement technique may have less correlation than reported above.

Few studies from the literature have measured or reported regional cerebral blood flow rates in chickens. No direct measurements (i.e. doppler flow, etc) of blood flow through the carotid arteries in chickens was found during my search of the literature. Merrill *et al.* (1981) calculated cerebral blood flow in adult leghorn roosters via injection of ^{141}Ceasium labelled microspheres and report a blood flow rate of 2 ml min^{-1} g^{-1} to their brain, in contrast to the 3.67 ml min^{-1} g^{-1} I report here. However, this discrepancy may be explained by the approach used by Merrill *et al.* (1981); injection of microspheres into the heart via one cannulated – and therefore blocked – carotid artery. Boelkins *et al.* (1973) also investigated regional blood flow in chickens using radioactive microspheres, reporting cerebellar blood flow values of 0.68 ml min^{-1} g^{-1}. This value stands in contrast to the values for cerebellar blood flow I report here of 6.1 ml min^{-1} g^{-1}, however, again, here one common carotid artery was cannulated. A paper by Wolfenson *et al.* (1978) used

radioactive microspheres to measure blood flow in a variety of different tissues in cross-bred laying hens. Their paper reports mass specific blood flow values in the telencephalon and cerebellum of 1.19 ml min^{-1} g^{-1} and 1.49 ml min^{-1} g^{-1} respectively. In this case the site of microsphere injection was the root of the aortic arch via catheterisation of the brachial artery – advancement of a catheter to this point may partially restrict blood flow through the carotids and lessen the resulting flow rate measurements potentially explaining the difference between the measurements presented herein of mass specific blood flow values in the telencephalon and cerebellum of 6.1 ml min^{-1} g^{-1} and 9.7 ml min^{-1} g^{-1} respectively in the laying hens. Some degree of variation must exist between measurements as Wolfenson *et al.* (1978) presents mass specific cerebellar blood flow values which are around two fold larger than Boelkins *et al.* (1973) and this variance is much less dramatic than the difference between the two studies and ours which represents a 2.4 to 9.0 fold difference. To aid comparison, mass specific blood flow values for the kidney and spleen were recorded for five of the seven layer replicates in this study, as reported by Hu *et al.* (2021) (Appendix B, Table S 4/5 - 5). Boelkins *et al.* (1973) reports a mass specific blood flow rate to the spleen of 4.81 ml min^{-1} g^{-1} and to the kidneys of 2.48 ml min^{-1} g^{-1}. Wolfenson *et al.* (1978) reports a mass specific blood flow rate to the spleen of 8.17 ml min^{-1} g^{-1} and to the kidneys of 2.07 ml min^{-1} g^{-1}. Here I report mass specific blood flow rates to the spleen of 5.61 ml min^{-1} g^{-1} and to the kidneys of 2.39 ml min^{-1} g^{-1} in the laying hens. I postulate that the reasoning for the discrepancy between brain blood flow measurements but not kidney or spleen measurements is due to partial restriction of cephalic blood flow due to the mode of microsphere injection used in each of these studies, which was avoided here through a direct cardiac approach to microsphere injection (Figure 5-1).

A further cause of this discrepancy may lie in the form of anaesthetic used. Wolfenson *et al.* (1978) used an unreported dose of 2% lidocaine. Lidocaine has a dose and agent specific biphasic response, increasing cerebral blood flow in moderate doses and reducing cerebral blood flow in large doses in humans (Slupe and Kirsch 2018). Boelkins *et al.* (1973) used sodium pentobarbital, a barbiturate which may have a reductive effect on cerebral blood flow rate (Slupe and Kirsch 2018). Merrill *et al.* (1981) used 2% procaine hydrochloride, which has little effect on cerebral blood flow rate (Scheinberg *et al.* 1952). Here I used ketamine and xylazine, which may increase cerebral blood flow rate (Zeiler *et al.* 2016; Slupe and Kirsch 2018). As blood oxygen saturation and ventilation rate were not recorded throughout the experiment it does remain possible that brain perfusion rates were elevated in this study as a reaction to hypoxia.

Equation 7 is used here to calculate blood flow rates in this paper is derived from measurements of named systemic arteries in mammals (Seymour *et al.* 2019b). This equation is used in the absence of an equation formulated specifically for avian taxa as the haemodynamic principles which dictate the relationship between blood flow rate and vascular calibre are the same in all vertebrates. Regardless, the foramen dimension

measurement technique appears to underestimate rather than overestimate the degree of cerebral perfusion, simply due to its inability to account for any other arteries which do not pass through osteoforamina. One way or another, much variation exists, and prediction of the amount of flow via sources other than the cerebral carotids has not been attempted here. Future work determining the directionality of the arteries which connect the cephalic and encephalic regions would allow further inferences to be made regarding the role of these arteries in different life history groups of chickens.

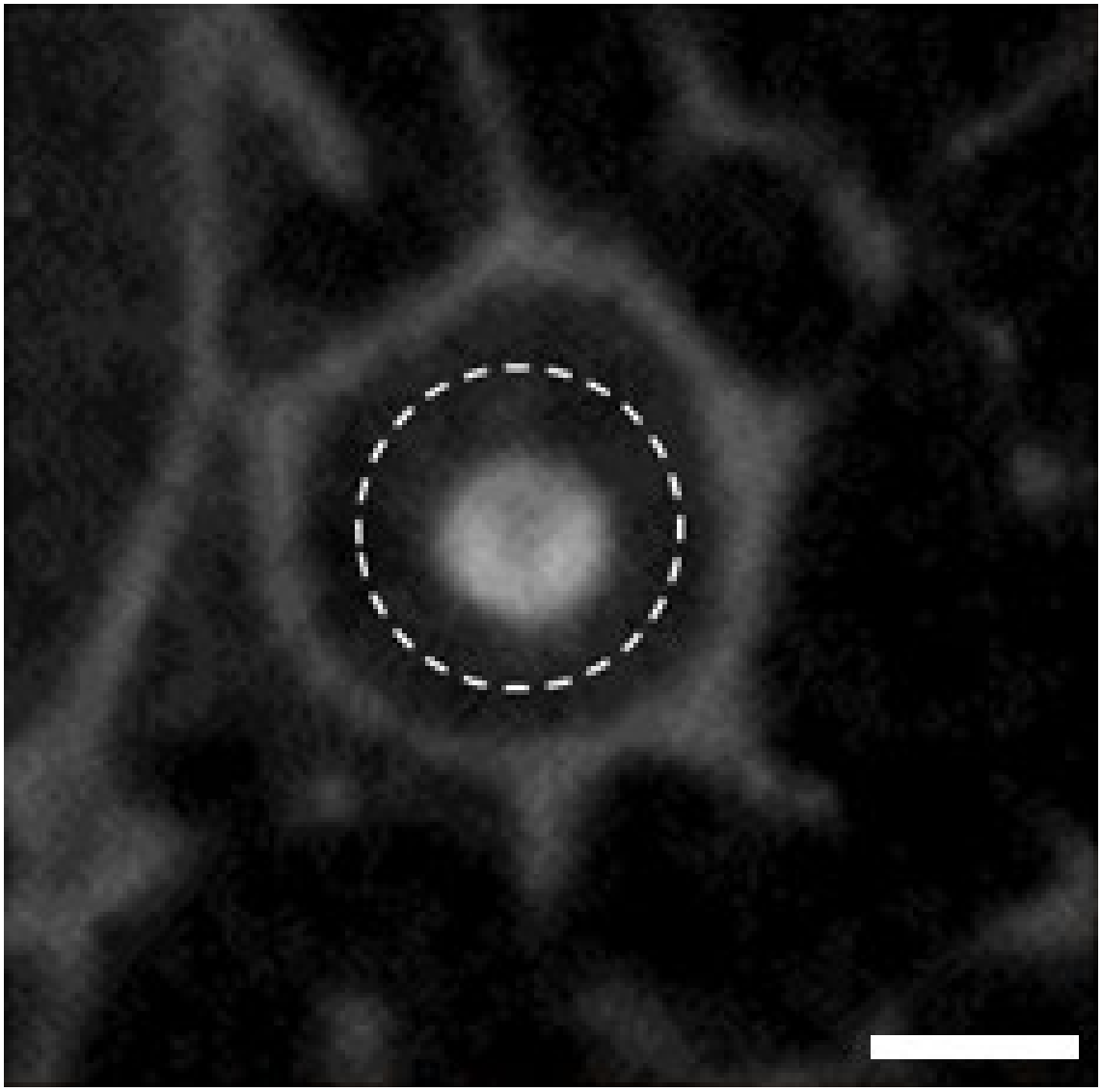

Figure 5-9. An image of a contrast perfused carotid artery typical of those obtained during this study. Bone tissue – including the osteoforamina – shows as a dull grey. The white circle in the centre of the image is the lumen of the contrast perfused carotid artery. Black areas are soft tissue. The dashed line represents the size of the lumen which should be observed according to the foramina wall thickness to lumen radius conversion ratio of w = 0.40. Scale bar is 0.06 mm.

Disappointingly, the pressurised contrast perfusion technique in this case proved to be invalid in terms of blood flow calculation (Figure 5-8, Figure 5-9 Table 5-3, Table 5-2). It is worth noting that some success was had with this technique in smaller arteries (Hu

2021; Hu *et al.* 2022), and Minnich and Lametschwandtner (2003) also report being able to calculate flow rates from casting of small arteries. Thus, I theorize that the failure of this approach here is related to the properties of larger, more thickly walled arteries, perhaps being so elastic as to compress and squeeze the contrast agent into a smaller volume before it has set into a solid, fully inflated structure. BriteVu was the chosen contrast agent due to its relatively low viscosity at injection temperature (70°C) when compared to other contrast agents. More success with the pressurised perfusion method may be had if a suitably less viscous contrast material were able to be obtained. Pressurised fixation of the vasculature prior to injection of contrast material may also yield more accurate estimates of inflated lumen sizes, but investigation of this approach is left for future study.

CONCLUSION

Unfortunately, I was unsuccessful in achieving accurate determinations of arterial lumen dimensions from the same contrast perfusion-based approach commonly used for mapping vascular networks in X-ray CT specimens. This shortcoming may be attributable to differences between the mechanical properties of the injection medium, arterial walls, and blood. Use of injection media with properties closer to that of blood may allow more accurate prediction of arterial lumen dimensions.

Perfusion rates obtained from microsphere perfusion matched those obtained from foramen measurement calculations in immature hens and roosters, but not in laying hens where the microsphere perfusion technique resulted in statistically greater values for blood flow rate. This divergence relates to a higher volumetric perfusion rate in the forebrain of laying hens than either roosters or immature hens. I hypothesize that this is due to an increased role of collateral cerebral circulation in mature laying hens which is not seen in roosters or immature hens. This may be related to behavioral changes associated with raising chicks. Regardless of the routes of perfusion, the role and triggers of cerebral metabolic increase at point-of-lay are as yet poorly understood. I conclude that microsphere perfusion supports the use of foramina measurements as a method of estimation of cerebral metabolism.

By adopting an approach to microsphere injection which avoids occlusion of the carotid arteries, measurements of cerebral perfusion which are elevated in respect to previous measurements of brain structure perfusion in chickens were obtained. Application of this approach stands to allow more in-depth examination of avian cognitive and sensory capabilities in the future.

CHAPTER 6

DISCUSSION AND CONCLUDING REMARKS

CEPHALIC AND ENCEPHALIC ARTERIAL ANATOMY AND PERFUSION IN BIRDS AND MAMMALS ASSESSED VIA MICROSPHERE CIRCULATION, CONTRAST INJECTION, AND OSTEOFORAMINA MEASUREMENT

The experimental work contained in this thesis explored cephalic circulation in birds and mammals and applied current best-practices in blood flow measurement to these clades. Four core topics were covered: the anatomy of cephalic arteries and their relationship to blood flow and metabolism in developing western grey kangaroos; the metabolic scaling of brain metabolism in an assortment of avian taxa with comparisons to mammals; the assessment of brain blood flow in chickens using different approaches; and the anatomy of the cephalic arteries of chickens. These taxa were chosen to represent their clades because of shared beneficial characteristics of their biology, detailed below.

In some groups of taxa cephalic and cerebral blood flow can be so complex that the use of the foramen technique becomes unworkable. This is generally due to the possession of intricate intertwined vascular structures called retia in the cephalic circulation, which complicate the use of the foramen technique. Fortunately however, the perfusion of the brain is much less complex in other groups, being essentially direct in most monotremes, marsupials, perissodactyls, rodents, lagomorphs, and primates (Baker 1979). Similarly, while some birds possess cryptic sources of cerebral perfusion, for many it is similar to what is seen in simpler mammals without retia. Therefore, the taxa studied in this thesis were specifically chosen for their straightforward brain perfusion regimes and availability. In particular, western grey kangaroos and domestic chickens were chosen as their common availability as commercial food species makes them good representatives of their groups and easy to obtain and study.

In the examination of the anatomy of cephalic arteries and their relationship to blood flow and metabolism in western grey kangaroos (Chapter 2) I performed dissections as a means to identify the vertebral arteries and their associated hard tissue structures. Blood flow rates through the internal carotid and vertebral arteries were calculated using the foramen technique and comparison was made with those of primates and marsupials recalculated from data in the literature. I found that internal carotid arteries supply about 70-80% of the brains cerebral blood flow with the vertebral arteries supplying 20-30%. Western grey ontogenetic development was found to occur in two phases, with initial rapid brain growth funded by a rapidly increasing cerebral blood flow

rate decreasing at a body mass of around 620 g. Brain growth and cerebral blood flow rate after this breakpoint occurs much more slowly.

In the assessment of the metabolic scaling of brain perfusion in a selection of avian taxa with comparisons to mammals (Chapter 3), I determined allometric scaling relationships for blood flow rate, brain size, and body mass in avian taxa ranging from ratites to passerines. Blood flow rates through the cerebral carotid arteries were examined across all avian taxa examined, and within individual avian clades, and comparison was made with those of mammals. Relationships noted in Aves as a whole do not hold when taxa are divided into their separate lineages, where a wide variety of exponents are resolved. Some avian clades exhibit exponents in line with those of the mammal groups, while others exhibit exponents, which are significantly and dramatically different from the mammal groups and other avian clades. Scaling relationships of psittacine and passerine birds were not dissimilar from the those of the mammalian groups, with passerine birds bearing the most similarities to haplorrhine primates of all clades examined. Palaeognaths presented the shallowest scaling exponents for all relationships examined, with palaeognath brain perfusion almost independent of body mass and palaeognath carotid canal radius almost independent of brain volume. Finally, I found that birds that have altricial young have steeper scaling exponents than birds that have precocial young, indicating this may be part of an adaptation towards higher cognition.

In Chapter 4 I produce a three-dimensional map of the cephalic arteries of the domestic fowl, *Gallus gallus domesticus* and compared and contrast against descriptions of other birds, principally galliforms. The major supply to the braincase ultimately comes from a branch of the common carotid artery – the cerebral carotid artery. Secondary supply comes from the ventral spinal artery. Three other arteries connect to the inside of the braincase: the ethmoid, orbital, and minor temporal cerebral artery. The minor temporal cerebral artery, which is a small artery supplying the cerebrum, was discovered and described for the first time. This chapter represents the first easily navigable map of the cerebral blood flow of the domestic chicken and will allow the scientific community to better comprehend the complexities of cerebral blood flow in avian taxa.

The final data chapter (Chapter 5) was a continuation of the work in chickens, where I present the results of investigations into the relationship between cerebral blood flow and regional brain metabolism using different approaches in major life history stages and gender groups of the domestic fowl, *Gallus gallus domesticus.* I use this chapter to provide justification for the methodology used in other chapters (foramen measurement) by contrasting with two other techniques of blood flow calculation – microsphere quantification and contrast assisted lumen measurement. Large arteries perfused with contrast media exhibit lumen sizes smaller than predicted from foramina dimensions, contrary to observations in smaller arteries. Cerebral blood flow values obtained via the use of fluorescent microspheres correlate with osteoforamina measurements in most

cases and validate the foramen technique as a method of estimation of cerebral perfusion. Adolescent hens present cerebral perfusion rates and volume-specific perfusion rates lower than laying hens. Roosters present cerebral perfusion rates that are not significantly different from either adolescent or laying hens, but volume-specific rates of perfusion in the telencephala, which are lower than in laying hens. I postulate that there is a relationship between sexual maturity or motherhood which drives an increase in cerebral metabolism in laying hens.

These four chapters advance the use of the foramen technique of to calculate blood flow and estimate brain metabolism. However, a core question behind the work in this thesis is whether brain metabolism can be taken as a proxy of cognition or intelligence. Examination of cerebral metabolism is a marked improvement over earlier gauges of cognition that relied on measurements of absolute or relative brain size. In the remainder of the thesis, I will discuss the relationship between brain metabolism, cognition, and intelligence, before addressing knowledge gaps and suggesting some future directions for research in this area.

DOES METABOLISM DESCRIBE COGNITION AND INTELLIGENCE?

The complex and interconnected nature of cognition and intelligence underlies the difficulty in their quantification and description. Intelligence describes the ability to understand perception, to learn, and to reason, while cognition describes the processes driving this thought or understanding, including experience, perception, and senses.

There seems to be a link between brain metabolism and cognitive capacity. Medical studies have outlined a connection between brain metabolism and cognition in a variety of conditions (Meyer *et al.* 1988; Reser 2009; Nikolaidis *et al.* 2016). The field of neuroenergetics considers brain metabolism to be at the core of cognitive processing (Strelnikov 2014; Geary 2018; Debatin 2020). Foramina studies have outlined a convincing trend relating cerebral perfusion to cognitive ability (Seymour *et al.* 2015; Seymour *et al.* 2016; Boyer and Harrington 2019; Harrington *et al.* 2019a; Seymour *et al.* 2019a). Cerebral metabolic studies of all sorts have coupled metabolism to cognition (Ohno *et al.* 1979; Bottoncetti *et al.* 1997; Karbowski 2012). This thesis presents many measurements of brain perfusion which may be taken as a measure of cognitive activity (Chapter 2, Chapter 3, Chapter 5). Logically, there should be some link between the concepts of brain energetics and cognition. However, this relationship is vague, likely due to the interrelated nature of cognition with intelligence.

Evidence for the link between brain metabolism and intelligence, on the other hand, is only vaguely established. Most work in the literature on this topic revolves around human studies of mental effort during tasks (Fidelman 1993; Larson *et al.* 1995; Neubauer

and Fink 2009; Nikolaidis *et al.* 2016), with little work undertaken on associating qualitative determinations of intelligence in animals with quantitative measures of brain metabolism or cognitive activity. The remainder of the work in the literature focuses either on one aspect or another without making any concerted effort to connect the two. It seems apparent that while brain blood flow can be linked to cognition, this is yet to be undertaken for intelligence.

The use of brain size measurements as proxies for cognitive capability or intelligence is common in the literature (Jerison 1977; Whiting and Barton 2003; Smaers *et al.* 2021), despite the fact that there is little reason that these should be good descriptors of the concepts. Conceptually, a large brain is thought to be indicative of intelligence due to the perceived increase in computational power afforded by more brain tissue (Spearman 1904; Font *et al.* 2019). However, this evaluation of relative brain size is ultimately simplistic as it ignores many of the complexities of the brain, including the regional differences that are important for particular aspects of cognition which may not directly translate to higher intelligence (Healy and Rowe 2007). The structures of the brain do not all possess the same degree of activity as one another, as demonstrated in Chapter 5 of this thesis with measures of metabolic intensity. Furthermore, brain morphologies are diverse across taxa as shown in figures in Chapter 2 and Chapter 3. As many techniques exist that allow measurement of cerebral blood flow rate or brain metabolism (Ohno *et al.* 1979; Bottoncetti *et al.* 1997; Karbowski 2012; Seymour *et al.* 2015), it is perhaps surprising that the use of brain size continues to pervade throughout the literature. Examination of brain metabolism is a marked improvement over earlier gauges of cognition that relied on brain size measurements, but it is necessary to concede that even this approach omits some of the detail that is required to properly relate intelligence.

Isolated from broader contextual information even measures of overall brain metabolism may not provide for comprehensive evaluation of cognition and intelligence. This is because measurement of overall brain metabolism may miss important intricacies in morphology and energetics at macro and micro regional scales. If this is the case, metabolic measurements – while more informative than other cognitive proxies – may indeed have some of the same problematic features of cognitive proxies in examination cognition and intelligence.

Comprehension of this variation in brain structure and energetics is critical due to the great diversity seen across taxa. In this thesis primates, marsupials, and birds were examined, yet until as recently as 2004 avian brains were not acknowledged in the literature for their fundamental differences in structure compared to mammalian brains (Reiner *et al.* 2004; Jarvis *et al.* 2005). This lack of proper understanding of the brains and behavioural capabilities of birds has pervaded science and culture for decades if not centuries with concepts such as the lack of olfaction in the aves, or lower degrees of

intelligence in ‘bird brained’ birds. This anthropocentric, mammalian centric, sluggish recognition of intelligence in taxa outside of *Homo sapiens* and those closely related to our species will take some work to correct.

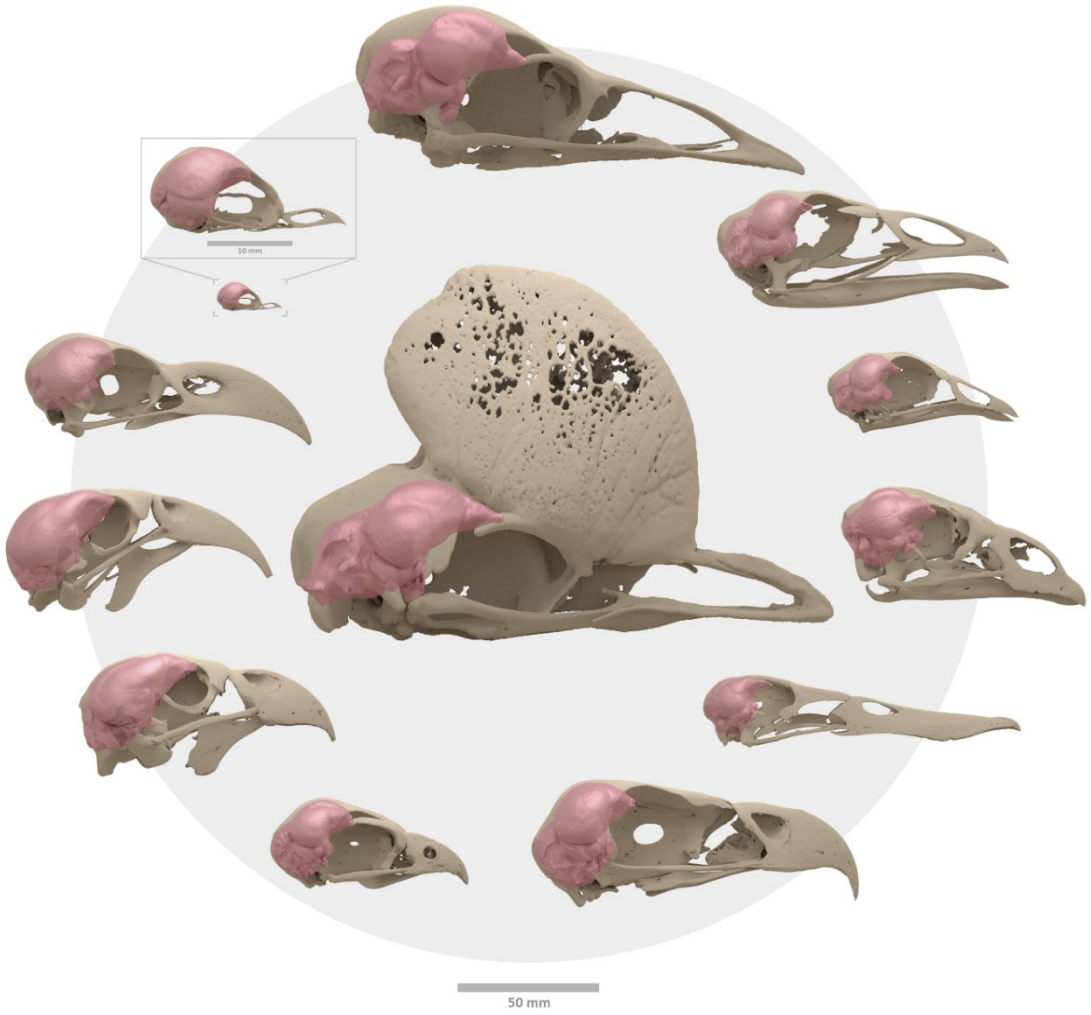

Figure 6-1. Different avian species present with vastly different brain architecture, presenting problems for the direct comparison of intelligence via measurements of absolute brain metabolism. Clockwise from top are an emu, turkey, malleefowl, cape barren goose, Australian shoveler, wedge-tailed eagle, peregrine falcon, kakapo, kea, white necked raven, and spotted pardalote. Centre is a southern cassowary.

In order to talk about the relationship between intelligence and brain metabolism we must find a way to delineate different investments in brain energetics between cognition (experience, perception, and senses) and higher intelligence (understanding, learning, and reasoning). Accounting for differences in energetic investment in olfaction, on visual acuity, on speech, on problem solving, or on any number of things, will be necessary before we can make statements on which animal is smarter than another which are quantitatively and objectively based. Further complexity is added to this task by variations in size, shape, and metabolic intensities (total and regional) in the brain between different taxa (Chapter 3, Chapter 5). It is my view that the interrelation of brain metabolism, cognition, and intelligence would be best described by probing brain metabolism

in greater detail than has been achieved in Chapter 2 and Chapter 3 of this thesis. Chapter 5 of this thesis presents a stronger methodology in this regard, allowing more in-depth discussion of the driving factors of cerebral metabolism and behaviour.

Using the methodologies currently available as of this writing, we could expect any difference in overall metabolic rate between brains with identical size and shape to be reflected in cognitive capability and intelligence. Assuming that there are generally fewer regional differences in structure and energetics in closely related species, it seems reasonable to expect the strength of the relation between overall brain metabolism and cognition and intelligence to be greater than those that compare disparate taxa. For example, findings by Seymour *et al.* (2016) regarding the evolution brain metabolism in Hominidae – that shared a common ancestor ~7 million years ago – may be more concrete than the findings presented herein comparing a broad spectrum of avian taxa which had 75 million years (Prum *et al.* 2015) for their brains to diverge from one another (Figure 6-1) (though obviously the speed of change of morphological characteristics is by no means constant in evolution).

As it currently stands linking cerebral perfusion directly to intelligence in disparate taxa is a difficult task. Some taxa that are perceived as highly intelligent have presented themselves with lower cerebral perfusion rates compared to taxa which are perceived as less intelligent. For instance, Chapter 2 outlines how diprotodonts present cerebral volumetric perfusion rates elevated above much of the haplorrhine taxa, despite primates outstripping diprotodonts in terms of social interaction, cognitive ability, innovation, and social learning (Reader and Laland 2002). Harrington et al. (2019b) report similar findings that euarchontan brains may be more energetically efficient than marsupial brains as a way of reducing the volumetric metabolic requirements of their large brains – a notion which I support. This inconsistency between reported intelligence and measured cerebral metabolism supports my notion that brain metabolism can be used as an objective quantitative measurement of cognition, but not of intelligence. Still, this discordance between brain metabolism (which logically should be dictated by cognition), and cognition and intelligence is somewhat enigmatic. I therefore present the below hypothesis;

$$\text{Cerebral Blood Flow} \propto \text{Cerebral Metabolism} \not\propto \text{Intelligence}$$

Proportionality of brain metabolism and intelligence

Cerebral blood flow must certainly be proportionate to cerebral metabolism, as dictated by the concept of symmorphosis; how an animal's 'design' is economical and matched to demand. Essentially, blood vessel configuration and architecture is designed in a way that best enables blood distribution with minimal energy loss (Weibel *et al.* 1991). If there is no cause requiring increased cerebral blood flow, then why provide it? A

cognate of the above hypothesis can be presented by further generalisation such that it can apply to other parts of the body, as so;

$$\text{Blood Flow} \propto \text{Metabolism} \not\propto \text{Function}$$

Proportionality of metabolism and function

This hypothesis seems to fit many casual observations of physiology. For instance examination of an animal's resting or maximal metabolic rate can inform us of the animal's activity levels, but gives us little information on its more nuanced behaviours. Similarly, looking at an animal's overall brain metabolism tell us little of the animal's intelligence.

Evolution is full of trade-offs. The evolution of life history traits are not independent of one another; improving the fitness or function of one trait often must come at the expense of the fitness or function of another trait (Morris 2009). These evolutionary trade-offs occur either due to resource limitation, or the conflicting requirements of opposing traits. Evolutionary history has many hopeful monsters, but no Darwinian monsters. The cognitive trade-off hypothesis advances that one such evolutionary trade-off occurred in the evolutionary history of *Homo sapiens* (Matsuzawa 2007; Matsuzawa 2009). In memory tests, human short-term memory is surpassed by that of chimpanzees, while in gauges of complex language skills humans far outclass chimpanzees. The cognitive trade-off hypothesis suggests that early hominids gained complex language at the sacrifice of short-term memory (Matsuzawa 2007; Matsuzawa 2009). Rationally, these cognitive trade-offs should extend to the evolutionary history of other taxa, and I posit that that is exactly what can be seen throughout the taxa studied in this thesis. Diprotodont marsupials are seen to have higher rates of volumetric cerebral perfusion than those of haplorrhine primates, despite diprotodonts outwardly possessing lesser intelligence than the primates (Chapter 2). In the Aves, the scaling of brain volume to body mass and brain perfusion to brain volume in Psittaciformes and Passeriformes aligns with those of haplorrhine primates, indicating that psittacine, passerine, and haplorrhine cognition evolved convergently (Chapter 3). However, the elevations of brain volume to body mass and brain perfusion to brain volume in galliform birds – game birds not ordinarily perceived as highly intelligent – are elevated above those of the psittacines, passerines, and haplorrhines (Chapter 3). No distinct one-to-one relationship between brain perfusion and intelligence can be identified from the work in this thesis. Whether this is due to an underestimation of the intelligence of some groups, or a misunderstanding of the relationship between cognition, intelligence, and brain perfusion remains to be established.

Ultimately, brain perfusion describes brain metabolism, brain metabolism describes cognition, and cognition describes the processes through which intelligence is supported. Comparison between cerebral metabolic measurements in different taxa stands to be a vast improvement over the current reliance on brain size measurements

when it comes to discussing cognition and intelligence. In future it may be possible to quantitatively examine intelligence between taxa as more measurements of brain metabolism on different regional scales become available. However, as these values remain sparsely reported in the literature, and as cognition and intelligence are so challenging to evaluate, it is difficult to begin to directly compare the efficacy of cerebral metabolic and brain size measurements at this time.

FUTURE PERSPECTIVES

Progress towards a better haemodynamic equation

One shortcoming of the current approach to cerebral blood flow calculation stems from the nature of the equations used. Currently, the best equations available for blood flow quantification are the mammalian equations from Seymour *et al.* (2019b). While these equations from Seymour *et al.* (2019b) are effective at describing flow rate, they are somewhat unintuitive as they are based on empirical measurements rather than being the result of logic regarding haemodynamics principles. These empirical equations can certainly be used to efficiently examine perfusion rates, but they fail to expand our understanding of how different haemodynamics factors are interrelated with one another. Nor do they set out to do so. It would be fantastic if there was a unified haemodynamics equation that encompassed all variables related to flow, but circulation is such a complex system that there is currently no such unified equation, and establishment of one may even prove impossible. Some things are still not accounted for and may be impossible to account for. As one example, low Hct values might be disadvantageous by resulting in a reduction in oxygen delivery to exercising tissues (Jenni *et al.* 2006). However, blood viscosity is reduced by reduced Hct, which can compensate any reductions in oxygen delivery by permitting an increase in blood flow rate (Breuer *et al.* 1995). Additionally, lower viscosity blood is easier for the heart to circulate, offering energetic efficiencies (Jenni *et al.* 2006). It is clear that many haemodynamic variables are closely interrelated (Figure 1-1 and Figure 1-2). Perhaps it is of little surprise that a universal equation in this area does not exist as calculations in fluid dynamics can be incredibly complex as those familiar with the famously unsolved Navier-Stokes equations can attest to. Hopefully in the future a unified haemodynamics equation will be developed.

Lumen size and the pressurised contrast perfusion technique

Given the use of the new empirical mammalian calculation (Seymour *et al.* 2019b), the current bottleneck in application of this technique is the determination of the lumen size. Over estimation of lumen size in foramina leads to an over estimation of blood flow rate while underestimation leads to an under estimation of blood flow rate. These mistakes have flow on effects when it comes to estimating the metabolism and metabolic

intensity of organs. This kind of error is particularly present in the case of foramina that carry structures other than a single artery as the space occupied by these other structures obviously cause over estimation of blood flow rates if not accounted for (Hu *et al.* 2020). The structures occupying the carotid foramina in humans are well documented; the carotid foramina carry only the internal carotid artery and a small accessory nerve that is buried in the fascia of the vessel wall (Paullus *et al.* 1977; von Overbeeke *et al.* 1991; Imai *et al.* 2022). Hence, blood flow calculations in the carotids are valid using this technique. In cases where a vein or nerve of significant size passes through the foramina along with the artery and are not accounted for, use of this technique will prove less accurate. A sensitivity study by Hu *et al.* (2020) showed that small errors in radius measurements can have a large effect on calculations of flow rate. A better way of determining the lumen size of arteries for measurement would be advantageous.

On the whole, the biggest shortcoming of the experiments presented in this thesis is that of the pressurised contrast perfusion technique (Chapter 5). I would argue that further studies should aim to improve upon the use of this technique simply due to its enormous potential. Hypothetically, a perfected version of this method, paired with the DCDVI (differential contrast dual vascular injection) technique of Porter and Witmer (2016) could be used to identify and quantify both arterial flow and venous drainage. This paired approach could allow a complete picture of individual vessels contributions to total and regional endocranial flow. In-depth examination of regional perfusion rates would give us a better understanding of cognition and intelligence, if we are able to tease apart exactly how different brain regions and their metabolic capacities impact these concepts.

Given the aforementioned shortcomings of the pressurised contrast perfusion technique for vascular calibre measurement (Chapter 5), one step in advancing this method would be identification of the best possible contrast agent. The perfect contrast experiment would be non-toxic, fast setting, able to fill arterial calibres at physiological pressures upon setting, capable of penetrating to capillary level (and be resolvable at high resolutions), would not induce shrinkage or otherwise damage tissues, and would allow follow up dissection and/or corrosion of cast materials. It is possible that a contrast material with all of these qualities is beyond the realms of obtainability. However, it is also possible that the correct contrast media and experimental method is within grasp but has yet to be correctly identified and implemented. Various contrast agents exist in angiography including Iodine-based and Gadolinium-based compounds (Goyen *et al.* 2000; Bremerich *et al.* 2007). Whether these compounds or some novel amalgamation of others is the answer is left to future investigations. Finally, further work on this technique also lies in the application of different technologies, such as Doppler ultrasound, live computed tomographic angiography, or functional magnetic resonance imaging.

Interesting candidate taxa

Perhaps the most interesting aspect to consider with regards to future use of the foramen technique for blood flow estimation is that of taxa that would make interesting candidates for study. From extant to extinct, there is a broad number of taxa that would inform upon the development and evolution of intelligence. These taxa represent interesting candidates due to unique cognitive capabilities, relationship to other groups, or prominence in the literature. I will briefly cover three groups of animals that I find particularly interesting: cetaceans, Aves and their ancestors, and marsupials.

The relative size of an organisms' brain has been frequently believed to be indicative of intelligence, with small brains relative to body mass being less cognitively complex than larger relative brains sizes (Whiting and Barton 2003). Among mammals, humans have the highest encephalisation quotient, immediately followed by cetaceans, with homo only exceeding that of cetaceans within the last few million years. (Marino 1996; Montgomery *et al.* 2013). Cognitive differences are apparent between humans and other mammals (Rilling 2006). Cetacea are comparatively large brained, with specific enlargement of the cerebellum, theorised to be due to the three-dimensional nature of their environment and reliance on echolocation (Clark *et al.* 2001). Cetaceans display complex memory capabilities, vocal behaviour, tool use, and self-recognition when subjected to mirror tests (Marino 2004). However there have been some significant doubts raised about both the structural complexity of the cetacean brain and its contribution to cognitive complexity (Patzke *et al.* 2015). It has been argued that the large cetacean brain functions more as a thermogenic organ than as a place of complex cognition (Manger 2006; Manger 2013). Although much work has been done into examining the intelligence of cetacean animals, little work has been undertaken regarding the quantification of the metabolic rate of the brain in this group. However, cephalic vascular patterns in cetaceans are inadequately described in the literature to allow straightforward use of the foramen technique. Cerebral blood flow in adult cetaceans is not derived solely from the internal carotid arteries but is complicated by numerous branching vascular networks that enter the skull through points that are not well described (Viamonte *et al.* 1968; Vogl and Fisher 1981; Geisler and Luo 1998). However, it is possible that examining cerebral perfusion in developing cetaceans could be more straight forward as the internal carotid is the sole rostral source of arterial flow to the developing brain in embryonic and early foetal ages in all mammals (Ashwell and Shulruf 2015; Ashwell and Shulruf 2016; Yu *et al.* 2020). One way or another, future examination of cetacean brain perfusion probably lies in the use of vascular contrast agents for mapping of vascular patterns.

The Aves presented in this thesis represent only a small snapshot of what is an extraordinarily diverse group of taxa (Chapter 3, Chapter 4, Chapter 5). Figure 3-2 displays the large gaps in the avian family tree that are yet to be filled in with further studies into

avian brain metabolism. Any expansion of the cursory peek into this area of study would be enlightening. However, among these 'gaps' in the avian tree, some groups stand out. Expansion of the accipitriformes and falconiformes analysis, and addition of other visual predators such as owls and night jars would inform on how these different groups tackle the 'trade' of cognition for visual acuity. Examination of avian taxa with distinct characteristics such as the columbiformes which possess magnetosensory abilities (Falkenberg *et al.* 2010), or the oilbirds and swiftlets which use echolocation would inform similarly (Brinkløv *et al.* 2013). New world vultures (cathartidae) would be interesting to examine alongside other avian taxa known for adept olfaction such as the procellariiformes (Bang 1966; Gagliardo *et al.* 2013; Grigg *et al.* 2017; Potier *et al.* 2019). Furthermore, there are many specimens of fossil avian taxa in natural history collections around the world which would make interesting candidates of their own. If we extend this expansion of the avian family tree by looking even further back into evolutionary history, non-avian dinosaurs are an enticing prospect. Since size is important in biology, dinosaurs continue to arouse great interest. Dinosaurs are renowned for their small brain volumes relative to their large body sizes. Evidence of the metabolic status and behaviour of extinct dinosaurs can be established from the state of their cerebral blood flow. Dinosaur crania have been examined to measure their cranial capacity and describe the path of cephalic arteries based upon fossil structures and studies of extant relatives (Martínez *et al.* 2016; Bourke *et al.* 2018; Porter and Witmer 2020). Determination of vasculature based solely on fossil evidence is limiting, but even a rudimentary glance at forces driving the behaviour and activity of long extinct taxa is greatly alluring.

There is some suggestion that carnivorous animals have larger brain sizes, or that predators are more intelligent than prey species (Martin 1984; Leonard *et al.* 2003). Meat eating is metabolically rewarding, and so eating more meat means the body has more metabolic energy to allocate. Whether this 'metabolic reward' can result in cognitive or metabolic changes in the brain could be determined through further comparative studies. One potential group which could be used to investigate this concept is the Dasyuromorphia (quolls, dunnarts, Tasmanian devils, and thylacines). The Diprotodontia and Dasyuromorphia are closely related australidelphian marsupials, however while diprotodonts trend towards herbivory, dasyuromorphs are largely carnivorous. As marsupials generally do not possess carotid retia (Baker 1979), dasyuromorphs are excellent candidates for the foramen technique. The dietary division between these groups could be explored in a future study to examine its impact on cerebral metabolism. Furthermore, adding Dasyuromorphia to the existing foramen technique dataset will inform upon allometric trajectories of a large proportion of the marsupialia, with the Didelphimorphia (opossums) and Peramelemorphia (bandicoots and bilbies) being the only other marsupial groups with a significant number of extant species.

Ultimately, comparison of existing flow rate and brain volume measurements with other groups of animals may reveal how evolution towards more metabolically active brains

occurs. Intelligence is ostensibly greatly beneficial for an organisms' survival but comes at no small metabolic cost. Determining whether or not the evolutionary trajectory of intelligence is unique to primates would have vast implications in the field of evolutionary biology.

A comment on the availability of descriptions of cerebral blood flow patterns

One important but understated finding from this thesis that ought to be highlighted is the lack of availability of descriptions of cerebral blood flow architecture in the literature. This thesis was the first to describe the cervical course of the vertebral arteries in western grey kangaroos; previously description of the path of the vertebral artery was essentially missing its atlantal segment. In western grey kangaroos the vertebral arteries pass through what this thesis terms the lateral atlantal foramina on their path to the braincase. This structure or an homologous one is present in dogs, pigs, horses, and ruminants, where it carries the vertebral artery (König *et al.* 2007; Schaller 2007; Evans and de Lahunta 2013; Tobias and Johnston 2013), and yet this foramen and its related structures had never been described in marsupials. That the course of such a major artery should be poorly described is a surprising omission.

This problem is not limited to the marsupials investigated here. Previous work in the literature has reported that arterial perfusion patterns in birds seem highly conserved (Porter and Witmer 2016). Indeed, in Chapter 4 I demonstrate a high level of conservation between chickens and turkeys (Porter and Witmer 2016). However, this is not to say that cerebral perfusion patterns were identical. A number of differences were observed between turkeys (Porter and Witmer 2016), guineafowl (Crowe and Crowe 1979), ducks and chickens. Of particular note is the discovery of what is labelled the minor temporal cerebral artery, which was not previously been reported in the literature despite the presence of the foramina, through which it passes in scans of other birds including many galliforms, anseriforms, and passerines (scans from Chapter 3, Chapter 4, and Chapter 5). Certainly, the overall significance of this small artery to the overall cerebral circulation is questionable, however I highlight its absence in the literature here as a symbol of a larger scale problem.

In birds even the directionality of some of the cephalic arteries is indeterminate at this time. In birds the cerebral carotid arteries principally supply the mid brain and forebrain via the encephalic, ventral optic lobe, cerebral, and ethmoid arteries. The orientation of the ethmoid and orbital arteries suggests that they allow blood to flow out of the brain towards the beak. However, whether these arteries actually act as a collateral source of blood flow into the brain has been much discussed the literature (Richards 1970; Kilgore *et al.* 1976; Kilgore *et al.* 1979; Midtgård 1984a; Midtgård 1984b; Arad *et al.* 1987; Arad 1990; Porter and Witmer 2016). Indeed, here my mapping of the blood flow pattern in chickens was inconclusive regarding the role of these arteries in supplying the braincase during normal circulation (Chapter 4).

Ultimately, while human circulation patterns are highly studied, the circulation patterns of other animals have been left wanting. In order to better understand cerebral metabolic rates and cognition in the future it will be important to develop a better understanding of these circulatory patterns. Without proper understanding of these blood flow patterns it will otherwise be hard to obtain accurate quantifications of cerebral blood flow.

CONCLUDING REMARKS

The work in this thesis has aimed to advance the use of the foramen technique of blood flow calculation. Much of the thesis is centred around the how blood flow relates to brain metabolism with inferences made about cognition and intelligence. However, the examination of intelligence is complex, and often subjective. Intelligence studies largely rely on comparative methods, evaluating the characteristics of the physiology and behaviour of one species in the light of another. This is true of the foramen technique presented throughout this thesis. Due to the limited scope of the current literature we currently only have a snapshot of the relationship between foramina dimensions, blood flow, cerebral metabolism, cognition, and intelligence. Currently, linking cerebral metabolism directly to intelligence across disparate taxa is a difficult task. Issues with the use of absolute brain metabolism for cognition and intelligence stem from differences in brain architecture and regional metabolism, and how different brain regions impact cognition and intelligence. For this reason, future investigations into the interactions of cerebral metabolism and intelligence should focus upon expanding the number of taxa assessed with this approach, on improving understanding of vascular pathways, and on exploring the drivers of regional brain metabolism. Hopefully, future studies will answer some of the many questions that this thesis has raised.

REFERENCES

Allan GH, Cassey P, Snelling EP, Maloney SK, Seymour RS (2014) Blood flow for bone remodelling correlates with locomotion in living and extinct birds. *Journal of Experimental Biology* **217**, 2956-2962.

Anetzberger H, Birkenmaier C (2016) The Microsphere Method for Investigating Bone Blood Flow. In 'Skeletal Circulation in Clinical Practice'. (Ed. RK Aaron) pp. 53-84. (World Scientific Singapore)

Anetzberger H, Thein E, Becker M, Zwissler B, Messmer K (2004) Microspheres accurately predict regional bone blood flow. *Clinical Orthopaedics and Related Research* **424**, 253-265.

Arad Z (1990) Avian brain cooling—a review. *Journal of Basic and Clinical Physiology and Pharmacology* **1**, 241.

Arad Z, Midtgård U (1984) Differences in the structure of the rete ophthalmicum among three breeds of domestic fowls, *Gallus gallus* f. domesticus (Aves). *Zoomorphology* **104**, 184-187.

Arad Z, Midtgård U, Bernstein MH (1987) Posthatching development of the rete ophthalmicum in relation to brain temperature of mallard ducks (*Anas platyrhynchos*). *Developmental Dynamics* **179**, 137-142.

Arad Z, Midtgård U, Bernstein MH (1989) Thermoregulation in turkey vultures. Vascular anatomy, arteriovenous heat exchange, and behavior. *Condor*, 505-514.

Archer M (1976) The basicranial region of marsupicarnivores (Marsupialia), interrelationships of carnivorous marsupials, and affinities of the insectivorous marsupial peramelids. *Zoological Journal of the Linnean Society* **59**, 217-322.

Aref MW, Akans E, Allen MR (2017) Assessment of regional bone tissue perfusion in rats using fluorescent microspheres. *Bone Reports* **6**, 140-144.

Arnold C, Matthews LJ, Nunn CL (2010) The 10kTrees website: A new online resource for primate phylogeny. *Evolutionary Anthropology: Issues, News, and Reviews* **19**, 114-118.

Ashwell KWS, Scofield RP (2008) Big birds and their brains: Paleoneurology of the New Zealand moa. *Brain, Behavior and Evolution* **71**, 151-166.

Ashwell KWS, Shulruf B (2015) Quantitative comparison of cerebral artery development in human embryos with other eutherians. *Journal of Anatomy* **227**, 286-296.

Ashwell KWS, Shulruf B (2016) Quantitative comparison of cerebral artery development in metatherians and monotremes with non-human eutherians. *Journal of Anatomy* **228**, 394-395.

Attwell D, Laughlin SB (2001) An energy budget for signaling in the grey matter of the brain. *Journal of Cerebral Blood Flow & Metabolism* **21**, 1133-45.

Bacon L, Thompson JP*, et al.* (1914). How it feels to be president: From the speech of president Wilson to the National Press Club at Washington, March 20, 1914. The Independent. New York, New York, Independent Publications Incorporated. **77:** 439.

Baker MA (1979) A brain-cooling system in mammals. *Scientific American* **240**, 130-9.

Balanoff AM, Bever GS*, et al.* (2015) Best practices for digitally constructing endocranial casts: examples from birds and their dinosaurian relatives. *Journal of Anatomy* **229**, 173-190.

Bang B (1966) The olfactory apparatus of tubenosed birds (Procellariiformes). *Cells Tissues Organs* **65**, 391-415.

Barfett JJ, Velauthapillai N*, et al.* (2014) Intra-vascular blood velocity and volumetric flow rate calculated from dynamic 4D CT angiography using a time of flight technique. *Int J Cardiovasc Imaging* **30**, 1383-92.

Basden K, Cooper D, Deane E (1996) Development of the blood-forming tissues of the tammar wallaby *Macropus eugenii*. *Reproduction, Fertility and Development* **8**, 989-994.

Baumel J (1975) Aves heart and blood vessels. *Sisson and Grossman's The Anatomy of the Domestic Animals (5th ed.)* **2**, 1968-2009.

Baumel JJ (1993) Handbook of avian anatomy: Nomina anatomica avium. *Publications of the Nuttall Ornithological Club (USA). no. 23.*

Baumel JJ, Gerchman L (1968) The avian intercarotid anastomosis and its homologue in other vertebrates. *American Journal of Anatomy* **122**, 1-18.

Bech C, Midtgård U (1981) Brain temperature and therete mirabile ophthalmicum in the Zebra finch (*Poephila guttata*). *Journal of Comparative Physiology B: Biochemical, Systemic, and Environmental Physiology* **145**, 89-93.

Bennett PM, Harvey PH (1985a) Brain size, development and metabolism in birds and mammals. *Journal of Zoology* **207**, 491-509.

Bennett PM, Harvey PH (1985b) Relative brain size and ecology in birds. *Journal of Zoology* **207**, 151-169.

Billerman S, Keeney B, Rodewald P, Schulenberg T, (Editors) (2020). Birds of the World. Cornell Laboratory of Ornithology, Ithaca, NY, USA. https://birdsoftheworld.org/bow/home [Accessed 2018-09-20].

Bock J, Braun K (1999) Filial imprinting in domestic chicks is associated with spine pruning in the associative area, dorsocaudal neostriatum. *European Journal of Neuroscience* **11**, 2566-2570.

Boelkins JN, Mueller WJ, Hall KL (1973) Cardiac output distribution in the laying hen during shell formation. *Comparative Biochemistry and Physiology Part A: Physiology* **46**, 735-743.

Boire D, Baron G (1994) Allometric comparison of brain and main brain subdivisions in birds. *Journal für Hirnforschung* **35**, 49-66.

Bonduriansky R, Day T (2003) The evolution of static allometry in sexually selected traits. *Evolution* **57**, 2450-2458.

Bottoncetti A, Pupi A, Meldolesi V (1997) Regional cerebral blood flow measured by microsphere technique in experimental animals: Technical notes for the use of albumin microspheres in rats. *Nuclear Medicine and Biology* **24**, 693-697.

Bourke JM, Porter WR, Witmer LM (2018) Convoluted nasal passages function as efficient heat exchangers in ankylosaurs (Dinosauria: Ornithischia: Thyreophora). *PLOS ONE* **13**, e0207381.

Boyer DM, Harrington AR (2018) Scaling of bony canals for encephalic vessels in euarchontans: Implications for the role of the vertebral artery and brain metabolism. *Journal of Human Evolution* **114**, 85-101.

Boyer DM, Harrington AR (2019) New estimates of blood flow rates in the vertebral artery of euarchontans and their implications for encephalic blood flow scaling: A response to Seymour and Snelling (2018). *Journal of Human Evolution* **128**, 93-98.

Boyer DM, Kirk EC*, et al.* (2016) Internal carotid arterial canal size and scaling in Euarchonta: Re-assessing implications for arterial patency and phylogenetic relationships in early fossil primates. *Journal of Human Evolution* **97**, 123-44.

Braun K, Scheich H, Schachner M, Heizmann CW (1985a) Distribution of parvalbumin, cytochrome oxidase activity and 14C-2-deoxyglucose uptake in the brain of the zebra finch. I Auditory and vocal motor systems. *Cell and Tissue Research* **240**, 101-115.

Braun K, Scheich H, Schachner M, Heizmann CW (1985b) Distribution of parvalbumin, cytochrome oxidase activity and 14C-2-deoxyglucose uptake in the brain of the zebra finch. II Visual system. *Cell and Tissue Research* **240**, 117-127.

Bremerich J, Bilecen D, Reimer P (2007) MR angiography with blood pool contrast agents. *European Radiology* **17**, 3017.

Breuer K, Lill A, Baldwin J (1995) Hematological and body-mass changes of small passerines overwintering in south-eastern Australia. *Australian Journal of Zoology* **43**, 31-38.

Brinkløv S, Fenton MB, Ratcliffe J (2013) Echolocation in Oilbirds and swiftlets. *Frontiers in Physiology* **4**.

Brody TB, Siegel PB, Cherry JA (1984) Age, body weight and body composition requirements for the onset of sexual maturity of dwarf and normal chickens. *British Poultry Science* **25**, 245-252.

Brown C (2015) Fish intelligence, sentience and ethics. *Animal Cognition* **18**, 1-17.

Browne JH, Gwynne DT (2022) Deceived, but not betrayed: static allometry suggests female ornaments in the long-tailed dance fly (*Rhamphomyia longicauda*) exaggerate condition to males. *Evolutionary Ecology*, 1-11.

Buchwalder T, Huber-Eicher B (2003) A brief report on aggressive interactions within and between groups of domestic turkeys (*Meleagris gallopavo*). *Applied Animal Behaviour Science* **84**, 75-80.

Burgoon DA, Kilgore DL, Motta PJ (1987) Brain temperature in the calliope hummingbird (*Stellula calliope*): A species lacking arete mirabile ophthalmicum. *Journal of Comparative Physiology B: Biochemical, Systemic, and Environmental Physiology* **157**, 583-588.

Burkart JM, Schubiger MN, van Schaik CP (2017) The evolution of general intelligence. *Behavioral and Brain Sciences* **40**.

Burnham KP, Anderson DR (2001) Kullback-Leibler information as a basis for strong inference in ecological studies. *Wildlife Research* **28**, 111-119.

Calder WA, III (1984) 'Size, Function, and Life History.' (Harvard University Press: Cambridge, Massachusetts, and London, England)

Cannon JR, Barker HR, Bradshaw SD, McDonald IR (1976) Gravity as the sole navigational aid to the newborn quokka. *Nature* **259**, 42-42.

Caputa M (2004) Selective brain cooling: A multiple regulatory mechanism. *Journal of Thermal Biology* **29**, 691-702.

Castoe TA, de Koning APJ*, et al.* (2011) Sequencing the genome of the Burmese python (*Python molurus bivittatus*) as a model for studying extreme adaptations in snakes. *Genome Biology* **12**, 406.

Changizi MA (2001) Principles underlying mammalian neocortical scaling. *Biological Cybernetics* **84**, 207-15.

Chokchaloemwong D, Prakobsaeng N, Sartsoongnoen N, Kosonsiriluk S, El Halawani M, Chaiseha Y (2013) Mesotocin and maternal care of chicks in native Thai hens (*Gallus domesticus*). *Hormones and Behavior* **64**, 53-69.

Clark CT, Smith KK (1993) Cranial osteogenesis in *Monodelphis domestica* (Didelphidae) and *Macropus eugenii* (Macropodidae). *Journal of Morphology* **215**, 119-149.

Clark DA, Mitra PP, Wang SSH (2001) Scalable architecture in mammalian brains. *Nature* **411**, 189-193.

Clarke J, Nicol S (1993) Blood viscosity of the little penguin, *Eudyptula minor*, and the Adélie penguin, *Pygoscelis adeliae*: Effects of temperature and shear rate. *Physiological Zoology* **66**, 720-731.

Cock AG (1966) Genetical aspects of metrical growth and form in animals. *Quarterly Review of Biology* **41**, 131-90.

Corfield JR, Wild JM, Hauber ME, Parsons S, Kubke MF (2008) Evolution of brain size in the Palaeognath lineage, with an emphasis on new zealand ratites. *Brain, Behavior and Evolution* **71**, 87-99.

Crowe T, Crowe A (1979) Anatomy of the vascular system of the head and neck of the helmeted guineafowl *Numida meleagris*. *Journal of Zoology* **188**, 221-233.

Dawson TJ (2012) 'Kangaroos.' (CSIRO Publishing: Collingwood, Victoria)

Dawson TJ, Finch E, Freedman L, Hume ID, Renfree MB, Temple-Smith PD (1989) Morphology and Physiology of the Metatheria. In 'Fauna of Australia '. (Eds DW Walton and BJ Richardson) pp. 401–1227. (AGPS Canberra: Canberra, Australia)

De Iuliis G (2007) 'The dissection of vertebrates : a laboratory manual.' (Elsevier/Academic Press: Boston)

De la Torre S, Snowdon CT (2009) Dialects in pygmy marmosets? Population variation in call structure. *American Journal of Primatology: Official Journal of the American Society of Primatologists* **71**, 333-342.

Debatin T (2020) Neuroenergetics and “general intelligence”: A systems biology perspective. *Journal of Intelligence* **8**, 31.

Dharmaretnam M, Vijtha V, Priyadharshini K, Jashini T, Vanthany K (2002) Ground scratching and preferred leg use in domestic chicks: Changes in motor control in the first two weeks post-hatching. *Laterality : Asymmetries of Body, Brain and Cognition.* **7**, 371-380.

Dial KP (2003) Evolution of avian locomotion: correlates of flight style, locomotor modules, nesting biology, body size, development, and the origin of flapping flight. *The Auk* **120**, 941-952.

Dobzhansky T (1973) Nothing in biology makes sense except in the light of evolution. *The American Biology Teacher* **35**, 125–129.

Dos Santos SE, Porfirio J, da Cunha FB, Manger PR, Tavares W, Pessoa L, Raghanti MA, Sherwood CC, Herculano-Houzel S (2017) Cellular scaling rules for the brains of marsupials: Not as “primitive” as expected. *Brain, Behavior and Evolution* **89**, 48-63.

Drzewiecki G, Field S, Moubarak I, Li JK-J (1997) Vessel growth and collapsible pressure-area relationship. *American Journal of Physiology-Heart and Circulatory Physiology* **273**, H2030-H2043.

du Boulay GH, Lawton M, Wallis A (1998) The story of the internal carotid artery of mammals: from Galen to sudden infant death syndrome. *Neuroradiology* **40**, 697-703.

Eastick DL, Tattersall GJ, Watson SJ, Lesku JA, Robert KA (2019) Cassowary casques act as thermal windows. *Scientific Reports* **9**, 1-7.

Emery NJ (2006) Cognitive ornithology: The evolution of avian intelligence. *Philosophical Transactions of the Royal Society of London B: Biological Sciences* **361**, 23-43.

Emery NJ, Clayton NS (2004a) The mentality of crows: convergent evolution of intelligence in corvids and apes. *Science (New York, N.Y.)* **306**, 1903.

Emery NJ, Clayton NS (2004b) The mentality of crows: Convergent evolution of intelligence in corvids and apes. *Science* **306**, 1903-1907.

Eslami P, Seo J-H, Rahsepar AA, Shafique A, Rollison SF, Lardo AC, Mittal R, Chen MY (2022) A noninvasive assessment of flow based on contrast dispersion in computed tomography angiography: A computational and experimental phantom study. *Journal of Biomechanical Engineering* **144**.

Evans HE, de Lahunta A (2013) 'Miller's Anatomy of the Dog.' (Elsevier Health Sciences: Pennsylvania, United States)

Falkenberg G, Fleissner G, Schuchardt K, Kuehbacher M, Thalau P, Mouritsen H, Heyers D, Wellenreuther G, Fleissner G (2010) Avian magnetoreception: Elaborate iron mineral containing dendrites in the upper beak seem to be a common feature of birds. *PLOS ONE* **5**, e9231.

Faury G, Maher GM, Li DY, Keating MT, Mecham RP, Boyle WA (1999) Relation between outer and luminal diameter in cannulated arteries. *American Journal of Physiology-Heart and Circulatory Physiology* **277**, H1745-H1753.

Fedde M, Wideman Jr R (1996) Blood viscosity in broilers: influence on pulmonary hypertension syndrome. *Poultry Science* **75**, 1261-1267.

Fedde MR, Guffy MM (1983) Routes of blood supply to the head of the Pekin duck. *Poultry Science* **62**, 1660-1664.

Fedde MR, Kiley JP, Powell FL, Scheid P (1982) Intrapulmonary CO_2 receptors and control of breathing in ducks: Effects of prolonged circulation time to carotid bodies and brain. *Respiration Physiology* **47**, 121-140.

Fidelman U (1993) Intelligence and the brain's energy consumption: what is intelligence? *Personality and Individual Differences* **14**, 283-286.

Fischer C, Schneider M, Carmeliet P (2006) Principles and Therapeutic Implications of Angiogenesis, Vasculogenesis and Arteriogenesis. In 'The Vascular Endothelium II'. (Eds S Moncada and A Higgs) pp. 157-212. (Springer: Dordrecht)

Font E, García-Roa R, Pincheira-Donoso D, Carazo P (2019) Rethinking the effects of body size on the study of brain size evolution. *Brain, Behavior and Evolution* **93**, 182-195.

Franklin DC, Garnett ST, Luck GW, Gutierrez-Ibanez C, Iwaniuk AN (2014) Relative brain size in Australian birds. *Emu: Austral Ornithology* **114**, 160-170.

Fristoe TS, Iwaniuk AN, Botero CA (2017) Big brains stabilize populations and facilitate colonization of variable habitats in birds. *Nature ecology & evolution* **1**, 1706-1715.

Gagliardo A, Bried J, Lambardi P, Luschi P, Wikelski M, Bonadonna F (2013) Oceanic navigation in Cory's shearwaters: evidence for a crucial role of olfactory cues for homing after displacement. *Journal of Experimental Biology* **216**, 2798-2805.

García-Cardeña G, Gimbrone MA (2006) Biomechanical Modulation of Endothelial Phenotype: Implications for Health and Disease. In 'The Vascular Endothelium II'. (Eds S Moncada and A Higgs) pp. 79-96. (Springer: Dordrecht)

Gayon J (2015) History of the concept of allometry. *American Zoologist* **40**, 748-758.

Geary DC (2018) Efficiency of mitochondrial functioning as the fundamental biological mechanism of general intelligence (g). *Psychological Review* **125**, 1028-1050.

Geisler JH, Luo Z (1998) Relationships of Cetacea to Terrestrial Ungulates and the Evolution of Cranial Vasculature in Cete. In 'The Emergence of Whales'. (Ed. JGM Thewissen) pp. 163-212. (Springer Science+Business Media: New York)

Gingerich P (2015) New partial skeleton and relative brain size in the Late Eocene Archaeocete *Zygorhiza Kochii* (Mammalia, Cetacea) from The Pachuta Marl of Alabama, with a note on contemporaneous Pontogeneus Brachyspondylus. *Contributions from the Museum of Paleontology, University of Michigan* **32**, 161-188.

Gjedde A, Monte SMDL, Caronna JJ (1977) Cerebral blood flow and oxygen consumption in rat, measured with microspheres or xenon. *Acta Physiologica Scandinavica* **100**, 273-281.

Goldman H, Sapirstein L (1973) Brain blood flow in the conscious and anesthetized rat. *American Journal of Physiology* **224**, 122-126.

Gould SJ (1966) Allometry and size in ontogeny and phylogeny. *Biological Reviews* **41**, 587 - 638.

Goyen M, Ruehm SG, Debatin JF (2000) MR-angiography: the role of contrast agents. *European Journal of Radiology* **34**, 247-256.

Greve JM, Les AS, Tang BT, Draney Blomme MT, Wilson NM, Dalman RL, Pelc NJ, Taylor CA (2006) Allometric scaling of wall shear stress from mice to humans: quantification using cine phase-contrast MRI and computational fluid dynamics. *American Journal of Physiology-Heart and Circulatory Physiology* **291**, H1700-H1708.

Gridley T (2010) Arteriovenous Patterning in the Vascular System. In 'Heart Development and Regeneration'. (Eds N Rosenthal and RP Harvey) pp. 529-541. (Academic Press: Boston)

Grigg NP, Krilow JM, Gutierrez-Ibanez C, Wylie DR, Graves GR, Iwaniuk AN (2017) Anatomical evidence for scent guided foraging in the turkey vulture. *Scientific Reports* **7**, 17408.

Guyton JR, Hartley CJ (1985) Flow restriction of one carotid artery in juvenile rats inhibits growth of arterial diameter. *American Journal of Physiology-Heart and Circulatory Physiology* **248**, H540-H546.

Hackett SJ, Kimball RT*, et al.* (2008) A phylogenomic study of birds reveals their evolutionary history. *Science* **320**, 1763-1768.

Harrington AR, Kuzawa CW, Boyer DM (2019a) Carotid foramen size in the human skull tracks developmental changes in cerebral blood flow and brain metabolism. *American Journal of Physical Anthropology* **169**, 161-169.

Harrington AR, Lange-Hodgson L, Weisbecker V, Boyer DM (2019b). Scaling of whole brain blood flow rate in marsupials and euarchontans. 88th Annual Meeting of the American Association of Physical Anthropologists. Cleveland, Ohio, United States, American Journal of Physical Anthropology.

Harris JJ, Attwell D (2012) The energetics of CNS white matter. *The Journal of Neuroscience* **32**, 356-371.

Harris Julia J, Jolivet R, Attwell D (2012) Synaptic energy use and supply. *Neuron* **75**, 762-777.

Harvey KJ, Warburton N (2010) Forelimb musculature of kangaroos with particular emphasis on the tammar wallaby *Macropus eugenii* (Desmarest, 1817). *Australian Mammalogy* **32**, 1-9.

Hawkins RA, Mans AM, Davis DW, Hibbard LS, Lu DM (1983) Glucose availability to individual cerebral structures is correlated to glucose metabolism. *Journal of Neurochemistry* **40**, 1013-8.

Healy SD, Rowe C (2007) A critique of comparative studies of brain size. *Proceedings of the Royal Society B: Biological Sciences* **274**, 453-464.

Herculano-Houzel S (2011a) Brains matter, bodies maybe not: the case for examining neuron numbers irrespective of body size. *Annals of the New York Academy of Sciences* **1225**, 191-199.

Herculano-Houzel S (2011b) Scaling of brain metabolism with a fixed energy budget per neuron: Implications for neuronal activity, plasticity and evolution. *PLOS ONE* **6**, e17514.

Hill L, Nabarro D (1895) On the exchange of blood-gases in brain and muscle during states of rest and activity. *The Journal of Physiology* **18**, 218.

Holliday CM, Ridgely RC, Balanoff AM, Witmer LM (2006) Cephalic vascular anatomy in flamingos (*Phoenicopterus ruber*) based on novel vascular injection and computed tomographic imaging analyses. *The Anatomical Record Part A: Discoveries in Molecular, Cellular, and Evolutionary Biology* **288**, 1031-1041.

Holt JP, Rhode EA, Kines H (1968) Ventricular volumes and body weight in mammals. *American Journal of Physiology* **215**, 704-715.

Hoskins P (1999) A review of the measurement of blood velocity and related quantities using Doppler ultrasound. *Proceedings of the Institution of Mechanical Engineers, Part H: Journal of Engineering in Medicine* **213**, 391-400.

Hossler FE, Olson KR (1984) Microvasculature of the avian eye: studies on the eye of the duckling with microcorrosion casting, scanning electron microscopy, and stereology. *American Journal of Anatomy* **170**, 205-21.

Hu Q (2021) Anatomy and physiology of bone perfusion in living and fossil birds as assessed by CT-scanning, microsphere distribution and osteoforamen measurement. Doctoral thesis, The University of Adelaide.

Hu Q, Nelson TJ, Seymour RS (2020) Bone foramen dimensions and blood flow calculation: best practices. *Journal of Anatomy* **236**, 357-369.

Hu Q, Nelson TJ, Seymour RS (2021) Regional femoral bone blood flow rates in laying and non-laying chickens estimated with fluorescent microspheres. *Journal of Experimental Biology* **224**.

Hu Q, Nelson TJ, Seymour RS (2022) Morphology of the nutrient artery and its foramen in relation to femoral bone perfusion rates of laying and non-laying hens. *Journal of Anatomy* **240**, 94-106.

Hu Q, Nelson TJ, Snelling EP, Seymour RS (2019) Femoral bone perfusion through the nutrient foramen during growth and locomotor development of western grey kangaroos (*Macropus fuliginosus*). *Journal of Experimental Biology* **221**, 168625.

Huxley JS, Teissier G (1936a) Terminologie et notation dans la description de la croissance relative. *Comptes Rendus des Seances de la Societe de Biologie et de Ses Filiales* **121**, 934–937.

Huxley JS, Teissier G (1936b) Terminology of relative growth. *Nature* **137**, 780-781.

Imai R, Mizutani K, Akiyama T, Horiguchi T, Takatsume Y, Toda M (2022) Imaging of the venous plexus of Rektorzik using CT-digital subtraction venography: a retrospective study. *Neuroradiology*.

Isler K, Christopher Kirk E, Miller JMA, Albrecht GA, Gelvin BR, Martin RD (2008) Endocranial volumes of primate species: scaling analyses using a comprehensive and reliable data set. *Journal of Human Evolution* **55**, 967-978.

Iwaniuk AN, Nelson JE (2003) Developmental differences are correlated with relative brain size in birds: a comparative analysis. *Canadian Journal of Zoology* **81**, 1913-1928.

Iwaniuk AN, Nelson JE, James HF, Olson SL (2004) A comparative test of the correlated evolution of flightlessness and relative brain size in birds. *Journal of Zoology* **263**, 317-327.

Jamniczky HA, Russell AP (2004) Cranial arterial foramen diameter in turtles: a quantitative assessment of size-independent phylogenetic signal. *Animal Biology* **54**, 417-436.

Jarvis ED, Güntürkün O*, et al.* (2005) Avian brains and a new understanding of vertebrate brain evolution. *Nature Reviews. Neuroscience* **6**, 151-159.

Jarvis ED, Mirarab S*, et al.* (2014) Whole-genome analyses resolve early branches in the tree of life of modern birds. *Science* **346**, 1320-1331.

Jenni L, Müller S, Spina F, Kvist A, Lindström Å (2006) Effect of endurance flight on haematocrit in migrating birds. *Journal of Ornithology* **147**, 531-542.

Jerison HJ (1973) 'Evolution of the brain and intelligence.' (Academic Press: New York)

Jerison HJ (1977) The theory of encephalization. *Annals of the New York Academy of Sciences* **299**, 146-160.

Johnston CE, Hartley C, Salisbury A-M, Wigley P (2012) Immunological changes at point-of-lay increase susceptibility to *Salmonella enterica* serovar enteritidis infection in vaccinated chickens. *PLOS ONE* **7**, e48195.

Jones MEH, Anderson CL, Hipsley CA, Müller J, Evans SE, Schoch RR (2013) Integration of molecules and new fossils supports a Triassic origin for Lepidosauria (lizards, snakes, and tuatara). *BMC Evolutionary Biology* **13**, 208.

Joseph N, Robinson F, Renema R, Thorsteinson K (2003) Comb growth during sexual maturation in female broiler breeders. *Journal of Applied Poultry Research* **12**, 7-13.

Kaihara S, Heerden PDV, Migita T, H. N. Wagner J (1968) Measurement of distribution of cardiac output. *Journal of Applied Physiology* **25**, 696-700.

Kamenskiy AV, MacTaggart JN, Pipinos II, Bikhchandani J, Dzenis YA (2012) Three-dimensional geometry of the human carotid artery.

Kamilar JM, Cooper N (2013) Phylogenetic signal in primate behaviour, ecology and life history. *Philosophical Transactions of the Royal Society of London B: Biological Sciences* **368**, 20120341.

Kamiya A, Togawa T (1980) Adaptive regulation of wall shear stress to flow change in the canine carotid artery. *American Journal of Physiology-Heart and Circulatory Physiology* **239**, H14-H21.

Kapusta A, Suh A, Feschotte C (2017) Dynamics of genome size evolution in birds and mammals. *Proceedings of the National Academy of Sciences* **114**, E1460-E1469.

Karbowski J (2007) Global and regional brain metabolic scaling and its functional consequences. *BMC Biology* **5**, 1-11.

Karbowski J (2011) Scaling of brain metabolism and blood flow in relation to capillary and neural scaling. *PLOS ONE* **6**, e26709.

Karbowski J (2012) Approximate invariance of metabolic energy per synapse during development in mammalian brains. *PLOS ONE* **7**, e33425.

Kear BP, Cooke BN, Archer M, Flannery TF (2007) Implications of a new species of the Oligo-Miocene kangaroo (Marsupialia: Macropodoidea) Nambaroo, from the Riversleigh World Heritage Area, Queensland, Australia. *Journal of Paleontology* **81**, 1147-1167.

Keklikoglou K, Arvanitidis C*, et al.* (2021) Micro-CT for biological and biomedical studies: A comparison of imaging techniques. *Journal of Imaging* **7**, 172.

Kilgore DL, Bernstein MH, Hudson DM (1976) Brain temperatures in birds. *Journal of Comparative Physiology B: Biochemical, Systemic, and Environmental Physiology* **110**, 209-215.

Kilgore DL, Boggs DF, Birchard GF (1979) Role of the rete mirabile ophthalmicum in maintaining the body-to-brain temperature difference in pigeons. *Journal of Comparative Physiology* **129**, 119-122.

Kilgore DL, Jr., Birchard GF, Boggs DF (1981) Brain temperatures in running quail. *Journal of Applied Physiology: Respiratory, Environmental and Exerccise Physiology* **50**, 1277-81.

Kjeld M, Ólafsson Ö (2008) Allometry (scaling) of blood components in mammals: connection with economy of energy? *Canadian Journal of Zoology* **86**, 890-899.

Klingenberg C, Zimmermann M (1992) Static, ontogenetic, and evolutionary allometry: A multivariate comparison in nine species of water striders. *American Naturalist* **140**, 601-620.

Kloos M, Weigel S, Luksch H (2019) Anatomy and physiology of neurons in layer 9 of the chicken optic tectum. *Frontiers in Neural Circuits* **13**, 1-16.

Knudsen EI (2004) Sensitive periods in the development of the brain and behavior. *Journal of Cognitive Neuroscience* **16**, 1412-1425.

Kodric-Brown A, Sibly RM, Brown JH (2006) The allometry of ornaments and weapons. *Proceedings of the National Academy of Sciences* **103**, 8733-8738.

König HE, Liebich H-G, Bragulla H (2007) 'Veterinary Anatomy of Domestic Mammals: Textbook and Colour Atlas.' (Schattauer Verlag: Stuttgart, Germany)

Krejza J, Arkuszewski M, Kasner SE, Weigele J, Ustymowicz A, Hurst RW, Cucchiara BL, Messe SR (2006) Carotid artery diameter in men and women and the relation to body and neck size. *Stroke* **37**, 1103-1105.

Ksepka DT, Balanoff AM*, et al.* (2020) Tempo and pattern of avian brain size evolution. *Current Biology* **30**, 2026-2036.e3.

Kumar D, Vinoth R, Raviraj A, Shankar CV (2017) Non-Newtonian and Newtonian blood flow in human aorta: a transient analysis. *Biomedical Research (India)* **28**, 3194-3203.

Kverková K, Marhounová L*, et al.* (2022) The evolution of brain neuron numbers in amniotes. *Proceedings of the National Academy of Sciences* **119**, e2121624119.

Langille BL (1996) Arterial remodeling: relation to hemodynamics. *Canadian Journal of Physiology and Pharmacology* **74**, 834-841.

Langille BL, Bendeck MP, Keeley FW (1989) Adaptations of carotid arteries of young and mature rabbits to reduced carotid blood flow. *American Journal of Physiology-Heart and Circulatory Physiology* **256**, H931-H939.

Larson GE, Haier RJ, LaCasse L, Hazen K (1995) Evaluation of a “mental effort” hypothesis for correlations between cortical metabolism and intelligence. *Intelligence* **21**, 267-278.

Leamy LJ, Atchley WR (1984) Static and evolutionary allometry of osteometric traits in selected lines of rats. *Evolution* **38**, 47 - 54.

Lee AK, Ward SJ (1989) Life Histories of Macropodoid Marsupials. In 'Kangaroos, Wallabies and Rat-Kangaroos'. (Eds GC Grigg, P Jarman, ID Hume and S Australian Mammal). (Surrey Beatty & Sons: Chipping Norton, New South Wales)

Lehoux S, Castier Y, Tedgui A (2006) Molecular mechanisms of the vascular responses to haemodynamic forces. *Journal of Internal Medicine* **259**, 381-392.

Lehoux S, Tedgui A (2003) Cellular mechanics and gene expression in blood vessels. *Journal of Biomechanics* **36**, 631-643.

Leonard WR, Robertson ML, Snodgrass JJ, Kuzawa CW (2003) Metabolic correlates of hominid brain evolution. *Comparative Biochemistry and Physiology Part A: Molecular & Integrative Physiology* **136**, 5-15.

Logothetis NK, Pauls J, Augath M, Trinath T, Oeltermann A (2001) Neurophysiological investigation of the basis of the fMRI signal. *Nature* **412**, 150-157.

Lou HC, Edvinsson L, MacKenzie ET (1987) The concept of coupling blood flow to brain function: Revision required? *Annals of Neurology* **22**, 289-297.

Makowski EL, Meschia G, Droegemueller W, Battaglia FC (1968) Measurement of umbilical arterial blood flow to the sheep placenta and fetus in utero. *Circulation Research* **23**, 623-631.

Manger P (2006) An examination of cetacean brain structure with a novel hypothesis correlating thermogenesis to the evolution of a big brain. *Biological Reviews of the Cambridge Philosophical Society* **81**, 293-338.

Manger P (2013) Questioning the interpretations of behavioral observations of cetaceans: is there really support for a special intellectual status for this mammalian order? *Neuroscience and Behavioral Physiology* **250**, 664-696.

Marino L (1996) What can dolphins tell us about primate evolution? *Evolutionary Anthropology: Issues, News, and Reviews* **5**, 81-86.

Marino L (2004) Cetacean brain evolution: Multiplication generates complexity. *Internation Journal of Comparative Psychology* **17**, 1-16.

Marino L (2017) Thinking chickens: a review of cognition, emotion, and behavior in the domestic chicken. *Animal Cognition* **20**, 127-147.

Martin RD (1981) Relative brain size and basal metabolic rate in terrestrial vertebrates. *Nature* **293**, 57-60.

Martin RD (1984) Body Size, Brain Size and Feeding Strategies. In 'Food Acquisition and Processing in Primates'. (Eds DJ Chivers, BA Wood and A Bilsborough) pp. 73-103. (Springer US: Boston, MA)

Martínez RDF, Lamanna MC, Novas FE, Ridgely RC, Casal GA, Martínez JE, Vita JR, Witmer LM (2016) A basal Lithostrotian Titanosaur (Dinosauria: Sauropoda) with a complete skull: Implications for the evolution and paleobiology of Titanosauria. *PLOS ONE* **11**, e0151661.

Matsuzawa T (2007) Comparative cognitive development. *Developmental Science* **10**, 97-103.

Matsuzawa T (2009) Symbolic representation of number in chimpanzees. *Current Opinion in Neurobiology* **19**, 92-98.

Maxwell MH, Robertson GW, McCorquodale CC (1992) Whole blood and plasma viscosity values in normal and ascitic broiler chickens. *British Poultry Science* **33**, 871-877.

McGinnis CH, Ringer RK (1965) Carotid and vertebral artery ligation in the chicken. *Poultry Science* **44**, 1600-1603.

Merrill GF, Russo RE, Halper JM (1981) Cardiac output distribution before and after endotoxin challenge in the rooster. *American Journal of Physiology-Regulatory, Integrative and Comparative Physiology* **241**, R67-R71.

Mespoulhès-Rivière C, Brandenberger O, Rossignol F, Robert C, Perkins J, Marie JP, Ducharme NG (2016) Feasibility, repeatability, and safety of ultrasound-guided stimulation of the first cervical nerve at the alar foramen in horses. *American Journal of Veterinary Research* **77 11**, 1245-1251.

Meyer JS, Rogers RL, Judd BW, Mortel KF, Sims P (1988) Cognition and cerebral blood flow fluctuate together in multi-infarct dementia. *Stroke* **19**, 163-169.

Midtgård U (1983) Scaling of the brain and the eye cooling system in birds: a morphometric analysis of the rete ophthalmicum. *Journal of Experimental Zoology Part A: Ecological Genetics and Physiology* **225**, 197-207.

Midtgård U (1984a) Blood vessels and the occurrence of arteriovenous anastomoses in cephalic heat loss areas of mallards, *Anas platyrhynchos* (Aves). *Zoomorphology* **104**, 323-335.

Midtgård U (1984b) Eye temperatures in birds and the significance of the rete ophthalmicum. *Videnskabelige Meddelelser Dansk Naturhistorisk Forening* **145**, 173-181.

Midtgård U, Arad Z, Skadhauge E (1983) Therete ophthalmicum and the relation of its size to the body-to-brain temperature difference in the fowl (*Gallus domesticus*). *Journal of Comparative Physiology* **153**, 241-246.

Minnich B, Lametschwandtner A (2003). Vascular corrosion casting–A basis for blood flow calculation in microvascular trees. International Workshop Advances in Vascular Casting. Salzburg, Austria.

Mitchell G, Skinner JD (2009) An allometric analysis of the giraffe cardiovascular system. *Comparative Biochemistry and Physiology Part A: Molecular & Integrative Physiology* **154**, 523-529.

Montgomery SH, Geisler JH, McGowen MR, Fox C, Marino L, Gatesy J (2013) The evolutionary history of cetacean brain and body size. *Evolution* **67**, 3339-3353.

Morris WF (2009) Life History. In 'The Princeton Guide to Ecology'. (Eds AL Simon, RC Stephen, HCJ Godfray, PK Ann, L Michel, BL Jonathan, W Brian and SW David) pp. 72-78. (Princeton University Press: Princeton, New Jersey, United States)

Mosso A (1892) Croonian lecture: The temperature of the brain, especially in relation to psychical activity. *Proceedings of the Royal Society of London* **51**, 83-85.

Muggeo VM (2008) segmented: an R package to fit regression models with broken-line relationships. *R News* **8**, 20-25.

Munn A, Dawson T (2003) Energy requirements of the red kangaroo (*Macropus rufus*): impacts of age, growth and body size in a large desert-dwelling herbivore. *Journal of Comparative Physiology B: Biochemical, Systemic, and Environmental Physiology* **173**, 575-582.

Nelson JE (1988) Growth of the Brain. In 'The Developing Marsupial: Models for Biomedical Research'. (Eds CH Tyndale-Biscoe and PA Janssens) pp. 86-100. (Springer-Verlag: Berlin)

Nelson JE (1992) Developmental staging in a marsupial *Dasyurus hallucatus*. *Anatomy and Embryology* **185**, 335-354.

Nesslinger CL (1956) Ossification centers and skeletal development in the postnatal *Virginia opossum*. *Journal of Mammalogy* **37**, 382-394.

Neubauer AC, Fink A (2009) Intelligence and neural efficiency. *Neuroscience & Biobehavioral Reviews* **33**, 1004-1023.

Neugebauer L (1845) Systema venosum avium cum eo mammalian et inprimis *hominis collatum*. *Novorum Actorum Academiae Caesareae Leopoldino-Carolinae Naturae Curiosorum* **21**, 519-697.

Neutze J, Wyler F, Rudolph A (1968) Use of radioactive microspheres to assess distribution of cardiac output in rabbits. *American Journal of Physiology-Legacy Content* **215**, 486-495.

Nicol C (2006) How animals learn from each other. *Applied Animal Behaviour Science* **100**, 58-63.

Nicol CJ (2015) Social Behaviour. In 'The Behavioural Biology of Chickens'. (Ed. CJ Nicol) pp. 104-127. (CAB International: Oxfordshire, UK)

Niedojadlo J, Bury A, Cichoń M, Sadowska ET, Bauchinger U (2018) Lower haematocrit, haemoglobin and red blood cell number in zebra finches acclimated to cold compared to thermoneutral temperature. *Journal of Avian Biology* **49**, jav-01596.

Nijhout HF, McKenna KZ (2019) Allometry, scaling, and ontogeny of form—An introduction to the symposium. In 'Proceedings of the Allometry, Scaling, and Ontogeny of Form'. Tampa, Florida. pp. 1275-1280. (Society for Integrative and Comparative Biology)

Nikolaidis A, Baniqued PL, Kranz MB, Scavuzzo CJ, Barbey AK, Kramer AF, Larsen RJ (2016) Multivariate associations of fluid intelligence and NAA. *Cerebral Cortex* **27**, 2607-2616.

Ninomiya H (2002) Vasculature of the ophthalmic rete in night herons (*Nycticorax nycticorax*): scanning electron microscopy of corrosion casts. *Veterinary Ophthalmology* **5**, 155-60.

Ødegaard S, Gilja OH, Gregersen H (2005) 'Basic and New Aspects of Gastrointestinal Ultrasonography.' (World Scientific Publishing: Singapore)

Oglat AA, Matjafri MZ, Suardi N, Oqlat MA, Abdelrahman MA, Oqlat AA (2018) A review of medical doppler ultrasonography of blood flow in general and especially in common carotid artery. *J Med Ultrasound* **26**, 3-13.

Ohno K, Pettigrew KD, Rapoport SI (1979) Local cerebral blood flow in the conscious rat as measured with 14C-antipyrine, 14C-iodoantipyrine and 3H-nicotine. *Stroke* **10**, 62-7.

Oktar SO, Yücel C, Karaosmanoglu D, Akkan K, Ozdemir H, Tokgoz N, Tali T (2006) Blood-flow volume quantification in internal carotid and vertebral arteries: Comparison of 3 different ultrasound techniques with phase-contrast MR imaging. *American Journal of Neuroradiology* **27**, 363-369.

Olkowicz S, Kocourek M, Lučan RK, Porteš M, Fitch WT, Herculano-Houzel S, Němec P (2016) Birds have primate-like numbers of neurons in the forebrain. *Proceedings of the National Academy of Sciences* **113**, 7255-7260.

Orme D, Freckleton R, Thomas G, Petzoldt T, Fritz S, Isaac N, Pearse W, Orme MD (2013) The caper package: Comparative analysis of phylogenetics and evolution in R. *R package version* **6**.

Orsi AM, Domeniconi RF, Artoni SMB, Joffre Filho G (2006) Carotid arteries in the dog: Structure and histophysiology. *International Journal of Morphology* **24**, 239-244.

Pagel M (1999) Inferring the historical patterns of biological evolution. *Nature* **401**, 877-884.

Pahwa PK, Pahwa GK (2014) 'Hydrogen Economy.' (The Energy and Resources Institute Press: New Delhi)

Patzke N, Spocter MA*, et al.* (2015) In contrast to many other mammals, cetaceans have relatively small hippocampi that appear to lack adult neurogenesis. *Brain Structure and Function* **220**, 361-383.

Paullus WS, Pait TG, Rhoton AL (1977) Microsurgical exposure of the petrous portion of the carotid artery. *Journal of Neurosurgery* **47**, 713-726.

Peltonen LM, Arieli Y, Marder J (1989) Brain temperature regulation of panting and non-panting pigeons exposed to extreme thermal conditions. *Comparative Biochemistry and Physiology Part A: Physiology* **92**, 91-96.

Pettit TN, Whittow GC, Grant GS (1981) Rete mirabile ophthalmicum in Hawaiian seabirds. *The Auk* **98**, 844-846.

Picasso MBJ, Tambussi CP, Degrange FJ (2010) Virtual reconstructions of the endocranial cavity of *Rhea americana* (aves, palaeognathae): Postnatal anatomical changes. *Brain, Behavior and Evolution* **76**, 176-184.

Pilbeam D, Gould SJ (1974) Size and scaling in human evolution. *Science* **186**, 892-901.

Pollen AA, Dobberfuhl AP, Scace J, Igulu MM, Renn SC, Shumway CA, Hofmann HA (2007) Environmental complexity and social organization sculpt the brain in Lake Tanganyikan cichlid fish. *Brain, Behavior and Evolution* **70**, 21-39.

Porter W, Witmer LM (2016) Avian cephalic vascular anatomy, sites of thermal exchange, and the rete ophthalmicum. *The Anatomical Record* **299**, 1461-1486.

Porter WR, Witmer LM (2020) Vascular patterns in the heads of Dinosaurs: Evidence for blood vessels, sites of thermal exchange, and their role in physiological thermoregulatory strategies. *The Anatomical Record* **303**, 1075-1103.

Potier S, Duriez O, Célérier A, Liegeois J-L, Bonadonna F (2019) Sight or smell: Which senses do scavenging raptors use to find food? *Animal Cognition* **22**, 49-59.

Prum RO, Berv JS, Dornburg A, Field DJ, Townsend JP, Lemmon EM, Lemmon AR (2015) A comprehensive phylogeny of birds (Aves) using targeted next-generation DNA sequencing. *Nature* **526**, 569-573.

Pyo J, Lowman RM (1959) The “ponticulus posticus” of the first cervical vertebra. *Radiology* **72**, 850-854.

R Core Team (2021). R: A language and environment for statistical computing. Vienna, Austria, R Foundation for Statistical Computing. Available at: https://www.R-project.org/.

Rattenborg NC, Martinez-Gonzalez D, Lesku JA (2009) Avian sleep homeostasis: convergent evolution of complex brains, cognition and sleep functions in mammals and birds. *Neuroscience and Biobehavioral Reviews* **33**, 253-270.

Rawson SD, Maksimcuka J, Withers PJ, Cartmell SH (2020) X-ray computed tomography in life sciences. *BMC Biology* **18**, 1-15.

Reader SM, Laland KN (2002) Social intelligence, innovation, and enhanced brain size in primates. *Proceedings of the National Academy of Sciences* **99**, 4436-4441.

Rees PM, Jepson P (1970) Measurement of arterial geometry and wall composition in the carotid sinus baroreceptor area. *Circulation Research* **26**, 461-467.

Reiner A, Perkel DJ*, et al.* (2004) Revised nomenclature for avian telencephalon and some related brainstem nuclei. *Journal of Comparative Neurology* **473**, 377-414.

Renfree MB (2006) Society for Reproductive Biology Founders' Lecture 2006. Life in the pouch: womb with a view. *Reproduction, Fertility and Development* **18**, 721-734.

Renfree MB, Holt AB, Green SW, Carr JP, Cheek DB (1982) Ontogeny of the brain in a marsupial (*Macropus eugenii*) throughout pouch life. *Brain Behavior and Evolution* **20**, 57-71.

Reser JE (2009) Alzheimer's disease and natural cognitive aging may represent adaptive metabolism reduction programs. *Behavioral and Brain Functions* **5**, 1-14.

Reynolds ML, Cavanagh ME, Dziegielewska KM, Hinds LA, Saunders NR, Tyndale-Biscoe CH (1985) Postnatal development of the telencephalon of the tammar wallaby (*Macropus eugenii*). An accessible model of neocortical differentiation. *Anatomy and Embryology* **173**, 81-94.

Richards S (1967) Anatomy of the arteries of the head in the domestic fowl. *Journal of Zoology* **152**, 221-234.

Richards S (1970) Brain temperature and the cerebral circulation in the chicken. *Brain Research* **23**, 265-268.

Ridgway S, Houser D*, et al.* (2006) Functional imaging of dolphin brain metabolism and blood flow. *Journal of Experimental Biology* **209**, 2902-2910.

Rilling JK (2006) Human and nonhuman primate brains: are they allometrically scaled versions of the same design? *Evolutionary Anthropology: Issues, News, and Reviews* **15**, 65-77.

Rogers LJ, Workman L (1993) Footedness in birds. *Animal Behaviour* **45**, 409-411.

Roth G (2015) Convergent evolution of complex brains and high intelligence. *Philosophical Transactions of the Royal Society of London B: Biological Sciences* **370**, 1-9.

Rubolini D, Liker A, Garamszegi LZ, Møller AP, Saino N (2015) Using the BirdTree.org website to obtain robust phylogenies for avian comparative studies: A primer. *Current Zoology* **61**, 959-965.

Runciman SIC, Baudinette RV, Gannon BJ, Lipsett J (1998) Morphometric analysis of postnatal lung development in the tammar wallaby: Light microscopy. *Respiration Physiology* **112**, 325-337.

Sandal PH, Damgaard M, Secher NH (2020) Comments on the Review 'Does mean arterial blood pressure scale with body mass in mammals? Effect of measurement of blood pressure' Acta Physiol (Oxf). *Acta Physiologica* **228**, e13407.

Sandrasegaran K (2014) Functional MR imaging of the abdomen. *Radiol Clin North Am* **52**, 883-903.

Sarkola T, Manlhiot C, Slorach C, Bradley TJ, Hui W, Mertens L, Redington A, Jaeggi E (2012) Evolution of the arterial structure and function from infancy to adolescence is related to anthropometric and blood pressure changes. *Arteriosclerosis, Thrombosis, and Vascular Biology* **32**, 2516-2524.

Saunders NR, Adam E, Reader M, Møllgård K (1989) *Monodelphis domestica* (grey short-tailed opossum): An accessible model for studies of early neocortical development. *Anatomy and Embryology* **180**, 227-236.

Scanes CG (2015) Blood. In 'Sturkie's Avian Physiology '. (Ed. CG Scanes) pp. 167-191. (Academic Press: San Diego)

Schaller B (2004) Physiology of cerebral venous blood flow: From experimental data in animals to normal function in humans. *Brain Research Reviews* **46**, 243-260.

Schaller O (2007) 'Illustrated veterinary anatomical nomenclature.' (Georg Thieme Verlag: Stuttgart. Germany)

Scheinberg P, Jayne HW, Blackburn LI, Rich M (1952) Studies of cerebral circulatory functions following intravenous administration of procaine hydrochloride. *American Medical Association Archives of Neurology & Psychiatry* **68**, 815-818.

Schjelderup-Ebbe T (1921) 'Beiträge zur Biologie und Sozial-und Individualpsychologie bei *Gallus domesticus*.' (Hans Alder: Greifswald)

Schmid-Schönbein H, Wells R, Goldstone J (1969) Influence of deformability of human red cells upon blood viscosity. *Circulation Research* **25**, 131-143.

Schneider NY, Fletcher TP, Shaw G, Renfree MB (2009) The olfactory system of the tammar wallaby is developed at birth and directs the neonate to its mother's pouch odours. *Reproduction* **138**, 849-57.

Schöning M, Hartig B (1998) The development of hemodynamics in the extracranial carotid and vertebral arteries. *Ultrasound in Medicine and Biology* **24**, 655-62.

Scott F (1906) On the metabolism and action of nerve cells. *Brain* **28**, 506-526.

Seddighi Y, Han H-C (2021) Buckling of arteries with noncircular cross sections: Theory and finite element simulations. *Frontiers in Physiology* **12**.

Sedlmayr JC (2002) Anatomy, evolution, and functional significance of cephalic vasculature in Archosauria. Ohio University.

Sedlmayr JC, Witmer LM (2002) Rapid technique for imaging the blood vascular system using stereoangiography. *The Anatomical Record* **267**, 330-336.

Serrat MA (2009) Measuring bone blood supply in mice using fluorescent microspheres. *Nature Protocols* **4**, 1749-1758.

Seymour RS, Angove SE, Snelling EP, Cassey P (2015) Scaling of cerebral blood perfusion in primates and marsupials. *Journal of Experimental Biology* **218**, 2631-2640.

Seymour RS, Bennett-Stamper CL, Johnston SD, Carrier DR, Grigg GC (2004) Evidence for endothermic ancestors of crocodiles at the stem of archosaur evolution. *Physiological and Biochemical Zoology* **77**, 1051-1067.

Seymour RS, Blaylock AJ (2000) The principle of Laplace and scaling of ventricular wall stress and blood pressure in mammals and birds. *Physiological and Biochemical Zoology* **73**, 389-405.

Seymour RS, Bosiocic V, Snelling EP (2016) Fossil skulls reveal that blood flow rate to the brain increased faster than brain volume during human evolution. *Royal Society Open Science* **3**, 160305.

Seymour RS, Bosiocic V, Snelling EP, Chikezie PC, Hu Q, Nelson TJ, Zipfel B, Miller CV (2019a) Cerebral blood flow rates in recent great apes are greater than in *Australopithecus* species that had equal or larger brains. *Proceedings of the Royal Society of London B: Biological Sciences* **286**, 20192208.

Seymour RS, Hu Q, Snelling EP (2020) Blood flow rate and wall shear stress in seven major cephalic arteries of humans. *Journal of Anatomy* **236**, 522-530.

Seymour RS, Hu Q, Snelling EP, White CR (2019b) Interspecific scaling of blood flow rates and arterial sizes in mammals. *Journal of Experimental Biology* **222**, jeb199554.

Seymour RS, Smith SL, White CR, Henderson DM, Schwarz-Wings D (2012) Blood flow to long bones indicates activity metabolism in mammals, reptiles and dinosaurs. *Proceedings of the Royal Society of London B: Biological Sciences* **279**, 451-456.

Seymour RS, Snelling EP (2019) Calculating brain perfusion of primates. *Journal of Human Evolution* **128**, 99-102.

Shedlock AM, Edwards SV (2009) Amniotes (amniota). In 'The Timetree of Life'. (Eds SB Hedges and S Kumar). (Oxford University Press: United States)

Simmonds MJ, Baskurt OK, Meiselman HJ, Pyne M, Kakanis M, Brenu E, Keane J, Christy R, Marshall-Gradisnik SM (2011) Haemorheology of the eastern grey kangaroo and the Tasmanian devil. *Australian Journal of Zoology* **59**, 26-34.

Singh I, Sandhu H, Herskovits M (1991) Bone vascularity. *Bone* **3**, 141-164.

Skilton MR, Boussel L, Bonnet F, Bernard S, Douek PC, Moulin P, Serusclat A (2011) Carotid intima–media and adventitial thickening: Comparison of new and established ultrasound and magnetic resonance imaging techniques. *Atherosclerosis* **215**, 405-410.

Slupe AM, Kirsch JR (2018) Effects of anesthesia on cerebral blood flow, metabolism, and neuroprotection. *Journal of Cerebral Blood Flow and Metabolism* **38**, 2192-2208.

Smaers JB, Rothman RS*, et al.* (2021) The evolution of mammalian brain size. *Science Advances* **7**, eabe2101.

Snelling EP, Taggart DA, Maloney SK, Farrell AP, Leigh CM, Waterhouse L, Williams R, Seymour RS (2015a) Scaling of left ventricle cardiomyocyte ultrastructure across development in the kangaroo *Macropus fuliginosus*. *Journal of Experimental Biology* **218**, 1767-1776.

Snelling EP, Taggart DA, Maloney SK, Farrell AP, Seymour RS (2015b) Biphasic allometry of cardiac growth in the developing kangaroo *Macropus fuliginosus*. *Physiological and Biochemical Zoology* **88**, 216-225.

Snowdon CT (2001) Social processes in communication and cognition in callitrichid monkeys: A review. *Animal Cognition* **4**, 247-257.

Soini P (1982) Ecology and population dynamics of the pygmy marmoset, *Cebuella pygmaea*. *Folia primatologica* **39**, 1-21.

Spataru C (2016) Morphological features of the axial skeleton to badger (*Meles meles*). *Lucrări ştiinţifice Seria medicină veterinară, Iași, Romania* **59**, 515-522.

Spearman C (1904) 'General intelligence,' objectively determined and measured. *The American Journal of Psychology* **15**, 201-293.

Stahl WR (1967) Scaling of respiratory variables in mammals. *Journal of Applied Physiology* **22**, 453-460.

Starck J (1993) Evolution of Avian Ontogenies. In 'Current Ornithology'. (Ed. DM Power) pp. 275-366. (Springer: Boston, Massachusetts)

Strelnikov K (2014) Neuroenergetics at the brain-mind interface: A conceptual approach. *Cognitive Processing* **15**, 297-306.

Stubbs DM (1992) The arcuate foramen. Variability in distribution related to race and sex. *Spine* **17**, 1502-1504.

Tandler J (1898) Zur vergleichenden Anatomie der Kopfarterien bei den Mammalia. *Denkschriften der mathematisch-naturwissenschaftlichen classe der kaiserlichen Akademie der Wissenschaften* **67**, 677-784.

Tattersall GJ, Arnaout B, Symonds MR (2017) The evolution of the avian bill as a thermoregulatory organ. *Biological Reviews* **92**, 1630-1656.

Tobias KM, Johnston SA (2013) 'Veterinary Surgery: Small Animal.' (Elsevier Health Sciences: Pennsylvania, United States)

Tommasi L (1999) Footedness in binocular and monocular chicks. *Laterality: Asymmetries of Body, Brain and Cognition* **4**, 89-95.

Tubbs RS, Johnson PC, Shoja MM, Loukas M, Oakes WJ (2007) Foramen arcuale: Anatomical study and review of the literature. *Journal of Neurosurgery: Spine* **6**, 31-34.

Tuculescu RA, Griswold JG (1983) Prehatching interactions in domestic chickens. *Animal Behaviour* **31**, 1-10.

Turner HN (1848) Observations relating to some of the foramina at the base of the skull in Mammalia, and on the classification of the order Carnivora. *Proceedings of the Zoological Society of London* **16**, 63-88.

Turnquist JE, Minugh-Purvis N (2012) Functional Morphology. In 'Nonhuman Primates in Biomedical Research (Second Edition)'. (Eds CR Abee, K Mansfield, S Tardif and T Morris) pp. 87-129. (Academic Press: Boston)

Tweed W, Minuck M, Mymin D (1972) Circulatory responses to ketamine anesthesia. *Anesthesiology: The Journal of the American Society of Anesthesiologists* **37**, 613-619.

Tzschentke B, Plagemann A (2006) Imprinting and critical periods in early development. *World's Poultry Science Journal* **62**, 626-637.

Tzschentke B, Rumpf M (2011) Embryonic development of endothermy. *Respiratory Physiology & Neurobiology* **178**, 97-107.

Vannucci RC, Vannucci SJ (2000) Glucose metabolism in the developing brain. *Seminars in Perinatology* **24**, 107-15.

Verduzco Mendoza a, Arch Tirado E, Contreras Figueroa ME, Leybón Ibarra J, Alfaro Rodríguez A, Licona Bonilla J (2009) Descripción anatómica de la vasculatura arterial carotidea-cerebral en el gallo doméstico *Gallus gallus* Linnaeus (Aves: Galliformes: Phasianidae). *Acta Zoológica Mexicana* **25**, 465-477.

Viamonte M, Morgane PJ, Galliano RE, Nagel EL, McFarland WL (1968) Angiography in the living dolphin and observations on blood supply to the brain. *American Journal of Physiology* **214**, 1225-1249.

Viscor G, Fuentes J, Palomeque J (1984) Blood rheology in the pigeon (*Columba livia*), hen (*Gallus gallus domesticus*), and black-headed gull (*Larus ridibundus*). *Canadian Journal of Zoology* **62**, 2150-2156.

Vogl AW, Fisher HD (1981) The internal carotid artery does not directly supply the brain in the Monodontidae (Order Cetacea). *Journal of Morphology* **170**, 207-214.

von Overbeeke JJ, Dujovny M, Dragovic L, Ausman JI (1991) Anatomy of the sympathetic pathways in the carotid canal. *Neurosurgery* **29**, 838-844.

Wang HU, Chen Z-F, Anderson DJ (1998) Molecular distinction and angiogenic interaction between embryonic arteries and veins revealed by ephrin-B2 and its receptor Eph-B4. *Cell* **93**, 741-753.

Wang R, Raykin J, Brewster LP, Gleason RL, Jr. (2017) A novel approach to assess the in situ versus ex vivo mechanical behaviors of the coronary artery. *J Biomech Eng* **139**, 0110101-7.

Wang Z, O'Connor TP, Heshka S, Heymsfield SB (2001) The reconstruction of Kleiber's law at the organ-tissue level. *The Journal of Nutrition* **131**, 2967-2970.

Warburton NM, Prideaux GJ (2021) The skeleton of *Congruus kitcheneri*, a semiarboreal kangaroo from the Pleistocene of southern Australia. *Royal Society Open Science* **8**, 202216.

Ward MR, Pasterkamp G, Yeung AC, Borst C (2000) Arterial remodeling mechanisms and clinical implications. *Circulation* **102**, 1186-1191.

Warren WC, Hillier LW*, et al.* (2008) Genome analysis of the platypus reveals unique signatures of evolution. *Nature* **453**, 175-183.

Watts CR, Stokes AW (1971) The social order of turkeys. *Scientific American* **224**, 112-119.

Weibel ER, Taylor CR, Hoppeler H (1991) The concept of symmorphosis: a testable hypothesis of structure-function relationship. *Proceedings of the National Academy of Sciences* **88**, 10357-10361.

Weinberg PD, Ethier CR (2007) Twenty-fold difference in hemodynamic wall shear stress between murine and human aortas. *Journal of Biomechanics* **40**, 1594-1598.

Weisbecker V, Goswami A (2010) Brain size, life history, and metabolism at the marsupial/placental dichotomy. *Proceedings of the National Academy of Sciences* **107**, 16216-16221.

Westerhof N (2006) 'Snapshots of Hemodynamics: An Aid for Clinical Research and Graduate Education.' (Springer: Dordrecht)

White CR (2003) Allometric analysis beyond heterogeneous regression slopes: Use of the Johnson-Neyman technique in comparative biology. *Physiological and Biochemical Zoology* **76**, 135-140.

White CR, Seymour RS (2014) The role of gravity in the evolution of mammalian blood pressure. *Evolution* **68**, 901-8.

Whiting B, Barton R (2003) The evolution of the cortico-cerebellar complex in primates: Anatomical connections predict patterns of correlated evolution. *Journal of Human Evolution* **44**, 3-10.

Wible JR (1986) Transformations in the extracranial course of the internal carotid artery in mammalian phylogeny. *Journal of Vertebrate Paleontology* **6**, 313-325.

Wilcox BR, Coulter NA, Rackley CE, Croom RD (1970) The effect of changing heart rate on blood flow, power dissipation, and resistance in the common carotid artery of man. *Annals of Surgery* **171**, 24-30.

Wilkes GE, Janssens PA (1986) Physiological and metabolic changes associated with weaning in the tammar wallaby, *Macropus eugenii. Journal of Comparative Physiology B: Biochemical, Systemic, and Environmental Physiology* **156**, 829-837.

Williams LE (1984) 'The voice and vocabulary of the wild turkey.' (Real Turkeys

Wilson SC, Sharp PJ (1975) Effects of progesterone and synthetic luteinizing hormone releasing hormone on the release of luteinizing hormone during sexual maturation in the hen (*Gallus domesticus*). *Journal of Endocrinology* **67**, 359-369.

Wolfenson D, Berman A, Frei YF, Snapir N (1978) Measurement of blood flow distribution by radioactive microspheres in the laying hen (*Gallus domesticus*). *Comparative Biochemistry and Physiology Part A: Physiology* **61**, 549-554.

Yamakami I, McIntosh TK (1989) Effects of traumatic brain injury on regional cerebral blood flow in rats as measured with radiolabeled microspheres. *Journal of Cerebral Blood Flow & Metabolism* **9**, 117-24.

Yu E, Ashwell KWS, Shulruf B (2020) Quantitative analysis of arterial supply to the developing brain in tetrapod vertebrates. *The Anatomical Record* **303**, 2309-2329.

Zeiler FA, Sader N, Gillman LM, Teitelbaum J, West M, Kazina CJ (2016) The cerebrovascular response to ketamine: A systematic review of the animal and human literature. *Journal of Neurosurgical Anesthesiology* **28**, 123-40.

Zeina A-R, Rosenschein U, Barmeir E (2007) Dimensions and anatomic variations of left main coronary artery in normal population: multidetector computed tomography assessment. *Coronary Artery Disease* **18**.

Zhou S, Fujita M, Yamamoto S (1999) Effects of feed intake and water intake on blood viscosity and plasma osmolality of broilers. *Japanese Poultry Society* **36**, 148-154.

APPENDIX A: 3D FIGURE INSTRUCTIONS

Instructions on the activation and use of a 3D PDF are given on the pages of this appendix as a means to assist in the use of Figure 4-3D.

Many mobile 3D PDF viewers will struggle with the 3D elements of this document due to the large size. To use 3D functionality, it is best to open this file on a desktop computer in Adobe Acrobat Reader, Adobe Acrobat Pro, or a similar program.

To activate 3D mode, first click on the chicken skull in the centre of the page. If 3D mode does not automatically activate, a pop-up banner message will appear at the top of the page stating that 3D content has been disabled. Enable 3D content by selecting "Trust this document always" in the Options drop down menu. Next, to activate 3D mode simply click on the chicken skull in the centre of the page again.

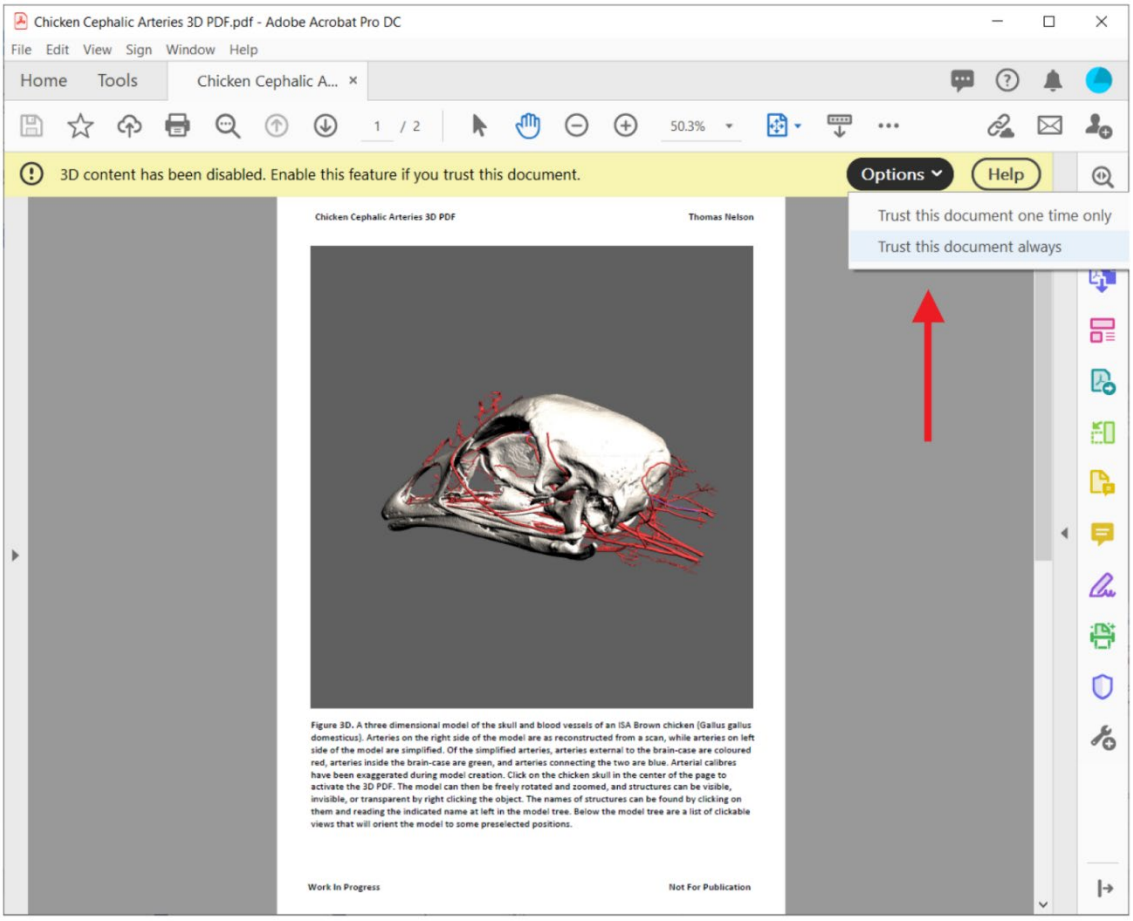

Figure I - 1. Instructions for activating Figure 4-3D.

Now that 3D mode is active, the model can then be freely rotated by clicking and dragging on the model and zoomed using the mouse wheel. The main controls for the model space are in the control bar highlighted in the green box in the below image. Changing

navigation mode will allow you to pan across the image which can be helpful to aid in viewing certain structures.

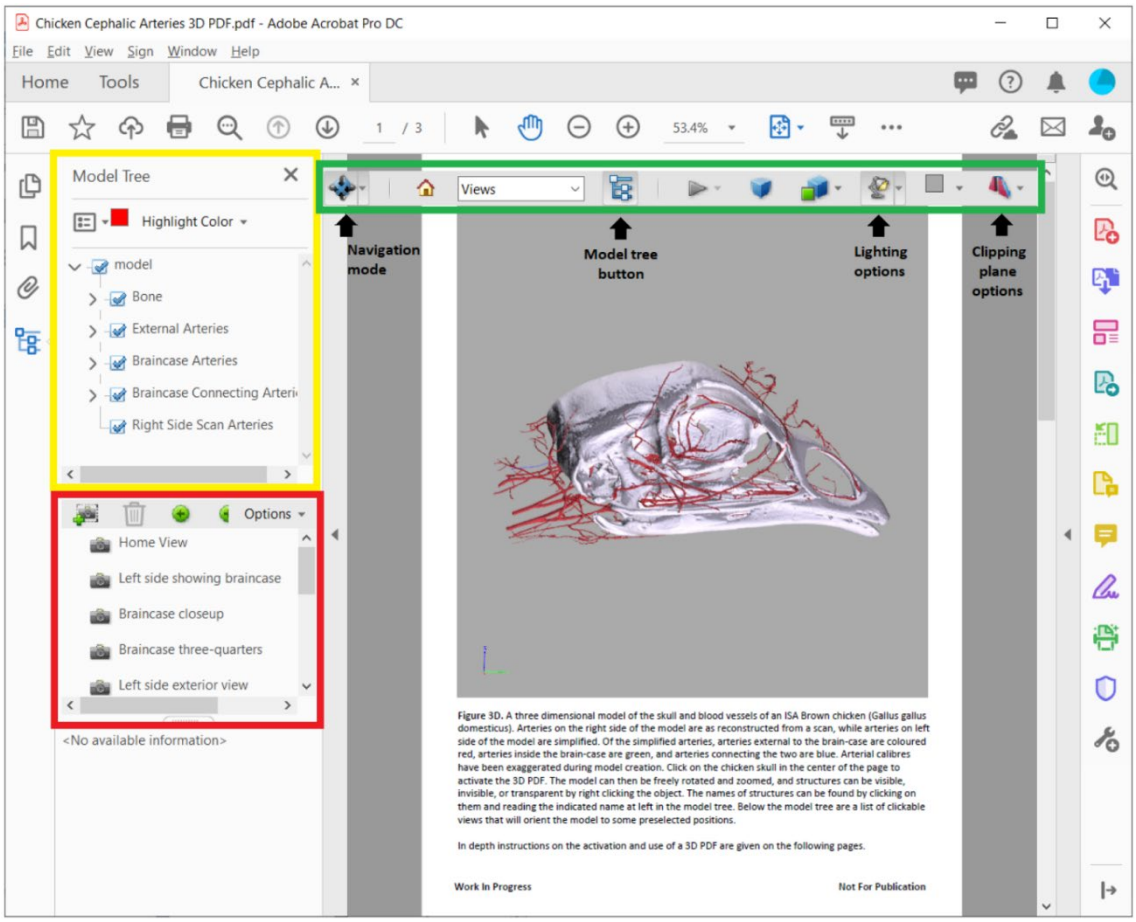

Figure I - 2. Diagram displaying the navigation tools for Figure 4-3D.

On the left of the window is the Model Tree, highlighted in yellow. If the model tree is not visible press the Model Tree button in the control bar. The Model Tree lists the structures displayed in the model. Clicking on the arrows will expand the groupings to show the names of the different structures in each. Pressing the check mark next to an object will toggle its visibility. Clicking on the names of structures will highlight them in the model and clicking on a structure in the model will highlight them in the model tree. Right clicking on a structure in the model tree allows you to zoom to that structure, isolate that structure (display only that structure), and render that structure transparent.

Below the model tree, highlighted in red are a list of clickable views that will orient the model to some preselected positions. Opening the model in a floating window (right click, View in Floating Window) will allow the model to remain open in a separate window for reference as pages are read.

APPENDIX B: SUPPLEMENTARY MATERIAL (DATA AND STATISTICS)

Chapter 2

Table S 2 - 1. Relationship between total cerebral arterial blood flow rate, brain volume and body mass across an ontological sequence in a large-bodied diprotodont marsupial, the western grey kangaroo, *Macropus fuliginosus*. Relationship between total cerebral arterial blood flow rate, brain volume and body mass across an ontological sequence in a large-bodied diprotodont marsupial, the western grey kangaroo, *Macropus fuliginosus*. Values for foramen radius and lumen radius are averages of left and right sides. Total $\dot{Q}$ is a sum of left and right arteries; for cerebral feeder arteries total $\dot{Q}$ is a sum of both left and right carotid and vertebral arteries.

Life stage	Specimen	Gender	Body mass (g)	Brain volume (ml)	Vertebral Arteries Foramen radius (cm)	Vertebral Arteries Lumen radius (cm)	Vertebral Arteries Total $\dot{Q}$ (ml min^{-1})	Carotid Arteries Foramen radius (cm)	Carotid Arteries Lumen radius (cm)	Carotid Arteries Total $\dot{Q}$ (ml min^{-1})	Cerebral feeder arteries Total $\dot{Q}$ (ml min^{-1})
In-pouch	R41	M	52	3.2	0.024	0.019	0.99	0.041	0.032	3.83	4.82
	R58	F	81	5.0	0.025	0.019	1.05	0.046	0.035	5.41	6.46
	R84	F	102	6.1	0.038	0.029	3.22	0.050	0.039	6.36	9.58
	R69	M	241	14	0.040	0.030	3.48	0.068	0.053	13.65	17.13
	R97	F	381	18	0.052	0.040	6.96	0.080	0.062	19.92	26.88
Post-pouch	R76	F	1002	26	0.055	0.042	7.87	0.113	0.087	44.42	52.29
	R96	M	1217	29	0.063	0.048	11.02	0.107	0.082	39.10	50.13
	R93	F	1791	35	0.073	0.056	15.98	0.121	0.093	52.08	68.06
	R92	F	2893	39	0.079	0.061	19.13	0.114	0.088	45.82	64.95
	R43	F	5568	41	0.086	0.066	23.48	0.136	0.105	69.12	92.60
	R46	F	7173	46	0.065	0.050	12.15	0.135	0.104	66.94	79.09
	R45	M	10889	47	0.088	0.068	25.04	0.139	0.107	71.83	96.87
	R49	F	14053	45	0.095	0.073	29.67	0.130	0.100	61.27	90.94
	R35	M	18147	52	0.098	0.076	32.34	0.146	0.112	79.91	112.25
	R33	F	21963	56	0.080	0.062	19.77	0.161	0.124	100.71	120.48
	R40	F	29258	71	0.081	0.063	20.47	0.166	0.128	107.84	128.30
	R51	F	32759	65	0.081	0.063	20.52	0.143	0.110	77.32	97.85
	R32	M	47299	74	0.108	0.083	39.95	0.181	0.139	130.73	170.68
	R50	M	62263	76	0.115	0.088	46.13	0.173	0.133	118.01	164.14

Table S 2 - 2. Comparison between lateral atlantal and carotid foramina measurements obtained by different measurement approaches. One approach saw minimum radius measurements obtained by measuring the minimum diameter of a foramen. An alternative approach uses a radius value obtained by measuring the area of a foramen and then converting that area to a radius value by assuming the area of a circle. This alternative approach allows us to obtain a radius measurement for blood flow calculation in cases where foramen cross sections are ellipsoid rather than perfectly circular. Ellipsoid foramina are common in diprotodonts. This approach is used as there is currently no blood flow quantification equation designed for ellipsoid foramina.

Life Stage	Specimen	Gender	Lateral Atlantal Foramina		Carotid Foramina	
			Minimum Radius (cm)	Area Converted to Radius (cm)	Minimum Radius (cm)	Area Converted to Radius (cm)
In-pouch	R41	M	0.022	0.024	0.035	0.041
	R58	F	0.024	0.025	0.043	0.046
	R84	F	0.036	0.038	0.046	0.050
	R69	M	0.039	0.040	0.059	0.068
	R97	F	0.049	0.052	0.071	0.080
Post-pouch	R76	F	0.051	0.055	0.101	0.113
	R96	M	0.056	0.063	0.094	0.107
	R93	F	0.067	0.073	0.114	0.121
	R92	F	0.069	0.079	0.096	0.114
	R43	F	0.074	0.086	0.115	0.136
	R46	F	0.046	0.065	0.115	0.135
	R45	M	0.075	0.088	0.112	0.139
	R49	F	0.065	0.095	0.102	0.130
	R35	M	0.062	0.098	0.130	0.146
	R33	F	0.056	0.080	0.140	0.161
	R40	F	0.065	0.081	0.130	0.166
	R51	F	0.063	0.081	0.110	0.143
	R32	M	0.086	0.108	0.151	0.181
	R50	M	0.095	0.115	0.135	0.173

Table S 2 - 3. Relationship between total carotid arterial blood flow rate, brain volume and body mass in haplorrhine primates. Values for body mass and brain volume are sourced from (Seymour *et al.* 2015). Foramen radius was recalculated by remeasuring the original microphotographs produced for measurement in the original paper (Seymour *et al.* 2015). Foramina in photographs were remeasured using a best fit ellipse (rather than measuring the minor diameter), this area was assumed to be circular, and its radius calculated to substitute into equations to estimate the rate of blood flow. Lumen radius, total internal carotid blood flow rate, and volumetric carotid blood flow rate are calculated according to the updated approach outlined in (Seymour *et al.* 2019a); lumen radius is calculated according to the updated ratio w = 0.30. Total internal carotid blood flow rate is calculated using *Equation 7*.

Species	Common Name	Family	Body mass M_b (g)	Brain volume V_{br} (ml)	Foramen radius r_{CF} (cm)	Lumen radius $r_{ICAlumen}$ (cm)	Total Blood Flow Rate $\dot{Q}_{ICA}$ (ml min^{-1})	Volumetric Flow Rate $\dot{Q}\cdot V_{br}^{-1}$ (ml min^{-1} ml^{-1})
Callithrix jacchus	Common marmoset	Callitrichidae	371.5	6.6	0.040	0.031	3.593	0.544
Callithrix pygmaea	Pygmy marmoset	Callitrichidae	116	7	0.046	0.035	4.951	0.707
Leontopithecus rosalia	Golden lion tamarin	Callitrichidae	620	12	0.051	0.040	6.709	0.559
Cacajao calvus	Bald-headed uakari	Cebidae	3165	100	0.119	0.092	50.343	0.503
Lagothrix lagotricha	Common woolly monkey	Cebidae	7280	110	0.126	0.097	56.939	0.518
Saimiri sciureus	Common squirrel monkey	Cebidae	790	20	0.058	0.044	8.875	0.444
Cercopithecus mitis	Blue monkey	Cercopithecidae	7930	71	0.085	0.066	22.931	0.323
Cercopithecus neglectus	De Brazza's monkey	Cercopithecidae	5740	65	0.106	0.081	38.008	0.585
Chlorocebus aethiops	Green monkey	Cercopithecidae	3620	67	0.112	0.086	43.557	0.650
Colobus satanas	Black colobus	Cercopithecidae	8910	79	0.093	0.071	27.764	0.351
Lophocebus albigena	Grey-cheeked mangabey	Cercopithecidae	7135	98	0.122	0.094	52.881	0.540
Macaca fascicularis	Crab-eating macaque	Cercopithecidae	4475	53.8	0.095	0.073	29.831	0.554
Macaca maura	Moor macaque	Cercopithecidae	9720	105	0.122	0.094	53.562	0.510
Macaca mulatta	Rhesus macaque	Cercopithecidae	8220	78.2	0.114	0.088	45.548	0.582
Macaca nemestrina	Pig-tailed macaque	Cercopithecidae	7575	111.5	0.121	0.093	52.294	0.469
Macaca nigra	Crested black macaque	Cercopithecidae	7680	150	0.132	0.101	63.545	0.424
Macaca ochreata	Booted macaque	Cercopithecidae	3950	98	0.117	0.090	48.651	0.496
Macaca radiata	Bonnet macaque	Cercopithecidae	3850	67	0.105	0.081	37.616	0.561
Macaca silenus	Long-tailed macaque	Cercopithecidae	7500	88.7	0.111	0.085	42.741	0.482
Mandrillus leucophaeus	Drill	Cercopithecidae	20000	160	0.161	0.124	100.368	0.627
Mandrillus sphinx	Mandrill	Cercopithecidae	26925	161.2	0.152	0.117	87.607	0.543
Nasalis larvatus	Proboscis monkey	Cercopithecidae	9820	78.5	0.116	0.089	46.999	0.599
Papio hamadryas	Hamadryas baboon	Cercopithecidae	16900	156.5	0.145	0.111	78.690	0.503
Presbytis melalophos	Mitred leaf monkey	Cercopithecidae	6590	70.5	0.116	0.089	47.178	0.669
Semnopithecus entellus	Gray langur	Cercopithecidae	12533	101.6	0.100	0.077	33.320	0.328
Trachypithecus obscurus	Dusky leaf monkey	Cercopithecidae	7900	105	0.119	0.091	49.657	0.473
Trachypithecus vetulus	Purple-faced leaf monkey	Cercopithecidae	7035	58	0.096	0.074	30.274	0.522
Gorilla gorilla	Western gorilla	Hominidae	145200	461	0.229	0.176	221.203	0.480
Homo sapiens	Modern humans	Hominidae	70000	1186	0.279	0.215	342.022	0.288
Pan troglodytes	Chimpanzee	Hominidae	49567	475	0.189	0.146	145.009	0.305
Pongo pygmaeus	Bornean orangutan	Hominidae	48290	375	0.183	0.141	134.730	0.359
Hylobates agilis	Agile gibbon	Hylobatidae	5880	115	0.120	0.092	51.147	0.445
Hylobates lar	Lar gibbon	Hylobatidae	5620	102.5	0.112	0.086	43.130	0.421
Hylobates syndactylus	Siamang	Hylobatidae	11900	120	0.151	0.116	86.854	0.724

Table S 2 - 4. Relationship between total carotid arterial blood flow rate, brain volume and body mass in Diprotodont marsupials. Values for body mass and brain volume are sourced from (Seymour *et al.* 2015). Foramen radius was recalculated by remeasuring the original microphotographs produced for measurement in the original paper (Seymour *et al.* 2015). Foramina in photographs were remeasured using a best fit ellipse (rather than measuring the minor diameter), this area was assumed to be circular, and its radius calculated to substitute into equations to estimate the rate of blood flow. Lumen radius, total internal carotid blood flow rate, and volumetric carotid blood flow rate are calculated according to the updated approach outlined in (Seymour *et al.* 2019a); lumen radius is calculated according to the updated ratio w = 0.30. Total internal carotid blood flow rate is calculated using *Equation 7*.

Species	Common Name	Family	Body mass M_b (g)	Brain volume V_{br} (ml)	Foramen radius (cm)	Lumen radius (cm)	Total $\dot{Q}_{ICA}$ (ml min^{-1})	Total $\dot{Q}/V_{br}$ (ml min^{-1} ml^{-1})
Acrobates pygmaeus	Feathertail glider	Acrobatidae	14	0.25	0.020	0.015	0.602	2.409
Cercartetus concinnus	Western pygmy possum	Burramyidae	17	0.28	0.019	0.015	0.521	1.862
Cercartetus nanus	Eastern pygmy possum	Burramyidae	70	0.55	0.024	0.019	1.006	1.830
Petaurus breviceps	Sugar glider	Petauridae	127	2.33	0.041	0.031	3.728	1.600
Pseudocheirus peregrinus	Common spotted cuscus	Phalangeridae	916	4.73	0.095	0.073	29.868	6.315
Hemibelideus lemuroides	Lemuroid ringtail possum	Pseudocheiridae	1026	3.35	0.046	0.035	4.996	1.491
Bettongia lesueur	Burrowing bettong	Potoroidae	1597	9.2	0.063	0.048	10.958	1.191
Aepyprymnus rufescens	Rufous bettong	Potoroidae	2500	13.32	0.068	0.052	13.267	0.996
Trichosurus vulpecula	Common brushtail possum	Phalangeridae	2532	9.8	0.062	0.048	10.663	1.088
Spilocuscus maculatus	Koala	Phalangeridae	4250	13.55	0.078	0.060	18.329	1.353
Phascolarctos cinereus	Common ringtail possum	Pseudocheiridae	5767	29.75	0.060	0.046	9.853	0.331
Dendrolagus matschiei	Huon tree-kangaroo	Macropodidae	6960	29	0.113	0.087	44.532	1.536
Notamacropus dorsalis	Black-striped Wallaby	Macropodidae	11250	26.6	0.142	0.109	75.424	2.835
Dendrolagus dorianus	Unicolored tree-kangaroo	Macropodidae	16500	38	0.118	0.090	48.818	1.285
Vombatus ursinus	Common wambat	Vombatidae	26000	60	0.124	0.095	54.932	0.916
Osphranter robustus	Common wallaroo	Macropodidae	29500	58.24	0.139	0.107	71.917	1.235
Lasiorhinus latifrons	Southern hairy-nosed wombat	Vombatidae	29917	56	0.138	0.106	70.642	1.261
Macropus fuliginosus	Western grey kangaroo	Macropodidae	41000	66.75	0.107	0.082	38.892	0.583
Osphranter rufus	Red kangaroo	Macropodidae	46250	51.575	0.171	0.131	114.955	2.229

Table S 2 - 5. Statistical information for the ANCOVAs relating body mass, brain volume, and total flow through carotid arteries across two phases of a western grey kangaroo life history sequence (part a).

Clade 1	Clade 2	X	Y	Slope				Elevation				Adjusted α	Significant at adjusted α	
				F-statistic	DFn	DFd	p-value	F-statistic	DFn	DFd	p-value		Slope	Elevation
In-Pouch	Post-Pouch	M_b	V_{br}	174.497	1	15	<0.001					0.0071	Y	-
			r_{ICF}	38.616	1	15	<0.001					0.0083	Y	-
			$\dot{Q}_{ICA}$	47.399	1	15	<0.001					0.0083	Y	-
		V_{br}	r_{ICF}	1.151	1	15	0.300	4.862	1	16	0.043			
			$\dot{Q}_{ICA}$	0.448	1	15	0.513	5.544	1	16	0.033			
	Overall	M_b	V_{br}	8.496	1	20	0.009	0.172	1	21	0.683	0.0071	N	N
			r_{ICF}	4.022	1	20	0.059	0.621	1	21	0.440			
			$\dot{Q}_{ICA}$	4.291	1	20	0.051	0.619	1	21	0.441			
		V_{br}	r_{ICF}	3.777	1	20	0.066	0.987	1	21	0.332			
			$\dot{Q}_{ICA}$	3.287	1	20	0.085	1.033	1	21	0.322			
	Interspecific	M_b	V_{br}	0.915	1	20	0.350	128.428	1	21	<0.001			
			r_{ICF}	0.537	1	20	0.472	17.651	1	21	<0.001			
			$\dot{Q}_{ICA}$	0.507	1	20	0.485	19.846	1	21	<0.001			
		V_{br}	r_{ICF}	0.079	1	20	0.781	1.705	1	21	0.206			
			$\dot{Q}_{ICA}$	0.067	1	20	0.798	1.314	1	21	0.265			
	Haplorrhini	M_b	V_{br}	0.575	1	35	0.453	2.307	1	36	0.138			
			r_{ICF}	0.701	1	35	0.408	13.960	1	36	0.001			
			$\dot{Q}_{ICA}$	0.920	1	35	0.344	13.937	1	36	0.001			
		V_{br}	r_{ICF}	0.077	1	35	0.783	18.812	1	36	<0.001			
			$\dot{Q}_{ICA}$	0.242	1	35	0.626	17.988	1	36	<0.001			
Post-Pouch	Overall	M_b	V_{br}	9.469	1	29	0.005					0.0071	Y	-
			r_{ICF}	10.125	1	29	0.003					0.0083	Y	-
			$\dot{Q}_{ICA}$	10.530	1	29	0.003					0.0083	Y	-
		V_{br}	r_{ICF}	0.161	1	29	0.691	0.148	1	30	0.703			
			$\dot{Q}_{ICA}$	0.549	1	29	0.465	0.193	1	30	0.664			

Continued in Table S 2 - 6. See Table S 2 - 6**Table S 3 - 13** for presentation information.

Table S 2 - 6. Statistical information for the ANCOVAs relating body mass, brain volume, and total flow through carotid arteries across two phases of a western grey kangaroo life history sequence (part b).

Clade 1	Clade 2	X	Y	Slope				Elevation				Adjusted α	Significant at adjusted α	
				F-statistic	DFn	DFd	p-value	F-statistic	DFn	DFd	p-value		Slope	Elevation
Post-Pouch	Interspecific	M_b	V_{br}	79.092	1	29	<0.001					0.0071	Y	-
			r_{ICF}	12.622	1	29	0.001					0.0083	Y	-
			$\dot{Q}_{ICA}$	14.642	1	29	0.001					0.0083	Y	-
		V_{br}	r_{ICF}	0.486	1	29	0.491	2.444	1	30	0.129			
			$\dot{Q}_{ICA}$	0.254	1	29	0.618	2.098	1	30	0.158			
	Haplorrhini	M_b	V_{br}	41.410	1	44	<0.001					0.0071	Y	-
			r_{ICF}	24.358	1	44	<0.001					0.0083	Y	-
			$\dot{Q}_{ICA}$	25.563	1	44	<0.001					0.0083	Y	-
		V_{br}	r_{ICF}	1.439	1	44	0.237	274.882	1	45	<0.001			
			$\dot{Q}_{ICA}$	1.010	1	44	0.320	273.124	1	45	<0.001			
Overall	Interspecific	M_b	V_{br}	59.288	1	34	<0.001					0.0071	Y	-
			r_{ICF}	5.524	1	34	0.025	137.986	1	35	<0.001	0.0083	N	Y
			$\dot{Q}_{ICA}$	7.248	1	34	0.011	121.457	1	35	<0.001	0.0083	N	Y
		V_{br}	r_{ICF}	6.926	1	34	0.013					0.0250	Y	-
			$\dot{Q}_{ICA}$	5.449	1	34	0.026	0.132	1	35	0.719	0.0250	N	N
	Haplorrhini	M_b	V_{br}	34.210	1	49	<0.001					0.0071	Y	-
			r_{ICF}	10.852	1	49	0.002					0.0083	Y	-
			$\dot{Q}_{ICA}$	10.539	1	49	0.002					0.0083	Y	-
		V_{br}	r_{ICF}	18.383	1	49	<0.001					0.0250	Y	-
			$\dot{Q}_{ICA}$	19.475	1	49	<0.001					0.0250	Y	-
Interspecific	Haplorrhini	M_b	V_{br}	0.003	1	49	0.954	214.172	1	50	<0.001			
			r_{ICF}	0.399	1	49	0.531	13.093	1	50	0.001			
			$\dot{Q}_{ICA}$	0.052	1	49	0.820	13.602	1	50	0.001			
		V_{br}	r_{ICF}	0.707	1	49	0.404	32.277	1	50	<0.001			
			$\dot{Q}_{ICA}$	0.117	1	49	0.734	32.711	1	50	<0.001			

See previous **Error! Reference source not found.**. When slopes were significantly different it was not possible to test whether elevations differed and cells for elevation are greyed out. Where tests were subjected to post-hoc Bonferroni correction cells appear in the three rightmost columns. When Bonferroni correction negated the significance between slopes, statistical information for comparison between elevations is given in greyed out cells to indicate that a result is from post-hoc testing.

Table S 2 - 6. Statistical information for the ANCOVAs relating body mass, brain volume, and total flow through cerebral feeding arteries across two phases of a western grey kangaroo life history sequence.

Clade 1	Clade 2	X	Y	Slope				Elevation				Adjusted α	Significant at adjusted α	
				F-statistic	DFn	DFd	p-value	F-statistic	DFn	DFd	p-value		Slope	Elevation
In-Pouch	Post-Pouch	M_b	r_{LAF}	8.926	1	15	0.009							
			$\dot{Q}_{VA}$	9.754	1	15	0.007							
			$\dot{Q}_{ICA+VA}$	61.134	1	15	<0.001					0.0167	Y	-
		V_{br}	r_{LAF}	0.107	1	15	0.748	0.160	1	16	0.695			
			$\dot{Q}_{VA}$	0.039	1	15	0.847	0.185	1	16	0.673			
			$\dot{Q}_{ICA+VA}$	0.505	1	15	0.488	4.977	1	16	0.041			
			$\dot{Q}_{ICA+VA} / V_{br}$	0.505	1	15	0.488	4.977	1	16	0.041			
	Overall	M_b	r_{LAF}	3.384	1	20	0.081	0.125	1	21	0.727			
			$\dot{Q}_{VA}$	3.455	1	20	0.078	0.133	1	21	0.719			
			$\dot{Q}_{ICA+VA}$	4.885	1	20	0.039	0.464	1	21	0.503	0.0167	N	N
		V_{br}	r_{LAF}	0.217	1	20	0.646	0.046	1	21	0.832			
			$\dot{Q}_{VA}$	0.157	1	20	0.696	0.043	1	21	0.837			
			$\dot{Q}_{ICA+VA}$	2.955	1	20	0.101	0.927	1	21	0.347			
			$\dot{Q}_{ICA+VA} / V_{br}$	2.955	1	20	0.101	0.927	1	21	0.347			
Post-Pouch	Overall	M_b	r_{LAF}	3.604	1	29	0.068	0.356	1	30	0.555			
			$\dot{Q}_{VA}$	3.945	1	29	0.057	0.391	1	30	0.537			
			$\dot{Q}_{ICA+VA}$	10.728	1	29	0.003					0.0167	Y	-
		V_{br}	r_{LAF}	0.001	1	29	0.981	0.005	1	30	0.944			
			$\dot{Q}_{VA}$	0.009	1	29	0.925	0.008	1	30	0.930			
			$\dot{Q}_{ICA+VA}$	0.422	1	29	0.521	0.182	1	30	0.673			
			$\dot{Q}_{ICA+VA} / V_{br}$	0.422	1	29	0.521	0.182	1	30	0.673			

When slopes were significantly different it was not possible to test whether elevations differed and cells for elevation are greyed out. Where tests were subjected to post-hoc Bonferroni correction cells appear in the three rightmost columns. When Bonferroni correction negated the significance between slopes, statistical information for comparison between elevations is given in greyed out cells to indicate that a result is from post-hoc testing.

Table S 2 - 6. Statistical information for the ANCOVAs of two sets of measurements of diprotodont marsupial and haplorrhine primate body masses, brain volumes, foramina dimensions, and carotid blood flow rates.

Clade 1	Clade 2	X	Y	Slope				Elevation				Adjusted α	Significant at adjusted α	
				F-statistic	DFn	DFd	p-value	F-statistic	DFn	DFd	p-value		Slope	Elevation
Haplorrhini Remeasured	Haplorrhini 2015	M_b	V_{br}	0.000	1	64	1.000	0.000	1	65	1.000			
			$\dot{Q}_{ICA}$	0.038	1	64	0.847	2.098	1	65	0.152			
			r_{ICF}	0.229	1	64	0.634	0.198	1	65	0.658			
		V_{br}	$\dot{Q}_{ICA}$	0.877	1	64	0.352	5.676	1	65	0.020			
			r_{ICF}	0.987	1	64	0.324	0.579	1	65	0.450			
			$\dot{Q}_{CA} / V_{br}$	6.613	1	64	0.012							
Diprotodont Remeasured	Diprotodontia 2015	M_b	V_{br}	0.000	1	34	1.000	0.000	1	35	1.000			
			$\dot{Q}_{ICA}$	2.546	1	34	0.120	31.691	1	35	<0.001			
			r_{ICF}	0.338	1	34	0.565	12.701	1	35	0.001			
		V_{br}	$\dot{Q}_{ICA}$	2.008	1	34	0.166	33.932	1	35	<0.001			
			r_{ICF}	0.151	1	34	0.700	12.850	1	35	0.001			
			$\dot{Q}_{CA} / V_{br}$	19.691	1	34	<0.001							

When slopes were significantly different it was not possible to test whether elevations differed and cells for elevation are greyed out. Where tests were subjected to post-hoc Bonferroni correction cells appear in the three rightmost columns. When Bonferroni correction negated the significance between slopes, statistical information for comparison between elevations is given in greyed out cells to indicate that a result is from post-hoc testing.

Chapter 3

Table S 3 - 1. Relationship between total cerebral arterial blood flow rate, brain volume and body mass across in Palaeognaths. Values for foramen radius and lumen radius are averages of left and right sides. Total $\dot{Q}$ is a sum of left and right arteries.

Specimen ID	Species	Common Name	Family	Young are	Body Mass M_b (g)	Brain Volume V_{br} (ml)	Foramen Radius r_{CF} (cm)	Total Flow Rate $\dot{Q}$ (ml min^{-1})	Volumetric Flow Rate $\dot{Q}\cdot Vbr^{-1}$ (ml min^{-1} ml^{-1})
B5051	*Apteryx owenii*	Kiwi	Apterygidae	Precocial	1415	8.71	0.056	6.83	0.79
B5075	*Dromaius novaehollandiae*	Emu	Casuariidae	Precocial	42500	25.47	0.065	9.81	0.39
B46991	*Casuarius casuarius*	Southern Cassowary	Casuariidae	Precocial	43500	35.74	0.071	12.51	0.35
B31329	*Rhea americana*	Rhea	Rheidae	Precocial	22500	19.75	0.054	6.35	0.32
B11411	*Struthio camelus*	Ostrich	Struthionidae	Precocial	123000	37.94	0.076	14.57	0.38
B31339	*Tinamus major*	Great Tinamous	Tinamidae	Precocial	975	3.75	0.047	4.55	1.22

Body masses and stage of hatchling development from Billerman *et al.* (2020).

Table S 3 - 2. Relationship between total cerebral arterial blood flow rate, brain volume and body mass across in Galliformes. Values for foramen radius and lumen radius are averages of left and right sides. Total $\dot{Q}$ is a sum of left and right arteries.

Specimen ID	Species	Common Name	Family	Young are	Body Mass M_b (g)	Brain Volume V_{br} (ml)	Foramen Radius r_{CF} (cm)	Total Flow Rate $\dot{Q}$ (ml min^{-1})	Volumetric Flow Rate $\dot{Q}\cdot Vbr^{-1}$ (ml min^{-1} ml^{-1})
B5084	*Leipoa ocellata*	Malleefowl	Megapodiidae	Precocial	2160	4.46	0.041	3.19	0.72
B31912	*Coturnix chinensis*	King Quail	Phasianidae	Precocial	39	0.52	0.028	1.14	2.18
B11478	*Coturnix novaezelandia pectoralis*	Stubble Quail	Phasianidae	Precocial	100	0.96	0.034	1.95	2.02
B34041	*Gallus gallus domesticus*	Domestic Chicken	Phasianidae	Precocial	968	3.72	0.057	7.17	1.93
B11543	*Pavo cristatus*	Peafowl	Phasianidae	Precocial	5000	7.18	0.065	9.95	1.39
B34049	*Meleagris gallopavo*	Turkey	Phasianidae	Precocial	7650	7.17	0.061	8.50	1.19

Body masses and stage of hatchling development from Billerman *et al.* (2020).

Table S 3 - 3. Relationship between total cerebral arterial blood flow rate, brain volume and body mass across in Anseriformes. Values for foramen radius and lumen radius are averages of left and right sides. Total $\dot{Q}$ is a sum of left and right arteries.

Specimen ID	Species	Common Name	Family	Young are	Body Mass M_b (g)	Brain Volume V_{br} (ml)	Foramen Radius r_{CF} (cm)	Total Flow Rate $\dot{Q}$ (ml min^{-1})	Volumetric Flow Rate $\dot{Q}\cdot Vbr^{-1}$ (ml min^{-1} ml^{-1})
B11913	*Anas crecca*	Eurasian Teal	Anatidae	Precocial	325	3.20	0.043	3.49	1.09
B31584	*Malacorhynchus membranaceus*	Pink Eared Duck	Anatidae	Precocial	376	3.08	0.042	3.39	1.10
B39358	*Anas gracilis*	Grey Teal	Anatidae	Precocial	500	3.70	0.041	3.13	0.85
B10905	*Anas rhynchotis*	Australian Shoveler	Anatidae	Precocial	699	3.41	0.041	3.25	0.95
B10357	*Anser anser (domesticus)*	Domestic Goose	Anatidae	Precocial	3315	13.16	0.053	5.93	0.45
B39767	*Cereopsis novaehollandiae*	Cape Barren Goose	Anatidae	Precocial	4135	9.05	0.057	7.20	0.80
B46127	*Cygnus Atratus*	Black Swan	Anatidae	Precocial	6225	12.96	0.078	15.36	1.19
B15140	*Cygnus olor*	Mute Swan	Anatidae	Precocial	7830	14.90	0.062	8.92	0.60

Body masses and stage of hatchling development from Billerman *et al.* (2020).

Table S 3 - 4. Relationship between total cerebral arterial blood flow rate, brain volume and body mass across in Accipitriformes. Values for foramen radius and lumen radius are averages of left and right sides. Total $\dot{Q}$ is a sum of left and right arteries.

Specimen ID	Species	Common Name	Family	Young are	Body Mass M_b (g)	Brain Volume V_{br} (ml)	Foramen Radius r_{CF} (cm)	Total Flow Rate $\dot{Q}$ (ml min^{-1})	Volumetric Flow Rate $\dot{Q}\cdot Vbr^{-1}$ (ml min^{-1} ml^{-1})
B48933	*Accipiter cirrhocephalus*	Collared Sparrowhawk	Accipitridae	Altricial	180	2.53	0.026	1.05	0.42
B48784	*Elanus axillaris*	Black-shouldered Kite	Accipitridae	Altricial	279	3.59	0.028	1.21	0.34
B55992	*Haliaeetus leucogaster*	White-bellied Sea-Eagle	Accipitridae	Altricial	2775	13.76	0.052	5.62	0.41
B39628	*Aquila audax*	Wedge-tailed Eagle	Accipitridae	Altricial	3601	17.08	0.056	6.79	0.40

Body masses and stage of hatchling development from Billerman *et al.* (2020).

Table S 3 - 5. Relationship between total cerebral arterial blood flow rate, brain volume and body mass across in Falconiformes. Values for foramen radius and lumen radius are averages of left and right sides. Total $\dot{Q}$ is a sum of left and right arteries.

Specimen ID	Species	Common Name	Family	Young are	Body Mass M_b (g)	Brain Volume V_{br} (ml)	Foramen Radius r_{CF} (cm)	Total Flow Rate $\dot{Q}$ (ml min^{-1})	Volumetric Flow Rate $\dot{Q}\cdot Vbr^{-1}$ (ml min^{-1} ml^{-1})
B46331	*Falco longipennis*	Australian Hobby	Falconidae	Altricial	256	3.67	0.032	1.63	0.45
B48782	*Falco peregrinus*	Peregrine Falcon	Falconidae	Altricial	920	7.32	0.042	3.40	0.47

Body masses and stage of hatchling development from Billerman *et al.* (2020).

Table S 3 - 6. Relationship between total cerebral arterial blood flow rate, brain volume and body mass across in Psittaciformes. Values for foramen radius and lumen radius are averages of left and right sides. Total $\dot{Q}$ is a sum of left and right arteries.

Specimen ID	Species	Common Name	Family	Young are	Body Mass M_b (g)	Brain Volume V_{br} (ml)	Foramen Radius r_{CF} (cm)	Total Flow Rate $\dot{Q}$ (ml min^{-1})	Volumetric Flow Rate $\dot{Q}\cdot Vbr^{-1}$ (ml min^{-1} ml^{-1})
B24332	*Nymphicus hollandicus*	Cockatiel	Cacatuidae	Altricial	90	2.64	0.031	1.59	0.60
B24336	*Callocephalon fimbriatum*	Gang-gang cockatoo	Cacatuidae	Altricial	280	8.27	0.038	2.60	0.31
B48439	*Probosciger aterrimus*	Palm cockatoo	Cacatuidae	Altricial	775	20.57	0.054	6.39	0.31
B10578	*Cacatua galerita*	Sulphur-crested cockatoo	Cacatuidae	Altricial	895	15.02	0.055	6.69	0.45
B47701	*Melopsittacus undalatus*	Budgerigar	Psittacidae	Altricial	28	1.15	0.024	0.83	0.72
B16736	*Neophema splendida*	Scarlet-chested parrot	Psittacidae	Altricial	40	1.14	0.023	0.73	0.64
B23984	*Cyclopsitta diophthalma*	Double-eyed fig parrot	Psittacidae	Altricial	41	2.07	0.035	2.07	1.00
B11807	*Aprosmictus scapularis*	Australian king parrot	Psittacidae	Altricial	242	4.82	0.038	2.69	0.56
B37527	*Eclectus roratus*	Eclectus parrot	Psittacidae	Altricial	485	8.49	0.040	3.04	0.36
B2321	*Nestor notabilis*	Kea	Strigopidae	Altricial	922	18.41	0.067	10.88	0.59
B5048	*Strigops habroptilus*	Kakapo	Strigopidae	Altricial	1975	16.49	0.045	4.10	0.25

Body masses and stage of hatchling development from Billerman *et al.* (2020).

Table S 3 - 7. Relationship between total cerebral arterial blood flow rate, brain volume and body mass across in Passeriformes. Values for foramen radius and lumen radius are averages of left and right sides. Total $\dot{Q}$ is a sum of left and right arteries.

Specimen ID	Species	Common Name	Family	Young are	Body Mass M_b (g)	Brain Volume V_{br} (ml)	Foramen Radius r_{CF} (cm)	Total Flow Rate $\dot{Q}$ (ml min^{-1})	Volumetric Flow Rate $\dot{Q}\cdot Vbr^{-1}$ (ml min^{-1} ml^{-1})
B55960	*Smicrornis brevirostris*	Weebill	Acanthizidae	Altricial	6	0.29	0.015	0.24	0.84
B36917	*Cyanocitta cristata*	Blue Jay	Corvidae	Altricial	85	2.93	0.032	1.74	0.59
B11191	*Pica pica*	Eurasian Magpie	Corvidae	Altricial	228	4.91	0.037	2.51	0.51
B32214	*Corvus bennetti*	Little Crow	Corvidae	Altricial	545	8.39	0.053	6.17	0.74
B38480	*Corvus tasmanicus*	Forest Raven	Corvidae	Altricial	650	11.85	0.055	6.59	0.56
B55786	*Corvus coronoides*	Australian Raven	Corvidae	Altricial	660	10.06	0.057	7.10	0.71
B29277	*Corvus albicollis*	White Necked Raven	Corvidae	Altricial	960	13.11	0.066	10.28	0.78
B40095	*Ephthianura tricolor*	Crimson Chat	Meliphagidae	Altricial	12	0.41	0.017	0.33	0.82
B56070	*Pardalotus punctatus*	Spotted Pardalote	Pardalotidae	Altricial	10	0.50	0.016	0.29	0.59

Body masses and stage of hatchling development from Billerman *et al.* (2020).

Table S 3 - 8. Statistical information for the ANCOVAs relating body mass, brain volume, foramina dimensions, and total carotid flow in the Aves, with comparisons to diprotodont and haplorrhine mammals (part a).

Clade 1	Clade 2	X	Y	Slope				Elevation				Adjusted α	Significant at adjusted α	
				F-statistic	DFn	DFd	p-value	F-statistic	DFn	DFd	p-value		Slope	Elevation
Aves	Palaeognathae	M_b	V_{br}	0.075	1	48	0.785	1.282	1	49	0.263			
			$\dot{Q}_{CA}$	3.792	1	48	0.057	1.804	1	49	0.186			
		V_{br}	$\dot{Q}_{CA}$	2.168	1	48	0.147	0.020	1	49	0.887			
			r_{CF}	2.007	1	48	0.163	0.031	1	49	0.861			
			$\dot{Q}_{CA} / V_{br}$	2.168	1	48	0.147	0.020	1	49	0.887			
	Galliformes	M_b	V_{br}	0.088	1	48	0.768	10.965	1	49	0.002			
			$\dot{Q}_{CA}$	0.107	1	48	0.744	0.079	1	49	0.780			
		V_{br}	$\dot{Q}_{CA}$	0.017	1	48	0.896	11.387	1	49	0.001			
			r_{CF}	0.008	1	48	0.930	11.252	1	49	0.002			
			$\dot{Q}_{CA} / V_{br}$	0.017	1	48	0.896	11.387	1	49	0.001			
	Anseriformes	M_b	V_{br}	0.094	1	50	0.761	1.171	1	51	0.284			
			$\dot{Q}_{CA}$	0.003	1	50	0.960	0.291	1	51	0.592			
		V_{br}	$\dot{Q}_{CA}$	0.036	1	50	0.850	3.238	1	51	0.078			
			r_{CF}	0.009	1	50	0.924	3.175	1	51	0.081			
			$\dot{Q}_{CA} / V_{br}$	0.036	1	50	0.850	3.238	1	51	0.078			
	Psittaciformes	M_b	V_{br}	4.492	1	53	0.039	9.097	1	54	0.039	0.0033	N	N
			$\dot{Q}_{CA}$	0.736	1	53	0.395	1.454	1	54	0.233			
		V_{br}	$\dot{Q}_{CA}$	0.157	1	53	0.693	3.396	1	54	0.071			
			r_{CF}	0.145	1	53	0.705	3.589	1	54	0.064			
			$\dot{Q}_{CA} / V_{br}$	0.157	1	53	0.693	3.396	1	54	0.071			
	Passeriformes	M_b	V_{br}	8.520	1	51	0.005	1.374	1	52	0.246	0.0033	N	N
			$\dot{Q}_{CA}$	15.419	1	51	<0.001					0.0036	Y	-
		V_{br}	$\dot{Q}_{CA}$	2.999	1	51	0.089	0.247	1	52	0.621			
			r_{CF}	2.662	1	51	0.109	0.177	1	52	0.676			
			$\dot{Q}_{CA} / V_{br}$	2.999	1	51	0.089	0.247	1	52	0.621			

Continued in Table S 3 - 9, Table S 3 - 10, Table S 3 - 11, Table S 3 - 12, and Table S 3 - 13. See Table S 3 - 13 for presentation information.

Table S 3 - 9. Statistical information for the ANCOVAs relating body mass, brain volume, foramina dimensions, and total carotid flow in the Aves, with comparisons to diprotodont and haplorrhine mammals (part b).

Clade 1	Clade 2	X	Y	Slope				Elevation				Adjusted α	Significant at adjusted α	
				F-statistic	DFn	DFd	p-value	F-statistic	DFn	DFd	p-value		Slope	Elevation
Aves	Diprotodontia	M_b	V_{br}	16.019	1	61	<0.001					0.0033	Y	-
			$\dot{Q}_{CA}$	13.601	1	61	<0.001					0.0036	Y	-
		V_{br}	$\dot{Q}_{CA}$	0.999	1	61	0.322	43.513	1	62	<0.001			
			r_{CF}	1.682	1	61	0.200	30.944	1	62	<0.001			
			$\dot{Q}_{CA}$ / V_{br}	16.994	1	61	<0.001	43.515	1	62	<0.001	0.0045	N	Y
	Haplorrhini	M_b	V_{br}	11.570	1	76	0.001					0.0033	Y	-
			$\dot{Q}_{CA}$	13.508	1	76	<0.001					0.0036	Y	-
		V_{br}	$\dot{Q}_{CA}$	2.234	1	76	0.139	3.308	1	77	0.073			
			r_{CF}	5.823	1	76	0.018	0.553	1	77	0.459	0.0100	N	N
			$\dot{Q}_{CA}$ / V_{br}	19.105	1	76	<0.001	3.262	1	77	0.074	0.0045	N	N
Palaeognathae	Galliformes	M_b	V_{br}	1.013	1	8	0.344	8.074	1	9	0.022			
			$\dot{Q}_{CA}$	2.919	1	8	0.126	0.104	1	9	0.756			
		V_{br}	$\dot{Q}_{CA}$	2.629	1	8	0.144	2.746	1	9	0.136			
			r_{CF}	2.464	1	8	0.155	2.732	1	9	0.137			
			$\dot{Q}_{CA}$ / V_{br}	2.629	1	8	0.144	2.746	1	9	0.136			
	Anseriformes	M_b	V_{br}	1.010	1	10	0.339	0.250	1	11	0.628			
			$\dot{Q}_{CA}$	5.018	1	10	0.049	0.600	1	11	0.455	0.0036	N	N
		V_{br}	$\dot{Q}_{CA}$	2.235	1	10	0.166	0.402	1	11	0.540			
			r_{CF}	2.246	1	10	0.165	0.425	1	11	0.529			
			$\dot{Q}_{CA}$ / V_{br}	2.235	1	10	0.166	0.402	1	11	0.540			
	Psittaciformes	M_b	V_{br}	10.438	1	13	0.007	19.310	1	14	<0.001	0.0033	N	Y
			$\dot{Q}_{CA}$	6.585	1	13	0.023	0.783	1	14	0.391	0.0036	N	N
		V_{br}	$\dot{Q}_{CA}$	3.025	1	13	0.106	6.510	1	14	0.024			
			r_{CF}	2.785	1	13	0.119	6.784	1	14	0.022			
			$\dot{Q}_{CA}$ / V_{br}	3.025	1	13	0.106	6.510	1	14	0.024			

See previous Table S 3 - 8. . Continued in Table S 3 - 10, Table S 3 - 11, Table S 3 - 12, and Table S 3 - 13. See Table S 3 - 13 for presentation information.

Table S 3 - 10. Statistical information for the ANCOVAs relating body mass, brain volume, foramina dimensions, and total carotid flow in the Aves, with comparisons to diprotodont and haplorrhine mammals (part c).

Clade 1	Clade 2	X	Y	Slope				Elevation				Adjusted α	Significant at adjusted α	
				F-statistic	DFn	DFd	p-value	F-statistic	DFn	DFd	p-value		Slope	Elevation
Palaeognathae	Passeriformes	M_b	V_{br}	28.597	1	11	<0.001					0.0033	Y	-
			$\dot{Q}_{CA}$	113.789	1	11	<0.001					0.0036	Y	-
		V_{br}	$\dot{Q}_{CA}$	24.518	1	11	<0.001					0.0125	Y	-
			r_{CF}	20.722	1	11	0.001					0.0100	Y	-
			$\dot{Q}_{CA} / V_{br}$	24.518	1	11	<0.001					0.0045	Y	-
	Diprotodontia	M_b	V_{br}	13.881	1	21	0.001					0.0033	Y	-
			$\dot{Q}_{CA}$	12.552	1	21	0.002					0.0036	Y	-
		V_{br}	$\dot{Q}_{CA}$	2.457	1	21	0.132	14.909	1	22	0.001			
			r_{CF}	2.375	1	21	0.138	10.464	1	22	0.004			
			$\dot{Q}_{CA} / V_{br}$	6.789	1	21	0.017	13.986	1	22	0.001	0.0045	N	Y
	Haplorrhini	M_b	V_{br}	9.248	1	36	0.004	87.472	1	37	<0.001	0.0033	N	Y
			$\dot{Q}_{CA}$	24.908	1	36	<0.001					0.0036	Y	-
		V_{br}	$\dot{Q}_{CA}$	16.955	1	36	<0.001					0.0125	Y	-
			r_{CF}	19.622	1	36	<0.001					0.0100	Y	-
			$\dot{Q}_{CA} / V_{br}$	38.157	1	36	<0.001					0.0045	Y	-
Galliformes	Anseriformes	M_b	V_{br}	0.043	1	10	0.841	32.940	1	11	<0.001			
			$\dot{Q}_{CA}$	0.056	1	10	0.817	0.088	1	11	0.773			
		V_{br}	$\dot{Q}_{CA}$	0.009	1	10	0.926	3.036	1	11	0.112			
			r_{CF}	0.001	1	10	0.978	3.050	1	11	0.111			
			$\dot{Q}_{CA} / V_{br}$	0.009	1	10	0.926	3.036	1	11	0.112			
	Psittaciformes	M_b	V_{br}	8.187	1	13	0.013	79.402	1	14	<0.001	0.0033	N	Y
			$\dot{Q}_{CA}$	0.980	1	13	0.340	0.504	1	14	0.490			
		V_{br}	$\dot{Q}_{CA}$	0.032	1	13	0.860	27.492	1	14	<0.001			
			r_{CF}	0.046	1	13	0.833	27.571	1	14	<0.001			
			$\dot{Q}_{CA} / V_{br}$	0.032	1	13	0.860	27.492	1	14	<0.001			

See previous Table S 3 - 8. , and Table S 3 - 9. Continued in Table S 3 - 11, Table S 3 - 12, and Table S 3 - 13. See Table S 3 - 13 for presentation information.

Table S 3 - 11. Statistical information for the ANCOVAs relating body mass, brain volume, foramina dimensions, and total carotid flow in the Aves, with comparisons to diprotodont and haplorrhine mammals (part d).

Clade 1	Clade 2	X	Y	Slope				Elevation				Adjusted α	Significant at adjusted α	
				F-statistic	DFn	DFd	p-value	F-statistic	DFn	DFd	p-value		Slope	Elevation
Galliformes	Passeriformes	M_b	V_{br}	36.113	1	11	<0.001					0.0033	Y	-
			$\dot{Q}_{CA}$	24.988	1	11	<0.001					0.0036	Y	-
		V_{br}	$\dot{Q}_{CA}$	3.160	1	11	0.103	31.937	1	12	<0.001			
			r_{CF}	2.496	1	11	0.142	28.903	1	12	<0.001			
			$\dot{Q}_{CA}$ / V_{br}	3.160	1	11	0.103	31.937	1	12	<0.001			
	Diprotodontia	M_b	V_{br}	9.758	1	21	0.005	13.646	1	22	0.001	0.0033	N	Y
			$\dot{Q}_{CA}$	4.356	1	21	0.049	0.280	1	22	0.602	0.0036	N	N
		V_{br}	$\dot{Q}_{CA}$	0.243	1	21	0.627	0.354	1	22	0.558			
			r_{CF}	0.307	1	21	0.586	0.002	1	22	0.967			
			$\dot{Q}_{CA}$ / V_{br}	2.875	1	21	0.105	10.519	1	22	0.004			
	Haplorrhini	M_b	V_{br}	5.959	1	36	0.020	138.160	1	37	<0.001	0.0033	N	Y
			$\dot{Q}_{CA}$	8.815	1	36	0.005	27.124	1	37	<0.001	0.0036	N	Y
		V_{br}	$\dot{Q}_{CA}$	1.942	1	36	0.172	16.040	1	37	<0.001			
			r_{CF}	3.765	1	36	0.060	29.805	1	37	<0.001			
			$\dot{Q}_{CA}$ / V_{br}	12.952	1	36	0.001	15.642	1	37	<0.001	0.0045	N	Y
Anseriformes	Psittaciformes	M_b	V_{br}	5.296	1	15	0.036	47.821	1	16	<0.001	0.0033	N	Y
			$\dot{Q}_{CA}$	0.555	1	15	0.468	0.868	1	16	0.366			
		V_{br}	$\dot{Q}_{CA}$	0.002	1	15	0.964	17.128	1	16	0.001			
			r_{CF}	0.024	1	15	0.878	16.940	1	16	0.001			
			$\dot{Q}_{CA}$ / V_{br}	0.002	1	15	0.964	17.128	1	16	0.001			
	Passeriformes	M_b	V_{br}	18.452	1	13	0.001					0.0033	Y	-
			$\dot{Q}_{CA}$	26.357	1	13	<0.001					0.0036	Y	-
		V_{br}	$\dot{Q}_{CA}$	2.931	1	13	0.111	5.188	1	14	0.040			
			r_{CF}	2.002	1	13	0.181	4.419	1	14	0.056			
			$\dot{Q}_{CA}$ / V_{br}	2.931	1	13	0.111	5.188	1	14	0.040			

See previous Table S 3 - 8. , Table S 3 - 9, and Table S 3 - 10. Continued in Table S 3 - 12, and Table S 3 - 13. See Table S 3 - 13 for presentation information.

Table S 3 - 12. Statistical information for the ANCOVAs relating body mass, brain volume, foramina dimensions, and total carotid flow in the Aves, with comparisons to diprotodont and haplorrhine mammals (part e).

Clade 1	Clade 2	X	Y	Slope				Elevation				Adjusted α	Significant at adjusted α	
				F-statistic	DFn	DFd	p-value	F-statistic	DFn	DFd	p-value		Slope	Elevation
Anseriformes	Diprotodontia	M_b	V_{br}	5.165	1	23	0.033	1.084	1	24	0.308	0.0033	N	N
			$\dot{Q}_{CA}$	2.319	1	23	0.141	11.647	1	24	0.002			
		V_{br}	$\dot{Q}_{CA}$	0.228	1	23	0.637	7.257	1	24	0.013			
			r_{CF}	0.225	1	23	0.640	4.016	1	24	0.057			
			$\dot{Q}_{CA} / V_{br}$	2.144	1	23	0.157	1.061	1	24	0.314			
	Haplorrhini	M_b	V_{br}	3.323	1	38	0.076	128.781	1	39	<0.001			
			$\dot{Q}_{CA}$	4.873	1	38	0.033	46.116	1	39	<0.001	0.0036	N	Y
		V_{br}	$\dot{Q}_{CA}$	1.691	1	38	0.201	2.597	1	39	0.115			
			r_{CF}	2.622	1	38	0.114	10.662	1	39	0.002			
			$\dot{Q}_{CA} / V_{br}$	9.585	1	38	0.004	2.552	1	39	0.118	0.0045	N	N
Psittaciformes	Passeriformes	M_b	V_{br}	0.274	1	16	0.608	1.766	1	17	0.202			
			$\dot{Q}_{CA}$	6.736	1	16	0.020	0.317	1	17	0.581	0.0036	N	N
		V_{br}	$\dot{Q}_{CA}$	6.773	1	16	0.019	2.698	1	17	0.119	0.0125	N	N
			r_{CF}	5.945	1	16	0.027	2.794	1	17	0.113	0.0100	N	N
			$\dot{Q}_{CA} / V_{br}$	6.773	1	16	0.019	2.709	1	17	0.118	0.0045	N	N
	Diprotodontia	M_b	V_{br}	0.085	1	26	0.773	73.591	1	27	<0.001			
			$\dot{Q}_{CA}$	1.039	1	26	0.317	1.335	1	27	0.258			
		V_{br}	$\dot{Q}_{CA}$	0.831	1	26	0.370	36.971	1	27	<0.001			
			r_{CF}	1.063	1	26	0.312	26.817	1	27	<0.001			
			$\dot{Q}_{CA} / V_{br}$	7.210	1	26	0.012	37.206	1	27	<0.001	0.0045	N	Y
	Haplorrhini	M_b	V_{br}	0.041	1	41	0.841	4.512	1	42	0.040			
			$\dot{Q}_{CA}$	2.129	1	41	0.152	15.737	1	42	<0.001			
		V_{br}	$\dot{Q}_{CA}$	4.854	1	41	0.033	11.433	1	42	0.002	0.0125	N	Y
			r_{CF}	9.046	1	41	0.004					0.0100	Y	-
			$\dot{Q}_{CA} / V_{br}$	25.994	1	41	<0.001	11.431	1	42	0.002	0.0045	N	Y

See previous Table S 3 - 8. , Table S 3 - 9, Table S 3 - 10, and Table S 3 - 11. Continued in Table S 3 - 13. See Table S 3 - 13 for presentation information.

Table S 3 - 13. Statistical information for the ANCOVAs relating body mass, brain volume, foramina dimensions, and total carotid flow in the Aves, with comparisons to diprotodont and haplorrhine mammals (part f).

Clade 1	Clade 2	X	Y	Slope				Elevation				Adjusted α	Significant at adjusted α	
				F-statistic	DFn	DFd	p-value	F-statistic	DFn	DFd	p-value		Slope	Elevation
Passeriformes	Diprotodontia	M_b	V_{br}	1.105	1	24	0.304	54.572	1	25	<0.001			
			$\dot{Q}_{CA}$	1.759	1	24	0.197	0.037	1	25	0.850			
		V_{br}	$\dot{Q}_{CA}$	0.649	1	24	0.428	17.751	1	25	<0.001			
			r_{CF}	0.219	1	24	0.644	10.857	1	25	0.003			
			$\dot{Q}_{CA} / V_{br}$	1.822	1	24	0.190	0.115	1	25	0.737			
	Haplorrhini	M_b	V_{br}	0.546	1	39	0.465	6.847	1	40	0.013			
			$\dot{Q}_{CA}$	2.238	1	39	0.143	4.535	1	40	0.040			
		V_{br}	$\dot{Q}_{CA}$	1.781	1	39	0.190	0.031	1	40	0.861			
			r_{CF}	0.014	1	39	0.908	3.542	1	40	0.067			
			$\dot{Q}_{CA} / V_{br}$	6.531	1	39	0.015	0.030	1	40	0.862	0.0045	N	N
Diprotodontia	Haplorrhini	M_b	V_{br}	0.003	1	49	0.954	214.172	1	50	<0.001			
			$\dot{Q}_{CA}$	0.052	1	49	0.820	13.602	1	50	0.001			
		V_{br}	$\dot{Q}_{CA}$	0.117	1	49	0.734	32.711	1	50	<0.001			
			r_{CF}	0.707	1	49	0.404	32.277	1	50	<0.001			
			$\dot{Q}_{CA} / V_{br}$	0.117	1	49	0.734	32.711	1	50	<0.001			

See previous Table S 3 - 8. , Table S 3 - 9, Table S 3 - 10, Table S 3 - 11, and Table S 3 - 12. When slopes were significantly different it was not possible to test whether elevations differed and cells for elevation are greyed out. Where tests were subjected to post-hoc Bonferroni correction cells appear in the three rightmost columns. When Bonferroni correction negated the significance between slopes, statistical information for comparison between elevations is given in greyed out cells to indicate that a result is from post-hoc testing.

Table S 3 - 14. Statistical information for the ANCOVAs relating body mass, brain volume, foramina dimensions, and total carotid flow in the Aves with respect to hatchling maturity.

Clade 1	Clade 2	X	Y	Slope				Elevation				Adjusted α	Significant at adjusted α	
				F-statistic	DFn	DFd	p-value	F-statistic	DFn	DFd	p-value		Slope	Elevation
Aves	Precocial	M_b	V_{br}	0.429	1	62	0.515	9.344	1	63	0.003			
			$\dot{Q}_{CA}$	4.074	1	62	0.048	0.005	1	63	0.945	0.0167	N	N
		V_{br}	$\dot{Q}_{CA}$	4.856	1	62	0.031							
			r_{CF}	4.386	1	62	0.040							
			$\dot{Q}_{CA} / V_{br}$	4.856	1	62	0.031							
	Altricial	M_b	V_{br}	9.847	1	68	0.003							
			$\dot{Q}_{CA}$	6.040	1	68	0.017					0.0167	Y	-
		V_{br}	$\dot{Q}_{CA}$	0.798	1	68	0.375	5.918	1	69	0.018			
			r_{CF}	0.664	1	68	0.418	5.919	1	69	0.018			
			$\dot{Q}_{CA} / V_{br}$	0.798	1	68	0.375	5.918	1	69	0.018			
Precocial		M_b	V_{br}	9.963	1	42	0.003							
			$\dot{Q}_{CA}$	17.017	1	42	<0.001					0.0167	Y	-
		V_{br}	$\dot{Q}_{CA}$	13.488	1	42	0.001							
			r_{CF}	11.632	1	42	0.001							
			$\dot{Q}_{CA} / V_{br}$	13.488	1	42	0.001							

When slopes were significantly different it was not possible to test whether elevations differed and cells for elevation are greyed out. Where tests were subjected to post-hoc Bonferroni correction cells appear in the three rightmost columns. When Bonferroni correction negated the significance between slopes, statistical information for comparison between elevations is given in greyed out cells to indicate that a result is from post-hoc testing.

Chapter 4 and Chapter 5

Table S 4/5 - 1. Perfusion rates of seven brain regions of *Gallus gallus domesticus* calculated according to the microsphere perfusion quantification technique (part a).

Specimen #	Life Stage	Body Mass (g)	Whole Brain			Brainstem			Cerebellum			Diencephalon		
			Volume (ml)	$\dot{Q}$ (ml min^{-1})	$\dot{Q}/V$ (ml min^{-1} g^{-1})	Volume (ml)	$\dot{Q}$ (ml min^{-1})	$\dot{Q}/V$ (ml min^{-1} g^{-1})	Volume (ml)	$\dot{Q}$ (ml min^{-1})	$\dot{Q}/V$ (ml min^{-1} g^{-1})	Volume (ml)	$\dot{Q}$ (ml min^{-1})	$\dot{Q}/V$ (ml $min^{-1}g^{-1}$)
C20	Before POL	1077	3.16	9.03	2.86	0.39	0.84	2.17	0.45	1.20	2.69	0.39	0.92	2.34
C24	Before POL	1218	3.24	8.05	2.49	0.26	0.57	2.25	0.45	1.35	3.02	0.48	0.96	2.01
C28	Before POL	1243	3.43	11.88	3.47	0.27	0.96	3.52	0.52	2.07	3.96	0.42	1.27	2.99
C31	Before POL	1357	3.33	11.94	3.59	0.30	1.04	3.41	0.45	2.04	4.55	0.37	1.04	2.84
C40	Before POL	1226	3.16	6.70	2.12	0.36	0.82	2.27	0.48	1.07	2.21	0.37	0.61	1.63
C41	Before POL	1356	3.34	14.63	4.38	0.35	1.50	4.24	0.52	2.76	5.31	0.40	1.33	3.30
C17	After POL	1497	3.74	16.32	4.36	0.39	1.73	4.46	0.53	2.74	5.19	0.56	1.82	3.26
C33	After POL	1777	3.73	12.93	3.46	0.39	0.99	2.57	0.51	2.25	4.38	0.43	1.15	2.70
C49	After POL	1899	3.47	17.21	4.95	0.36	1.76	4.84	0.47	2.81	5.93	0.42	1.65	3.89
C58	After POL	1754	3.29	17.97	5.47	0.33	1.75	5.36	0.48	3.31	6.89	0.40	1.52	3.78
C61	After POL	1826	3.47	17.80	5.13	0.36	1.71	4.68	0.49	3.03	6.20	0.45	1.61	3.60
C62	After POL	2045	3.28	15.74	4.80	0.31	1.51	4.95	0.45	3.03	6.67	0.39	1.37	3.53
C63	After POL	1705	3.35	20.39	6.08	0.34	2.00	5.87	0.48	3.60	7.46	0.41	1.95	4.72
C25	Rooster	1463	3.25	12.38	3.80	0.25	1.09	4.34	0.44	2.11	4.76	0.42	1.30	3.06
C37	Rooster	1406	3.35	8.43	2.52	0.30	0.76	2.52	0.54	1.84	3.37	0.36	0.71	1.96
C38	Rooster	2355	3.56	12.46	3.50	0.33	1.18	3.61	0.52	2.19	4.21	0.37	1.02	2.78
C42	Rooster	2203	4.05	11.02	2.72	0.39	0.92	2.37	0.57	1.95	3.45	0.40	0.94	2.38
C43	Rooster	2659	4.23	20.57	4.86	0.40	1.82	4.60	0.59	3.40	5.77	0.52	2.06	3.93
C46	Rooster	1752	3.40	15.70	4.62	0.37	1.73	4.72	0.44	2.56	5.81	0.38	1.50	3.89

$\dot{Q}$ – Perfusion rate; V – Region volume.

Table S 4/5 - 2. Perfusion rates of seven brain regions of *Gallus gallus domesticus* calculated according to the microsphere perfusion quantification technique (part b).

Specimen #	Life Stage	Body Mass (g)	Left telencephalon			Right telencephalon			Left Tectum			Right Tectum		
			Volume (ml)	$\dot{Q}$ (ml min^{-1})	$\dot{Q}/V$ (ml min^{-1} g^{-1})	Volume (ml)	$\dot{Q}$ (ml min^{-1})	$\dot{Q}/V$ (ml min^{-1} g^{-1})	Volume (ml)	$\dot{Q}$ (ml min^{-1})	$\dot{Q}/V$ (ml min^{-1} g^{-1})	Volume (ml)	$\dot{Q}$ (ml min^{-1})	$\dot{Q}/V$ (ml min^{-1} g^{-1})
C20	Before POL	1077	0.77	1.74	2.27	0.75	3.03	4.03	0.21	0.47	2.29	0.21	0.82	3.97
C24	Before POL	1218	0.83	1.90	2.30	0.85	2.24	2.65	0.20	0.48	2.43	0.19	0.55	2.94
C28	Before POL	1243	0.90	2.63	2.94	0.87	3.27	3.74	0.22	0.79	3.56	0.22	0.89	4.15
C31	Before POL	1357	0.90	3.03	3.38	0.88	3.17	3.63	0.22	0.80	3.57	0.21	0.82	3.85
C40	Before POL	1226	0.80	1.73	2.17	0.78	1.64	2.11	0.18	0.43	2.36	0.19	0.40	2.16
C41	Before POL	1356	0.83	3.44	4.16	0.83	3.73	4.50	0.21	0.91	4.37	0.20	0.96	4.89
C17	After POL	1497	0.83	3.87	4.67	0.90	3.88	4.31	0.26	1.17	4.48	0.28	1.11	4.03
C33	After POL	1777	0.98	3.07	3.13	0.96	3.91	4.07	0.23	0.75	3.29	0.24	0.81	3.37
C49	After POL	1899	0.91	4.45	4.87	0.89	4.36	4.89	0.20	1.05	5.21	0.21	1.13	5.49
C58	After POL	1754	0.85	4.58	5.39	0.81	4.49	5.53	0.21	1.17	5.63	0.21	1.15	5.56
C61	After POL	1826	0.91	4.76	5.23	0.86	4.37	5.08	0.20	1.10	5.53	0.20	1.23	6.11
C62	After POL	2045	0.88	3.94	4.50	0.87	3.85	4.42	0.19	1.05	5.45	0.19	1.00	5.23
C63	After POL	1705	0.87	5.23	6.01	0.87	4.98	5.75	0.18	1.36	7.58	0.20	1.25	6.28
C25	Rooster	1463	0.89	3.01	3.40	0.88	3.20	3.63	0.18	0.83	4.64	0.19	0.84	4.43
C37	Rooster	1406	0.90	1.93	2.15	0.86	2.16	2.52	0.20	0.48	2.42	0.19	0.56	2.93
C38	Rooster	2355	0.97	3.34	3.46	0.94	2.94	3.14	0.21	0.86	4.16	0.24	0.93	3.96
C42	Rooster	2203	1.09	2.83	2.61	1.13	2.88	2.55	0.24	0.74	3.10	0.25	0.75	3.05
C43	Rooster	2659	1.15	5.23	4.55	1.15	5.72	4.99	0.20	1.11	5.50	0.23	1.24	5.45
C46	Rooster	1752	0.91	3.64	4.01	0.90	4.08	4.52	0.19	1.09	5.63	0.21	1.11	5.33

$\dot{Q}$ – Perfusion rate; V – Region volume.

Table S 4/5 - 3. Whole brain perfusion rates of *Gallus gallus domesticus* calculated from the dimensions of the cerebral carotid canal according to the foramen dimension measurement technique.

Specimen #	Life Stage	Body Mass M_b (g)	Brain Volume V_{br} (ml)	Average foramen radius r_{CF} (cm)	Corrected lumen radius $r_{ICALumen}$ (cm)	Total Blood Flow Rate $\dot{Q}$ (ml min^{-1})	Volumetric Flow Rate $\dot{Q}$ / V_{br} (ml min^{-1} ml^{-1})
C19	Before POL	1567	3.62	0.06	0.04	8.08	2.23
C21	Before POL	883	3.33	0.06	0.04	8.73	2.62
C29	Before POL	1251	3.58	0.06	0.04	6.90	1.93
C44	Before POL	1384	3.46	0.07	0.05	13.33	3.86
C45	Before POL	1114	3.87	0.07	0.05	11.09	2.86
C47	Before POL	1462	3.70	0.07	0.05	11.33	3.07
C32	After POL	1521	3.68	0.08	0.05	14.63	3.97
C34	After POL	1855	3.62	0.06	0.04	9.04	2.50
C35	After POL	1580	3.99	0.06	0.05	9.32	2.33
C36	After POL	1949	3.94	0.07	0.05	10.13	2.57
C57	After POL	1726	3.70	0.06	0.05	9.78	2.65
C66	After POL	1916	3.89	0.06	0.04	8.51	2.19
C67	After POL	1891	3.97	0.06	0.04	8.89	2.24
C50	Rooster	2558	4.47	0.07	0.05	10.59	2.37
C51	Rooster	1973	4.41	0.07	0.05	13.74	3.12
C52	Rooster	2355	4.45	0.07	0.05	10.73	2.41
C54	Rooster	2218	4.19	0.07	0.05	11.34	2.71
C55	Rooster	2139	4.44	0.07	0.05	13.31	3.0
C56	Rooster	2241	4.41	0.07	0.05	11.18	2.53

Table S 4/5 - 4. Whole brain perfusion rates of *Gallus gallus domesticus* calculated from the dimensions of the arterial lumen according to the pressurised contrast perfusion technique.

Specimen #	Life Stage	Body Mass M_b (g)	Brain Volume V_{br} (ml)	Average lumen radius r_{lumen} (cm)	Total Blood Flow Rate $\dot{Q}$ (ml min^{-1})	Volumetric Flow Rate $\dot{Q}$ / V_{br} (ml min^{-1} ml^{-1})
C19	Before POL	1567	3.62	0.026	2.36	0.65
C21	Before POL	883	3.33	0.024	2.00	0.60
C29	Before POL	1251	3.58	0.019	1.11	0.31
C44	Before POL	1384	3.46	0.027	2.49	0.72
C45	Before POL	1114	3.87	0.026	2.28	0.59
C47	Before POL	1462	3.7	0.023	1.77	0.48
C32	After POL	1521	3.68	0.026	2.40	0.65
C34	After POL	1855	3.62	0.019	1.04	0.29
C35	After POL	1580	3.99	0.023	1.65	0.41
C36	After POL	1949	3.94	0.030	3.43	0.87
C57	After POL	1726	3.7	0.021	1.39	0.38
C66	After POL	1916	3.89	0.026	2.42	0.62
C67	After POL	1891	3.97	0.024	1.90	0.48
C50	Rooster	2558	4.47	0.025	2.01	0.45
C51	Rooster	1973	4.41	0.024	1.95	0.44
C52	Rooster	2355	4.45	0.024	1.84	0.41
C54	Rooster	2218	4.19	0.021	1.28	0.30
C55	Rooster	2139	4.44	0.020	1.15	0.26
C56	Rooster	2241	4.41	0.020	1.23	0.28

Table S 4/5 - 5. Perfusion rates of the spleen and left and right kidneys of recorded from five *Gallus gallus domesticus* laying hens calculated according to the microsphere perfusion quantification technique as reported in Hu *et al.* (2021).

Specimen #	Life Stage	Body Mass (g)	Spleen			Left Kidney			Right Kidney		
			Mass (g)	$\dot{Q}$ (ml min^{-1})	$\dot{Q}/V$ (ml min^{-1} g^{-1})	Mass (g)	$\dot{Q}$ (ml min^{-1})	$\dot{Q}/V$ (ml min^{-1} g^{-1})	Mass (g)	$\dot{Q}$ (ml min^{-1})	$\dot{Q}/V$ (ml min^{-1} g^{-1})
C49	After POL	1899	2.27	5.40	2.38	5.01	12.00	2.39	11.05	5.16	2.14
C58	After POL	1754	1.44	7.07	4.90	3.97	15.71	3.96	14.46	3.67	3.94
C61	After POL	1826	1.85	2.72	1.47	5.89	4.69	0.80	4.37	5.90	0.74
C62	After POL	2045	1.56	18.81	12.03	7.19	13.65	1.90	15.00	6.78	2.21
C63	After POL	1705	1.97	14.33	7.28	5.22	14.96	2.86	14.07	4.80	2.93

Table S 4/5 - 6. Full two-way ANOVA multiple comparisons descriptive statistics table for brain segment masses from the microsphere infusion technique.

Brain Structure	Age Classes	Mean Difference	SE of Difference	P Value	95% Confidence Interval		Summary
					Lower Bound	Upper Bound	
Brain Stem	Young vs. Layers	-0.0312	0.03	>0.9999	-0.1409	0.07853	ns
	Young vs. Roosters	-0.01607	0.03113	>0.9999	-0.1299	0.09780	ns
	Layers vs. Roosters	0.01513	0.03	>0.9999	-0.09459	0.1249	ns
Cerebellum	Young vs. Layers	-0.01074	0.03	>0.9999	-0.1205	0.09898	ns
	Young vs. Roosters	-0.03927	0.03113	0.9995	-0.1531	0.07460	ns
	Layers vs. Roosters	-0.02852	0.03	>0.9999	-0.1382	0.08120	ns
Diencephalon	Young vs. Layers	-0.02988	0.03	>0.9999	-0.1396	0.07984	ns
	Young vs. Roosters	-0.002233	0.03113	>0.9999	-0.1161	0.1116	ns
	Layers vs. Roosters	0.02765	0.03	>0.9999	-0.08207	0.1374	ns
Left Telencephalon	Young vs. Layers	-0.05462	0.03	0.9608	-0.1643	0.05510	ns
	Young vs. Roosters	-0.1464	0.03113	0.0013	-0.2602	-0.03252	**
	Layers vs. Roosters	-0.09176	0.03	0.2352	-0.2015	0.01796	ns
Right Telencephalon	Young vs. Layers	-0.05422	0.03	0.9635	-0.1639	0.05550	ns
	Young vs. Roosters	-0.1494	0.03113	0.0009	-0.2632	-0.03550	***
	Layers vs. Roosters	-0.09515	0.03	0.1825	-0.2049	0.01458	ns
Left Tectum	Young vs. Layers	-0.003379	0.03	>0.9999	-0.1131	0.1063	ns
	Young vs. Roosters	0.003483	0.03113	>0.9999	-0.1104	0.1173	ns
	Layers vs. Roosters	0.006862	0.03	>0.9999	-0.1029	0.1166	ns
Right Tectum	Young vs. Layers	-0.01628	0.03	>0.9999	-0.1260	0.09344	ns
	Young vs. Roosters	-0.0168	0.03113	>0.9999	-0.1307	0.09706	ns
	Layers vs. Roosters	-0.0005214	0.03	>0.9999	-0.1102	0.1092	ns

Summary column indicates the significance of the p-value, where ns indicates non-significance ($p > 0.05$), one asterisk indicates $p \leq 0.05$, two asterisks $p \leq 0.01$, three asterisks $p \leq 0.001$, and four asterisks $p \leq 0.0001$.

Table S 4/5 - 7. Full two-way ANOVA multiple comparisons descriptive statistics table for blood flow rate from the microsphere infusion technique.

Brain Structure	Age Classes	Mean Difference	SE of Difference	P Value	95% Confidence Interval		Summary
					Lower Bound	Upper Bound	
Brain Stem	Young vs. Layers	-0.6804	0.3053	0.7968	-1.797	0.4362	ns
	Young vs. Roosters	-0.2942	0.3168	>0.9999	-1.453	0.8646	ns
	Layers vs. Roosters	0.3862	0.3053	0.9995	-0.7304	1.503	ns
Cerebellum	Young vs. Layers	-1.219	0.3053	0.0173	-2.336	-0.1028	*
	Young vs. Roosters	-0.5926	0.3168	0.9494	-1.751	0.5661	ns
	Layers vs. Roosters	0.6268	0.3053	0.8876	-0.4898	1.743	ns
Diencephalon	Young vs. Layers	-0.5589	0.3053	0.9587	-1.675	0.5577	ns
	Young vs. Roosters	-0.2313	0.3168	>0.9999	-1.390	0.9274	ns
	Layers vs. Roosters	0.3275	0.3053	>0.9999	-0.7890	1.444	ns
Left Telencephalon	Young vs. Layers	-1.86	0.3053	<0.0001	-2.976	-0.7430	****
	Young vs. Roosters	-0.9166	0.3168	0.3296	-2.075	0.2421	ns
	Layers vs. Roosters	0.943	0.3053	0.2202	-0.1735	2.060	ns
Right Telencephalon	Young vs. Layers	-1.414	0.3053	0.0017	-2.531	-0.2978	**
	Young vs. Roosters	-0.6488	0.3168	0.8897	-1.808	0.5099	ns
	Layers vs. Roosters	0.7655	0.3053	0.6045	-0.3511	1.882	ns
Left Tectum	Young vs. Layers	-0.4464	0.3053	0.9966	-1.563	0.6701	ns
	Young vs. Roosters	-0.2056	0.3168	>0.9999	-1.364	0.9531	ns
	Layers vs. Roosters	0.2409	0.3053	>0.9999	-0.8757	1.357	ns
Right Tectum	Young vs. Layers	-0.3556	0.3053	0.9999	-1.472	0.7610	ns
	Young vs. Roosters	-0.1634	0.3168	>0.9999	-1.322	0.9953	ns
	Layers vs. Roosters	0.1922	0.3053	>0.9999	-0.9244	1.309	ns

Summary column indicates the significance of the p-value, where ns indicates non-significance ($p > 0.05$), one asterisk indicates $p \leq 0.05$, two asterisks $p \leq 0.01$, three asterisks $p \leq 0.001$, and four asterisks $p \leq 0.0001$.

Table S 4/5 - 8. Full two-way ANOVA multiple comparisons descriptive statistics table for volumetric blood flow from the microsphere infusion technique.

Brain Structure	Age Classes	Mean Difference	SE of Difference	P Value	95% Confidence Interval		Summary
					Lower Bound	Upper Bound	
Brain Stem	Young vs. Layers	-1.696	0.5405	0.197	-3.673	0.2805	ns
	Young vs. Roosters	-0.7132	0.561	0.9995	-2.765	1.338	ns
	Layers vs. Roosters	0.9833	0.5405	0.9612	-0.9936	2.960	ns
Cerebellum	Young vs. Layers	-2.48	0.5405	0.0021	-4.456	-0.5026	**
	Young vs. Roosters	-0.9376	0.561	0.9837	-2.989	1.114	ns
	Layers vs. Roosters	1.542	0.5405	0.3554	-0.4350	3.519	ns
Diencephalon	Young vs. Layers	-1.124	0.5405	0.8757	-3.101	0.8528	ns
	Young vs. Roosters	-0.4843	0.561	>0.9999	-2.536	1.567	ns
	Layers vs. Roosters	0.6398	0.5405	0.9998	-1.337	2.617	ns
Left Telencephalon	Young vs. Layers	-1.961	0.5405	0.0546	-3.938	0.01617	ns
	Young vs. Roosters	-0.4939	0.561	>0.9999	-2.545	1.558	ns
	Layers vs. Roosters	1.467	0.5405	0.4513	-0.5101	3.444	ns
Right Telencephalon	Young vs. Layers	-1.422	0.5405	0.512	-3.399	0.5548	ns
	Young vs. Roosters	-0.1174	0.561	>0.9999	-2.169	1.934	ns
	Layers vs. Roosters	1.305	0.5405	0.6734	-0.6722	3.282	ns
Left Tectum	Young vs. Layers	-2.213	0.5405	0.0124	-4.190	-0.2359	*
	Young vs. Roosters	-1.147	0.561	0.8912	-3.198	0.9047	ns
	Layers vs. Roosters	1.066	0.5405	0.9191	-0.9110	3.043	ns
Right Tectum	Young vs. Layers	-1.491	0.5405	0.4198	-3.468	0.4862	ns
	Young vs. Roosters	-0.5321	0.561	>0.9999	-2.584	1.519	ns
	Layers vs. Roosters	0.9586	0.5405	0.9698	-1.018	2.936	ns

Summary column indicates the significance of the p-value, where ns indicates non-significance ($p > 0.05$), one asterisk indicates $p \leq 0.05$, two asterisks $p \leq 0.01$, three asterisks $p \leq 0.001$, and four asterisks $p \leq 0.0001$.

APPENDIX C: SCAN PARAMETERS, RECONSTRUCTION SETTINGS, MEASUREMENT RESOLUTION (METADATA)

Chapter 2

Table M 2 - 1. Selected imaging and reconstruction parameters for western grey specimens scanned using the Skyscan-1076 Micro-CT scanner at Adelaide Microscopy. The Skyscan-1076 Micro-CT scanner and Philips Ingenuity Core 128 scanner are used for different purposes (analytical vs clinical), and thus the parameters appearing here are different from those listed in Table ROO128.

Specimen	Type of Motion	Source Voltage (kV)	Source Current (uA)	Exposure (ms)	Filter	Rotation Step (°)	Frame Averaging	Corrections Applied During Reconstruction
R41	Step and Shoot	70	139	4123	Al 0.5mm	0.6	2	*
R58	Step and Shoot	80	124	590	Al 1.0mm	0.6	2	*
R84	Step and Shoot	80	124	590	Al 1.0mm	0.6	2	*
R69	Step and Shoot	100	100	1180	Al 1.0mm	0.6	2	*
R97	Step and Shoot	100	100	1180	Al 1.0mm	0.6	2	*
R76	Step and Shoot	100	100	1180	Al 1.0mm	0.6	2	*
R96	Step and Shoot	100	100	1180	Al 1.0mm	0.6	2	*
R93	Step and Shoot	100	100	158	Al 1.0mm	0.6	2	*
R92	Step and Shoot	100	100	158	Al 1.0mm	0.6	2	*
R43	Step and Shoot	100	100	158	Al 1.0mm	0.6	2	*

* Smoothing (1); Misalignment Compensation; Ring Artefact Reduction (10); Beam-Hardening Correction (30%); Find Z-Connection; Find X/Y Shift; Find Rotation; Apply Fusion.

Table M 2 - 2. Selected imaging and reconstruction parameters for western grey specimens scanned using the Philips Ingenuity Core 128 scanner at Sound Radiology. The Skyscan-1076 Micro-CT scanner and Philips Ingenuity Core 128 scanner are used for different purposes (analytical vs clinical), and thus the parameters appearing here are different from those listed in Table ROO1076.

Specimen #	Type of Motion	Peak Voltage (kV)	Exposure Current (mAs)	Filter	Slice Thickness (mm)	Slice Interval (mm)	Rotation time	Pitch	Collimation	Recon Mode	Render Mode	Enhancement	Matrix	Resolution Setting	Windowing
R46	Helical	120	200	Y-Sharp	0.67	0.33	0.4	0.349	20 x 0.625	iDose4 Level 3	Average	-1.0	1024	Ultra High	C700, W4000
R45	Helical	120	200	Y-Sharp	0.67	0.33	0.4	0.349	20 x 0.625	iDose4 Level 3	Average	-1.0	1024	Ultra High	C700, W4000
R49	Helical	120	200	Y-Sharp	0.67	0.33	0.4	0.349	20 x 0.625	iDose4 Level 3	Average	-1.0	1024	Ultra High	C700, W4000
R35	Helical	120	200	Y-Sharp	0.67	0.33	0.4	0.349	20 x 0.625	iDose4 Level 3	Average	-1.0	1024	Ultra High	C700, W4000
R33	Helical	120	200	Y-Sharp	0.67	0.33	0.4	0.349	20 x 0.625	iDose4 Level 3	Average	-1.0	1024	Ultra High	C700, W4000
R40	Helical	120	200	Y-Sharp	0.67	0.33	0.4	0.349	20 x 0.625	iDose4 Level 3	Average	-1.0	1024	Ultra High	C700, W4000
R51	Helical	120	200	Y-Sharp	0.67	0.33	0.4	0.349	20 x 0.625	iDose4 Level 3	Average	-1.0	1024	Ultra High	C700, W4000
R32	Helical	120	200	Y-Sharp	0.67	0.33	0.4	0.349	20 x 0.625	iDose4 Level 3	Average	-1.0	1024	Ultra High	C700, W4000
R50	Helical	120	200	Y-Sharp	0.67	0.33	0.4	0.349	20 x 0.625	iDose4 Level 3	Average	-1.0	1024	Ultra High	C700, W4000

Table M 2 - 3. Voxel dimensions used for various aspects of Chapter 2. Specimens are sorted by increasing body mass. Specimens "Roo 41" through "Roo 43" were scanned using the Skyscan-1076 Micro-CT scanner at Adelaide Microscopy. Specimens "Roo 46 through "Roo 50" were scanned using the Philips Ingenuity Core 128 scanner at Sound Radiology. Reconstruction dimensions represent the dimensions of the voxels following the reconstruction – these are the dimensions of the original, unaltered voxels. Foramen measurements were taken using the maximum possible voxel resolution. For specimens obtained from Adelaide Microscopy, no dataset resizing was required. Resizing was necessary for specimens obtained from Sound Radiology as isometric voxels were required for one measurement program. Voxels were resized using DataViewer and Fiji by saving the dataset as an image sequence and scaling by a factor that would correct the Z dimensions of the image sequence. Endocast measurements were taken using the maximum possible voxel resolution. Maximum possible voxel resolution for endocast measurement was determined by dataset size as endocast segmentation is a memory intensive process. Specimens imaged at Adelaide Microscopy were resized to optimise voxel resolution against the computer performance trade-off. Specimens imaged at Sound Radiology did not require resizing for endocast measurement.

Specimen #	Voxel Dimensions (µm) - Reconstruction			Voxel Dimensions (µm) - Foramen			Voxel Dimensions (µm) - Endocast		
	X	Y	Z	X	Y	Z	X	Y	Z
R41	8.7	8.7	8.7	8.7	8.7	8.7	17.4	17.4	17.4
R58	17.3	17.3	17.3	17.3	17.3	17.3	34.6	34.6	34.6
R84	17.4	17.4	17.4	17.4	17.4	17.4	34.8	34.8	34.8
R69	17.4	17.4	17.4	17.4	17.4	17.4	34.8	34.8	34.8
R97	17.4	17.4	17.4	17.4	17.4	17.4	69.6	69.6	69.6
R76	17.4	17.4	17.4	17.4	17.4	17.4	69.6	69.6	69.6
R96	17.4	17.4	17.4	17.4	17.4	17.4	69.6	69.6	69.6
R93	34.8	34.8	34.8	34.8	34.8	34.8	69.6	69.6	69.6
R92	34.8	34.8	34.8	34.8	34.8	34.8	69.6	69.6	69.6
R43	34.8	34.8	34.8	34.8	34.8	34.8	69.6	69.6	69.6
R46	304.6875	304.6875	330	304.6875	304.6875	304.6875	304.6875	304.6875	330
R45	199.2188	199.2188	330.0204	199.2188	199.2188	199.2188	199.2188	199.2188	330.0204
R49	216.7969	216.7969	330	216.7969	216.7969	216.7969	216.7969	216.7969	330
R35	229.4922	229.4922	330	229.4922	229.4922	229.4922	229.4922	229.4922	330
R33	205.0781	205.0781	330	205.0781	205.0781	205.0781	205.0781	205.0781	330
R40	228.5156	228.5156	330	228.5156	228.5156	228.5156	228.5156	228.5156	330
R51	244.1406	244.1406	330	244.1406	244.1406	244.1406	244.1406	244.1406	330
R32	325.5208	325.5208	330	325.5208	325.5208	325.5208	325.5208	325.5208	330
R50	244.1406	244.1406	330	244.1406	244.1406	244.1406	244.1406	244.1406	330

Chapter 3

Table M 3 - 1. Selected imaging and reconstruction parameters for Avian specimens from Chapter 3. These were scanned using the Skyscan-1076 Micro-CT scanner at Adelaide Microscopy. The Skyscan-1076 Micro-CT scanner and Philips Ingenuity Core 128 scanner are used for different purposes (analytical vs clinical), and thus the parameters appearing here are different from those listed in Table BIRDS128.

Specimen #	Type of Motion	Source Voltage (kV)	Source Current (uA)	Exposure (ms)	Filter	Rotation Step (°)	Frame Averaging	Corrections Applied During Reconstruction
B5051	Step and Shoot	80	124	1475	Al 0.5mm	0.5	2	†
B31339	Step and Shoot	80	124	1475	Al 0.5mm	0.5	2	†
B5084	Step and Shoot	80	124	1475	Al 0.5mm	0.5	2	†
B31912	Step and Shoot	59	141	4123	Al 0.5mm	0.5	2	†
B11478	Step and Shoot	59	141	4123	Al 0.5mm	0.5	2	†
B34041	Step and Shoot	80	120	1475	Al 0.5mm	0.5	2	†
B11543	Step and Shoot	80	120	1475	Al 0.5mm	0.5	2	†
B34049	Step and Shoot	80	120	1475	Al 0.5mm	0.5	2	†
B11913	Step and Shoot	59	141	4123	Al 0.5mm	0.5	2	†
B31584	Step and Shoot	59	141	4123	Al 0.5mm	0.5	2	†
B39358	Step and Shoot	59	141	4123	Al 0.5mm	0.5	2	†
B10905	Step and Shoot	80	120	1475	Al 0.5mm	0.5	2	†
B10357	Step and Shoot	80	120	1475	Al 0.5mm	0.5	2	†
B39767	Step and Shoot	80	120	1475	Al 0.5mm	0.5	2	†
B46127	Step and Shoot	80	120	1475	Al 0.5mm	0.5	2	†
B15140*	Step and Shoot	100	100	316	Al 0.5mm	0.5	2	†

† Smoothing (1); Misalignment Compensation; Ring Artefact Reduction (10); Beam-Hardening Correction (30%); Find Z-Connection; Find X/Y Shift; Find Rotation; Apply Fusion. *B15140 scanned twice. Initial scans on Philips Ingenuity Core 128 medical grade CT provided insufficient resolution for foramina measurement. Subsequent scan was performed using Skyscan-1076 Micro-CT.

Table M 3 - 2. Selected imaging and reconstruction parameters for Avian specimens from Chapter 3 which were scanned using the Skyscan-1076 Micro-CT scanner at Adelaide Microscopy, continued. See Table M 3 - 1 for rest of specimens scanned using the Skyscan-1076 Micro-CT scanner. The Skyscan-1076 Micro-CT scanner and Philips Ingenuity Core 128 scanner are used for different purposes (analytical vs clinical), and thus the parameters appearing here are different from those listed in Table M 3 - 3.

Specimen #	Type of Motion	Source Voltage (kV)	Source Current (uA)	Exposure (ms)	Filter	Rotation Step (°)	Frame Averaging	Corrections Applied During Reconstruction
B48933	Step and Shoot	59	141	4123	Al 0.5mm	0.5	2	†
B48784	Step and Shoot	80	120	1475	Al 0.5mm	0.5	2	†
B55992	Step and Shoot	100	100	474	Al 0.5mm	0.5	2	†
B39628	Step and Shoot	100	100	474	Al 0.5mm	0.5	2	†
B46331	Step and Shoot	59	141	4123	Al 0.5mm	0.5	2	†
B48782	Step and Shoot	80	120	1475	Al 0.5mm	0.5	2	†
B24332	Step and Shoot	59	141	4123	Al 0.5mm	0.5	2	†
B24336	Step and Shoot	59	141	4123	Al 0.5mm	0.5	2	†
B48439	Step and Shoot	80	120	1475	Al 0.5mm	0.5	2	†
B10578	Step and Shoot	80	120	1475	Al 0.5mm	0.5	2	†
B47701	Step and Shoot	59	141	4123	Al 0.5mm	0.5	2	†
B16736	Step and Shoot	59	141	4123	Al 0.5mm	0.5	2	†
B23984	Step and Shoot	59	141	4123	Al 0.5mm	0.5	2	†
B11807	Step and Shoot	59	141	4123	Al 0.5mm	0.5	2	†
B37527	Step and Shoot	80	120	1475	Al 0.5mm	0.5	2	†
B2321	Step and Shoot	80	120	1475	Al 0.5mm	0.5	2	†
B5048	Step and Shoot	80	120	1475	Al 0.5mm	0.5	2	†
B55960	Step and Shoot	59	141	4123	Al 0.5mm	0.5	2	†
B36917	Step and Shoot	59	141	4123	Al 0.5mm	0.5	2	†
B11191	Step and Shoot	80	120	1475	Al 0.5mm	0.5	2	†
B32214	Step and Shoot	80	120	1475	Al 0.5mm	0.5	2	†
B38480	Step and Shoot	80	120	1475	Al 0.5mm	0.5	2	†
B55786	Step and Shoot	80	120	1475	Al 0.5mm	0.5	2	†
B29277	Step and Shoot	80	120	1475	Al 0.5mm	0.5	2	†
B40095	Step and Shoot	59	141	4123	Al 0.5mm	0.5	2	†
B56070	Step and Shoot	59	141	4123	Al 0.5mm	0.5	2	†

† Smoothing (1); Misalignment Compensation; Ring Artefact Reduction (10); Beam-Hardening Correction (30%); Find Z-Connection; Find X/Y Shift; Find Rotation; Apply Fusion.

Table M 3 - 3. Selected imaging and reconstruction parameters for Avian specimens from Chapter 3 which were scanned using the Philips Ingenuity Core 128 scanner at Sound Radiology. The Skyscan-1076 Micro-CT scanner and Philips Ingenuity Core 128 scanner are used for different purposes (analytical vs clinical), and thus the parameters appearing here are different from those listed in Table M 3 - 1 and Table M 3 - 2.

Specimen #	Type of Motion	Peak Voltage (kV)	Exposure Current (mAs)	Filter	Slice Thickness (mm)	Slice Interval (mm)	Rotation time	Pitch	Collimation	Recon Mode	Render Mode	Enhancement	Matrix	Resolution Setting	Windowing
B5075	Helical	120	200	Y-Sharp	0.67	0.33	0.4	0.349	20 x 0.625	iDose4 Level 3	Average	-1	1024	Ultra High	C700, W4000
B46991	Helical	120	200	Y-Sharp	0.67	0.33	0.4	0.349	20 x 0.625	iDose4 Level 3	Average	-1	1024	Ultra High	C700, W4000
B31329	Helical	120	200	Y-Sharp	0.67	0.33	0.4	0.349	20 x 0.625	iDose4 Level 3	Average	-1	1024	Ultra High	C700, W4000
B11411	Helical	120	200	Y-Sharp	0.67	0.33	0.4	0.349	20 x 0.625	iDose4 Level 3	Average	-1	1024	Ultra High	C700, W4000
B15140*	Helical	120	200	Y-Sharp	0.67	0.33	0.4	0.349	20 x 0.625	iDose4 Level 3	Average	-1	1024	Ultra High	C700, W4000

*B15140 scanned twice. Initial scans on Philips Ingenuity Core 128 medical grade CT provided insufficient resolution for foramina measurement. Subsequent scan was performed using Skyscan-1076 Micro-CT.

Table M 3 - 4. Voxel dimensions used for various aspects of Chapter 3. Specimens with voxel dimensions under 100 µm were scanned using the Skyscan-1076 Micro-CT scanner at Adelaide Microscopy. Specimens with voxel dimensions over 100 µm were scanned using the Philips Ingenuity Core 128 scanner at Sound Radiology. Reconstruction dimensions represent the dimensions of the voxels following the reconstruction – these are the dimensions of the original, unaltered voxels. Foramen measurements were taken using the maximum possible voxel resolution. For specimens obtained from Adelaide Microscopy, no dataset resizing was required. Resizing was necessary for specimens obtained from Sound Radiology as isometric voxels were required for one measurement program. Voxels were resized using DataViewer and Fiji by saving the dataset as an image sequence and scaling by a factor that would correct the Z dimensions of the image sequence. Endocast measurements were taken using the maximum possible voxel resolution. Maximum possible voxel resolution for endocast measurement was determined by dataset size as endocast segmentation is a memory intensive process. Specimens imaged at Adelaide Microscopy were resized to optimise voxel resolution against the computer performance trade-off. Specimens imaged at Sound Radiology did not require resizing for endocast measurement. Continued in Table M 3 - 5.

Specimen #	Voxel Dimensions (µm) - Reconstruction			Voxel Dimensions (µm) - Foramen			Voxel Dimensions (µm) - Endocast		
	X	Y	Z	X	Y	Z	X	Y	Z
B5051	17.000	17.000	17.000	17.000	17.000	17.000	34.000	34.000	34.000
B5075	236.328	236.328	330.000	236.328	236.328	236.328	236.328	236.328	236.328
B46991	234.375	234.375	330.000	234.375	234.375	234.375	234.375	234.375	234.375
B31329	236.328	236.328	330.000	236.328	236.328	236.328	236.328	236.328	236.328
B11411	244.141	244.141	330.000	244.141	244.141	244.141	244.141	244.141	244.141
B31339	17.000	17.000	17.000	17.000	17.000	17.000	34.000	34.000	34.000
B5084	17.000	17.000	17.000	17.000	17.000	17.000	34.000	34.000	34.000
B31912	8.500	8.500	8.500	8.500	8.500	8.500	17.000	17.000	17.000
B11478	8.500	8.500	8.500	8.500	8.500	8.500	17.000	17.000	17.000
B34041	17.000	17.000	17.000	17.000	17.000	17.000	34.000	34.000	34.000
B11543	17.000	17.000	17.000	17.000	17.000	17.000	34.000	34.000	34.000
B34049	17.000	17.000	17.000	34.000	34.000	34.000	34.000	34.000	34.000
B11913	8.500	8.500	8.500	8.500	8.500	8.500	17.000	17.000	17.000
B31584	8.500	8.500	8.500	8.500	8.500	8.500	17.000	17.000	17.000
B39358	8.500	8.500	8.500	8.500	8.500	8.500	17.000	17.000	17.000
B10905	17.000	17.000	17.000	17.000	17.000	17.000	34.000	34.000	34.000
B10357	17.000	17.000	17.000	17.000	17.000	17.000	34.000	34.000	34.000
B39767	17.000	17.000	17.000	17.000	17.000	17.000	34.000	34.000	34.000
B46127	17.000	17.000	17.000	17.000	17.000	17.000	34.000	34.000	34.000
B15140*	234.375 34.000	234.375 34.000	330.000 34.000	34.000	34.000	34.000	234.375	234.375	234.375

*B15140 scanned twice. Initial scans on Philips Ingenuity Core 128 medical grade CT provided insufficient resolution for foramina measurement. Subsequent scan was performed using Skyscan-1076 Micro-CT.

Table M 3 - 5. Voxel dimensions used for various aspects of Chapter 3 continued. See Table M 3 - 4 for a description.

Specimen #	Voxel Dimensions (µm) - Reconstruction			Voxel Dimensions (µm) - Foramen			Voxel Dimensions (µm) - Endocast		
	X	Y	Z	X	Y	Z	X	Y	Z
B48933	8.500	8.500	8.500	8.500	8.500	8.500	17.000	17.000	17.000
B48784	17.000	17.000	17.000	17.000	17.000	17.000	34.000	34.000	34.000
B55992	34.000	34.000	34.000	34.000	34.000	34.000	68.000	68.000	68.000
B39628	34.000	34.000	34.000	34.000	34.000	34.000	68.000	68.000	68.000
B46331	8.500	8.500	8.500	8.500	8.500	8.500	34.000	34.000	34.000
B48782	17.000	17.000	17.000	17.000	17.000	17.000	34.000	34.000	34.000
B24332	8.500	8.500	8.500	8.500	8.500	8.500	17.000	17.000	17.000
B24336	8.500	8.500	8.500	8.500	8.500	8.500	34.000	34.000	34.000
B48439	17.000	17.000	17.000	17.000	17.000	17.000	34.000	34.000	34.000
B10578	17.000	17.000	17.000	17.000	17.000	17.000	34.000	34.000	34.000
B47701	8.500	8.500	8.500	8.500	8.500	8.500	17.000	17.000	17.000
B16736	8.500	8.500	8.500	8.500	8.500	8.500	17.000	17.000	17.000
B23984	8.500	8.500	8.500	8.500	8.500	8.500	17.000	17.000	17.000
B11807	8.500	8.500	8.500	8.500	8.500	8.500	17.000	17.000	17.000
B37527	17.000	17.000	17.000	17.000	17.000	17.000	34.000	34.000	34.000
B2321	17.000	17.000	17.000	34.000	34.000	34.000	34.000	34.000	34.000
B5048	17.000	17.000	17.000	17.000	17.000	17.000	34.000	34.000	34.000
B55960	8.500	8.500	8.500	8.500	8.500	8.500	17.000	17.000	17.000
B36917	8.500	8.500	8.500	8.500	8.500	8.500	17.000	17.000	17.000
B11191	17.000	17.000	17.000	17.000	17.000	17.000	34.000	34.000	34.000
B32214	17.000	17.000	17.000	17.000	17.000	17.000	34.000	34.000	34.000
B38480	17.000	17.000	17.000	17.000	17.000	17.000	34.000	34.000	34.000
B55786	17.000	17.000	17.000	17.000	17.000	17.000	34.000	34.000	34.000
B29277	17.000	17.000	17.000	17.000	17.000	17.000	34.000	34.000	34.000
B40095	8.500	8.500	8.500	8.500	8.500	8.500	17.000	17.000	17.000
B56070	8.500	8.500	8.500	8.500	8.500	8.500	17.000	17.000	17.000

Chapter 4 and Chapter 5

Table M 4/5 - 1. Selected imaging and reconstruction parameters for chicken specimens scanned using the Skyscan-1276 Micro-CT scanner at Adelaide Microscopy.

Specimen #	Type of Motion	Source Voltage (kV)	Source Current (uA)	Exposure (ms)	Filter	Rotation Step (°)	Frame Averaging	Corrections Applied During Reconstruction
C19	Step and Shoot	95	200	650	Al+Cu	0.4	2	*
C21	Step and Shoot	95	200	650	Al+Cu	0.4	2	*
C29	Step and Shoot	95	200	715	Al+Cu	0.4	2	*
C44	Step and Shoot	95	200	715	Al+Cu	0.4	2	*
C45	Step and Shoot	95	200	715	Al+Cu	0.4	2	*
C47	Step and Shoot	95	200	715	Al+Cu	0.4	2	*
C32	Step and Shoot	95	200	715	Al+Cu	0.4	2	*
C34	Step and Shoot	95	200	715	Al+Cu	0.4	2	*
C35	Step and Shoot	95	200	715	Al+Cu	0.4	2	*
C36	Step and Shoot	95	200	715	Al+Cu	0.4	2	*
C57	Step and Shoot	95	200	715	Al+Cu	0.4	2	*
C66	Step and Shoot	95	200	715	Al+Cu	0.4	2	*
C67	Step and Shoot	95	200	715	Al+Cu	0.4	2	*
C50	Step and Shoot	95	200	715	Al+Cu	0.4	2	*
C51	Step and Shoot	95	200	715	Al+Cu	0.4	2	*
C52	Step and Shoot	95	200	715	Al+Cu	0.4	2	*
C54	Step and Shoot	95	200	715	Al+Cu	0.4	2	*
C55	Step and Shoot	95	200	715	Al+Cu	0.4	2	*
C56	Step and Shoot	95	200	715	Al+Cu	0.4	2	*
C3	Step and Shoot	100	200	400	Al+Cu	0.6	2	*

* Smoothing (1); Misalignment Compensation; Ring Artefact Reduction (10); Beam-Hardening Correction (30%); Find Z-Connection; Find X/Y Shift; Find Rotation; Apply Fusion.

Table M 4/5 - 2. Voxel dimensions used for various aspects of Chapter 4 and Chapter 5. Specimens were scanned using the Skyscan-1276 Micro-CT scanner at Adelaide Microscopy. Reconstruction dimensions represent the dimensions of the voxels following the reconstruction – these are the dimensions of the original, unaltered voxels. Foramen measurements were taken using the maximum possible voxel resolution. Endocast measurements were taken using the maximum possible voxel resolution. Maximum possible voxel resolution for endocast measurement was determined by dataset size as endocast segmentation is a memory intensive process. Specimens imaged at Adelaide Microscopy were resized to optimise voxel resolution against the computer performance trade-off.

Specimen #	Voxel Dimensions (µm) - Reconstruction			Voxel Dimensions (µm) - Foramen			Voxel Dimensions (µm) - Endocast		
	X	Y	Z	X	Y	Z	X	Y	Z
C19	20.477975	20.477975	20.477975	20.477975	20.477975	20.477975	40.95595	40.95595	40.95595
C21	20.477975	20.477975	20.477975	20.477975	20.477975	20.477975	40.95595	40.95595	40.95595
C29	20.520667	20.520667	20.520667	20.520667	20.520667	20.520667	41.041334	41.041334	41.041334
C44	20.513401	20.513401	20.513401	20.513401	20.513401	20.513401	41.026802	41.026802	41.026802
C45	20.513401	20.513401	20.513401	20.513401	20.513401	20.513401	41.026802	41.026802	41.026802
C47	20.519759	20.519759	20.519759	20.519759	20.519759	20.519759	41.039518	41.039518	41.039518
C32	20.477975	20.477975	20.477975	20.477975	20.477975	20.477975	40.95595	40.95595	40.95595
C34	20.516126	20.516126	20.516126	20.516126	20.516126	20.516126	41.032252	41.032252	41.032252
C35	20.517034	20.517034	20.517034	20.517034	20.517034	20.517034	41.034068	41.034068	41.034068
C36	20.512492	20.512492	20.512492	20.512492	20.512492	20.512492	41.024984	41.024984	41.024984
C57	20.477975	20.477975	20.477975	20.477975	20.477975	20.477975	40.95595	40.95595	40.95595
C66	20.515217	20.515217	20.515217	20.515217	20.515217	20.515217	41.030434	41.030434	41.030434
C67	20.506134	20.506134	20.506134	20.506134	20.506134	20.506134	41.012268	41.012268	41.012268
C50	20.512492	20.512492	20.512492	20.512492	20.512492	20.512492	41.024984	41.024984	41.024984
C51	20.515217	20.515217	20.515217	20.515217	20.515217	20.515217	41.030434	41.030434	41.030434
C52	20.516126	20.516126	20.516126	20.516126	20.516126	20.516126	41.032252	41.032252	41.032252
C54	20.508859	20.508859	20.508859	20.508859	20.508859	20.508859	41.017718	41.017718	41.017718
C55	20.507042	20.507042	20.507042	20.507042	20.507042	20.507042	41.014084	41.014084	41.014084
C56	20.505225	20.505225	20.505225	20.505225	20.505225	20.505225	41.01045	41.01045	41.01045
C3	20.528842	20.528842	20.528842	20.528842	20.528842	20.528842	41.057684	41.057684	41.057684